

Journal of
Mechanics of
Materials and Structures

Special issue on
Recent Advances in Impact Engineering

Volume 2, N° 10

December 2007

JOURNAL OF MECHANICS OF MATERIALS AND STRUCTURES

<http://www.jomms.org>

EDITOR-IN-CHIEF Charles R. Steele
ASSOCIATE EDITOR Marie-Louise Steele
Division of Mechanics and Computation
Stanford University
Stanford, CA 94305
USA

BOARD OF EDITORS

D. BIGONI University of Trento, Italy
H. D. BUI École Polytechnique, France
J. P. CARTER University of Sydney, Australia
R. M. CHRISTENSEN Stanford University, U.S.A.
G. M. L. GLADWELL University of Waterloo, Canada
D. H. HODGES Georgia Institute of Technology, U.S.A.
J. HUTCHINSON Harvard University, U.S.A.
C. HWU National Cheng Kung University, R.O. China
IWONA JASIUK University of Illinois at Urbana-Champaign
B. L. KARIHALOO University of Wales, U.K.
Y. Y. KIM Seoul National University, Republic of Korea
Z. MROZ Academy of Science, Poland
D. PAMPLONA Universidade Católica do Rio de Janeiro, Brazil
M. B. RUBIN Technion, Haifa, Israel
Y. SHINDO Tohoku University, Japan
A. N. SHUPIKOV Ukrainian Academy of Sciences, Ukraine
T. TARNAI University Budapest, Hungary
F. Y. M. WAN University of California, Irvine, U.S.A.
P. WRIGGERS Universität Hannover, Germany
W. YANG Tsinghua University, P.R. China
F. ZIEGLER Technische Universität Wien, Austria

PRODUCTION


PAULO NEY DE SOUZA Production Manager
SHEILA NEWBERY Senior Production Editor
SILVIO LEVY Scientific Editor

See inside back cover or <http://www.jomms.org> for submission guidelines.

Regular subscription rate: \$500 a year.

Subscriptions, requests for back issues, and changes of address should be sent to Mathematical Sciences Publishers, 798 Evans Hall, Department of Mathematics, University of California, Berkeley, CA 94720-3840.

©Copyright 2008. Journal of Mechanics of Materials and Structures. All rights reserved.

 mathematical sciences publishers

MECHANICS OF POLYCARBONATE DURING HIGH-RATE TENSION

SAI S. SARVA AND MARY C. BOYCE

Polymeric materials often undergo large inhomogeneous deformations at high rates during their use in various impact-resistant energy-absorbing applications. For better design of such structures, a comprehensive understanding of high-rate deformation under various loading modes is essential. In this study, the behavior of polycarbonate was studied during tensile loading at high strain rates, using a split-collar type split Hopkinson tension bar (SHTB). The effects of varying strain rate, overall imposed strain magnitude and specimen geometry on the mechanical response were examined. The chronological progression of deformation was captured with a high-speed rotating mirror CCD camera. The deformation mechanics were further studied via finite element simulations using the ABAQUS/Explicit code together with a recently developed constitutive model for high-rate behavior of glassy polymers. The mechanisms governing the phenomena of large inhomogeneous elongation, single and double necking, and the effects of material constitutive behavior on the characteristics of tensile deformation are presented.

1. Introduction

Polymeric materials are known to exhibit strong strain-rate sensitivity in many aspects of mechanical behavior including initial stiffness, yield stress, post-yield behavior and final failure. The mechanisms governing this rate dependence are particularly pronounced at very high rates, such as those occurring during impact loading events. Polymers are also known to exhibit a difference in properties in tension when compared to compression, where the yield stress depends on the pressure [Argon 1973; Spitzig and Richmond 1979; Caddell and Kim 1981], and the post-yield strain hardening depends on the developing molecular orientation [Arruda and Boyce 1993]. The compressive and tensile behavior of polymers has been widely studied under quasistatic conditions. The high-rate compressive behavior of polymers has been a topic of recent investigation by several groups [Walley and Field 1994; Moy et al. 2003; Mulliken and Boyce 2004, 2006; Siviior et al. 2005; Richeton et al. 2006]. In contrast, the high-rate tensile behavior has not been thoroughly studied due to the complex nature of the experimental techniques. However, it is important that the tensile properties be accurately evaluated to gather a complete understanding of the mechanics governing deformation at high rates and to help improved physics-based constitutive modeling of the high-rate behavior. In particular, a polymer which may deform in a ductile manner at low rates in tension may become brittle at high rates.

Keywords: dynamic tension, Hopkinson bar, polycarbonate, multiple necking, finite element modeling, ABAQUS.

This research was supported by the AFOSR through Defense University Research Initiative on Nanotechnology, under contract No. F49620-01-1-0447 and the ONR through contract No. N00014-04-10469 and, in part, by the Dupont–MIT Alliance. The authors acknowledge the high-rate test facilities of the MIT Institute for Soldier Nanotechnologies.

1.1. Background. The mechanical behavior of materials at high rates has been extensively studied over the past half of a century using numerous experimental procedures ranging from Taylor impact to split Hopkinson pressure bar (SHPB) to flyer-plate impact tests. Amongst these procedures, SHPB testing has been instrumental in obtaining high-rate stress-strain behavior. The history and theory of the SHPB are well documented [Kolsky 1963; Follansbee 1985; Gray 2000]. The basic design of a SHPB consists of a specimen sandwiched between two long rods, called the incident (or input) bar and the transmission (or output) bar. A shorter striker bar is impacted on to the incident bar, sending an elastic compressive pulse down the bar to the sample; this pulse gets partly reflected and partly transmitted due to the impedance mismatch between the bars and the sample. The incident, reflected, and transmitted pulses are measured using strain gauges attached to the bars and the stress-strain behavior of the sample is calculated using one-dimensional elastic wave theory. Though initially used for compression testing of metals, nominally at strain rates up to 10^4 s^{-1} , the SHPB has since been modified by many researchers to extend its capabilities to test a complete spectrum of materials (ceramics, polymeric/soft materials, composites), and a range of loading modes (tension, torsion); for some relevant examples, see [Chen et al. 1999; 2000; Gray 2000; Gray and Blumenthal 2000; Field et al. 2004].

High-rate studies of polymers in compression with the SHPB are further complicated due to their low density, low modulus and low yield stress. The low densities and low elastic wave velocities ultimately result in low impedances. The low impedance results in low amplitude of transmitted pulses, which increases the signal-to-noise ratio. To address these problems, many modifications have been suggested by various researchers. Low impedance bars made of titanium and magnesium have been used by Gray et al. [1997; 1998]. Polymeric bars have also been used to help reduce the impedance mismatch between the sample and the bars, thus increasing the magnitude of transmitted pulses [Wang et al. 1994; Zhao and Gary 1995; Sawas et al. 1998]. Chen et al. [1999] incorporated a hollow aluminum transmission bar to reduce the cross-sectional area ratio between the sample and the bar and improve the signal magnitude.

The earliest design changes to the SHPB to enable tensile loading conditions were made by Harding et al. [1960] during studies of metal alloys. In this design, the specimen is threaded between the incident and transmission bars and a tensile pulse is directly generated in the incident bar. One method of generating the tensile pulse incorporates a flange on the free end of the incident bar and a hollow striker bar that surrounds the incident bar. The striker bar is propelled towards the flange (in the direction away from the sample) to induce the incident tensile pulse. The principles of data analysis for the tensile tests are the same as those for compressive tests. An alternate design by Lindholm and Yeakley [1968] incorporates a solid incident bar and a hollow transmission bar. The inner diameter of the transmission bar is larger than the incident bar. A hat-shaped specimen is sandwiched between the bars such that the top of the hat rests on the end of the incident bar. The incident bar along with the sample then slides into the transmission bar until the brim of the hat rests against the hollow transmission bar. Upon the passing of a compressive pulse, the sample is loaded such that the sides of the hat are stressed in tension. Data analysis is again similar to compressive tests. The drawbacks for this design arise mainly from complexities due to the specimen geometry.

In a third design by Nicholas [1981], a threaded sample is attached between the two bars; a split collar surrounds the sample and is snugly sandwiched between the two bars. This collar enables the transmission of the initial compressive pulse into the second bar without loading the sample. The subsequent reflected tensile pulse (from the free rear end of the second bar) then loads the sample. This design is

desirable for its simplicity and has been used for the present studies. It is discussed further in [Section 2.1](#). The experimental difficulties in high-rate tensile testing are compounded by the large lengths and, often, the necessity to use samples of complex shapes. (Henceforth, we shall refer to a sample's gauge length more simply as its length and similarly refer to its gauge diameter as its diameter.) The large lengths increase the duration to attain dynamic equilibrium, invalidating a large portion of acquired data. Often pulse shaping techniques are necessary to increase the rise time of the loading pulses, delay the yield event until after dynamic equilibrium, and improve the quality of data. Also, large lengths limit the attaining of very large strain rates. Furthermore, as with all tensile tests, once specimen necking occurs, the data is not easily reduced to material stress-strain data.

Recently, a few studies have explored the testing of polymers under dynamic tension. [Chen et al. \[2002\]](#) studied the dynamic tensile behavior of Epon 828/T-403 epoxy and poly(methyl methacrylate) (PMMA) at strain rates up to 1200 s^{-1} using a SHTB with a hollow transmission bar. They noted that failure strains in dynamic tension were lower than during static tests; these two materials are brittle in tension and the failure strains were in the 5% range. [Cheng and Chen \[2003\]](#) studied the tensile stress-stretch behavior of ethylene-propylene-diene ter polymer (EPDM rubber) at stretching rates of $2800\text{--}3200\text{ s}^{-1}$ and demonstrated that the mechanical properties depended significantly on the stretching rate and that a Mullins effect (cyclic softening) also occurs under dynamic conditions. [Rae and Brown \[2005\]](#) studied properties of poly(tetrafluoroethylene) in high-rate tension with the help of a SHTB incorporated with a titanium transmission bar and observed moderate strain-rate and temperature sensitivity.

Significant advances have also been made in modeling the large strain, temperature, and rate-dependent constitutive behavior of glassy polymers and the underlying deformation micro-mechanisms [[Boyce et al. 1988](#); [Arruda and Boyce 1993](#); [Arruda et al. 1995](#)]. [Mulliken and Boyce \[2004; 2006\]](#) have recently further enhanced these previous constitutive models to incorporate mechanisms that are activated during high loading rates. An overview of micro-mechanisms of high-rate behavior of amorphous polymers is provided in [Section 2.2.1](#). The uniaxial tensile behavior of PC at rates exceeding 1000 s^{-1} is then presented using a SHTB facility designed and built for this purpose. The SHTB tests are numerically simulated and understood utilizing finite element analysis together with the physically based high-rate constitutive model of [Mulliken and Boyce \[2006\]](#).

2. Investigation protocol

2.1. Experimental procedures.

2.1.1. Split-collar SHTB. A split collar type SHTB was used for the present studies; [Figure 1](#) shows a schematic of the SHTB setup. 7075-T6 aluminum bars (diameter = 19.75 mm) were chosen to minimize the bar-polymer sample impedance mismatch and enhance the signal-to-noise ratio. The rear/second bar (1.524 m) was shorter than the front/first bar (3.048 m) and both contained threaded holes to accommodate samples. A representative sample geometry is shown in [Figure 1](#). The striker bar was approximately 48 cm in length and propelled using a pneumatic punch. The impact velocities of the striker bar were of the order of 20 ms^{-1} . The split collar (diameter = 25.4 mm; inner diameter = 12.7 mm) was tightly sandwiched between the bars, encompassing the sample. Upon impact of the striker bar, a compressive pulse lasting approximately $200\text{ }\mu\text{s}$ is generated in the first bar and travels down the length of the bar. On reaching the split collar, it shunts the sample and travels through the collar into the rear bar. In

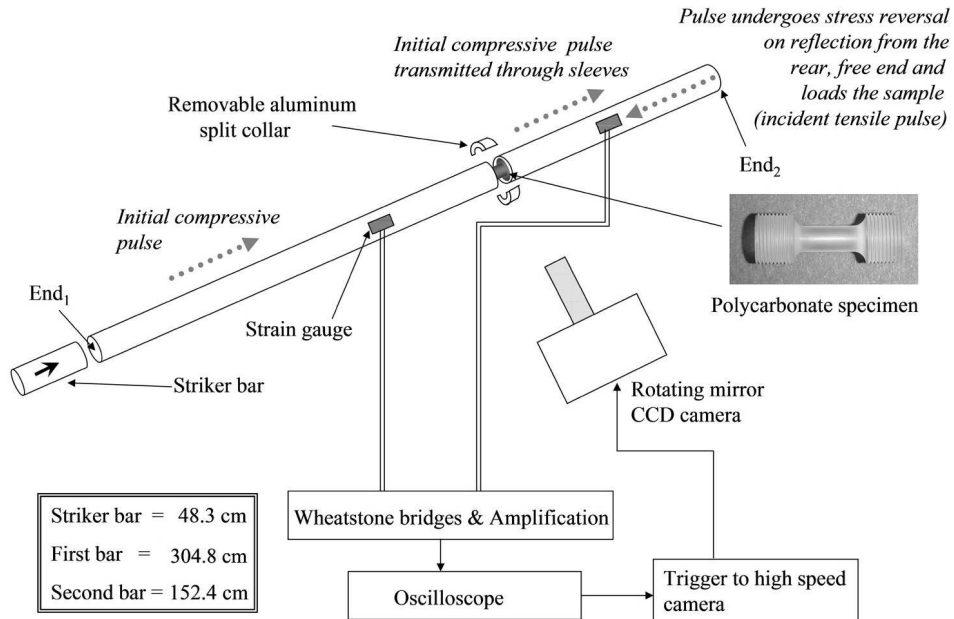


Figure 1. Schematic of the split-collar SHTB.

practice, it is not possible to prevent prestraining the sample; however, any prestraining is well below the elastic limit. The cross sectional area of the collar was chosen such that the initial compressive pulse was mostly transferred to the rear bar. Though a small portion of the initial pulse was reflected from the first bar-collar interface, the length of the first bar and the position of the strain gauges were such that this portion of the pulse and its subsequent reflection from the free end of the first bar (End₁ in Figure 1) did not interfere with the recording of the test data. The compressive pulse transmitted through the collar undergoes stress reversal upon rebounding from the free end of the rear bar (End₂ in Figure 1). The smaller rear bar length helps reduce the distance the tensile pulse travels to reach the sample, thus minimizing its dispersive distortion. Upon reaching the sample, the pulse loads the sample in tension, whereas the collar that is not physically joined to the bars remains unloaded. So, in effect, the rear bar acts as the ‘incident bar’ and the front bar acts as the ‘transmission bar’. The samples were machined to attach tightly to the bars. Also, pure annealed copper pulse shapers were placed at End₁ to cushion the impact of the striker bar. The pulse shaper lengthened the rise time considerably, leading to a delay in attaining peak stresses, thus improving dynamic equilibrium in the sample and also dampening the high frequency oscillations in the pulses [Gray and Blumenthal 2000].

The incident tensile, reflected, and transmitted pulses were measured with strain gauges attached on the bars at appropriate lengths. The gauge signals were routed through a Vishay 2100 strain gauge conditioner and amplifier system. The frequency response of the conditioner was extended to 50 kHz. The signals were acquired using a Lecroy Waverunner 14 bit oscilloscope. Figure 2 shows the raw strain gauge-signals gathered from separate strain gauges on the two bars. A small portion of the initial pulse that reflects from the bar-collar interface is also shown.

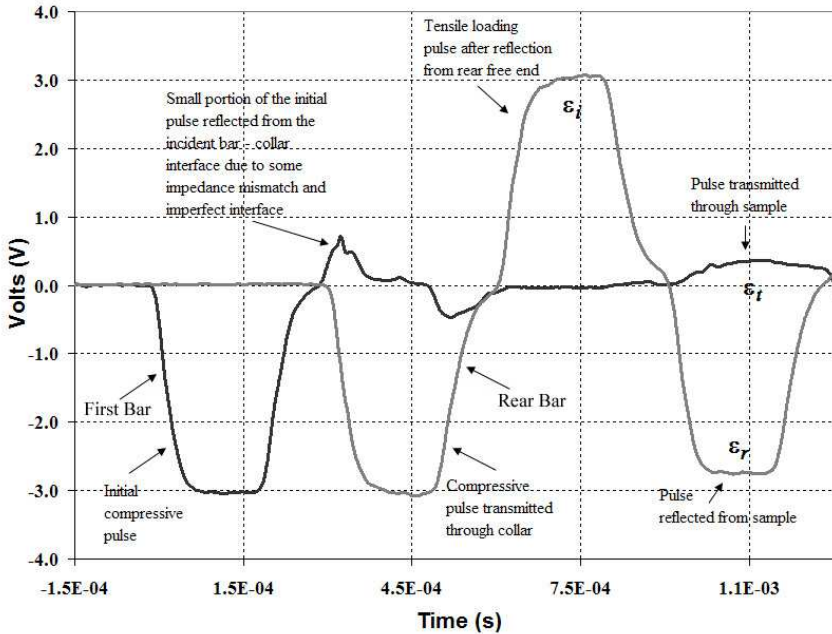


Figure 2. Raw strain gauge signals acquired during a dynamic tension test.

The axial force-displacement for the front and rear ends of the sample can be calculated from the incident ϵ_i , reflected ϵ_r and transmitted ϵ_t pulses using the relationships detailed here. The end displacements are

$$u_1 = c_0 \int (\epsilon_i - \epsilon_r) dt \quad u_2 = c_0 \int \epsilon_t dt.$$

Similarly the forces on the ends are:

$$F_1 = EA_0(\epsilon_i + \epsilon_r), \quad F_2 = EA_0\epsilon_t.$$

The force calculations on the two ends can be compared to verify how long it takes to achieve dynamic equilibrium during a test. [Figure 3](#) shows a comparison of forces at the incident and transmitted ends, calculated using $(\epsilon_i + \epsilon_r)$ and ϵ_t , respectively. Additionally, the above relationships also help calculate the time-resolved velocities of the end surfaces, which can be used as boundary conditions for finite element simulations. [Figure 4](#) shows the velocity profiles of the incident bar-specimen interface and transmission bar-specimen interface during a sample test.

2.1.2. High-speed photography. A Cordin 550 rotating mirror high-speed CCD camera with a Nikon 100 mm macro lens, capable of acquiring images at a frame rate of 2 million frames per second, was used to photograph the dynamic deformation of tensile samples. Because the collar encompasses the specimen, front and back windows were machined into the collar halves to help view the sample. Also, for samples with smaller lengths, a C-shaped collar was used to help photograph the sample. The camera was triggered via the oscilloscope, which had sent out a rising edge TTL trigger pulse after it had been

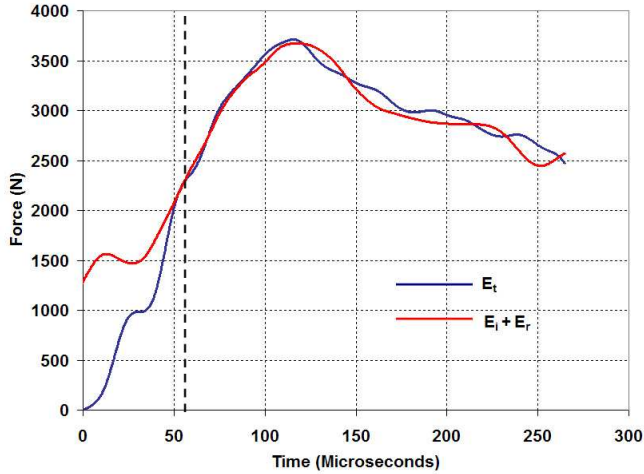


Figure 3. Sample time-resolved force signals calculated using $\epsilon_i + \epsilon_r$ and ϵ_t during a dynamic tension test.

triggered by the incident strain gauge pulse. A built-in trigger delay was used to synchronize the capture of images with the tensile test. The camera in turn triggered a high performance strobe for better illumination, which was placed behind the specimen for silhouette lighting of the specimen. The camera was programmed to record a sequence of 32 separate images at prescribed time intervals, and images were acquired from a point of view normal to the specimen.

2.1.3. Sample design. PC was chosen for the study due to its excellent combination of stiffness, strength, toughness, ductility, impact resistance, and transparency. Machine-grade PC was procured from GE Polymershapes in the form of a 12.7 mm diameter extruded rod. Threaded samples with varying length

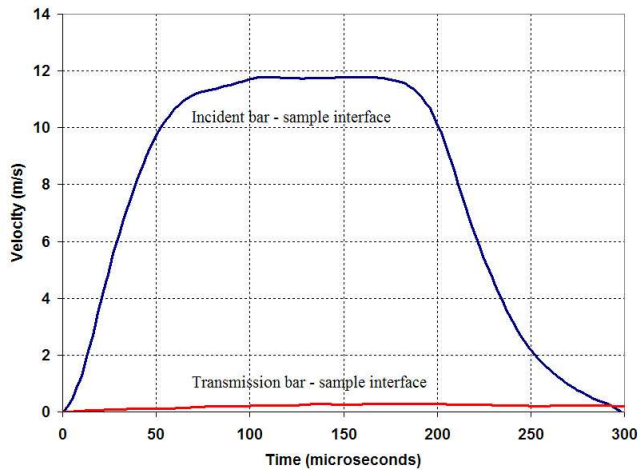


Figure 4. Sample time-resolved velocity profiles acquired during a dynamic tension test.

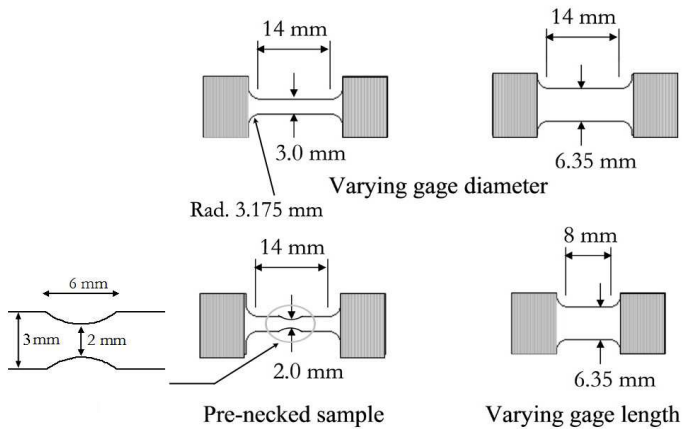


Figure 5. Sample geometries of specimens.

L_g and diameter D_g were machined to help achieve a range of strains and strain rates; see Figure 5. The maximum length L_g was ~ 14 mm (overall sample length ~ 20 mm).¹ Additionally, pre-necks were machined in the gauge section for some specimens to induce locally large deformations without using extremely large loading pulses. Compressive Hopkinson bar tests (strain rate $\sim 4 \times 10^3 \text{ s}^{-1}$) of specimens machined axially and transversely from the shipped rod samples showed the material to be fairly isotropic.

2.2. Numerical simulations.

2.2.1. Constitutive model. The stress-strain behavior of glassy polymers depends strongly on strain rate and temperature, and there exists a transitional threshold depending on strain rate and temperature beyond which the strain rate sensitivity significantly increases. The [Ree and Eyring \[1955\]](#) model for yield captures this transitional behavior using multiple thermally activated processes. Using data over a wide range in temperatures, but at quasistatic strain rates 10^{-4} s^{-1} to 10^{-1} s^{-1}), [Bauwens \[1972\]](#) related this transition in rate sensitivity to the secondary β viscoelastic transition.

[Mulliken and Boyce \[2004; 2006\]](#) have recently identified and quantitatively characterized this same β transition at very high strain rates. They conducted a comprehensive analytical and experimental study to examine the viscoelastic and viscoplastic behavior of glassy polymers. Dynamic mechanical analysis (DMA) was used to characterize the viscoelastic behavior of PC with focus on rate-dependent shifts of material transitions. These transitions (α , β) are observed to undergo temperature shifts with increasing strain rate, albeit at varying rates. Based upon the DMA test data, [Mulliken and Boyce \[2006\]](#) developed an analytical expression for the elastic modulus by decomposing the storage modulus into its respective α and β components to help predict the elastic behavior over a wide range of strain rates and temperatures, by appropriately shifting the storage modulus to the conditions (temperature and strain rate) at which the material can be expected to undergo a significant change in mechanical behavior.

¹It takes a minimum of three complete reverberations of the stress wave to attain dynamic equilibrium [[Follansbee 1985](#)], implying a duration of approximately $40 \mu\text{s}$ for this length. In practice, it may take even longer. The true duration must be physically verified by comparing the time-resolved forces on the front and back end [[Gray and Blumenthal 2000](#)].

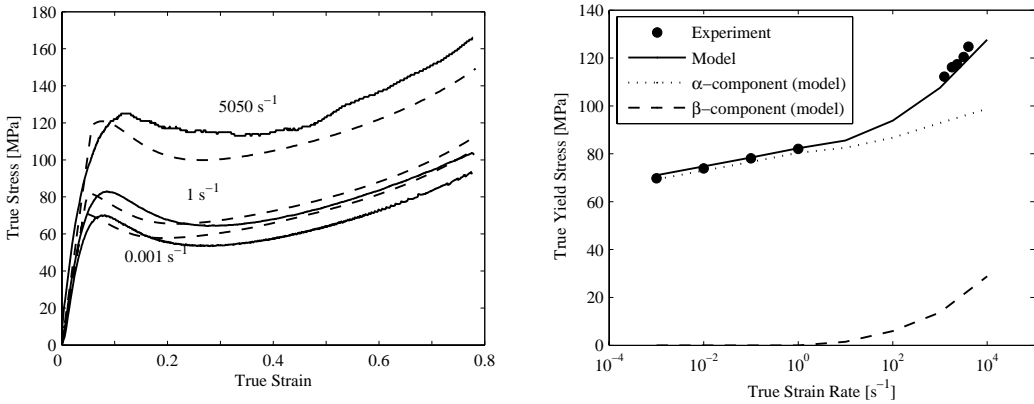


Figure 6. Experimental and model results of the uniaxial compressive stress-strain behavior over a range in strain rates; to the right, yield stress (data and model predictions) as a function of strain rate [Mulliken and Boyce 2006].

Large deformation uniaxial compression tests were conducted on PC under quasistatic and dynamic conditions to determine the rate-dependent yield and post-yield behavior. Figure 6 (left) shows the stress-strain curves for PC for both quasistatic and dynamic compressive tests. The constitutive behavior shows that yield is well defined and followed by strain softening and subsequent strain hardening. Rate sensitivity manifests in the form of increasing yield and flow stress values with increasing strain rate. At right, Figure 6 shows the yield stress plotted against strain rate. The yield stress is seen to increase linearly with strain rate. However, two distinct regions of strain rate sensitivity are observed, indicating a significant material transition in rate sensitivity at $\sim 1.5 \times 10^2 \text{ s}^{-1}$ at room temperature. This insight concerning the strain-rate sensitivity of the viscoelastic transitions was incorporated into a constitutive model by Mulliken and Boyce [2004; 2006].

Constitutive models to describe three-dimensional, temperature and rate dependent, finite-strain deformation of thermoplastic materials have been developed, for example, by Boyce et al. [1988], Arruda and Boyce [1993] and Arruda et al. [1995], and experimentally validated at low to moderate strain rates and

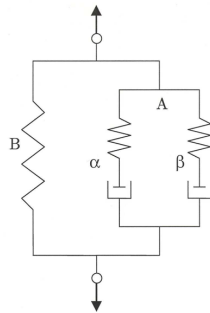


Figure 7. One-dimensional interpretation of the constitutive model [Mulliken and Boyce 2006].

temperatures for a variety of homogeneous and inhomogeneous loading conditions where the strain rates were less than 5 s^{-1} . The rate-dependent three-dimensional constitutive model, developed by Mulliken and Boyce [2006], extends the predictive capabilities to high rates and low temperatures. Figure 7 shows the one-dimensional rheological interpretation of the new model. Segment B is a nonlinear Langevin spring, which represents the molecular network resistance to stretching and alignment. Segment A has two subsegments (α and β) in parallel, each with an elastic spring and viscoplastic dashpot in series. Segment A represents the intermolecular resistance to chain-segment rotation. The two subsegments (α and β) indicate the two distinct thermally activated processes, associated with different molecular-level motions. For PC, the α process relates to the rotation of the polymer main chain and the β process to the local rotations of the main-chain phenyl group. At high temperatures and low strain rates, the contributions due to the β component are minimal and intermolecular resistance is primarily due to the α process. However, at higher rates/lower temperatures, the β process must be activated adding to the intermolecular resistance. The complete three-dimensional, finite-strain kinematical details and material description can be found in [Mulliken and Boyce 2006].

Figure 6 also demonstrates the accuracy of the model in describing the high-rate behavior of PC. At left, it shows the predicted stress-strain curves plotted against the experimentally obtained curves at three different strain rates. At right, it displays the model predictions² of yield stress versus strain rate compared to the experimental data. The yield stress values from α and β components are also plotted. The significance of the identification of the contribution made by the β process and its implementation into the constitutive model is evident. The adiabatic conditions at high rates result in significant temperature rise in polymers [Arruda et al. 1995; Garg et al. 2006], which can result in significant post-yield thermal softening; the amount of thermal softening in PC has been found to be modest [Garg et al. 2006] and hence its effect on the stress-strain behavior will be neglected here.

2.2.2. Stress-strain behavior of PC in tension. The constitutive response of PC under tension is distinctly different than under compression. Figure 8 shows a comparison of true stress-strain curves obtained using the constitutive model [Mulliken and Boyce 2006] at a range of strain rates ($0.001\text{--}10,000 \text{ s}^{-1}$) to simulate homogeneous uniaxial compression and tension. The inset in Figure 8 compares the effect of strain rate on the compressive and tensile yield stress. The tensile curves also display rate sensitivity: at the same strain rates, the yield stress values are observed to be lower in tension than in compression, due to pressure sensitivity of yield. Compared to compression, the strain hardening in tension is more dramatic and occurs at lower strains, a result of the strain-induced alignment of polymer chains. In tension, the molecular chains align uniaxially along the axis of elongation, whereas, in compression, the chains align in a plane normal to axis of compression, giving the very different strain hardening behavior.

Depending on the tensile stress-strain behavior of the polymer, tensile loading will produce a homogeneous elongation, a concentrated neck, or a neck that stabilizes and propagates up and down the

²As reported in [Sarva et al. 2007], the material parameters for the Mulliken–Boyce constitutive model for Lexan 9034 grade PC manufactured by GE Polymers are as follows: the storage modulus as a function of strain rate and temperature, Poisson ratio $\nu_\alpha = \nu_\beta = 0.38$; preexponential factors $\gamma_{0,\alpha}^p = 2.94 \times 10^{16} \text{ s}^{-1}$, $\gamma_{0,\beta}^p = 3.39 \times 10^5 \text{ s}^{-1}$; activation energies $\Delta G_\alpha = 3.744 \times 10^{-19} \text{ J}$, $\Delta G_\beta = 3.769 \times 10^{-20} \text{ J}$; softening slope $h_\alpha = 300 \text{ MPa}$; ratio of steady state to initial intrinsic resistance $s_{ss,\alpha}/s_{0,\alpha} = 0.58$; pressure coefficients $\alpha_{p,\alpha} = 0.168$, $\alpha_{p,\beta} = 0.245$; limiting chain extensibility $\sqrt{N} = 1.52$; rubbery modulus $nk\theta = 14.2 \times 10^6 \text{ MPa}$; density $\rho = 1210 \text{ kg m}^{-3}$; specific heat $C_p = 1200 \text{ J (kg-K)}^{-1}$; strain rate threshold $\dot{\epsilon}_{th} = 1 \times 10^{-4} \text{ s}^{-1}$.

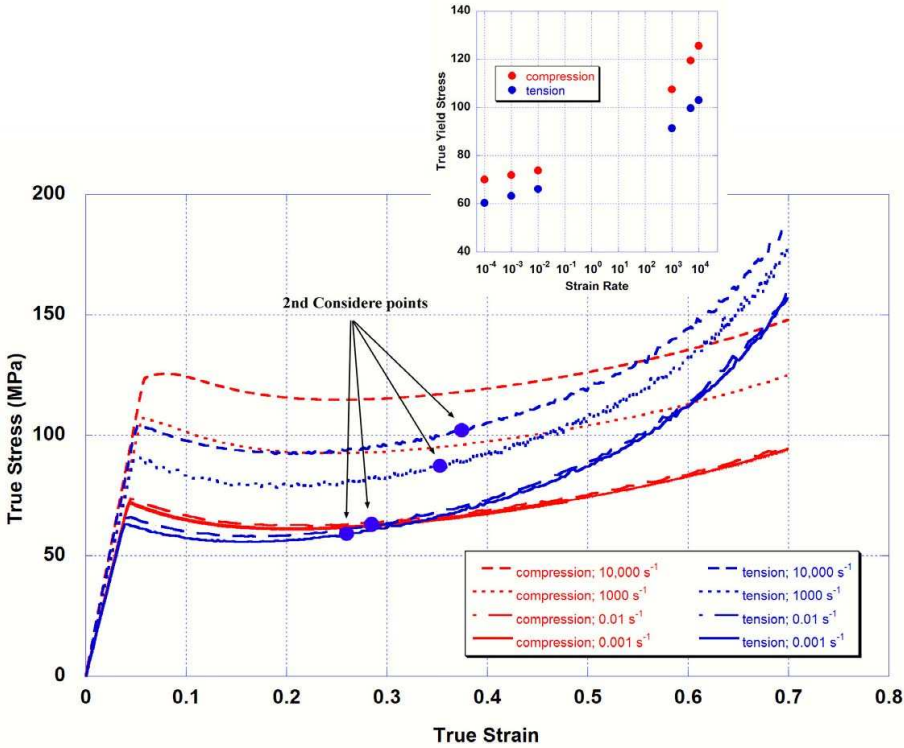


Figure 8. A comparison of the simulated true stress-strain behavior of PC in tension and compression at various strain rates.

specimen length (a process often referred to as cold drawing). A [Considère \[1885\]](#) construction identifies which tensile behavior a material will follow. Following Considère, a neck will initiate when the strain hardening slope fails to overcome the area reduction with tensile strain that occurs at $d\sigma/d\epsilon = \sigma$ (σ = true stress; ϵ = true strain). A neck will stabilize and propagate axially if the strain hardening has increased significantly to compensate for the area reduction as identified by the occurrence of a second Considère point ($d\sigma/d\epsilon = \sigma$) at a later strain. For our case of polycarbonate, the small plateau and/or softening after yield makes the yield point constitute the first Considère point, and a neck will initiate in tension. At larger strains, strain hardening is also significant enough that a second Considère point is found and the neck will stabilize and propagate. The second Considère points for each strain rate are depicted in the stress-strain curves of [Figure 8](#). This necking and cold drawing behavior will be studied further in the experimental data as well as the finite element simulations of the various tensile tests.

2.2.3. Finite element modeling. The constitutive model, outlined in [Section 2.2.1](#) and detailed in [\[Mulliken and Boyce 2006\]](#), was implemented into a commercial finite element code, ABAQUS/Explicit, through a user-defined material subroutine. Numerical simulations were conducted to study the deformation behavior of PC samples during quasistatic and dynamic tensile loading. The specimens were modeled as axisymmetric, and 4-node quadrilateral reduced-integration elements (ABAQUS type CAX4) were used. The aluminum Hopkinson bars were not included for simplicity. Experimentally obtained

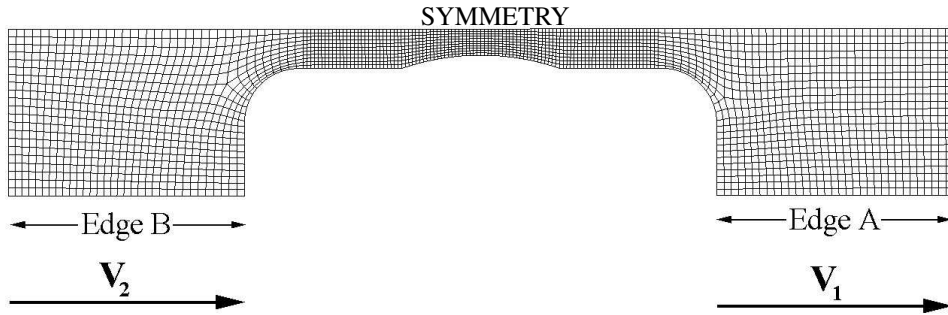


Figure 9. Sample axisymmetric mesh geometry for a precarved neck specimen.

time-resolved velocity profiles of the specimen bar interfaces, similar to those shown in [Figure 4](#), were used as the boundary conditions for the simulations. [Figure 9](#) shows a sample geometry that was used for a precarved neck specimen; a finer mesh was chosen for the gauge section, because the deformation was mostly concentrated in this region. The mesh density was varied from coarse to fine to verify that the chosen mesh provided accurate solutions, and a combined viscous-stiffness form of hourglass control (weight factor = 0.5) was used. No significant variation in results was observed when the viscous-stiffness weight factor was varied from zero (no damping) to one (pure damping). The velocity boundary conditions were applied to the gripping sides (see Edge A and Edge B in [Figure 9](#)). Simulations were also performed and studied wherein the boundary conditions were slightly varied (see [Appendix A](#)).

3. Results

Tensile tests were conducted for a range of loading conditions. First, for reference and comparison, quasistatic tensile tests were conducted on specimens with uniform diameters at two nominal strain rates. Then, dynamic tension experiments were conducted on a wide array of specimens with varying geometries. The length and diameter were altered and, in some instances, gentle ‘precarved neck’ regions were specified to vary the extent of inhomogeneity in the resulting deformation progressions. For each geometry, experiments were conducted with increasing striker bar velocity to increase the severity of loading. The experimental results for various cases in the form of nominal stress-strain relationships and photographs of the specimen at various stages of deformation are presented; the nominal stress is calculated as the force divided by the initial cross-sectional area and nominal strain is the increase in specimen length divided by the initial length, taken to be the length of the region with constant cross-sectional area (see [Figure 5](#)). Finite element simulations³ are presented for a few select specimen geometries to detail the mechanics of the deformation progression.

3.1. Quasistatic tests. As indicated earlier, the stress-strain behavior of PC will result in the classic necking and cold-drawing tensile behavior of polymers (for example and discussion, see [Boyce and](#)

³The material parameters for the following FEM simulations were chosen as follows: the limiting chain extensibility is $\sqrt{N} = 1.61$, the pressure coefficients are $\alpha_{p,\alpha} = \alpha_{p,\beta} = 0.105$, and the β -transition shift rate is $\sim 20^\circ\text{C}$ per decade of strain rate. The remaining material parameters are the same as those enumerated in Footnote 2 of [Section 2.2.1](#) and also reported in [\[Sarva et al. 2007\]](#).

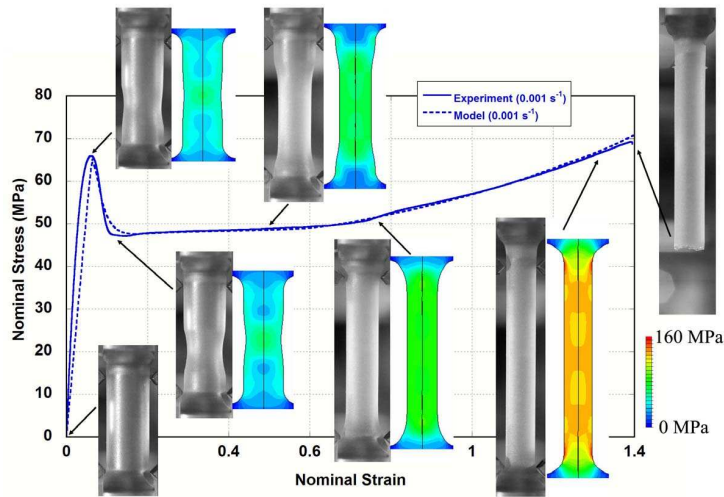


Figure 10. Nominal stress-strain behavior of PC in tension at a nominal strain rate of 0.001 s^{-1} .

Haward 1997]). To review this behavior, quasistatic tensile tests were performed using a Zwick screw driven mechanical tester. Figure 10 shows the nominal tensile stress-strain curve for one such test of a PC specimen ($L_g = 14 \text{ mm}$, $D_g = 6 \text{ mm}$) at a nominal strain rate of 0.001 s^{-1} . Photographs of the specimen at various stages of deformation are shown on the figure. The nominal stress-strain curve displays elastic elongation until yield, at which point a neck initiates in the gauge. The neck continues to develop, resulting in a dropping force level (and nominal stress) due to a combination of strain softening in the material and the localized reduction of the specimen cross-sectional area. The neck stabilizes due to the material strain hardening at large strains and axially propagates at near constant force level (and near constant neck diameter). Once the neck has traveled the full gauge length, the force begins to increase significantly due to straining and corresponding strain hardening of the highly strained gauge material. The model-predicted nominal stress-strain curve and the contours of axial stress at various stages of deformation are also shown in Figure 10 for comparison; the model is observed to accurately predict all features of quasistatic tensile behavior.

3.2. Dynamic tests.

3.2.1. Central necking in gauges with small aspect ratio: specimens with 6 mm diameter. Dynamic tension tests were conducted on specimens with 6 mm diameter and three different lengths: $\sim 5 \text{ mm}$, $\sim 8 \text{ mm}$ and $\sim 14 \text{ mm}$. Figure 11 shows the nominal stress-strain data; the dotted vertical lines indicate approximately when dynamic equilibrium was achieved in the specimens. In the above data, dynamic equilibrium occurs prior to the initial yielding of the specimen. The varying striker bar velocities and specimen lengths helped achieve a range of strain rates. The increase in the impact velocity of the striker bar also led to an increase in the attained total strain magnitudes. Overall strain rates ranging from $\sim 500 \text{ s}^{-1}$ to 900 s^{-1} for the 14 mm length samples, $\sim 1000 \text{ s}^{-1}$ to 1400 s^{-1} for the 8 mm length samples, and $\sim 1400 \text{ s}^{-1}$ to 1600 s^{-1} for the 5 mm length samples were achieved. Table 1 lists the data (yield stress, strain rate) pairs found for these tests, showing the rate dependence of yield. The initial yield

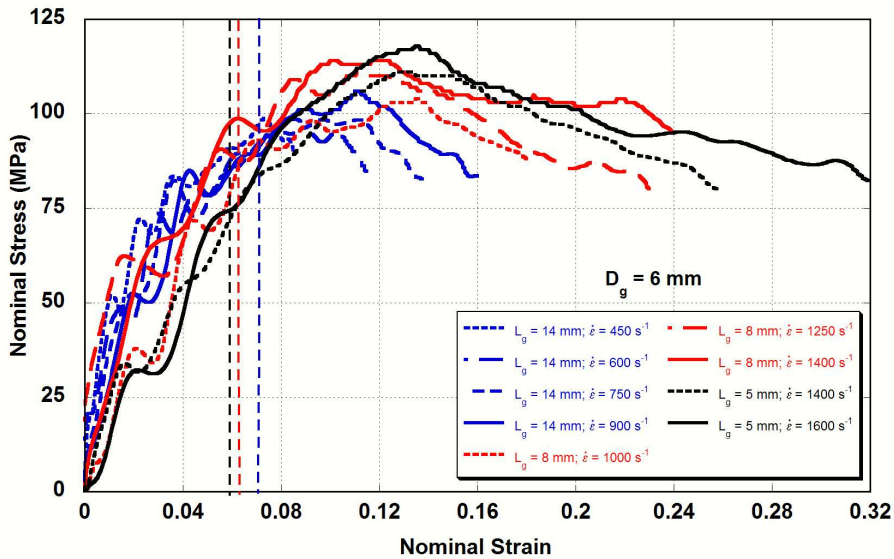


Figure 11. Nominal stress-strain relationships for tests with $D_g = 6$ mm, $L_g = 5$ mm, 8 mm and 14 mm at the indicated nominal strain rates $\dot{\epsilon}$.

stress is found to range from ~ 96 MPa at 600 s^{-1} to ~ 112 MPa at 1600 s^{-1} . After yield, the nominal stress decreases and a neck has initiated.

Figure 12 (top) shows high-speed photographs of an 8 mm length sample captured at various time intervals ($90 \mu\text{s}$, $200 \mu\text{s}$ and $300 \mu\text{s}$) corresponding to nominal strains of 0.06, 0.18 and 0.27 for the

Gauge Length - L_g (mm)	Nominal (Local) Strain Rate (s^{-1})	Nominal Yield Stress (MPa)
14	600 (1500)	96
14	750 (1875)	97
14	900 (2250)	100
8	1000 (2500)	102
8	1000 (2500)	102.5
8	1250 (3125)	108
8	1400 (3500)	112
5	1400 (3500)	106
5	1400 (3500)	108
5	1600 (4000)	106
5	1600 (4000)	112
5	1600 (4000)	112.5

Table 1. Yield stress at various strain rates for specimens with $D_g = 6$ mm.

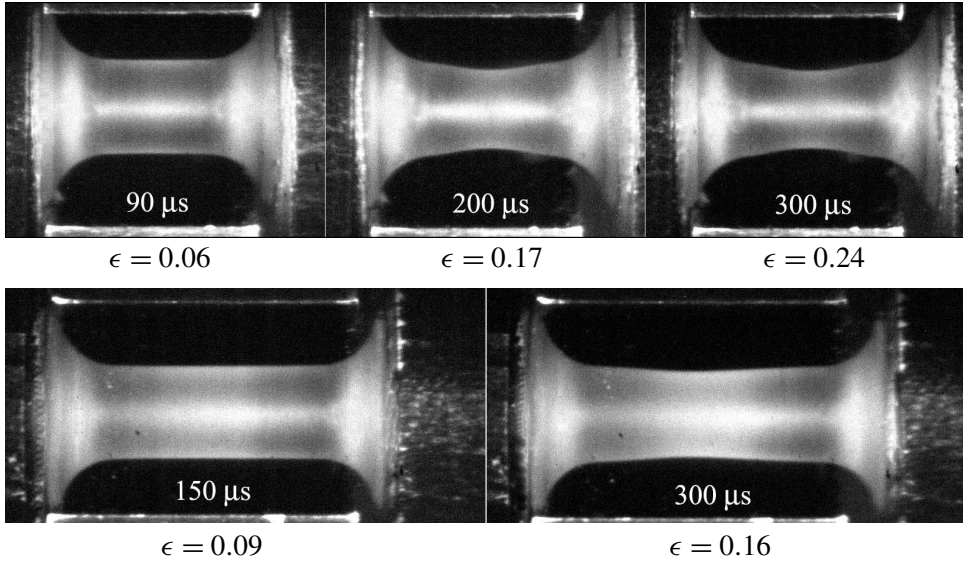


Figure 12. High-speed photographs for tests with $D_g = 6$ mm. Above, with $L_g = 8$ mm at a nominal strain rate $\dot{\epsilon} = 1400$ s $^{-1}$, and below, with $L_g = 14$ mm at $\dot{\epsilon} = 900$ s $^{-1}$.

dynamic tension test at 1400 s $^{-1}$. Until yield, the gauge uniformly elongates. At yield, a neck initiates at the middle whereupon deformation then localizes in the neck. The imposed conditions were not severe enough to fully develop the neck such that neck propagation would occur. Figure 12 (at bottom) shows the high-speed photographs captured during the deformation of a 14 mm length sample at 150 and 300 μ s, corresponding to nominal strains of 0.09 and 0.17. The 14 mm length sample also formed a single central neck at the center.

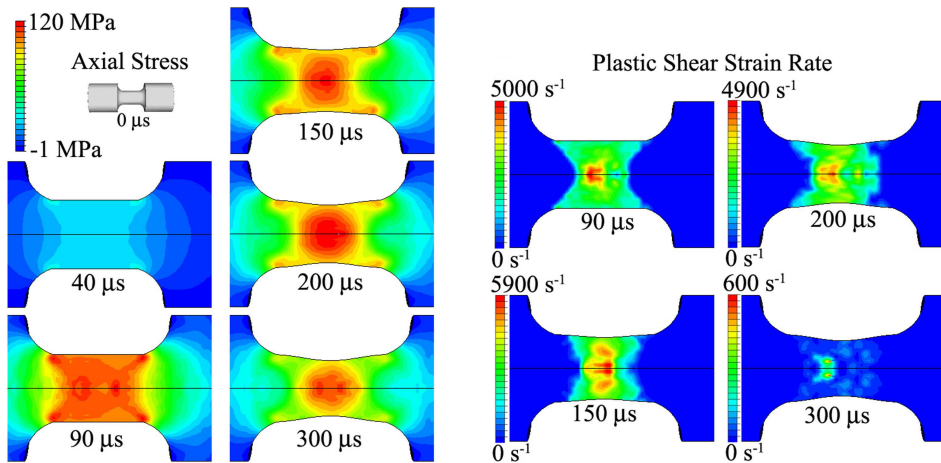


Figure 13. Progression of axial stress (left) and the effective plastic shear strain rate (right) during a test with $D_g = 6$ mm and $L_g = 8$ mm at $\dot{\epsilon} = 1400$ s $^{-1}$.

Simulations were performed to examine the mechanics of high-rate deformation in tension. Figure 13 (left) shows the contours of axial stress at various times during the deformation when $L_g = 8$ mm at 1400 s^{-1} . The intervals were chosen to enable a direct comparison with the high-speed photographs. The displacement initiates from the incident end, resulting in stress fields emanating from that end. After the initial stress wave reverberations, the stress is found to be relatively uniform in the gauge region as shown at $40 \mu\text{s}$ and $90 \mu\text{s}$, which corresponds to elastic deformation. Yielding then occurs at a stress level of 120 MPa and deformation then localizes in a neck at $150 \mu\text{s}$; stress levels are then higher in the neck region due to the reduced cross-sectional area. At $300 \mu\text{s}$, the stress levels in the neck begin to drop indicating the end of the test. The simulation is seen to replicate the inhomogeneous deformation profile observed in the high-speed photographs accurately.

Figure 13 (right) shows the concurrent evolution of the effective plastic shear strain rate. At $90 \mu\text{s}$, the plastic deformation has just initiated and begun to localize in the neck region. By $150 \mu\text{s}$ the deformation is fully localized in the neck and the local effective plastic shear strain rates reach values greater than 5000 s^{-1} in some pockets of the necked area. The effective plastic shear strain rate then diminishes as the sample is unloaded.

Figure 14 shows the simulated stress-strain data for a few tests with $L_g = 8$ mm and $L_g = 14$ mm. The corresponding experimental results were shown in Figure 11. The nodal reaction force outputs at the two opposite ends were used to calculate the nominal stress-strain relationships. The simulated curves agree favorably with the experimental results and also indicate the ambiguity in clearly identifying the precise yield stress from these tests; the stress levels are similar and also replicated are the features of the yield at ~ 0.1 strain, post-yield decrease in nominal stress, and rate sensitivity.

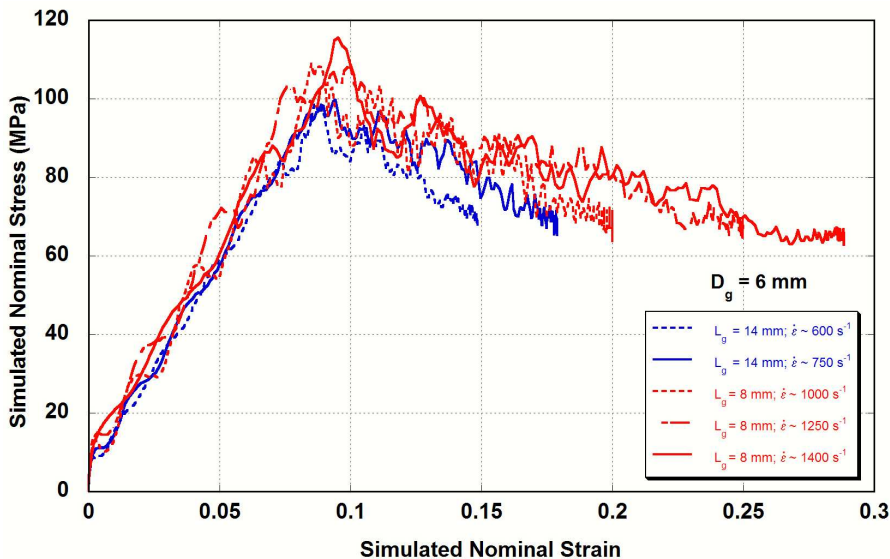


Figure 14. Simulation of stress-strain relationships for a few tests with $D_g = 6$ mm, $L_g = 8$ mm and $L_g = 14$ mm, shown experimentally in Figure 11.

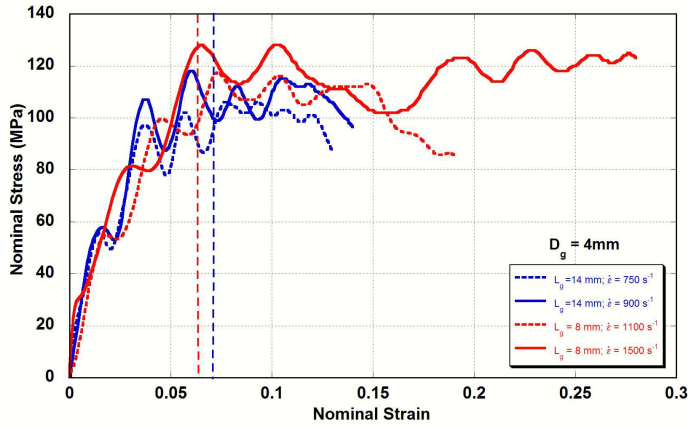


Figure 15. Nominal stress-strain relationships for tests with $D_g = 4$ mm and $L_g = 8$ mm and 14 mm.

3.2.2. Transition to double necking in gauges with large aspect ratio: specimens with 4 mm diameter. Samples with diameter of 4 mm were tested to examine the effects of aspect (L/D) ratio on the mechanics of necking during dynamic loading conditions. Figure 15 shows the nominal stress-strain data for the 8 mm and 14 mm length samples. The strains and strain rates attained are similar to those observed for the corresponding 6 mm diameter samples. Yield strains for these specimens are again observed to be in the ~ 0.1 range (similar to those observed in Figure 11).

Figure 16 shows high-speed photographs for tests with $L_g = 8$ mm and 14 mm. For the 8 mm length sample, elongation causes a single distinctive neck to form at the center. However, the bottom group shows that when the sample length is increased to 14 mm, the deformation mode undergoes a transition. The frame at $150 \mu\text{s}$ shows no necking. Further elongation leads to nearly simultaneous initiation of two distinct necks located equidistant from the center; see the frame at $225 \mu\text{s}$. Each neck further develops as seen in the frame at $280 \mu\text{s}$. This double necking has also been observed in metals by other researchers [Wood 1967; Rusinek et al. 2005] and is attributed to wave propagation during dynamic tensile elongation.

3.2.3. Specimens with 3 mm diameter. To further examine the phenomenon of multiple necking, samples were machined with even greater L/D ratio ($D_g = 3$ mm; $L_g = 8$ mm and 14 mm). The samples were tested, and Figure 17 shows the nominal stress-strain relationships. Overall nominal strain rates in the range of 800 s^{-1} and 1600 s^{-1} were achieved. Nominal stress levels well above 100 MPa are observed.

The top of Figure 18 shows high-speed photographs of the specimen with $L_g = 8$ mm at 1600 s^{-1} at various time intervals corresponding to nominal strains of 0.07, 0.21 and 0.3. The bottom of Figure 18 shows the silhouette photographs captured through the window in the collar for a test on a 14 mm length sample at 800 s^{-1} at various time intervals, corresponding to nominal strains of 0.08, 0.12 and 0.15. Similar to the 4 mm diameter samples, these show a single neck formation for the 8 mm length specimen and a double neck formation for the 14 mm length specimen. The loading conditions are such that the double necks become more fully developed for this 3 mm diameter case than those observed

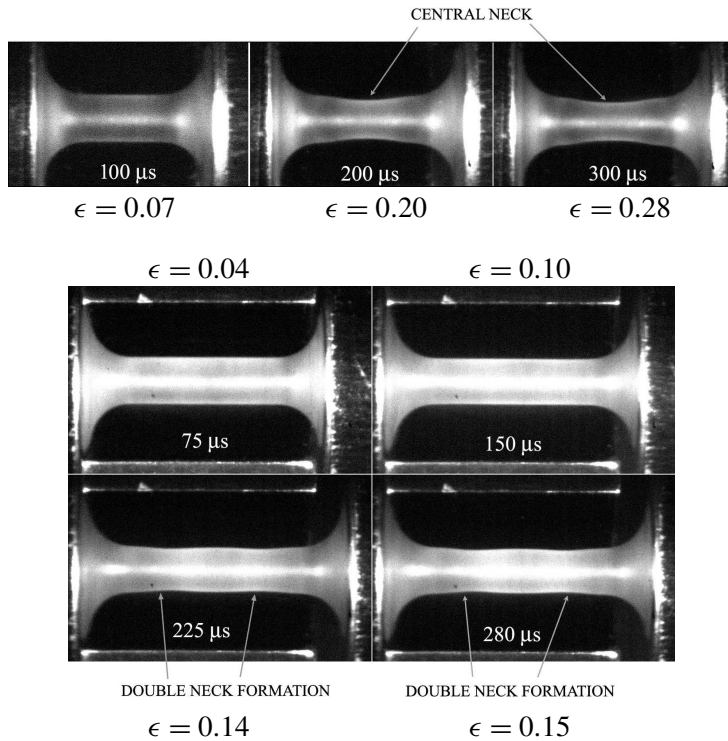


Figure 16. High-speed photographs for tests with $D_g = 4$ mm. At top, $L_g = 8$ mm and $\dot{\epsilon} = 1500$ s⁻¹. At bottom, $L_g = 14$ mm and $\dot{\epsilon} = 900$ s⁻¹.

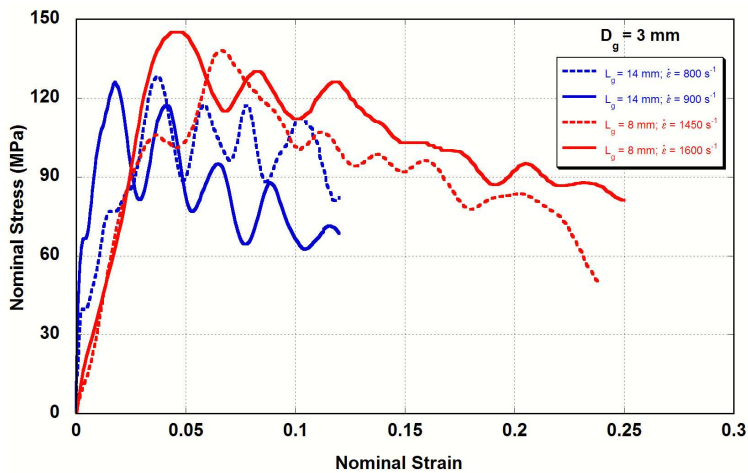


Figure 17. Nominal stress-strain relationships for tests with $D_g = 3$ mm and $L_g = 8$ mm and 14 mm.

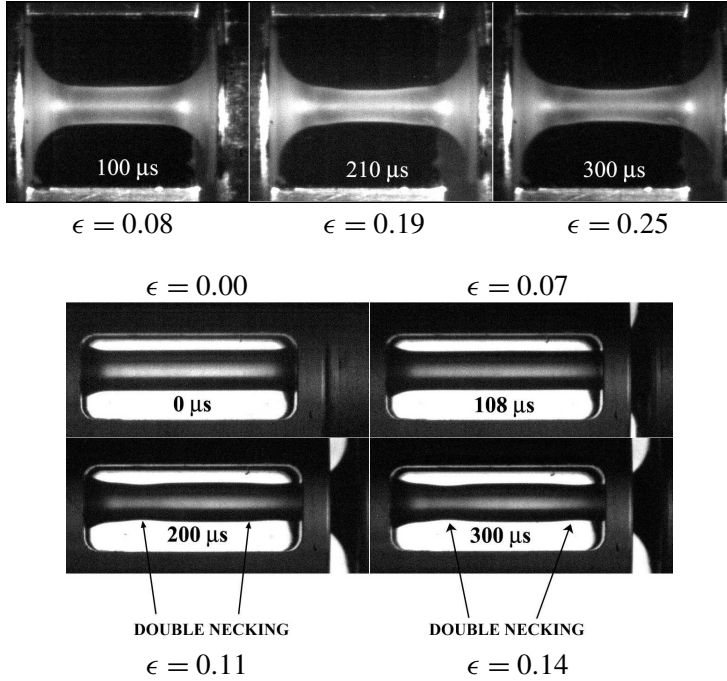


Figure 18. High-speed photographs for tests with $D_g = 3$ mm. At top, with $L_g = 8$ mm at $\dot{\epsilon} = 1600$ s⁻¹. At bottom, with $L_g = 14$ mm at $\dot{\epsilon} = 800$ s⁻¹.

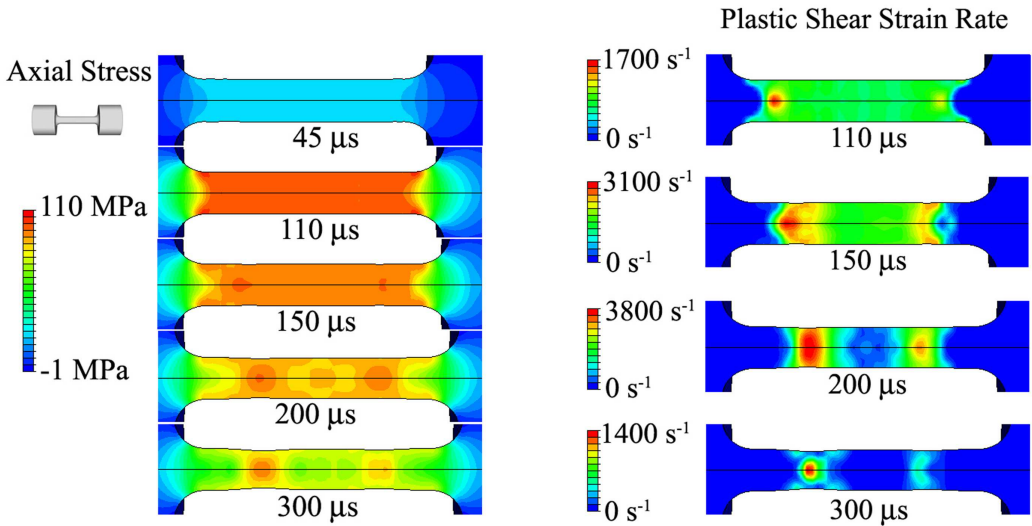


Figure 19. Progression of axial stress (left) and the effective plastic shear strain rate (right) during a test with $D_g = 3$ mm and $L_g = 14$ mm at $\dot{\epsilon} = 800$ s⁻¹.

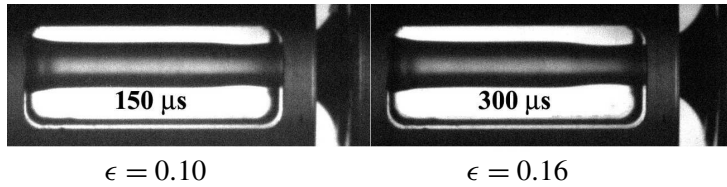


Figure 20. High-speed photographs for tests with $D_g = 3$ mm and $L_g = 14$ mm at $\dot{\epsilon} = 900$ s $^{-1}$.

earlier in the 4 mm diameter case (of the same length). At greater overall elongation, the left neck is observed to become dominant.

Simulations were performed to examine the double necking phenomenon. Figure 19 (left and right) shows the contours of axial stress and effective plastic shear strain rate, respectively, during a test with $D_g = 3$ mm and $L_g = 14$ mm at 800 s $^{-1}$. The contours show uniform deformation until reaching initial yield whereupon two necks initiate equidistant from the two ends. The second neck is seen to initiate within a few microseconds after the first neck initiates. As the deformation continues, the left neck begins to dominate.

3.2.4. The effect of loading velocity. The striker bar velocity and hence the strain rate were further increased for samples with $D = 3$ mm and $L_g = 14$ mm. Figure 20 shows the high speed photographs for such a test at a strain rate of 900 s $^{-1}$. Interestingly, as the loading velocity is further increased, the deformation mode changes to the formation of a single deep neck towards the incident/loading end; these observations were repeated for two tests performed under the same conditions. For slender gauges, the number of necks formed, their location, and which one becomes dominant are dependent on the elongation velocity and the boundary conditions (see Appendix A for a brief discussion of the gripping mechanism). The single neck formation at one end seen in Figure 20 has also been observed by Wood [1967] during tests on metals at higher elongation rates.

3.2.5. Drawing of neck in gauges with locally reduced cross section: specimens with 3 mm diameter and a 2 mm diameter precarved neck. SHTBs typically have limitations in the total displacement that can be attained during a test; the experimental limit was ~ 3 mm in the present equipment. Hence, a reduced diameter region (to be referred to as ‘precarved neck’) was precarved/machined in the gauge section to

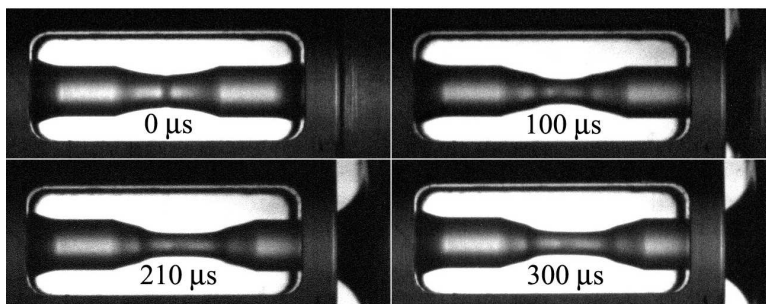


Figure 21. High-speed photographs obtained during a test with $D_g = 3$ mm, $L_g = 14$ mm and precarved neck diameter of 2 mm at an elongation rate of 9 ms $^{-1}$.

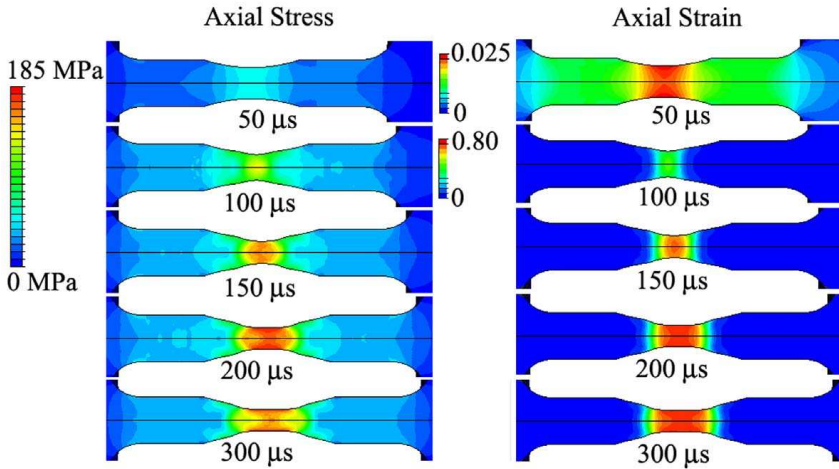


Figure 22. Progression of axial stress (left) and axial strain (right) during a test with $D_g = 3$ mm, $L_g = 14$ mm, and a precurved neck diameter of 2 mm.

enhance the local strain level so that it reaches a region of the stress-strain curve that exhibits significant strain hardening (recall [Figure 8](#)), enabling the neck to stabilize and axially propagate. [Figure 21](#) depicts the high-speed photographs obtained during a test on a sample with a precurved neck ($D_g \sim 3$ mm; $L_g \sim 14$ mm; precurved neck diameter ~ 2 mm). The deformation initially localizes in the precurved neck. As the necked region axially strains, the material strain hardening stabilizes the neck and the neck propagates. Since the precurved neck geometry is tapered (as opposed to being of initially uniform diameter), the location that first yields and further necks will continue to axially strain (and experience ongoing reduction in diameter) as the neck also axially propagates.

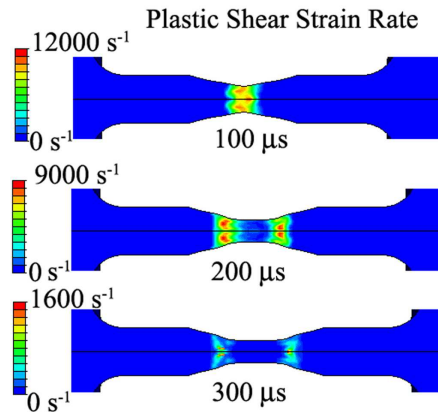


Figure 23. Contours of effective plastic shear strain rate at shown intervals during a test with $D_g = 3$ mm, $L_g = 14$ mm and precurved neck diameter of 2 mm.

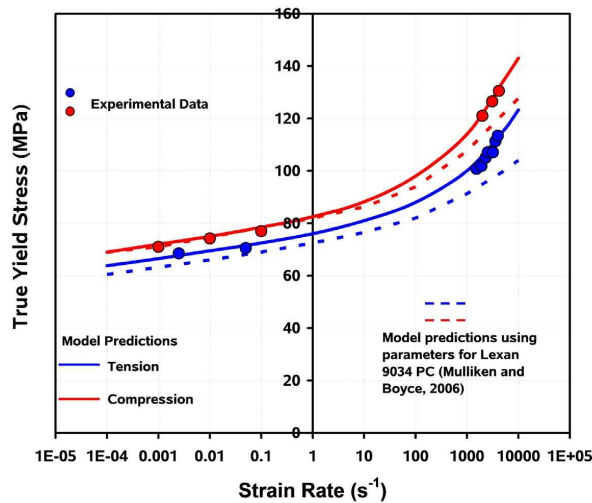


Figure 24. Comparison of the experimentally observed compressive and tensile yield stress values at various strain rates and the corresponding model predictions.

Simulations of the dynamic loading of the precarved specimen were found to successfully predict the details of the observed progression of deformation. Figure 22 shows the evolution of axial stress and axial strain contours during the test. The simulation is found to replicate the experimentally observed deformation profiles of Figure 21. Figure 23 shows the evolution of the effective plastic shear strain rate. The locally reduced cross-section of the precarved region has helped accomplish much greater local effective plastic shear strain rates than in samples with the larger uniform diameters. Effective plastic shear strain rates as high as 10000 s^{-1} are observed during the initial stages of plastic deformation. As the test progresses, the active plastic deformation rates are highest in the shoulder regions adjacent to the plastically developed neck, signifying axial propagation of the neck, that is, a cold drawing process.

4. Discussion

Figure 24 shows a comparison of the experimentally observed true yield stress values in compression⁴ and tension for the investigated PC and the corresponding model predictions. As expected, the yield stress values display an increased rate sensitivity at high rates in both compression and tension, and the yield stress values in tension are slightly lower than the corresponding values in compression at similar strain rates, due to the pressure sensitivity of yield. Note that the inhomogeneous nature of the initial yield during tension results in a locally higher strain rate at yield when compared to the nominal rate; through simulations we have determined this amplification to be by a factor of approximately 2.5.

Although some studies have been conducted to examine the effects of loading velocity on the necking in tensile metallic specimens, the phenomenon of dynamic necking in polymers has been largely unexplored. The earliest systematic experiments on dynamic necking were performed by Wood [1967] using tensile specimens made of various steels and alloys. He observed that as the extension rate is

⁴The high rate compression tests were performed on a compressive SHPB at MIT.

Aspect ratio	Gauge Dia.	Gauge Length	Strain Rate (Nominal)	Necking Mode
0.83	6 mm	5 mm	1400–1600 s ⁻¹	single central neck
1.33	6 mm	8 mm	1000–1400 s ⁻¹	single central neck
2.33	6 mm	14 mm	450–900 s ⁻¹	single central neck
2.00	4 mm	8 mm	1300–1500 s ⁻¹	single central neck
2.66	3 mm	8 mm	1450–1600 s ⁻¹	single central neck
3.50	4 mm	14 mm	600–900 s ⁻¹	double necking
4.66	3 mm	14 mm	600–800 s ⁻¹	double necking, neck opposite to loading side grows dominant
4.66	3 mm	14 mm	900 s ⁻¹	single neck, neck forms close to loading side

Table 2. A list of necking patterns for various test geometries and strain rates.

increased, the ductility of the material (defined as strain at failure) initially increases, then plateaus at higher velocities, and finally rapidly diminishes upon reaching a critical velocity. Correspondingly, the mode of necking changes from formation of a neck anywhere along the gauge section at static loading rates, to formation of a neck close to the fixed side as the velocity is increased, to the formation of symmetric double necks with fracture occurring at either neck, to formation of double necks with fracture occurring close to the loading end, and finally to induction of a single neck with fracture occurring close to the loading end.

Table 2 enumerates the inhomogeneous deformation modes for various test geometries and strain rates observed in the present study. For samples where the aspect ratio of the gauge section is less than three, the dynamic extension results in a single neck formation in the middle for strain rates up to 1600 s⁻¹. As the gauge is made more slender and the aspect ratio is increased (beyond three), the deformation mode changes to an almost simultaneous formation of two necks equidistant from the center. Note that a sample with $L_g = 14$ mm and $D_g = 6$ mm (Figure 12, bottom) shows a single neck, whereas samples with the same length but with 4 mm and 3 mm diameter show double necking (Figures 16, bottom, and 18, bottom). In the sample with $L_g = 14$ mm and $D_g = 3$ mm, which was tested at a strain rate of 800 s⁻¹, it is observed that with elongation, the neck opposite to the incident end grows dominant. When the strain rate was further increased for this geometry (to 900 s⁻¹), the necking mode then changed to formation of a single neck close to the incident end. These complex necking patterns arise from the wave propagation characteristics and the resulting interactions that depend on the specimen geometry and loading rate. The above test results do not span the gamut of necking modes recorded by Wood [1967], but the observed transitions are consistent with his experimental results on metals.

Along with the effects of geometry and rate, the stress-strain behavior of the material will strongly govern the necking behavior observed during dynamic tensile loading. Here, finite element simulations were conducted to examine the effects of stress-strain behavior on specimen deformation, while density and boundary conditions were kept the same. The material parameters in the model [Mulliken and Boyce 2006] were varied to obtain five different stress-strain behaviors as depicted in Figure 25 for a

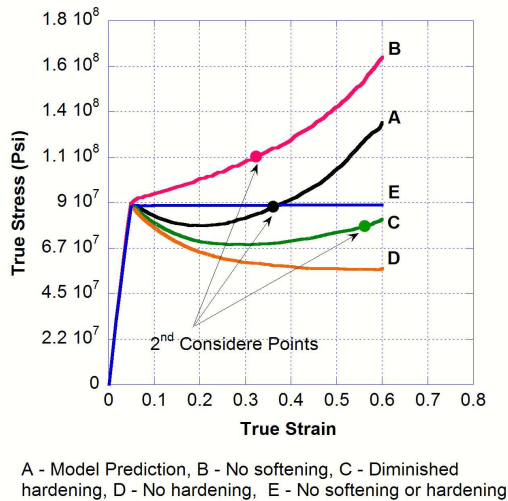


Figure 25. Comparison of five different cases of stress-strain behavior under uniaxial tension at $\dot{\epsilon} = 1000 \text{ s}^{-1}$.

strain rate of 1000 s^{-1} (the rate sensitivity of yield is identical for each case; it is the post-yield behavior that is varied as shown). Curve A shows the model prediction of the actual PC material. In curve B, post-yield strain softening has been suppressed and strain hardening begins immediately after yield; however, at these strain rates, the stress levels are such that this level of strain hardening does not suppress neck initiation (that is, this constitutive response does exhibit a first Considère point and also a second stabilizing Considère point). In curve C, the strain softening has been maintained and the strain hardening has been reduced, resulting in the second Considère point occurring at a much later strain. In curve D, the hardening has been completely eliminated, resulting in the extreme strain softening and no second Considère point. Finally, in curve E, both softening and hardening have been suppressed, resulting in constant stress levels after rate dependent yield and no second Considère point. Here, the effects of these five stress-strain behaviors on the neck initiation phenomenon during dynamic tensile loading of a high aspect ratio bar ($L_g = 14 \text{ mm}$ and $D_g = 3 \text{ mm}$) at a nominal strain rate of 800 s^{-1} are studied and the effects of these stress-strain behaviors on the deformation of the precarved neck case (and corresponding neck evolution with large strains) are also studied.

Figure 26 (left) shows the effect of constitutive behavior on the deformation of the high aspect ratio bar ($L_g = 14 \text{ mm}$ and $D_g = 3 \text{ mm}$) at a nominal strain rate of 800 s^{-1} . Contours of chain stretch⁵ (λ_{chain}) are plotted at $300 \mu\text{s}$ for each case. Case A shows the model prediction of the actual PC experiment which captures the observed behavior. For case B, a very gentle neck is initiated and the axial deformation is spread over a greater length of the specimen, significantly reducing the maximum induced stretch levels; this behavior is attributed to the strain hardening that ensues immediately after yield which tends to begin to stabilize and spread the deformation soon after initial yield. In case C, it is observed that the greater

⁵Stretch on a chain in an eight-chain network $\lambda_{\text{chain}} = \sqrt{\text{trace}(\bar{\mathbf{B}}_B)/3}$, where $\bar{\mathbf{B}}_B = (\det \mathbf{F})^{-2/3} \mathbf{F} \mathbf{F}^T$ and \mathbf{F} is the deformation gradient.

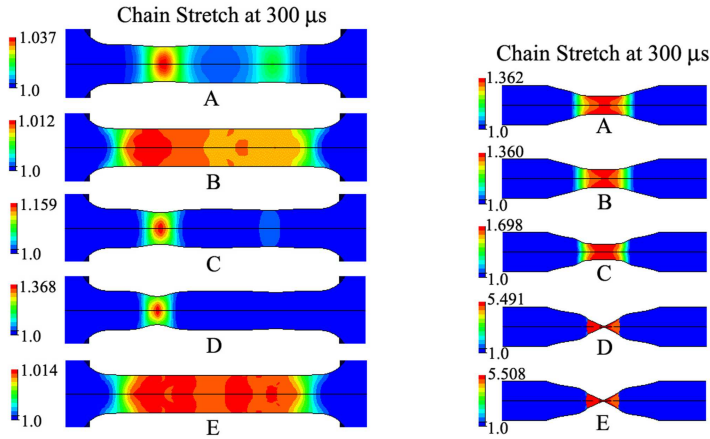


Figure 26. Left: effect of constitutive behavior on the necking for a test with $D_g = 3$ mm, $L_g = 14$ mm at $\dot{\epsilon} = 800$ s $^{-1}$. Right: with $D_g = 3$ mm, $L_g = 14$ mm and precarved neck diameter = 2 mm at $\dot{\epsilon} = 9$ ms $^{-1}$.

strain softening and delayed strain hardening results in the double neck formation where the deformation is found to be more localized with even more prominent neck formation than the reference case A. In case D, where the hardening has been eliminated, the localization is extreme and one neck is greatly dominant. For case E, a single neck initiates, albeit in a more gentle manner than those cases with strain softening, demonstrating as expected the role of strain softening in highly localizing the deformation.

Figure 26 (right) shows the effect of constitutive behavior on the deformation of a 3 mm diameter sample with a 2 mm precarved neck. Case A shows the model prediction which captures the experimentally observed drawing of the neck. Case B, in which the softening has been suppressed, shows the deformation profile to be similar due to the presence of the initial precarved neck region (where the precarved neck aids in creating the initial local neck—this material exhibits a relatively weak first Considère point in its inherent behavior); the post-yield strain hardening then axially propagates the deformation. Case C exhibits a greater stretching of the necked region prior to axial propagation of the neck (cold drawing) due to the second Considère point occurring at a larger axial strain. In case D, in which the hardening is eliminated, the deformation fully localizes in a neck which never stabilizes (no second Considère point) as expected; note that failure was not incorporated in the model. In case E, in which both softening and hardening are removed, the deformation also fully localizes in an unstable neck, as expected.

5. Summary

Polymers are extensively used in applications where they are routinely subjected to deformations at large strain rates, but very few studies of the dynamic tensile behavior of polymers have been conducted due to the intricate nature of the experimental techniques as well as the difficulty in capturing the subtleties of the constitutive stress-strain behavior in simulations. Yet, it is essential that polymers are tested under dynamic tension for a complete evaluation of their high-rate constitutive behavior and also for studying the progression of such typically inhomogeneous deformations. In this study, a comprehensive experimental and finite element study of polycarbonate was conducted to examine the mechanics of inhomogeneous

deformations over wide ranging conditions of high-rate tension. A range of test conditions was achieved by varying the loading velocity and modifying the specimen geometry. The high-rate tensile yield behavior was quantified at nominal strain rates of $500\text{--}1500\text{ s}^{-1}$ and compared with the quasistatic tensile behavior. Depending on the aspect ratio and the cross sectional area, deformation modes ranging from single necking to double necking to drawing of the neck were observed. For each case, the progression of deformation was recorded through high speed photography and the mechanics were examined using finite element simulations along with a three-dimensional elastic-viscoplastic constitutive model for the high-rate behavior of glassy polymers. The model accurately predicted the deformation profiles for the entire spectrum of test conditions. The changes in necking behavior of polymers under dynamic tension had hitherto not been characterized. At high rates, in addition to the material stress-strain behavior and its rate sensitivity, the inhomogeneous deformation modes were seen to be governed by wave propagation effects and the ensuing interaction with specimen geometry. A parametric finite element study was also performed to examine the effects of stress-strain behavior on the necking mode. These observations also indicated that it is critical that the constitutive model accurately predict all features of the stress-strain behavior to capture the overall inhomogeneous deformations. This study accomplishes a quantitative study of tensile yield stress of polycarbonate, characterizes the necking modes for a multitude of test conditions, unravels the mechanics of tensile elongation, and validates a high-rate constitutive model for a range of inhomogeneous deformations.

Appendix A. The effects of boundary conditions

Ideally, it is preferred that the gripping method have very little bearing on the tensile deformation of the specimen, but it is often observed to affect the dynamic deformation patterns. In a gripping technique such as that used in the present study (threaded ends), one has to pay careful attention to the consistency in the machining of these ends, since small variations in the threading dimensions can lead to changes in the gripping mode. To examine the effects of such variations, numerical simulations were performed with slightly altered boundary conditions.

Figure 27 compares three such variations in boundary conditions. In case A, the grip region perimeter is restrained in the radial direction and the velocity profiles are applied to these sides to model a tightly threaded sample. The simulated deformation profile displays double necking, in which the right neck is more dominant. In case B, the perimeter is still radially restrained, but the velocity profiles are applied only to the opposing parallel faces and not to the entire sides. This results in a deformation mode change such that a greatly dominant neck is formed to the left. In the third case, the boundary conditions are changed so that the perimeter is no longer radially constrained, and the velocity profiles are applied to grip region as shown. These conditions represent a scenario in which the sample is loosely threaded in the bars, allowing for radial movement of the dog-bone ends. For this case, the simulation matches the experimentally observed double necking seen in the high speed photographs (Figure 18, bottom), wherein the left neck is more dominant. These results clearly demonstrate the susceptibility of the deformation mode to the gripping method and the need for careful consideration of such factors when analyzing the dynamic deformations.

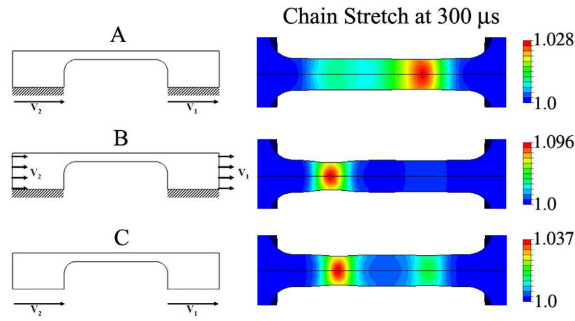


Figure 27. Effect of boundary conditions on the deformation of a sample with $D_g = 3$ mm, $L_g = 14$ mm at $\dot{\epsilon} = 800$ s $^{-1}$; contours of chain stretch at 300 μ s are plotted.

Appendix B. The effect of variation in density

Similarly, simulations were performed to examine the effects of variations in the material density. The density was varied at intervals from $0.1 \rho_{PC}$ to $2 \rho_{PC}$ ($\rho_{PC} = 1.21$ g/cm 3), while the remaining material parameters were unchanged. The deformation modes were seen to vary significantly as the density was varied (see Figure 28). As the material density increased, simulations showed a marked reduction in the wave propagation speed (note that the longitudinal elastic wave speed $C_e \sim \sqrt{E/\rho}$; E = Elastic Modulus), slowing the deformation process. The resulting necking pattern then depended on how the wave propagates within the specific specimen geometry. These results show the manner in which any mass inertia effects during the dynamic loading may affect the wave propagation, ultimately affecting the overall deformation.

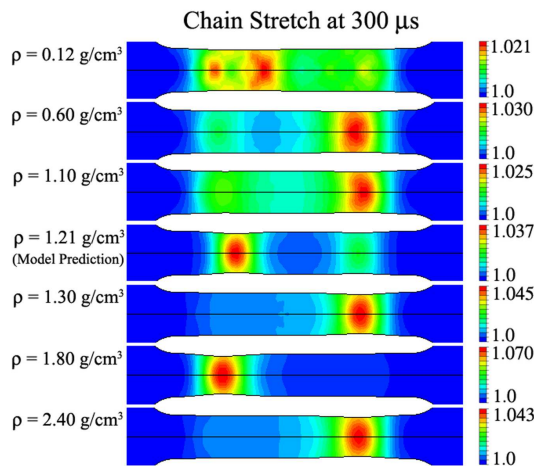


Figure 28. Effect of density on the deformation of a sample with $D_g = 3$ mm, $L_g = 14$ mm at $\dot{\epsilon} = 800$ s $^{-1}$; contours of chain stretch at 300 μ s are plotted.

Acknowledgements

The authors thank Adam D. Mulliken for providing the user subroutine for the constitutive model and Mohit Garg and Sharon Y. Soong for their assistance during the experiments.

References

- [Argon 1973] A. S. Argon, “A theory for the low-temperature plastic deformation of glassy polymers”, *Philos. Mag.* **28**:4 (1973), 839–865.
- [Arruda and Boyce 1993] E. M. Arruda and M. C. Boyce, “Evolution of plastic anisotropy in amorphous polymers during finite straining”, *Int. J. Plasticity* **9**:6 (1993), 697–720.
- [Arruda et al. 1995] E. M. Arruda, M. C. Boyce, and R. Jayachandran, “Effects of strain rate, temperature and thermomechanical coupling on the finite strain deformation of glassy polymers”, *Mech. Mater.* **19**:2-3 (1995), 193–212.
- [Bauwens 1972] J. C. Bauwens, “Relation between the compression yield stress and the mechanical loss peak of bisphenol-A-polycarbonate in the β transition range”, *J. Mater. Sci.* **7**:5 (1972), 577–584.
- [Boyce and Haward 1997] M. C. Boyce and R. N. Haward, “The post yield deformation of glassy polymers”, pp. 213–293 in *The physics of glassy polymers*, edited by R. N. Haward and R. Young, Chapman and Hall, London, 1997.
- [Boyce et al. 1988] M. C. Boyce, D. A. Parks, and A. S. Argon, “Large inelastic deformation of glassy polymers. part I: Rate dependent constitutive model”, *Mech. Mater.* **7**:1 (1988), 15–33.
- [Caddell and Kim 1981] R. M. Caddell and J. W. Kim, “Influence of hydrostatic pressure on the yield strength of anisotropic polycarbonate”, *Int. J. Mech. Sci.* **23**:2 (1981), 99–104.
- [Chen et al. 1999] W. Chen, B. Zhang, and M. J. Forrester, “A split-Hopkinson bar technique for low-impedance materials”, *Exp. Mech.* **39**:2 (1999), 81–85.
- [Chen et al. 2000] W. Chen, F. Lu, and B. Zhou, “A quartz-crystal-embedded split Hopkinson pressure bar for soft materials”, *Exp. Mech.* **40** (2000), 1–6.
- [Chen et al. 2002] W. Chen, F. Lu, and M. Cheng, “Tension and compression tests of two polymers under quasi-static and dynamic loading”, *Polym. Test.* **21**:2 (2002), 113–121.
- [Cheng and Chen 2003] M. Cheng and W. Chen, “Experimental investigation of the stress-stretch behavior of EPDM rubber with loading rate effects”, *Int. J. Solids Struct.* **40**:18 (2003), 4749–4768.
- [Considère 1885] A. G. Considère, “Mémoire sur l’emploi du fer et de l’acier dans les constructions”, *Annales des Ponts et Chaussées (ser. 6)* **9** (1885), 574–775.
- [Field et al. 2004] J. E. Field, S. M. Walley, W. G. Proud, H. T. Goldrein, and C. R. Siviour, “Review of experimental techniques for high rate deformation and shock studies”, *Int. J. Impact Eng.* **30**:7 (2004), 725–775.
- [Follansbee 1985] P. S. Follansbee, *The Hopkinson bar*, vol. 8, 9th ed., American Society for Metals, Metals Park, OH, 1985.
- [Garg et al. 2006] M. Garg, A. D. Mulliken, and M. C. Boyce, “Temperature rise in polymeric materials during high rate deformation”, *J. Appl. Mech.* (2006). Accepted for publication.
- [Gray 2000] G. T. Gray, *Classic split-Hopkinson pressure bar testing*, vol. 8, 10th ed., ASM International, Materials Park, OH, 2000.
- [Gray and Blumenthal 2000] G. T. Gray and W. R. Blumenthal, *Split-Hopkinson pressure bar testing of soft materials*, vol. 8, 10th ed., ASM International, Materials Park, OH, 2000.
- [Gray et al. 1997] G. T. Gray, W. R. Blumenthal, C. P. Trujillo, and R. W. Carpenter, “Influence of temperature and strain rate on the mechanical behavior of adiprene L-100”, *Journal de Physique (France) IV Colloquium, C3 (EURODYMAT 97)* **7** (1997), 523–528.
- [Gray et al. 1998] G. T. Gray, C. M. Cady, and W. R. Blumenthal, “Influence of temperature and strain rate on the constitutive behavior of Teflon and Nylon”, pp. 955–958 in *Plasticity 99: constitutive and damage modeling of inelastic deformation and phase transformation*, edited by A. S. Kahn, Neat Press, Fulton, MD, 1998.
- [Harding et al. 1960] J. Harding, E. O. Wood, and J. D. Campbell, “Tensile testing of materials at impact rates of strain”, *J. Mech. Eng. Sci.* **2** (1960), 88–96.
- [Kolsky 1963] H. Kolsky, *Stress waves in solids*, Dover, New York, 1963.

- [Lindhholm and Yeakley 1968] U. S. Lindholm and L. M. Yeakley, “High strain-rate testing: tension and compression”, *Exp. Mech.* **8**:1 (1968), 1–9.
- [Moy et al. 2003] P. Moy, T. Weerasooriya, A. Hsieh, and W. Chen, “Strain rate response of a poly-carbonate under uniaxial compression”, pp. 269–275 in *Proceedings of the SEM Annual Conference on Experimental and Applied Mechanics* (Charlotte, NC), 2003.
- [Mulliken and Boyce 2004] A. D. Mulliken and M. C. Boyce, “Low to high strain rate deformation of amorphous polymers”, pp. Paper No. 197 in *Proceedings of the 2004 SEM X International Congress and Exposition on Experimental and Applied Mechanics*, Costa Mesa, CA, 2004.
- [Mulliken and Boyce 2006] A. D. Mulliken and M. C. Boyce, “Mechanics of rate-dependent elastic-plastic deformation of glassy polymers from low to high strain rates”, *Int. J. Solids Struct.* **43**:5 (2006), 1331–1356.
- [Nicholas 1981] T. Nicholas, “Tensile testing of materials at high rates of strain”, *Exp. Mech.* **21**:5 (1981), 177–185.
- [Rae and Brown 2005] P. J. Rae and E. N. Brown, “The properties of poly(tetrafluoroethylene) (PTFE) in tension”, *Polymer* **46**:19 (2005), 8128–8140.
- [Ree and Eyring 1955] T. Ree and H. Eyring, “Theory for non-newtonian flow I. Solid plastic system”, *J. Appl. Phys.* **26**:7 (1955), 793–800.
- [Richeton et al. 2006] J. Richeton, S. Ahzi, K. S. Vecchio, F. C. Jiang, and R. R. Adharapurapu, “Influence of temperature and strain rate on the mechanical behavior of three amorphous polymers: Characterization and modeling of the compressive yield stress”, *Int. J. Solids Struct.* **43**:7-8 (2006), 2318–2335.
- [Rusinek et al. 2005] A. Rusinek, R. Zaera, J. R. Klepaczko, and R. Cheriguene, “Analysis of inertia and scale effects on dynamic neck formation during tension of sheet steel”, *Acta Mater.* **53**:20 (2005), 5387–5400.
- [Sarva et al. 2007] S. Sarva, A. D. Mulliken, and M. C. Boyce, “Mechanics of Taylor impact testing of polycarbonate”, *Int. J. Solids Struct.* **44**:7-8 (2007), 2381–2400.
- [Sawas et al. 1998] O. Sawas, N. S. Brar, and R. A. Brockman, “Dynamic characterization of compliant materials using an all-polymeric split Hopkinson bar”, *Exp. Mech.* **38**:3 (1998), 204–210.
- [Sivior et al. 2005] C. R. Sivior, S. M. Walley, W. G. Proud, and J. E. Field, “The high strain rate compressive behaviour of polycarbonate and polyvinylidene difluoride”, *Polymer* **46**:26 (2005), 12546–12555.
- [Spitzig and Richmond 1979] W. A. Spitzig and O. Richmond, “Effect of hydrostatic pressure on the deformation behavior of polyethylene and polycarbonate in tension and in compression”, *Polym. Eng. Sci.* **19**:16 (1979), 1129–1139.
- [Walley and Field 1994] S. M. Walley and J. E. Field, “Strain rate sensitivity of polymers in compression from low to high rates”, *DYMAT J.* **1**:3 (1994), 211–227.
- [Wang et al. 1994] L. Wang, K. Labibes, Z. Azari, and G. Pluvinaige, “Generalization of split Hopkinson bar technique to use viscoelastic bars”, *Int. J. Impact Eng.* **15**:5 (1994), 669–686.
- [Wood 1967] W. W. Wood, “Experimental mechanics at velocity extremes - very high strain rates”, *Exp. Mech.* **7**:10 (1967), 441–446.
- [Zhao and Gary 1995] H. Zhao and G. Gary, “A three dimensional analytical solution of the longitudinal wave propagation in an infinite linear viscoelastic cylindrical bar. Application to experimental techniques”, *J. Mech. Phys. Solids* **43**:8 (1995), 1335–1348.

Received 19 May 2007. Accepted 23 May 2007.

SAI S. SARVA: saisarva@mit.edu

Department of Mechanical Engineering, Massachusetts Institute of Technology, 77 Massachusetts Avenue, Cambridge, MA 02139, United States

MARY C. BOYCE: mboyce@mit.edu

Department of Mechanical Engineering, Massachusetts Institute of Technology, 77 Massachusetts Avenue, Cambridge, MA 02139, United States

<http://meche.mit.edu/people/faculty/index.html?id=11>

TWO-DIMENSIONAL SHOCK INDUCED COLLAPSE OF GAS BUBBLE NEAR A SEMIINFINITE DEFORMABLE SOLID

WENFENG XIE AND YIN LU YOUNG

In this paper, the effect of shock-induced collapse of a single gas bubble on the transient fluid and solid response is numerically investigated. The jet-like bubble collapse and subsequent strong pressure loading on a nearby semiinfinite deformable solid structure are captured and simulated using a multiphase compressible hydrodynamic model. The objective is to understand the fluid-structure interaction mechanisms, including the effect of the compressibility of the solid medium on the bubble dynamics and shock wave propagation, and the effect of shock wave propagation on the transient stress distribution within the solid. Numerical results demonstrate that the bubble collapse can impart very high pressure pulses to the nearby structure, leading to very high stresses sustained by the solid. The solid can experience significant deformation, including yielding, depending on the local fluid conditions.

1. Introduction

Cavitation bubble collapse near a solid boundary can be found in many fields of engineering. Settings include marine (propellers, torpedoes, and ships) and civil structures (dams and spillways). In addition, cavitation bubble dynamics can be relevant to many biomedical applications including shock wave lithotripsy, drug delivery, and other high intensity ultrasonic therapies [Zhong et al. 1997; Ohl and Irink 2003; Ohl and Wolfrum 2003]. Shock-induced collapse of gas bubbles near solid boundaries exhibits very complex dynamics involving nonspherical bubbles, jet formation, jet impact on structure, jet-induced shock-structure interaction, and subsequent structural deformation.

A number of theoretical and experimental studies have explored cavitation bubble dynamics near solid boundaries [Knapp et al. 1970; Tomita and Shima 1986; Philipp and Lauterborn 1998; Tomita et al. 2002]. It has been found that the bubble is no longer spherically symmetric during collapse near a solid boundary. A liquid jet develops on the side of the bubble opposite the boundary and travels toward the boundary. The bubble collapses when the liquid jet penetrates the side of the bubble facing the boundary [Lindau and Lauterborn 2003]. Subsequently, a high velocity jet and strong pressure pulses are directed toward the solid, which can severely erode it.

It is important to know when a structure will deform or even fail under strong pressure. Earlier numerical studies on elastic structural response of air/underwater shock loads can be found in [Houlston et al. 1985; McCoy and Sun 1997], where the dynamic response of isotropic materials subject to blast loading was modeled using finite element method (FEM). Recently, analytical modeling and numerical

Keywords: bubble collapse, multiphase model, fluid-structure interaction, shock-bubble interaction.

The authors are grateful to the Office of Naval Research for their financial support through Grant no. N00014-05-1-0694, and the National Science Foundation through Grant no. 0530759.

analysis have been conducted to investigate the shock response of sandwich plates subjected to underwater blast loading [Xue and Hutchinson 2004; Deshpande and Fleck 2005; Deshpande et al. 2006]. They represented pressure loads by the acoustic approximation but did not account for the nonlinearity of fluid compressibility. To overcome this difficulty, [Kambouchev et al. 2006] extended Taylor's analysis to include nonlinear compressibility effects of the fluid medium and developed a numerical method based on the Lagrangian formulation of the compressible Eulerian equations. This method has been tested against various blast intensities and was recently employed to study metal sandwich plates subjected to intense air shocks [Vaziri and Hutchinson 2007]. It should be noted that Kambouchev et al. [2006] focused on the dynamic response of the rigid plates and assumed that the plate deformation and stress-wave propagation through the plate are negligible. This assumption is valid for stiff materials like steel or copper but may not be for softer ones like aluminum and plastic, where significant energy dissipates through the fluid-solid interface and the stress-wave propagation becomes important [Xie et al. 2007b; Xie et al. 2006].

In most fluid-structure interaction models involving underwater explosions or cavitation collapse, the fluid pressure loads are imposed as boundary conditions for the solid model which calculates the structural response, and the fluid and structure models are not fully coupled. However, the structural motion and deformation can have a significant countereffect on the fluid. Therefore, full coupling between the fluid and structural solvers is important for practical applications. Kalumuck et al. [1995] and Chahine et al. [2003] simulated a loosely-coupled fluid-structure interaction (FSI) using a BEM-FEM coupled numerical scheme, examining interactions between a fluid and either rigid or deformable structures. Both papers ignored fluid compressibility and assumed a potential flow, which are common assumptions in the study of bubble dynamics. However, the potential flow assumption is actually not valid for fluid simulations having shock waves where the effect of fluid and/or air compressibility is significant.

During the shock-induced collapse of a gas bubble near a solid boundary, the resulting bubble collapse is very violent due to strong shock impact, which can lead to severe damage of the solid boundary. Due to the strong short-duration pressure loads, the solid can be simulated as a compressible fluid medium governed by the hydro-elasto-plastic equation of state [Tang and Sotiropoulos 1999; Xie et al. 2006]. Therefore, the system can be treated as a gas-water-solid three-phase compressible system and can thus be solved using a multiphase compressible hydrodynamic solver [Xie et al. 2007b; Xie et al. 2006]. The objective of this paper is to investigate the effect of shock-induced bubble collapse on a nearby semiinfinite solid and the countereffect of solid deformation on the fluid and bubble dynamics and on the shock wave propagation. The stress distribution within the compressible solid is also presented and analyzed.

2. Numerical methodology

In this work, all mediums are assumed to be compressible and isotropic, and interactions between mediums are always considered in the multiphase hydrodynamic computations. Therefore, the numerical method must be able to capture moving material interfaces. Due to strong shock wave propagation and high density ratios between the fluid mediums, the numerical method should be high-order (at least second), high resolution, and robust. The present numerical method, called the multiphase compressible hydrodynamic model (MCHM), comprises a second-order Monotone Upstream-centered Scheme for

Conservation Laws (MUSCL)—developed by Van Leer [1974] for calculating the fluid variables of the region away from the interfaces—and an explicit characteristic method [Xie et al. 2007b] for calculating the variables (pressure, velocity and entropy) at the interfaces.

2.1. Governing equations for compressible flows. The governing equations used in the present study are the Navier-Stokes equations for compressible flows, where the effects of turbulence and surface tension at the interfaces are neglected. This is a typical and realistic assumption for simulating flows in cold water and under high pressure conditions where the effects of temperature changes, surface tension, and turbulence are very small compared to the mechanical driving force (pressure) of the system. The conservative form of the two-dimensional Navier-Stokes equations can be written as

$$\frac{\partial U}{\partial t} + \frac{\partial F(U)}{\partial x} + \frac{\partial G(U)}{\partial y} = \frac{\partial F_v(U)}{\partial x} + \frac{\partial G_v(U)}{\partial y}, \quad (2-1)$$

where

$$\begin{aligned} U &= [\rho, \rho u, \rho v, E]^T, \\ F(U) &= [\rho u, \rho u^2 + p, \rho uv, (E + p)u]^T, \\ G(U) &= [\rho v, \rho uv, \rho v^2 + p, (E + p)v]^T, \\ F_v(U) &= \left[0, \frac{2}{3}\mu(2u_x - v_y), \mu(u_y + v_x), \frac{2}{3}\mu(2u_x - v_y)u + \mu(u_y + v_x)v \right]^T, \\ G_v(U) &= \left[0, \mu(u_y + v_y), \frac{2}{3}\mu(2v_y - u_x), \mu(u_y + v_x)u + \frac{2}{3}\mu(2v_y - u_x)v \right]^T. \end{aligned}$$

Here ρ is the gas flow density, $p = p(e, \rho)$ is the pressure, u and v are the flow velocities in the x (horizontal) and y (vertical) directions. E is the total energy and is given as $E = \rho e + 0.5\rho(u^2 + v^2)$, where e is the internal energy per unit mass. μ is the dynamic viscosity of the fluid. To close the Navier-Stokes Equation (2-1), equations of state (EOS) are required to represent the constitutive behavior of each medium, that is, for the gas, water, and solid. The typical equations of state for gas and water are the perfect gas law and Tait's equation:

$$\begin{aligned} p &= (\gamma_g - 1)\rho e, \\ p &= B(\rho/\rho_0)^{\gamma_l} - B + A, \end{aligned}$$

where γ_g is the ratio of specific heat for gas and is set to be 1.4. p_0 and ρ_0 are 10^5 Pa and 1000 kg/m^3 . B , A and γ_l are constants of Tait's EOS and are set to 3.31×10^8 Pa, 10^5 Pa, and 7.0.

The hydro-elasto-plastic (HEP) equation of state is used to describe the fluid-like constitutive material behavior of the solid when subject to short-duration, high-impact loads. The HEP equation of state can be derived by decomposing the total stress and strain into a mean hydrodynamic component and a deviator component [Tang and Sotiropoulos 1999; Xie et al. 2006]:

$$p = p_h(\rho) + \frac{4}{3}s(\rho_0, \tau_0, \rho). \quad (2-2)$$

Equation (2–2) assumes the material’s ability to support a deviator stress s can be described by the longitudinal and bulk wave speeds, and isentropic loading and unloading behavior. $p_h(\rho)$ and $s(\rho_0, \tau_0, \rho)$ denote the mean (hydrostatic) stress and deviator stress (difference between the principal stresses in the longitudinal and transverse directions) in the solid, and can be expressed as follows:

$$p_h(\rho) = \frac{m}{\beta} \left(\left(\frac{\rho}{\rho_a} \right)^\beta - 1 \right) + p_a, \quad (2-3)$$

$$s = \begin{cases} \tau, & |\tau| < Y/2, \\ Y \operatorname{sign}(\tau)/2, & |\tau| \geq Y/2, \end{cases}$$

where $\partial_t \tau = G/\rho \partial_t \rho$. Also $m = E/[3(1 - 2\mu)]$, Y , $G = E/[2(1 + \mu)]$, and β are the bulk modulus, the yield stress, the modulus of rigidity, and a model constant. E and μ are Young’s modulus and Poisson’s ratio. The values of these parameters can be found in Table 1. Note that the first of Equation (2–3) is equivalent to Murnaghan pressure-volume equation, while the second is the Von Mises yield criterion. For simple tension/compression, Equation (2–2) can be written as:

$$p = \begin{cases} p_h(\rho) + \frac{2}{3}Y, & \rho \geq \rho_2, \\ p_h(\rho) + \frac{4}{3} \left(G \ln \frac{\rho}{\rho_0} + \tau_0 \right), & \rho_1 < \rho \leq \rho_2, \\ p_h(\rho) - \frac{2}{3}Y, & \rho < \rho_1, \end{cases} \quad (2-4)$$

where $\rho_1 = \rho_0 \exp(-(2\tau_0 + Y)/2G)$ and $\rho_2 = \rho_0 \exp(-(2\tau_0 - Y)/2G)$ represent the equivalent compression and tension yield densities corresponding to a strain-hardening material. p_a , ρ_a , ρ_0 and τ_0 are the reference pressure, reference density, initial density, and initial shear stress. To yield more insight into the structural response, the normalized solid deviator stress ($2s/Y$) can be calculated to assess potential

Parameter	Value
p_a	1.0 bar
ρ_a	2700 kg/m ³
β	5.275
m	6.863×10^{10} Pa
G	5.224×10^{10} Pa
Y	2.70×10^8 Pa
τ_0	0.0 Pa

Table 1. Material properties of aluminum represented by the hydro-elasto-elastic equation of state.

yielding of a compressible structure. The value of $2s/Y$ is between -1.0 and 1.0 . If $2s/Y = 1.0$ or -1.0 , the structure has reached the Von Mises yield criterion.

It should be noted that the HEP is only valid for short time intervals when a very strong shock load is suddenly imposed normal to a semiinfinite homogeneous, isotropic solid. The HEP is able to capture both elastic and plastic deformations. That is, the solid can be under plastic compression, plastic tension, or elastic deformation for $\rho \geq \rho_2$, $\rho \leq \rho_1$, and $\rho_1 \leq \rho \leq \rho_2$, respectively. It should be emphasized that the current HEP equation of state ignores the propagation of shear (s -type) waves, and assumes the pressure (p -type) waves to travel along the principal directions. Hence, it is restricted to the modeling of very strong shock loads acting normal to the solid surface over a very short duration. For more general loading scenarios, or far more complex material behaviors, the solid should be modeled using the actual stress-strain constitutive relationships.

2.2. Multiphase compressible hydrodynamic model. For simulating multiphase compressible flow, the main difficulty is capturing material interfaces, where calculating one fluid medium requires information from adjacent fluid mediums. Due to different equations of state across the interfaces, the direct calculation of nearby flow variables without additional techniques for treating interfaces would lead to numerical oscillations near the interfaces. Therefore, an efficient and robust interface treatment technique is necessary. The multiphase compressible hydrodynamic model (MCHM) employs an explicit characteristic method to calculate interface variables (pressure, velocity and entropy), which is simplified from the modified ghost fluid method (MGFM by Liu et al. [2003]) and has been validated with one-dimensional analytical solutions in [Xie et al. 2007b]. Formulation of the explicit characteristic method for two-dimensional problems starts from the characteristic equations for Equation (2-1) in the normal direction of the material interface:

$$\begin{aligned} \frac{dp_I}{dt} + \rho_{IL}c_{IL} \frac{du_I}{dt} &= 0, & \text{along } \frac{dx}{dt} &= u_I + c_{IL}, \\ \frac{dp_I}{dt} - \rho_{IR}c_{IR} \frac{du_I}{dt} &= 0, & \text{along } \frac{dx}{dt} &= u_I - c_{IR}. \end{aligned} \quad (2-5)$$

Here subscripts I , IL , and IR refer to the interface, the left side of the interface, and the right side of the interface; $\rho_{IL}(\rho_{IR})$ and $c_{IL}(c_{IR})$ are the density and sound speed at the left (right) side of the interface; u_I and p_I are the normal velocity and pressure at the interface. The spatial coordinates of the transient gas bubble interface and water-structure interface are tracked as zero levels of ϕ and ψ , two scalar level set indicator functions which can be solved using the transportation equation [Osher and Sethian 1988]:

$$\frac{\partial \phi}{\partial t} + (\vec{u} \cdot \nabla)\phi = 0, \quad \frac{\partial \psi}{\partial t} + (\vec{u} \cdot \nabla)\psi = 0.$$

If $\rho_{IL}c_{IL}$ and $\rho_{IR}c_{IR}$ are assumed to be piecewise constant between each time step, Equation (2-5) can be approximated as

$$\begin{aligned} \frac{P_I - P_{IL}}{\rho_{IL}c_{IL}} + (u_I - u_{IL}) &= 0, \\ \frac{P_I - P_{IR}}{\rho_{IR}c_{IR}} - (u_I - u_{IR}) &= 0. \end{aligned}$$

Solving these for the interface pressure and normal velocity gives

$$\begin{aligned} u_I &= \frac{p_{IL} - p_{IR} + \rho_{IL}u_{IL}c_{IL} + \rho_{IR}u_{IR}c_{IR}}{\rho_{IL}c_{IL} + \rho_{IR}c_{IR}}, \\ p_I &= \frac{p_{IL}\rho_{IR}c_{IR} + p_{IR}\rho_{IL}c_{IL} + (u_{IL} - u_{IR})\rho_{IL}c_{IL}\rho_{IR}c_{IR}}{\rho_{IL}c_{IL} + \rho_{IR}c_{IR}}, \end{aligned} \quad (2-6)$$

where the values of $p_{IL}(p_{IR})$, $\rho_{IL}(\rho_{IR})$, $u_{IL}(u_{IR})$ and $c_{IL}(c_{IR})$ are taken from the left or right side of the interface in the normal direction.

It should be noted that tension waves are created due to suction from the cavity. The waves propagate in both the fluid and solid, which may lead to negative stresses in the vicinity of the fluid-structure interface and a subsequent (slight) negative p_{IR} or negative p_I due to numerical inaccuracy. However, if cavitation occurs near the fluid-solid interface, the acoustic impedance ($\rho_{IL}c_{IL}$) on the liquid side is negligible compared to ($\rho_{IR}c_{IR}$) on the solid side because the pressure and sound speed are (extremely) low in the cavitation region. As a result, $\rho_{IR}c_{IR} \gg \rho_{IL}c_{IL}$. Thus, Equation (2-6) can be simplified as follows:

$$\begin{aligned} u_I &= u_{IR}, \\ p_I &= p_{IL} + [u_{IL} - u_{IR}]\rho_{IL}c_{IL}. \end{aligned}$$

Here, the second member avoids the numerical prediction of a negative interface pressure when cavitation occurs near the fluid-solid interface.

3. Results and discussions

3.1. One-dimensional validation studies. First, two one-dimensional shock tube cases are computed to validate the current method for fluid-structure problems associated with shock impact on a structure. For the shock tube problem, there is an analytical solution derived from the Riemann problem [Toro 1997], which can be used to validate numerical methods for multiphase compressible flows. Both cases involve water-solid two-phase flows, where the high pressure lies in the water side (left). The computational domain is [0.0 m, 1.0 m] distributed uniformly with 200 grid points, the CFL number is 0.9, and the interface is initially at 0.4 m. The initial conditions for these two cases are:

Case 1: $u_l = 10$ m/s, $p_l = 2000$ bar, $u_r = 0$ m/s, $p_r = 1$ bar, $\rho_r = 7800$ kg/m³,

Case 2: $u_l = 50$ m/s, $p_l = 25000$ bar, $u_r = -5$ m/s, $p_r = 25$ bar, $\rho_r = 7.800088$ kg/m³.

Case 1. A water stream impinges onto a stationary solid, leading to shock wave propagation within the water and the solid. The computation is run to a final time of 5.0×10^{-3} s. Figure 1 shows pressure profiles calculated by the multiphase model and by the analytical model. The multiphase model's predictions compare well with the analytical solutions, and it captures accurately both shock waves within the water and the solid.

Case 2. Unlike Case 1, where the solid is initially stationary, Case 2 investigates what happens when the solid is already moving toward the water. The solution gives a shock wave in both water and solid. The computation is to run to a final time of 5.0×10^{-3} s. The strong impact leads to two strong shock

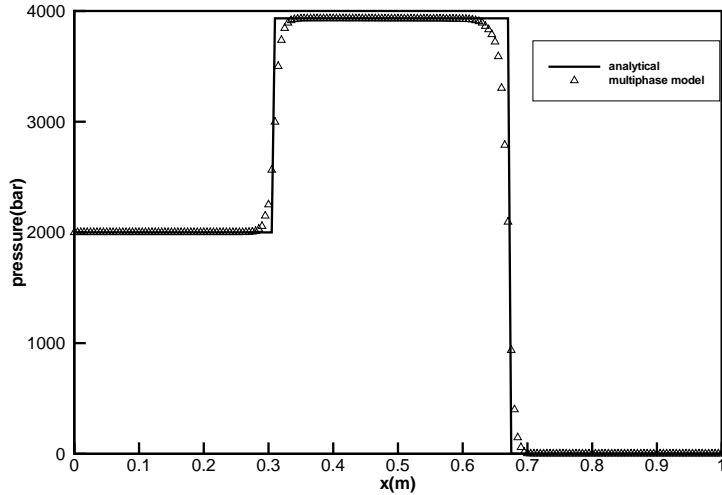


Figure 1. Pressure profiles for shock impact on structural boundary (case 1), where a right-moving ($u = 10$ m/s) water stream hits a stationary solid.

waves propagating at a high speed. The pressure profile produced by the multiphase model is in excellent agreement with the analytical solution, as shown in [Figure 2](#).

3.2. Two-dimensional applications. The two-dimensional problem's configuration is shown in [Figure 3](#). The shock waves, generated from the left boundary, hits a gas bubble with an initial radius of 0.5 m, leading to the collapse of the gas bubble. To investigate the effect of structural compressibility on the fluid and structural responses, the boundary is studied both as rigid and as compressible. The computational domain is $x \times y \in [-2, 2] \times [-4, 4]$ for the rigid case and $x \times y \in [-2, 6] \times [-4, 4]$ for the aluminum

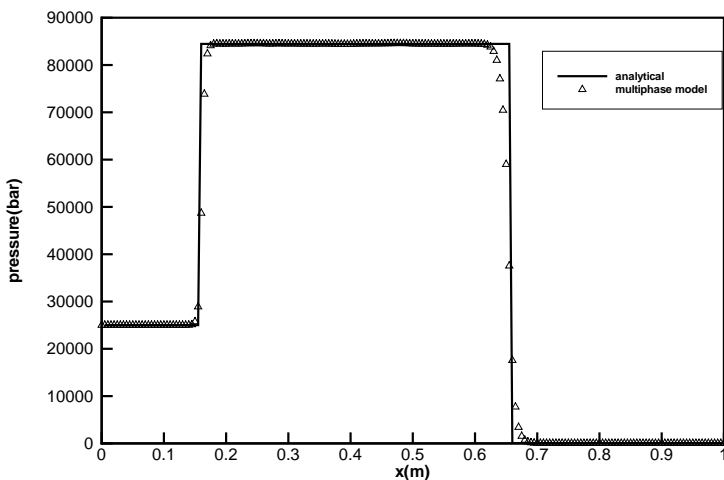


Figure 2. Pressure profiles for strong shock impact on structural boundary (case 2), where a right-moving ($u = 50$ m/s) water stream hits a left-moving solid ($u = -5$ m/s).

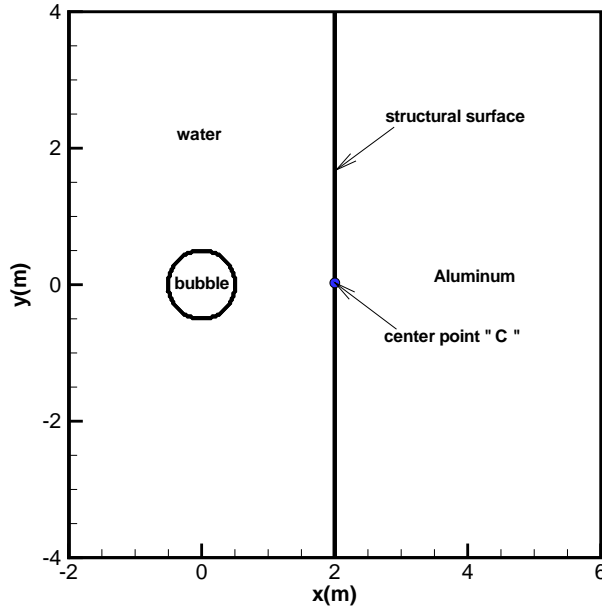


Figure 3. Schematic diagram for computations.

case, where the water-aluminum interface is at $y = 2m$. Uniform grids of size 160×320 and 320×320 (with $\Delta x = \Delta y = 1/40$ m) are placed in the computational domain for the rigid and aluminum case, respectively. Nonreflective boundary conditions are used for all four boundaries because the structure is considered to be semiinfinite. The initial conditions for two-dimensional computations are:

- (i) Shock waves: $p = p_{\max} \exp(-t/t_{\text{decay}})$, $p_{\max} = 20000$ bar, $t_{\text{decay}} = 0.4$ ms.
- (ii) Shock waves: gas bubble: $\rho_g = 1.0$ kg/m³, $p_g = 1.0$ bar, $u_g = 0.0$ m/s, $v_g = 0.0$ m/s, $\gamma_g = 1.4$.
- (iii) Shock waves: water: $\rho_l = 1000$ kg/m³, $p_l = 1.0$ bar, $u_l = 0.0$ m/s, $v_l = 0.0$ m/s, $\gamma_l = 7.0$.
- (iv) Shock waves: aluminum: $\rho_s = 2700$ kg/m³, $p_s = 1.0$ bar, $u_s = 0.0$ m/s and $v_s = 0.0$ m/s.

For two-dimensional computations, the CFL number is set to 0.45. To ensure the stability of computation, the time step is constrained by

$$\Delta t_f = \text{CFL} \frac{\min(\Delta x, \Delta y)}{\max_{i,j}(|u_{i,j}| + |v_{i,j}| + c_{i,j})}, \quad (3-1)$$

where Δx and Δy are step sizes for x and y directions, and $u_{i,j}$, $v_{i,j}$, and $c_{i,j}$ are the flow velocity along the x -direction, the flow velocity along y -direction, and the flow sound speed.

To investigate the convergence of the current method for multidimensional applications, a grid resolution study is conducted. A series of uniform grids, 161×161 (with $\Delta x = \Delta y = 1/20$ m), 241×241 (with $\Delta x = \Delta y = 1/30$ m), and 321×321 (with $\Delta x = \Delta y = 1/40$ m), are employed. The pressure-time history at the center C of the aluminum boundary surface C is shown in Figure 4a, and the corresponding pressure profiles along $y = 0$ at $t = 2.40$ ms are shown in Figure 4b. The two-dimensional computations converge well.

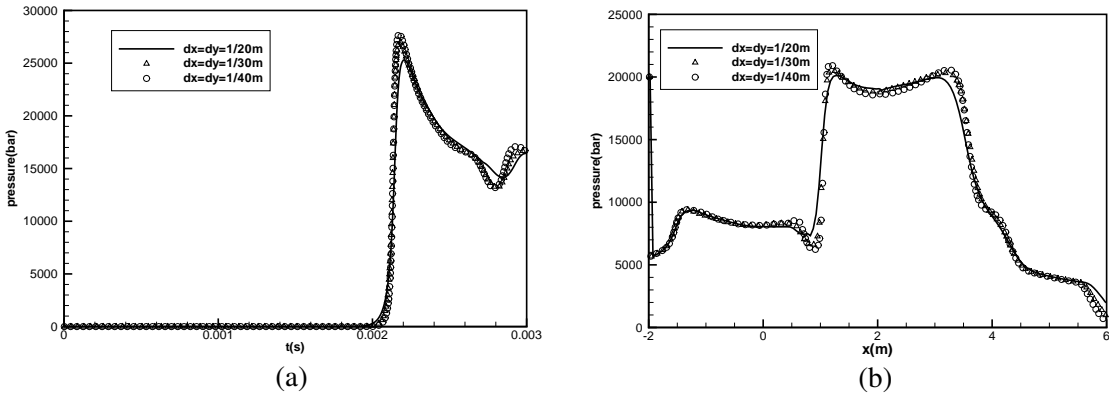


Figure 4. Convergence analysis: (a) pressure time histories at the center C of the structural surface; (b) pressure profiles along $y = 0$ at $t = 2.40$ ms (aluminum).

The remainder of this section contains an investigation of the collapse of a gas bubble near a semi-infinite rigid boundary and near an aluminum boundary.

First, a time series of pressure contours and velocity vectors are shown in [Figure 5a](#) through [Figure 6b](#) for the rigid boundary case. At time 1.20 ms ([Figure 5a](#)), the shock waves generated from the left boundary impact compress the left surface of the gas bubble, leading to a nonspherical bubble. The shock-bubble interaction creates rarefaction waves propagating spherically away from the bubble. At $t = 1.50$ ms ([Figure 5b](#)), the gas bubble has been compressed, and a toroidal bubble is formed. The velocity vectors point towards the right side of the rigid boundary due to low pressure inside. At $t = 1.65$ ms ([Figure 5c](#)), the cavitation bubble is near collapse. Large velocity gradients develop around the right bubble interface, pointing towards the rigid boundary. The cavitation bubble collapses after $t = 1.80$ ms ([Figure 5d](#)), resulting in a high-speed, high-pressure shock wave that propagates spherically outward. At this time, the initial shock waves from the left boundary approach the rigid solid boundary. At time 2.10 ms ([Figure 6a](#)), the shock wave generated from the bubble collapse has almost reached the rigid boundary, while the initial shock waves have already impacted and reflected from it, except at the region near its center. Obviously, the gas bubble itself will cushion the center, reducing the initial shock loading. [Figure 6a](#) and [Figure 6b](#) show that two tiny bubbles are created after the original large bubble collapses. In the model, the level set technique automatically changes the interface numbers (from one to two gas bubbles). At $t = 2.55$ ms ([Figure 6b](#)), the shock wave generated from the bubble's collapse has arrived at and reflected from the rigid boundary. A very high pressure region develops near the center region of the rigid boundary, because the reflected shock wave merges with the new shock wave generated by the collapse of the gas bubble.

The peak flow velocity appears near $x = 0.0$ m at $t = 1.25$ ms, because the low bubble pressure allows the flow to move into it at a higher velocity. The flow velocity decreases when the bubble is compressed as the internal pressure increases and because rarefaction waves propagate against the flow. After $t = 1.25$ ms, the flow velocity starts to decrease as energy dissipates into the surrounding fluid and as the flow interacts with shock waves reflecting from the solid boundary ($t = 2.25$ ms and 2.70 ms). To illustrate shock loading on the rigid boundary, pressure distributions along the rigid boundary at different

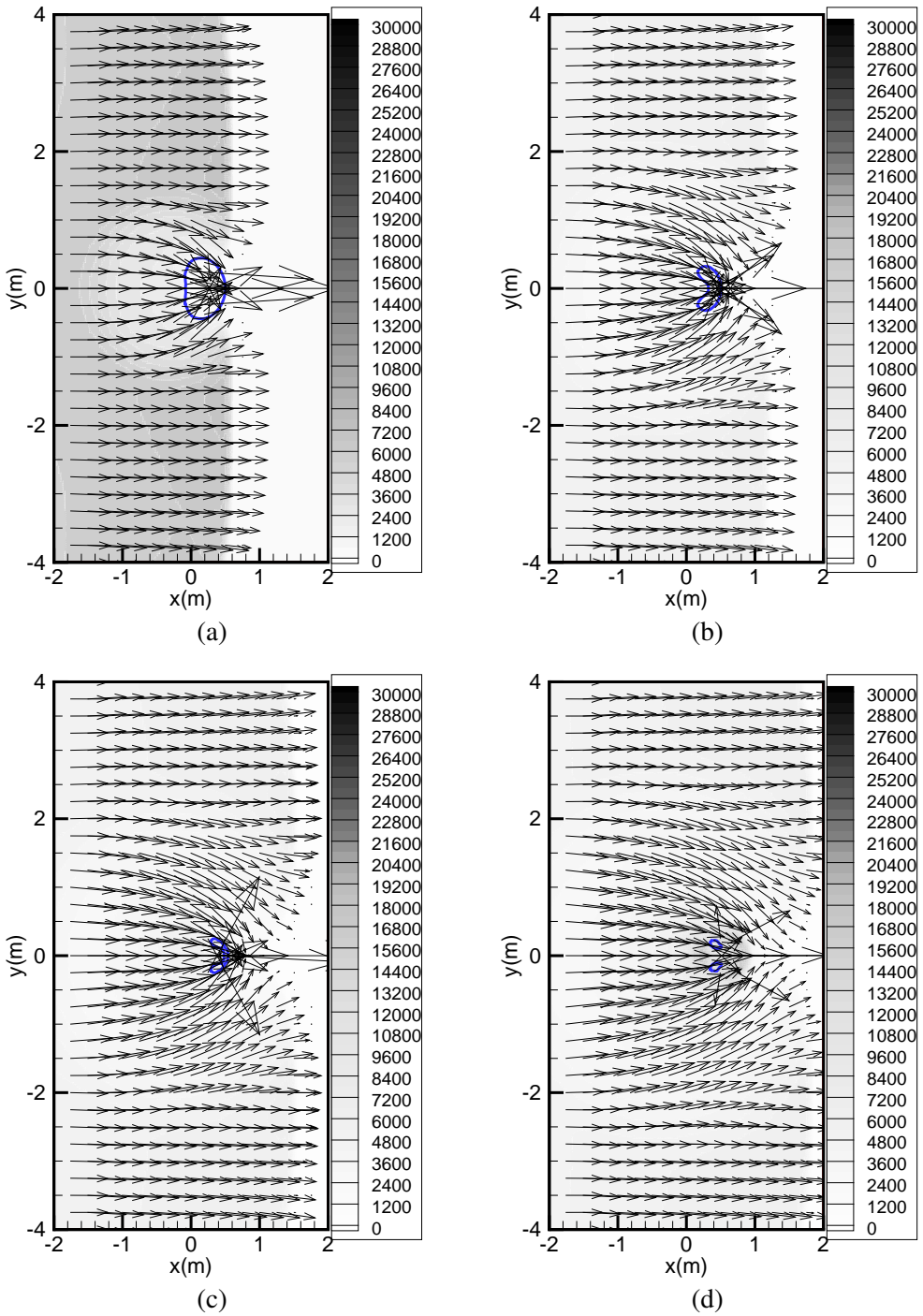


Figure 5. Pressure contours and velocity vectors for bubble collapse near a rigid boundary: (a) $t = 1.20$ ms, (b) $t = 1.50$ ms, (c) $t = 1.65$ ms, (d) $t = 1.80$ ms.

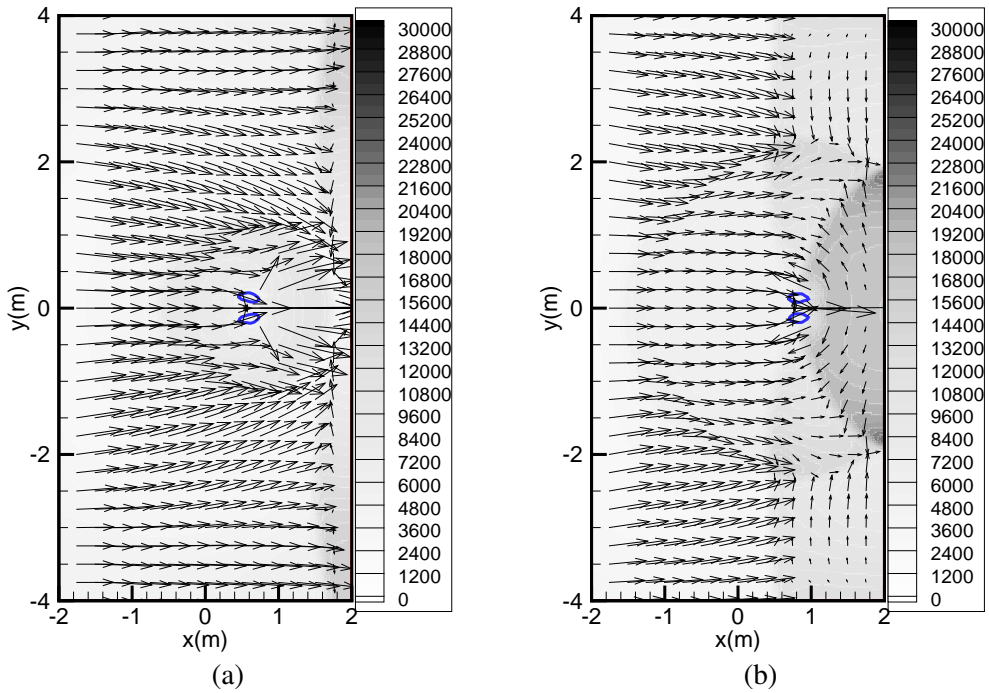


Figure 6. Later pressure contours and velocity vectors for bubble collapse near a rigid boundary: (a) $t = 2.10$ ms, (b) $t = 2.55$ ms.

times after the bubble collapse are shown in [Figure 8](#). At $t = 1.95$ ms, the pressure pulse caused by the bubble

[Figure 7](#) depicts a time series of velocity profiles along $y = 0$. collapse has not yet reached the rigid boundary, while the initial shock wave has already reflected from the rigid boundary. The presence of

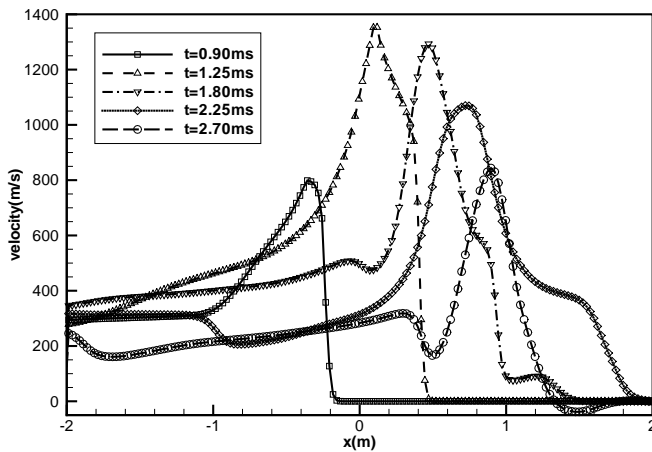


Figure 7. Velocity profiles along $y = 0$ (rigid boundary case).

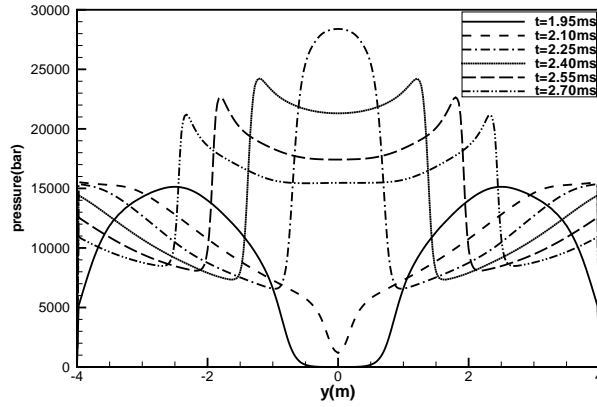


Figure 8. Pressure distributions along the structural surface (rigid boundary case).

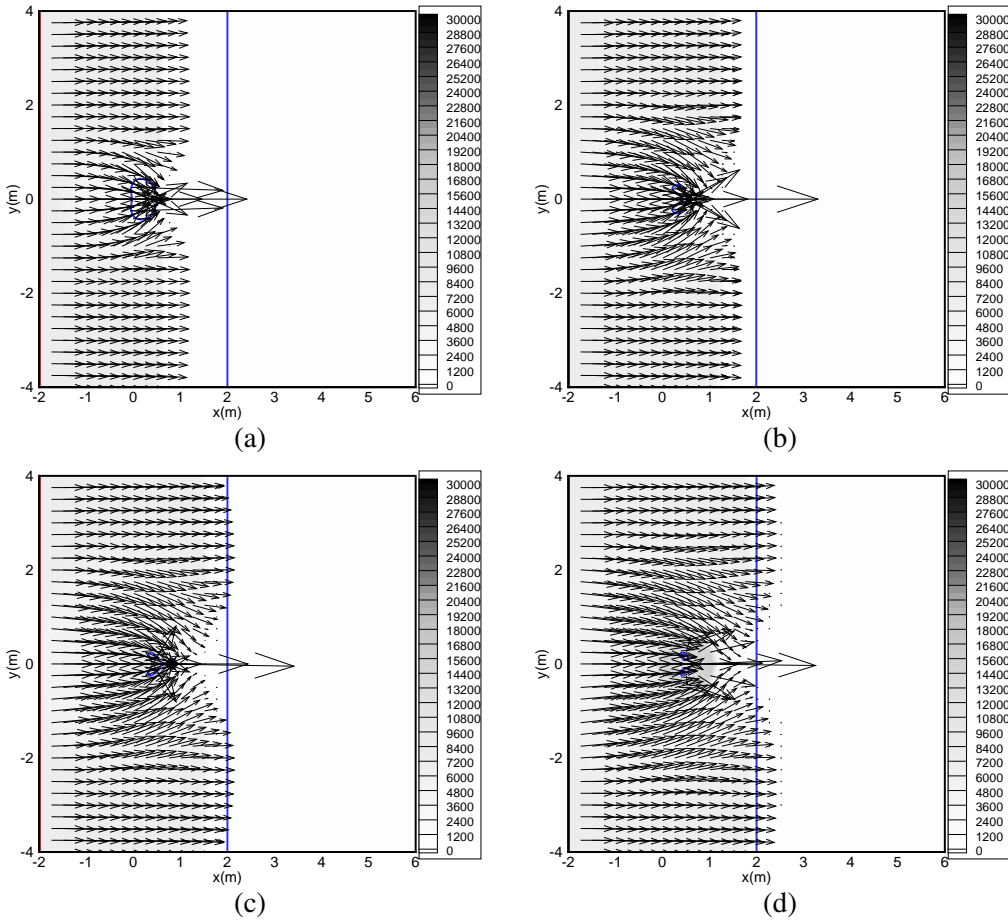


Figure 9. Pressure contours and velocity vectors for the aluminum boundary: (a) $t = 1.20$ ms, (b) $t = 1.50$ ms, (c) $t = 1.65$ ms, (d) $t = 1.80$ ms.

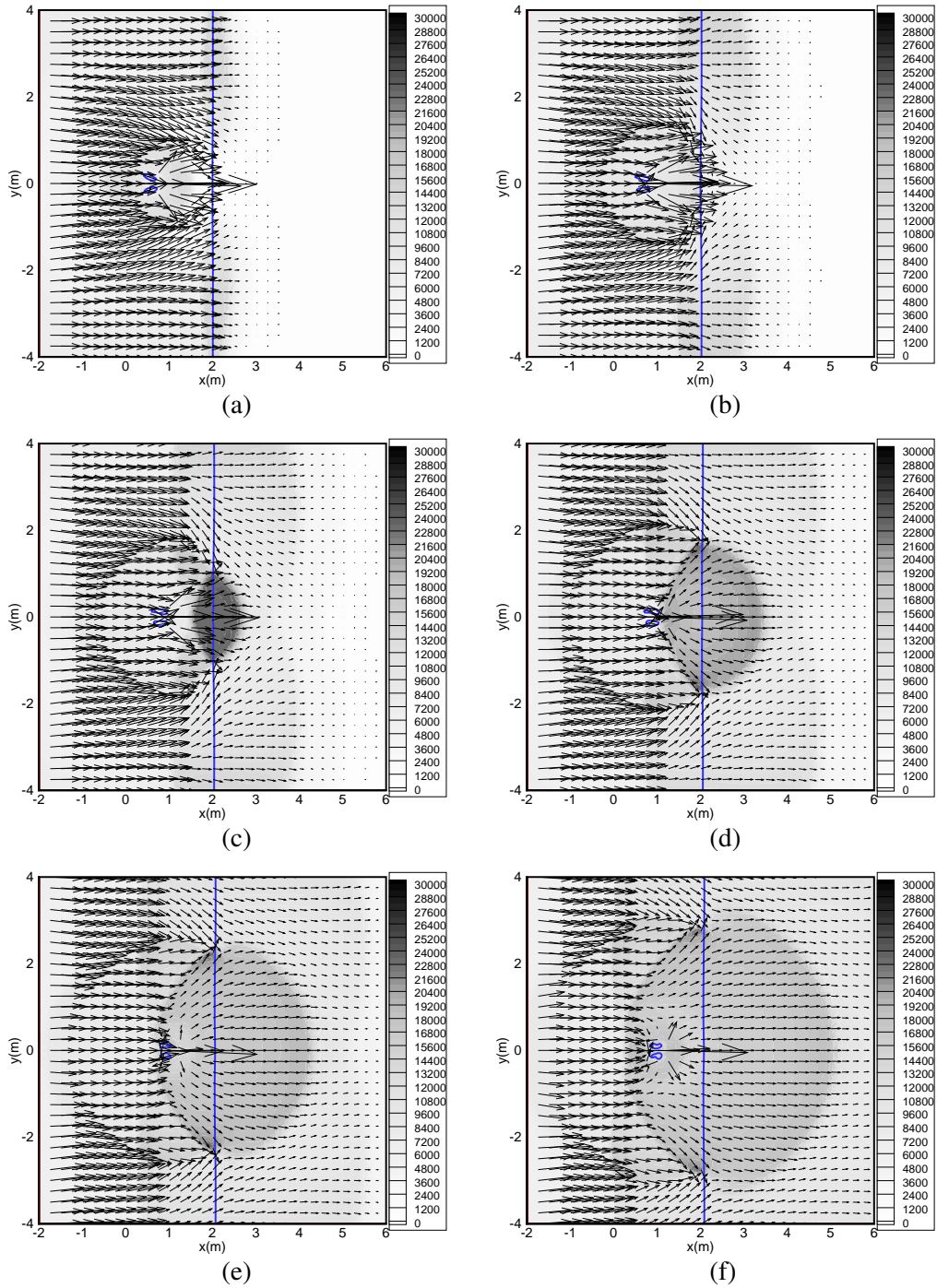


Figure 10. Later pressure contours and velocity vectors for the aluminum boundary: (a) $t = 1.95$ ms, (b) $t = 2.10$ ms, (c) $t = 2.25$ ms, (d) $t = 2.40$ ms, (e) $t = 2.55$ ms, (f) $t = 2.70$ ms.

the bubble maintains atmospheric pressure near the center, but the pressure away from there is very high due to the initial shock wave. The pressure pulse reaches the solid boundary at around $t = 2.10$ ms. Thus, the pressure at the center region of the solid boundary starts to increase and reaches its highest value at $t = 2.25$ ms as the secondary shock generated from the bubble collapse arrives. After that, the pressure here decreases due to interaction between the initial shock wave and the rarefaction waves reflected from the solid and bubble boundaries (from $t = 2.25$ ms to $t = 2.70$ ms).

For the semiinfinite solid body made of aluminum, the flow physics is similar to the rigid boundary case before the shock waves impact on the boundary (see Figure 9a). The fluid-solid boundary is shown as a vertical solid line. When the initial shock wave hits the aluminum boundary at $t = 1.95$ ms, the shock wave both reflects from it and propagates through it (see Figure 10a). When the shock wave caused by bubble collapse reaches the boundary, the velocity is particularly high at the center region, leading to the structural deformation and shock propagation through the center (Figure 10). The shock wave generated from the bubble collapse propagates throughout the structural domain and can lead to significant stress within the structure. The deformation of the aluminum boundary away from the center can be observed in Figure 10e and Figure 11. More displacement occurs away from the center ($y = 0$) for $t \leq 2.1$ ms due to the air cushioning effect provided by the collapsing bubble. For $t > 2.1$ ms, more displacement occurs at the center due to the highly focused pressure reload created by the collapse.

To examine the fluid and structural response, the fluid pressure p contours (lines) and the normalized solid deviator stress $2s/Y$ contours (flooded) are plotted together at times 1.80 ms, 1.95 ms, 2.10 ms, and 2.25ms in Figure 12. $|2s/Y| = 1$ implies the material has yielded and is in the strain hardening regime. Beginning at the initial shock wave impact on the solid boundary at $t = 1.80$ ms (Figure 12a), the normalized solid deviator stress increases with time, and, at $t = 1.95$ ms, the aluminum material begins

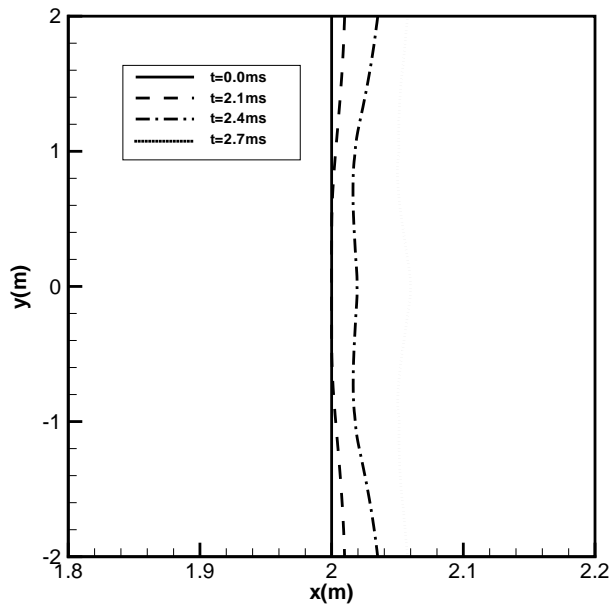


Figure 11. The progressive deformation of the aluminum boundary.

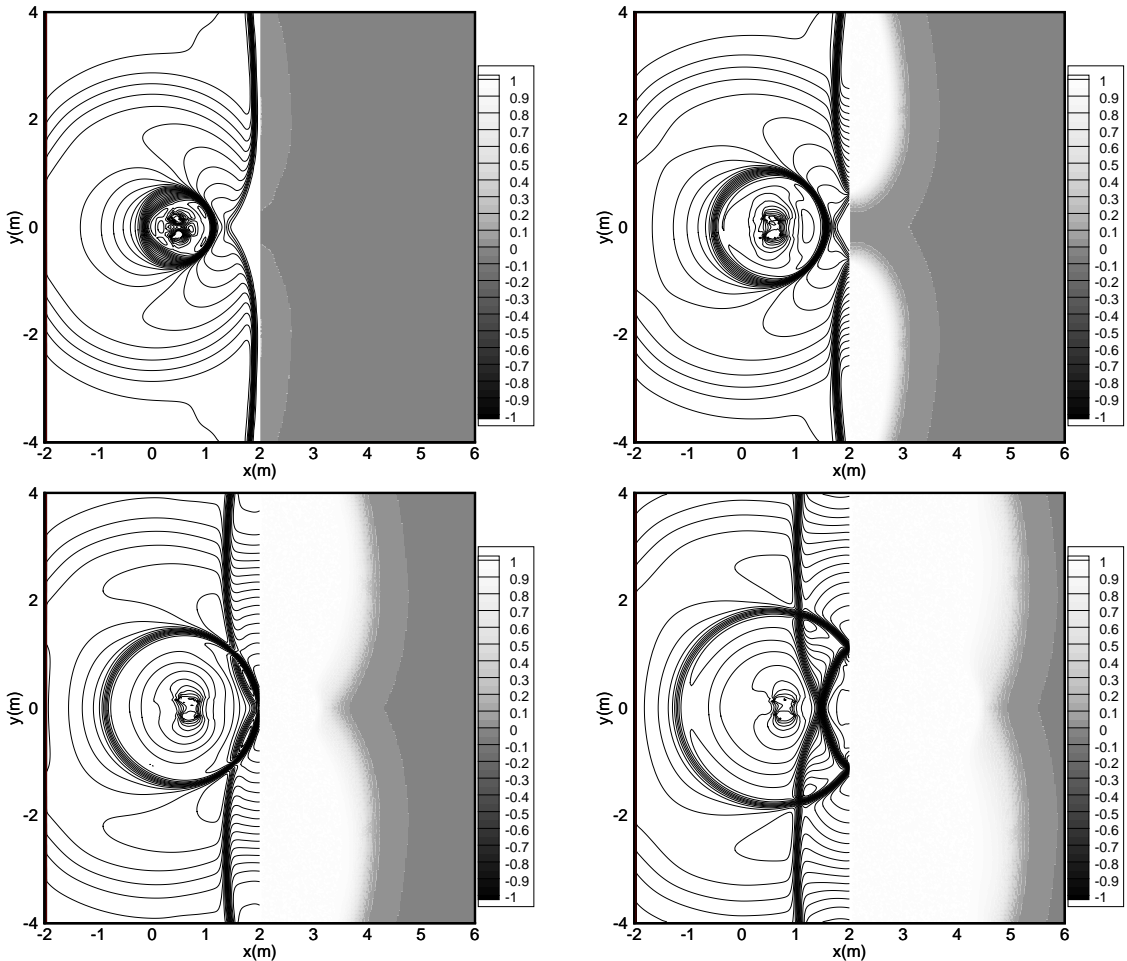


Figure 12. Fluid pressure contours (lines) and $2s/Y$ normalized deviator stress contours (flood) for the aluminum boundary: (a) $t = 1.80$ ms, (b) $t = 1.95$ ms, (c) $t = 2.10$ s, (d) $t = 2.25$ ms.

to experience plastic deformation, except at the center (see [Figure 12b](#)) because of the aforementioned cushioning. At $t = 2.10$ ms, the shock wave generated from the bubble collapse hits the boundary, leading to plastic deformation at the center ([Figure 12c](#)). The entire solid region almost yields at $t = 2.25$ ms due to the combined initial shock loading and gas bubble reloading ([Figure 12d](#)). It can be concluded that a gas bubble near the structural surface first helps to reduce the shock load, but then generates a strong focused secondary reload when it collapses.

The velocity profiles along $y = 0$ for a series of times are provided in [Figure 13](#) to exhibit the time varying flow variables, which are similar to the rigid boundary case. It should be noted that the center of the structural surface moves during the pressure reload from the bubble collapse. This can be seen at $t = 2.40$ ms and $t = 2.70$ ms in [Figure 11](#). In addition, the pressure distributions along the surface are shown in [Figure 14](#) to illustrate the pressure loading of the aluminum boundary. The pressure peaks at

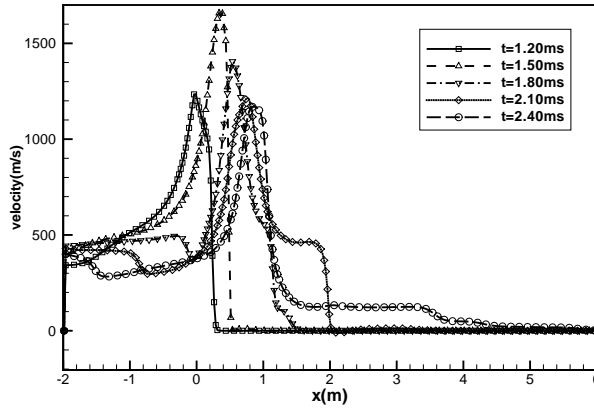


Figure 13. Velocity profiles along $y = 0$ (aluminum boundary case).

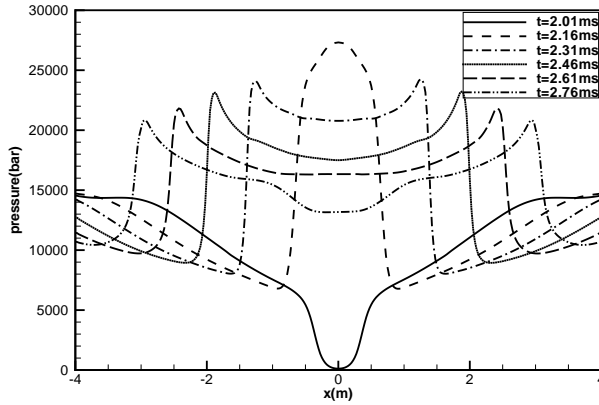


Figure 14. Pressure distributions along structural surface (aluminum boundary case).

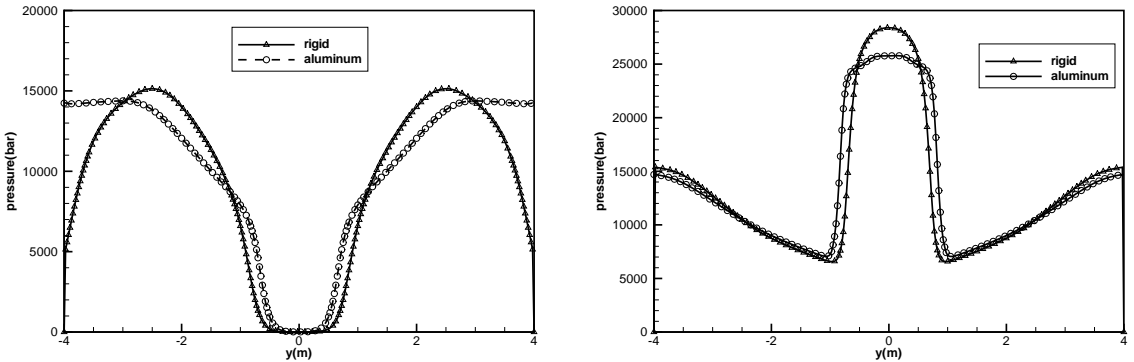


Figure 15. Comparison of pressure distributions along structural surface for the rigid case and the aluminum case: (a) before gas bubble reload at $t = 1.95$ ms, (b) after gas bubble reload at $t = 2.25$ ms.

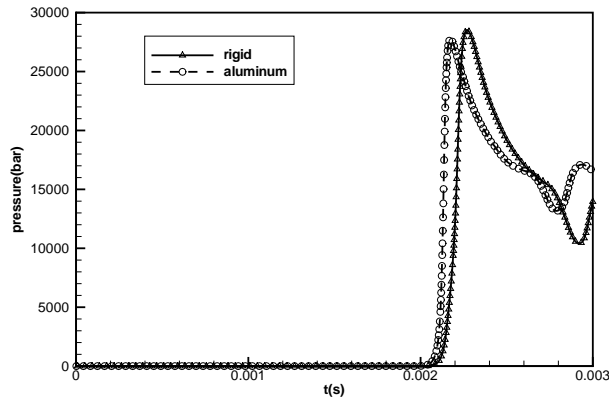


Figure 16. Comparison of pressure histories at the center C for both the rigid and the aluminum boundary.

$t = 2.16$ ms for the center point C as it experiences the pressure loading created by the bubble collapse. In addition, pressure distributions along the rigid boundary and the aluminum boundary before the gas bubble reload at $t = 1.95$ ms, and after gas bubble reload at $t = 2.25$ ms, are shown in Figure 15a and 15b for comparison. Figure 15a shows that pressures away from the gas bubble for the rigid case are higher than for the aluminum case, because energy dissipates in the deformable aluminum. The pressure distributions near the bottom/top regions of the structural surface (left and right regions in Figure 15a) are different for the rigid and the aluminum cases, again mainly because of shock energy dissipates through solid deformation.

The shock reflects more weakly from the aluminum surface than from the rigid surface, because of the fully reflective boundary condition. Due to the strong reflected shock from the rigid surface, the pressure near the rigid boundary drops more rapidly than it does near the aluminum, leading to a lower predicted pressure distribution near the bottom and top regions of the structural surface. After the bubble collapse, Figure 15b shows that the peak pressure at the center due to gas bubble reload for the rigid case is higher than for the aluminum case. This is once again due to the energy dissipation through the aluminum material.

The pressure histories at the center C are recorded and compared for the rigid and aluminum cases. Figure 16 shows that the initial shock wave arrives at the boundary at approximately the same time but the rate of pressure increase and the peak interface pressure for rigid and aluminum boundaries are different. The peak pressure is higher for the rigid boundary because it does not dissipate energy. However, the rate of pressure increase is lower for the rigid boundary due to interaction between the initial shock wave and the reflected rarefaction wave. The differences between the rigid and aluminum boundaries are not significant due to the relatively high elastic modulus of aluminum and due to the short load duration, both of which limit the energy dissipated through deformation.

To understand the influence of the bubble on the interface pressure, the pressure history at the center C is compared with and without the gas bubble in Figure 17. The results indicate that the initial shock wave arrives at the boundary much later when there is a gas bubble than when there is not, due to the air cushioning effect. However, when the bubble is forced to implode from high shock load, the peak

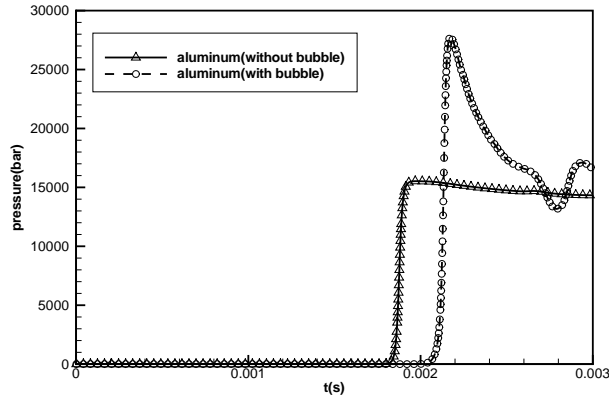


Figure 17. Comparison of pressure histories at center point C for the aluminum boundary with and without the gas bubble.

pressure caused by the collapse and the delayed shock impact are both much higher than the peak pressure caused by the initial shock wave without the bubble. Thus, it is important to consider the effect of gas bubbles for the overall assessment of structural response to a high intensity shock load.

4. Concluding remarks

A multiphase compressible hydrodynamic model was applied to study multidimensional shock-bubble-structure interactions. In particular, the shock-induced collapse of a gas bubble near a planar compressible solid wall has been investigated. A toroidal collapse of gas bubble and a strong shock generated from bubble collapse have been observed. During the bubble collapse, a high-velocity, high-pressure, jet-like fluid flow hits the center region of the boundary. The collapse is so violent that the pressure impulse release rivals the initial shock wave. The deformation of aluminum boundary is due to the initial shock loading and the subsequent shock-induced collapse of the bubble. It is found that a gas bubble near the center of the structural surface helps to reduce initial shock loading there but then causes a stronger shock reload due to the high intensity microjet created as it collapses. In addition, the gas-water and water-solid interfaces are well represented, the change in the number of interfaces is captured automatically, and symmetric flow fields are obtained. It should be noted that the current model has some severe limitations. The hydro-elasto-plastic (HEP) model assumes the deviatoric stress to be secondary, but this is only reasonable when the structure is under strong impact normal to the planar solid surface; the HEP ignores the shear (s -type) waves and assumes the pressure (p -type) waves travel along the principal directions, which limits its applicability to shock duration, strong shock loading normal to a homogeneous isotropic planar structure. The current Eulerian fluid/Eulerian solid has been validated against the one-dimensional analytical solutions for the shock-tube problem, but additional experimental validation studies are needed, especially for the HEP equation of state. To simulate general fluid-structure interaction involving arbitrary shock loads on anisotropic or inhomogeneous mediums, the solid dynamics can be better captured using a Lagrangian-FEM solver where the solid behavior is described using the material stress-strain constitutive relationships. A one-dimensional Eulerian fluid/Lagrangian solid approach has been presented in [Xie et al. 2007a]. A two-dimensional extension of the Eulerian-Lagrangian solver is ongoing.

References

- [Chahine et al. 2003] G. L. Chahine, K. M. Kalumuck, and C.-T. Hsiao, “Simulation of surface piercing body coupled response to underwater bubble dynamics utilizing 3DynaFS, a three-dimensional BEM code”, *Comput. Mech.* **32** (2003), 319–326.
- [Deshpande and Fleck 2005] V. S. Deshpande and N. A. Fleck, “One-dimensional shock response of sandwich beams”, *J. Mech. Phys. Solids* **53** (2005), 23–47.
- [Deshpande et al. 2006] V. S. Deshpande, A. Heaver, and N. A. Fleck, “An underwater shock simulator”, *Proc. R. Soc. A* **462** (2006), 1021–1041.
- [Houlston et al. 1985] R. Houlston, J. E. Slate, N. Pegg, and C. G. Desrochers, “On analysis of structural response of ship panels subjected to air blast loading”, *Comput. Struct.* **21** (1985), 273–289.
- [Kalumuck et al. 1995] K. M. Kalumuck, R. Duraiswami, and G. L. Chahine, “Bubble dynamics fluid-structure interaction simulation by coupling fluid BEM and Structural FEM codes”, *J. Fluids. Struct.* **9** (1995), 861–883.
- [Kambouchev et al. 2006] N. Kambouchev, L. Noels, and R. Radovitzky, “Nonlinear compressibility effects in fluid–structure interaction and their implications on the air-blast loading of structures”, *J. Appl. Phys.* **100** (2006), 1–10.
- [Knapp et al. 1970] R. P. Knapp, J. W. Daily, and F. G. Hammitt, *Cavitation*, McGraw-Hill, 1970.
- [Lindau and Lauterborn 2003] O. Lindau and W. Lauterborn, “Cinematographic observation of the collapse and rebound of a laser-produced cavitation bubble near a wall”, *J. Fluid Mech.* **479** (2003), 327–348.
- [Liu et al. 2003] T. G. Liu, B. C. Khoo, and K. S. Yeo, “Ghost fluid method for strong shock impacting on material interface”, *J. Comput. Phys.* **190** (2003), 651–681.
- [McCoy and Sun 1997] R. W. McCoy and C. T. Sun, “Fluid-structure interaction analysis of a thick-section composite cylinder subjected to underwater blast loading”, *Compos. Struct.* **31** (1997), 45–55.
- [Ohl and Irink 2003] C. D. Ohl and R. Irink, “Shock-wave-induced jetting of micron-size bubbles”, *Phys. Rev. Lett.* **90** (2003), 214502.
- [Ohl and Wolfrum 2003] C. D. Ohl and B. Wolfrum, “Detachment and sonoporation of adherent HeLa-cells by shock wave-induced cavitation”, *Biochim. Biophys. Acta* **1624** (2003), 131–138.
- [Osher and Sethian 1988] S. Osher and J. A. Sethian, “Fronts propagating with curvature dependent speed. Algorithms based on Hamilton-Jacobi formulations”, *J. Comput. Phys.* **79** (1988), 12–49.
- [Philipp and Lauterborn 1998] A. Philipp and W. Lauterborn, “Cavitation erosion by single laser-produced bubbles”, *J. Fluid Mech.* **361** (1998), 75–116.
- [Tang and Sotiropoulos 1999] H. S. Tang and F. Sotiropoulos, “A second-order Godunov method for wave problems in coupled solid-water-gas systems”, *J. Comput. Phys.* **151** (1999), 790–815.
- [Tomita and Shima 1986] Y. Tomita and A. Shima, “Mechanisms of impulsive pressure generation and damage pit formation by bubble collapse”, *J. Fluid Mech.* **169** (1986), 535–564.
- [Tomita et al. 2002] Y. Tomita, P. B. Robinson, R. P. Tong, and J. R. Blake, “Growth and collapse of cavitation bubbles near a curved rigid boundary”, *J. Fluid Mech.* **466** (2002), 259–283.
- [Toro 1997] E. F. Toro, *Riemann solvers and numerical methods for fluid dynamics*, Springer Publication Company, 1997.
- [Van Leer 1974] B. Van Leer, “Towards the ultimate conservative difference schemes II: Monotonicity and conservative combined in a second-order scheme”, *J. Comput. Phys.* **14** (1974), 361–370.
- [Vaziri and Hutchinson 2007] A. Vaziri and J. W. Hutchinson, “Metal sandwich plates subject to intense air shocks”, *Int. J. Solids Struct.* **44** (2007), 2021–2035.
- [Xie et al. 2006] W. F. Xie, Y. L. Young, and T. G. Liu, *Multiphase modeling of dynamic fluid-structure interaction during close-in explosion*, 2006. under review.
- [Xie et al. 2007a] W. F. Xie, Z. K. Liu, and Y. L. Young, *An Eulerian-Lagrangian approach for fluid-structure interaction with large solid deformation and fluid cavitation*, 2007. Under review.
- [Xie et al. 2007b] W. F. Xie, Y. L. Young, T. G. Liu, and B. C. Khoo, “Dynamic response of deformable structures subjected to shock load and cavitation reload”, *Comput. Mech.* **40** (2007), 667–681.

[Xue and Hutchinson 2004] Z. Xue and J. W. Hutchinson, “A comparative study of blast-resistant metal sandwich plates”, *Int. J. Impact Eng.* **30** (2004), 1283–1305.

[Zhong et al. 1997] P. Zhong, F. H. Cocks, I. Cioanta, and G. M. Preminger, “Controlled, forced collapse of cavitation bubbles for improved stone fragmentation during shock wave lithotripsy”, *J. Urology* **158** (1997), 2323–2328.

Received 18 May 2007. Accepted 23 May 2007.

WENFENG XIE: wxie@princeton.edu

Dept of Civil and Environmental Engineering, E-228, EQUAD, Princeton University, Princeton, New Jersey 08544, United States

YIN LU YOUNG: yyoung@princeton.edu

Dept of Civil and Environmental Engineering, E-326, EQUAD, Princeton University, Princeton, New Jersey 08544, United States

EXPERIMENTAL AND COMPUTATIONAL EVALUATION OF COMPRESSIVE RESPONSE OF SINGLE AND HEX-ARRAYED ALUMINUM TUBES

SIA NEMAT-NASSER, MAHMOUD REZA AMINI, JEOM YONG CHOI AND JON ISAACS

We report experiments and simulations of the dynamic and quasistatic compressive response of single and hex-arrayed thick aluminum tubes. The investigation aims to further characterize how tube-based sandwich structures absorb energy. First, we study by compression tests the quasistatic buckling of single tubes of 7075 aluminum, an alloy showing sufficient ductility and plasticity to make it potentially a good choice for energy absorbing devices. The experiments show geometry-dependent buckling modes. The corresponding finite element numerical simulations correlate well and will help estimate the maximum load level, and the buckling and postbuckling responses. Second, we study the dynamic buckling of sandwiched, hex-arrayed 3003 aluminum tubes. The simulations and experimental results correlate well and show a remarkable increase in energy absorbing capacity, which is caused by the postbuckling interaction of neighboring tubes. They also show that, as the tube spacing is decreased, the overall energy absorbed increases significantly. We also simulate how varying tube length and thickness affect the buckling of the array under dynamic loading.

1. Introduction

Metal components absorb energy well because they deform before failing. Plastic deformation, specifically plastic tube buckling, can effectively dissipate large amounts of energy. Circular tubes can absorb more energy with their favorable stroke length per unit mass.

Sandwich structures, consisting of two plates separated by metal tubes, may mitigate impulsive (short duration) loads. Reid [1993] suggested tubes exhibit excellent energy absorbing characteristics when loaded by high velocity impacts. Others have suggested ways to improve the crashworthiness of sandwiches, for example, by varying the tubes' cross sectional geometry. Among all the cross sections examined by Mamalis et al. [2003], thick-walled circular tubes exhibited the most stable crash mode. The experimental investigations—for example, [Lee 1962; Batterman 1965; Horton et al. 1966; Johnson et al. 1977; Nemat-Nasser et al. 2007]—have shown that relatively thick shells (radius to thickness ratio $R/t < 50$) buckle axisymmetrically, whereas this symmetry breaks for thinner shells and they instead buckle in a diamond pattern. Lee [1962], Batterman [1965], and Tennyson and Muggeridge [1969] have found that initial imperfections can significantly influence diamond-shaped circumferential mode buckling (when $R/t < 100$), according to an incremental theory.

In contrast to the elastic response, Gerard [1962] reported in inelastic buckling that the axisymmetric solution always corresponds to a lower buckling stress than the asymmetric solution with circumferential

Keywords: sandwich structures, aluminum tubes, dynamic compression, quasistatic compression, LS_DYNA, physics-based material model.

This work has been supported by ONR (MURI) grant N000140210666 to the University of California, San Diego, with Dr. Roshdy G. Barsoum as program manager.

modes, and that the imperfections are of no significance in either case. Theoretical investigations also suggest that plastic buckling is less sensitive to imperfection than elastic. (See Gellin [1979], who used J_2 -deformation theory to model thick shells with sinusoidal axisymmetric imperfections).

Using a J_2 corner theory plasticity model, Tvergaard [1983b] compared the elastic and plastic response in cylindrical shells with initial axisymmetric imperfections and showed that they bifurcate into a nonaxisymmetric shape. For sufficiently thin-walled shells, the bifurcation occurs before the load maximum. In thick-walled shells, the axisymmetric deformations are stable beyond the maximum load, at which the collapse localizes into a single outward buckled mode. His investigations also show that localization delays bifurcation considerably, such that a sufficiently thick-walled shell collapses in an axisymmetric mode. Budiansky and Hutchinson [1966] have shown that tubes collapse at lower loading under dynamic compression than under static loading. In other studies, Karagiozova et al. [2000] studied the inertial effects on axisymmetrically deformed cylindrical shells. Weingarten et al. [1964] have experimentally quantified how the buckling coefficient varies with R/t .

In this paper, we report our experimental and numerical investigations of the dynamic and quasistatic response of thick ($R/t < 20$) hex-arrayed and single aluminum tubes under axial compressive loads. We considered aluminum alloys that have good ductility and plasticity at low temperatures and high strain rates, and that do not fracture [Nemat-Nasser and Guo 2004]. We do not address the effects of edge constraint, imperfection, and tube length because they do not significantly influence the plastic buckling and postbuckling of thick cylindrical tubes. This assumption is supported by extensive experimental and numerical investigations over the last 50 years.

We present the results of two series of experiments. One consists of quasistatic experiments of single tubes, and the other involves dynamic impact experiments of hex-arrayed tubes. We used an Instron hydraulic testing machine and a Hopkinson bar apparatus for these experiments, respectively. First, we measured the energy absorbing characteristics of single 7075 aluminum tubes under quasistatic loading. Next, we measured through dynamic impact (compression) tests the dynamic behavior of sandwiched, hex-arrayed 3003 aluminum tubes. We accompanied both of these experiments with finite element simulations. The experiments and simulations show that tight, hexagonally packed sandwiches maintain their load carrying capacity even after the initial buckling, as each tube becomes supported by its neighbors. Finite-element simulations also show how varying tube length and thickness (with constant outer diameter) affects the structure's ability to absorb energy. We find that as the thickness and length increase, the absorbed energy per unit mass also increases, but stops growing at a maximum level; however, if the two geometrical parameters are disproportionately increased, that energy may drop noticeably.

From these experiments and simulations of the dynamic behavior of sandwich structures with tube cores, we conclude that finite element models properly informed by experimental measurements can reliably predict the overall behavior of complex tube-based sandwich structures. Such models can thus become a powerful tool for designing optimal energy absorbing sandwich structures subject to dynamic and static loads.

2. Experimental procedure and results

Designing crashworthy structures, that is, structures capable of withstanding and mitigating the effect of impact, requires understanding structural dynamics and also the properties and deformation mechanisms

of the material and the larger structure. Axially compressed aluminum tubes absorb energy particularly well, due to their plastic buckling deformation modes. In this section, we report on experiments on the quasistatic compressive behavior of aluminum tubes and pair them with simulations to better understand their deformation mechanisms. All the tubes used in this research are thick-walled with $R/t < 20$. Consequently, we find, the tubes collapse plastically, and the buckling mode and load are insensitive to imperfections and to the length to radius ratio L/R above the proportional limit. As pointed out by Tvergaard [1983b], this can be best explained by axisymmetric localization, which occurs mainly in thick cylindrical shells. We too have observed this localization.

In the following subsection, we describe quasistatic experiments on 7075 aluminum tubes and, in the next subsection, dynamic experiments on the 3003 aluminum hex-arrayed tubes.

2.1. Quasistatic experiments and results. We performed two quasistatic experiments on two different 7075 aluminum tubes. They are loaded using an Instron hydraulic testing machine with a specially designed arbor. The first tube (tube-I), has $R/t = 18$, while the second (tube-II) has $R/t = 6$. The theory of cylindrical shell buckling considers both tubes to have thick shells, since ($R/t < 100$), and they both buckle plastically.

2.1.1. Tube I experiment. Tube I is a 7075 aluminum rod machined into a thick-walled tube of outer diameter 4.50 mm, wall thickness 0.127 mm ($R/t = 18$), and length 11.80 mm. It has a uniform thickness with accurately cut ends. Figure 1 shows a photograph of the arbor consisting of two maraging steel bars (of maraging steel), an aluminum tube specimen, and an extensometer. The specimen is sandwiched between the two bars in the arbor. The experimental setup fixes the tube's ends against lateral displacement but allows them to rotate. The first quasistatic buckling test is conducted at 295 K (room temperature). The load displacement is controlled with a crosshead speed of about 10^{-3} mm/s. An extensometer measures the axial displacement; it is attached to the arbor and calibrated before testing. Signals from the load cell and the extensometer go to a data acquisition system, the SCXI 1001, using Labview software. We analyze these acquired data using suitable calibration factors. Simultaneously, photographs are taken by a digital camera with a close-up lens. The photographs are paired, at each buckling step, with the

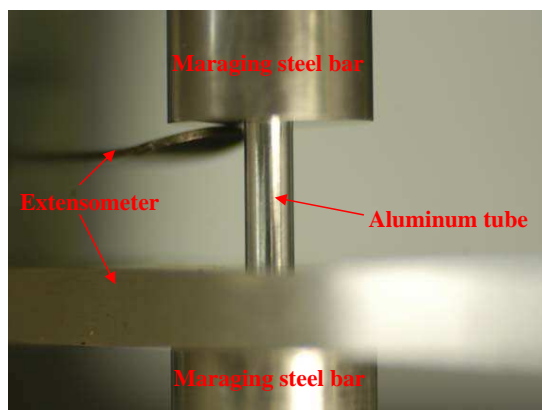


Figure 1. Experimental setup for quasistatic buckling test of 7075 aluminum tube.

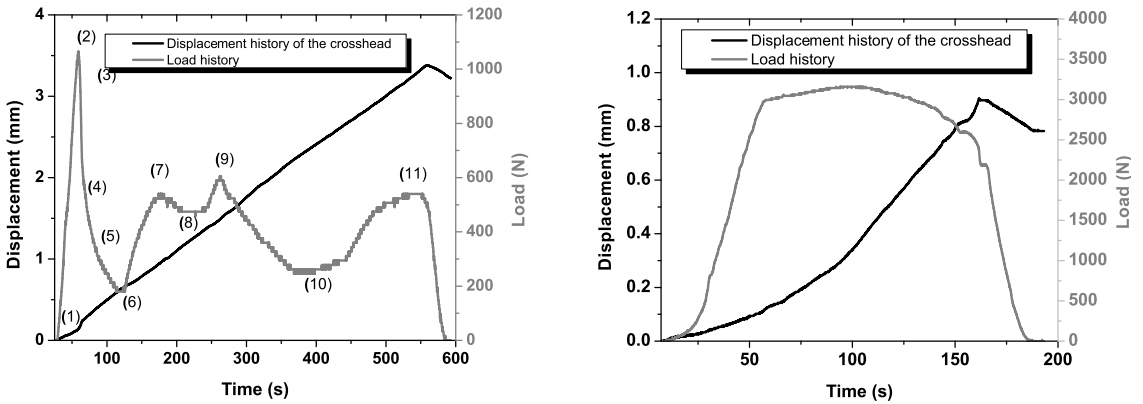


Figure 2. Displacement versus time for aluminum tube-I; displacement-controlled loading with crosshead speed of 6.71×10^{-3} mm/s and corresponding load history. At right, the same for tube-II with crosshead speed 5.33×10^{-2} mm/s.

corresponding load state. Figure 2 (left) displays the load and displacement history for a crosshead speed of 6.71×10^{-3} mm/s.

In the initial stages, the tube deforms in an axisymmetric pattern near one end, as shown in Figure 3. As the axial load is slowly increased, a short axisymmetric bulge develops near one end of the tube (step 1); This bulge continues to grow as the load continues to increase toward a maximum value (step 2); during this time, the load versus displacement curve is linear, indicating elastic deformation. The peak loading corresponds to the first buckling fold. Afterward, the load drops off while the bulge develops into an axisymmetric ring (from step 3 to step 6). The maximum load that the tube can sustain is defined to be the buckling load; the corresponding mode is the buckling mode. This buckling mode is called a ring mode in the literature.

After the initial symmetric or concentric deformation, the tube begins to deform in an asymmetric or diamond (third harmonic) mode at a load less than the buckling load (steps 9 and 11 in Figure 3). We note

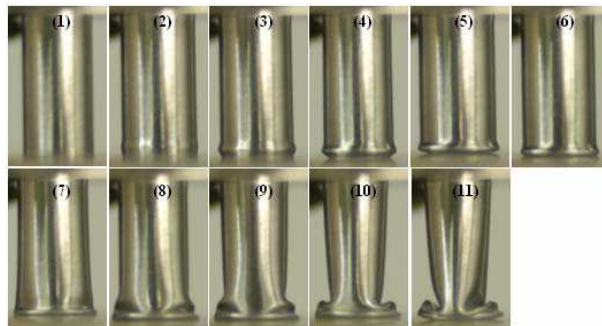


Figure 3. Photographs of aluminum tube-I buckling in uniaxial compression; displacement-controlled loading with crosshead speed 6.71×10^{-3} mm/s; numbers indicate the load state in Figure 2; see [Nemat-Nasser et al. 2006].

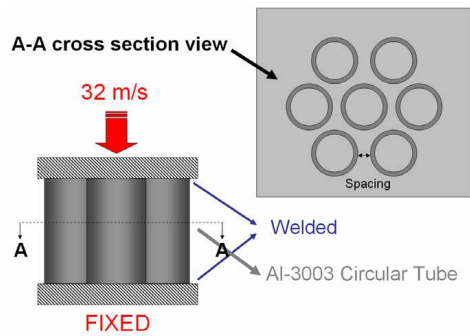


Figure 4. Schematic cross-sectional and lateral views of a hex-arrayed tube structure.

that the static axial crushing tests by Mamalis and Johnson [1983] and Abramowicz and Jones [1984] on aluminum circular cylinders exhibited similar behavior.

2.1.2. Tube II experiment. Tube II is a 7075 aluminum rod machined into a thick-walled tube of outer diameter 4.52 mm, wall thickness 0.381 mm ($R/t = 6$), and length 8.76 mm. The experimental setup is exactly the same as in the first experiment. The total displacement in this test is less than 1 mm, and no postbuckling folding is observed. Figure 2 (right) displays how the load and displacement vary with time under displacement-controlled loading with a crosshead speed of 5.33×10^{-2} mm/s.

2.2. Dynamic experiments and results. The hex-arrayed tube structure consists of two square plates and seven 3003 aluminum tubes, each of outer diameter 15.87 mm, wall thickness 1.65 mm, and height 12.7 mm ($R/t = 5$). Figure 4 shows the cross sectional and lateral views. Each sample is individually fabricated, and hence it may have slight geometric and dimensional imperfections.

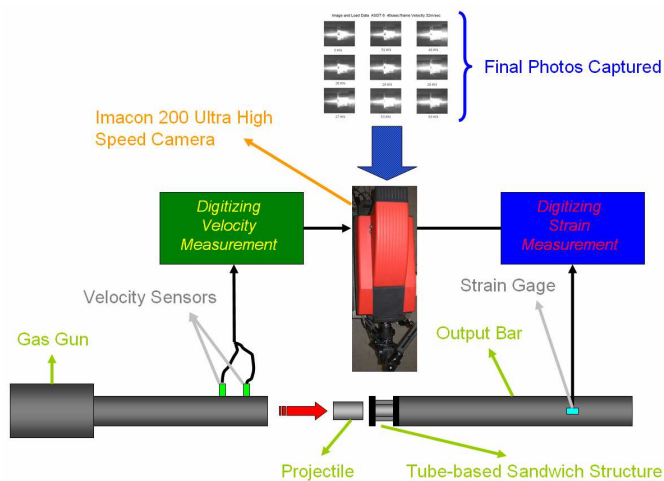


Figure 5. Schematic view of the dynamic compression test of hex-arrayed tubes and Hopkinson bar equipment setup.

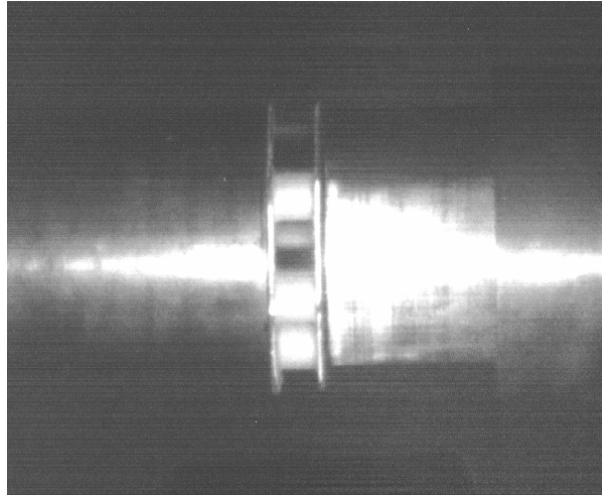


Figure 6. A photo of the hex-arrayed structure attached to the output Hopkinson bar.

The dynamic tests use a single Hopkinson bar setup, shown in Figures 5, 6 and 7. A hex-arrayed sandwich structure is impacted by a striker bar at 32m/s. The deformation process is documented using an Imacon 200 high-speed camera. Just before impact, the striker bar velocity is measured by the sensors near the end of the gas gun. The force transmitted through the structure is measured by a strain gauge attached to the 3 inch output bar. The 7075 aluminum striker bar has a 3 inch (7.62 cm) diameter, length 4.5 inch (11.43 cm), and weight 1460 g. Below, we report our experimental results for three tests, denoted as test-I, test-II, and test-III, corresponding to tube spacings of less than 0.1 inch (2.5 mm), 0.2 inch (5 mm), and 0.5 inch (12.5 mm). Figure 8 shows the top view of two such hex-arrayed structures.

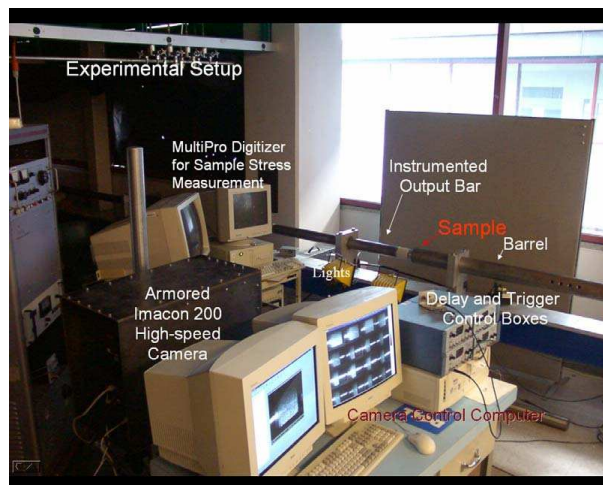


Figure 7. Experimental setup for dynamic compression test of hex-arrayed tubes.

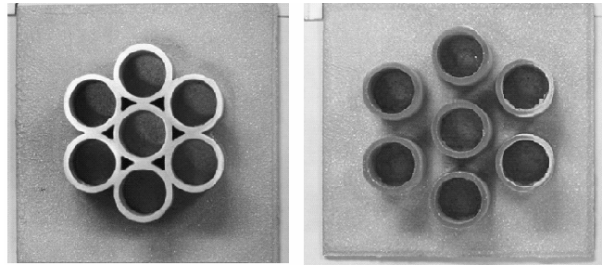


Figure 8. Top view of the hex-arrayed 3003 aluminum tubes. (a) compact spacing (< 0.1 inch), (b) loose spacing ($= 0.5$ inch).

Figure 9 shows the deformed configuration of the test-II specimen captured by the high-speed camera at $40\ \mu\text{s}$ time intervals. In Figure 10 the vertical lines mark the camera timing, and the curve plots the compressive load transmitted through the sandwich structure, as recorded by the strain gauge attached to the output bar.

Figure 11 presents the load versus displacement curves of three tests. The load is normalized by the mass of the corresponding structure to properly compare arrayed tube structures of different length, thickness, and outer diameter. The load versus displacement curves show that the transmitted postbuckling load decreases as the tube spacing is increased. The response of the two structures with greater tube spacing (0.2 inch and 0.5 inch) follows the classic tube buckling pattern: the load drops off after reaching a peak value, although there is slight postbuckling interaction of the 0.2 inch spaced tubes. On the other hand, because adjacent tubes interact in the tightly-packed structure (0.1 inch tube spacing), their postbuckling plastic deformation is interrelated and more complex. A slightly larger buckling load is essentially maintained over the entire deformation process and even increases at large displacements.

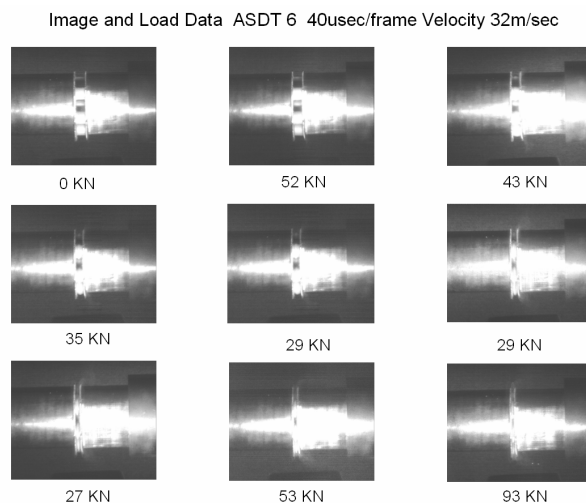


Figure 9. The deformed shape of the test II specimen captured by an Imacon-200 high-speed camera at $40\ \mu\text{s}$ intervals.

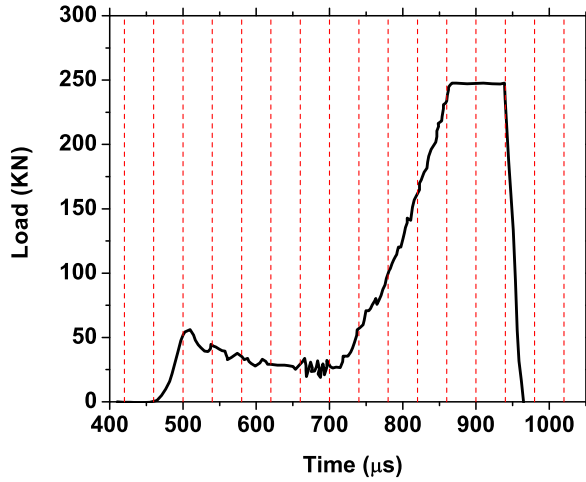


Figure 10. The vertical lines show the camera timing and the curve presents the compressive load history of the structure obtained from the strain gauges attached to the output bar.

3. Material models

We detail the material constitutive models used in this study. For the tubes, we use the Johnson–Cook material model that is already provided by the LS-DYNA, using material parameters that have been experimentally established by [Rule and Jones \[1998\]](#) for 7075 aluminum. In this model the flow stress τ is expressed as

$$\tau = (A + B\gamma^n)(1 + C \ln \dot{\epsilon}^*)(1 - T^{*m}),$$

where $\dot{\epsilon}^* = \dot{\gamma}/\dot{\gamma}_0$ is the dimensionless strain rate, ($\dot{\gamma}_0$ is normally taken to be 1.0/s); the parameters A , B and C , are material constants; γ is the effective plastic strain; and T^* is a normalized temperature

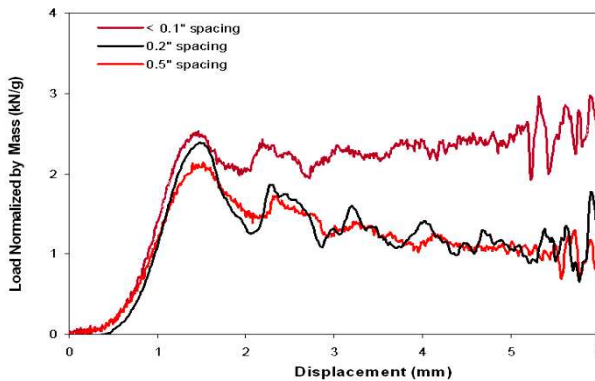


Figure 11. Illustration of normalized load-displacement experimental relations for test-I, test-II and test-III; Load is normalized by the mass of the system. Tube dimensions: OD = 15.87 mm; wall thickness = 1.65 mm; and length = 12.7 mm.

defined by

$$T^* = \frac{T - T_r}{T_m - T_r},$$

where $T_m = 877$ K is the melting temperature of the material. T is the material's actual temperature, and T_r is a reference temperature which must be less than the lowest temperature of interest; we have used $T_r = 298$ K. The complete expression for the Johnson–Cook model for 7075 aluminum is (in MPa)

$$\tau = (452 + 457\gamma^{0.357})(1 + 0.01 \ln \dot{\epsilon}^*)(1 - T^{*1.1}),$$

where,

$$T^* = \frac{T - 298}{579}.$$

To model the 3003 aluminum tubes, we have implemented a user-defined physics-based (PB) material model [Nemat-Nasser and Guo 2004] into LS-DYNA. This is an elastic-viscoplastic constitutive model developed using the kinetics and kinematics of dislocation motion; see [Nemat-Nasser 2004] for details. We evaluate the resulting macroscopic constitutive parameters using a series of quasistatic and dynamic experiments over a broad range of temperatures and strain rates. The model is thus reliable and can be used to simulate high strain-rate deformations, for example, those involved in blast-induced plastic deformations and shear banding. In this model the flow stress τ is expressed as a function of temperature T , effective plastic strain γ , and effective plastic strain rate $\dot{\gamma}$ as

$$\tau = \begin{cases} c_0 + c_1\gamma^n + \tau^0 \left(1 - \left[\frac{-kT}{G_0} \left(\ln \frac{\dot{\gamma}}{\dot{\gamma}_0} + \ln f(\gamma, T) \right) \right]^{\frac{1}{q}} \right)^{\frac{1}{p}} f(\gamma, T), & \text{for } T \leq T_c, \\ c_0 + c_1\gamma^{n_1}, & \text{for } T \geq T_c, \end{cases}$$

where

$$f(\gamma, T) = 1 + a \left[1 - \left(\frac{T}{T_m} \right)^2 \right] \gamma^m, \quad T_c = \frac{-G_0}{k} \left(\ln \frac{\dot{\gamma}}{\dot{\gamma}_0} + \ln f(\gamma, T) \right)^{-1}$$

and where G_0 is the total energy of the short-range barrier to the motion of dislocations, measured per atom; k is the Boltzmann constant; $\dot{\gamma}_0$ is a reference strain rate; T_m is the melting temperature; and c_0 , c_1 , τ^0 , n , m , p , q , and a are material parameters. Nemat-Nasser [2004] detail the parameters used in the PB model. The final constitutive relation for this material is

$$\tau = \begin{cases} 64\gamma^{0.4} + 72 \left\{ 1 - \left[-3.2 \times 10^{-5} T \left(\ln \frac{\dot{\gamma}}{2 \times 10^{10}} + \ln f(\gamma, T) \right) \right]^{\frac{1}{2}} \right\}^{\frac{3}{2}} f(\gamma, T), & \text{for } T \leq T_c, \\ 64\gamma^{0.4}, & \text{for } T \geq T_c, \end{cases}$$

where

$$f(\gamma, T) = 1 + 6 \left[1 - \left(\frac{T}{916} \right)^2 \right] \gamma^{0.05}, \quad T_c = \left[-3.2 \times 10^5 \left(\ln \frac{\dot{\gamma}}{2 \times 10^{10}} + \ln f(\gamma, T) \right) \right]^{-1}$$

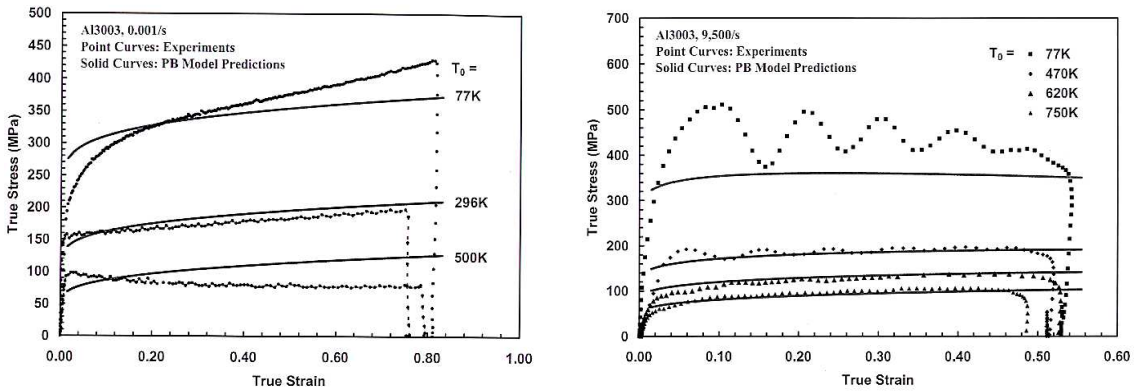


Figure 12. Comparison of PB-model (physical-based model) predictions with experimental results at strain rates of 0.0001/s and 9500/s. Initial temperatures obtained by Nemat-Nasser and Guo [2004].

the stress is in MPa, and T is in degrees Kelvin. Figure 12 compares the experimental results with the PB-model predictions at strain rates of 10^{-3} /s and 9500/s, for indicated initial temperatures. As is seen, the model correlates well with the experimental data.

4. Numerical simulation procedures

We now report the results of our simulations of the nonlinear dynamic and static deformation and buckling of single and hex-arrayed tubes. We used the finite element LS-DYNA 970 code that incorporates experimentally-based nonlinear material models, including strain-rate and temperature effects. The code is based on an updated Lagrangian formulation; it is fully vectorized and can be used to analyze the transient dynamic response of solids and structures [Hallquist 2001].

4.1. Finite element model. We model hex-arrayed and single tubes using 4-node Belytschko–Tasy shell elements with two Gauss integration points through the thickness and an hourglass viscosity to damp out the zero-energy modes. The mesh density is optimized to capture smoothly and with reasonable computational cost the buckling geometry and structural collapse. The code automatically models the contact between adjacent tubes through its single-surface contact option. We model the sandwich plates as rigid walls and consider the nodes of the tubes as slave nodes. We assume fixed boundary conditions at both ends of all the tubes, because, in our experiments, the tubes are welded to the top and bottom plates of the sandwich structure.

4.2. Numerical integration of plasticity model. To apply the constitutive models presented in Section 3 for the three-dimensional calculations, the J_2 -plasticity model is integrated using a radial return algorithm. In this semiimplicit backward Euler method, increments in the effective plastic strain and temperature are calculating after the time step, and then the flow-stress condition is enforced. Given the total strain tensor ε_n , the plastic strain tensor ε_n^P , the effective plastic strain γ_n , the stress tensor σ_n at time n , and the total strain-increment tensor $\Delta\varepsilon = \dot{\varepsilon}\Delta t$, the code computes the quantities $(\varepsilon_{n+1}, \varepsilon_{n+1}^P, \gamma_{n+1}, \sigma_{n+1})$, as follows:

(i) The trial stress $\sigma^{(0)}$ is computed by the elastic predictor using

$$\sigma^{(0)} = \sigma_n + 2G \Delta \varepsilon' + K \text{trace}(\Delta \varepsilon),$$

where $\Delta \varepsilon'$ is the deviator of the total strain-increment tensor, G is the shear modulus, and K is the bulk modulus.

(ii) The effective plastic strain rate $\dot{\gamma}_{n+1}$ follows from assuming the strain increment is all plastic. This is a reasonable approximation because the elastic part is negligibly small.

(iii) The effective trial stress $\bar{\sigma}^{(0)}$ is computed and compared with the current flow stress, $\tau(\gamma_n, \dot{\gamma}_{n+1}, T_n)$ (discussed in Section 3). If the trial state is elastic, the effective plastic strain, plastic strain-rate, and temperature are not updated, and the trial stress is used as the stress at the end of the time step. However, if the effective trial stress exceeds the flow stress, then the radial return algorithm for plastic loading is applied in four steps:

(a) Initialization:

$$k = 0, \quad \varepsilon^{p(0)} = \varepsilon_n^p, \quad \gamma^{(0)} = \gamma_n, \quad \Delta \gamma^{(0)} = 0, \quad (4-1)$$

where k is the iteration counter and superscripts correspond to the iteration number.

(b) Check flow stress at the k th iteration:

$$f^{(k)} = \bar{\sigma}^{(k)} - \tau(\gamma^{(k)}, \dot{\gamma}_{n+1}, T_n). \quad (4-2)$$

If $f^{(k)} < \text{TOL}$ (an arbitrary small number, here 10^{-5}), then the iteration has converged and the temperature is updated; otherwise the process is continued.

(c) Compute the increment in the effective plastic strain:

$$\delta \gamma = \frac{\bar{\sigma}^{(0)} - 3G \Delta \gamma - \tau(\gamma^{(k)}, \dot{\gamma}_{n+1}, T_n)}{3G + \frac{\partial \tau}{\partial \gamma}(\gamma^{(k)}, \dot{\gamma}_{n+1}, T_n)}, \quad \Delta \gamma^{(k+1)} = \Delta \gamma^{(k)} + \delta \gamma. \quad (4-3)$$

(d) Update the plastic strain tensor, effective plastic strain and total stress, set $k \leftarrow k + 1$, and go to step (iii.b).

5. Numerical simulation of single-tube buckling

In this section, we present results of the finite element simulation of the quasistatic tube buckling and compare them with the experiments. We compare both the buckling load and mode, and focus on the postbuckling behavior. We discuss some relevant published analytical results.

In general, the finite element simulations agree well with the experimental results, both for the buckling load and the buckling mode. On the other hand, the previously published analytical predictions we have examined do not seem to yield accurate estimates of the buckling load, nor do they predict the observed postbuckling behavior.

5.1. Computational results. The simulation of tube-I predicts that the tube initially buckles at one end in an axisymmetric mode. As the crushing continues, the buckling mode changes from an axisymmetric bulge to a triangular shape. The mode changes during the postbuckling process because the boundary condition changes for the remaining unbuckled portion of the cylinder. The simulated buckling mode and

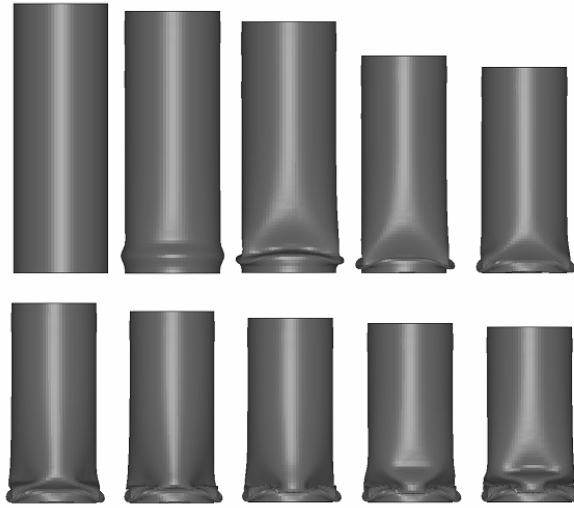


Figure 13. Sequence of plots from deformation and buckling of the 7075 aluminum tube-I in the finite element model with uniaxial compression; displacement-controlled loading with crosshead speed 6.71×10^{-3} mm/s, presented in Figure 2.

its changes during loading agree fairly well with the experimental results; see Figures 13 (left) and 14 (left).

For the simulation, we apply the displacement boundary conditions discussed for the experiments in Figure 2. It predicts the buckling load to be 910 N, whereas the experimental buckling load is 1051 N,

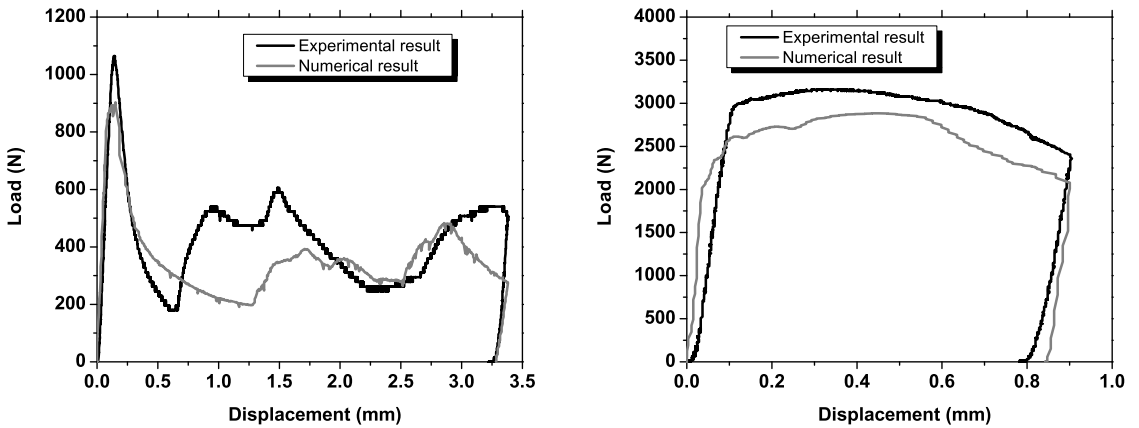


Figure 14. Comparison of experimental and numerical load variation with displacement of the crosshead for 7075 aluminum tube-I, of dimensions: OD = 4.50 mm; wall thickness = 0.127 mm; and length = 11.80 mm. At right, the same for tube-II, of dimensions: OD = 4.52 mm; wall thickness = 0.381 mm; and length = 8.76 mm.

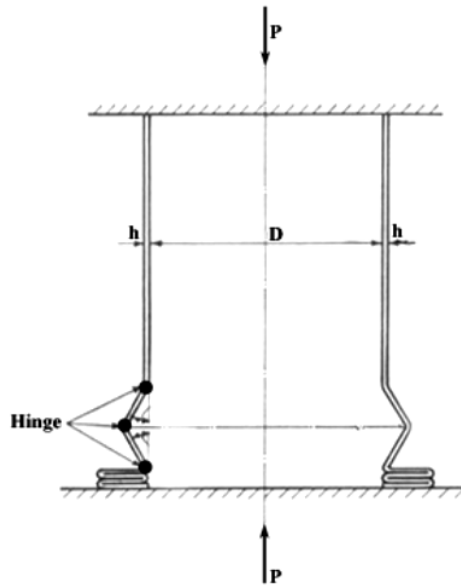


Figure 15. Axisymmetric axial buckling collapse mechanism due to Alexander [1960].

for a 13.4% error. The simulation produces three postbuckling peaks which agree with the experimental results both in number and in their approximate values.

Abramowicz and Jones [1984] have provided a comprehensive review and substantial data on the axisymmetric buckling modes of cylindrical shells. Their analysis is based on work done by Alexander [1960]. Their assumed buckling mechanism, illustrated in Figure 15, takes place in a section of length $2H$ and consists of three stationary (relative to the material) plastic hinges separating two outward moving portions which stretch circumferentially. Abramowicz and Jones determine the crushing force P_B in terms of the material properties and tube geometry after minimizing the global work and arrive at the following expression:

$$\frac{4P_B}{\sigma_0 t^2} = 20.79 \left(\frac{D}{t} \right)^{1/2} + 11.90,$$

where σ_0 is the yield stress of the material, t is the thickness, and D is the outer diameter. For our experiment described above, this equation gives $P_B = 225.5$ N, whereas, the experimental mean crushing force is approximately 452 N. This significant underestimation typifies predictions of this analysis and is ascribed by Alexander [1960] to the assumption that the convolutions flatten into discs. That assumption is inconsistent with our experimental observations and numerical simulations. Ignoring the plastic hardening is another possible reason for this underestimation.

For aluminum tube-II, shown in Figures 14 (right) and 16 (right), the numerical model provides a reasonable representation of the experimental results, both for the buckling load and the buckling mode. The simulation predicts the buckling load to be around 2600 N, whereas, the experiment shows a buckling load of 2950 N, for an 11.8% error. Figure 14 compares the experimental and numerical load-displacement curves. The simulation predicts that the buckling starts at the end of the tube and also

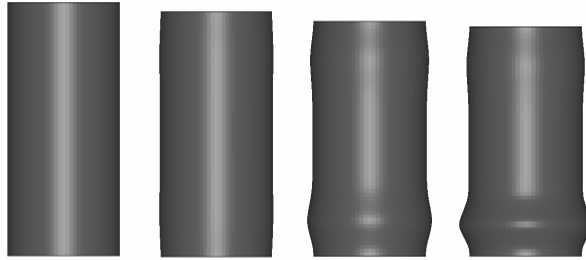


Figure 16. Sequence of plots from simulating deformation and buckling of the thick 7075 aluminum tube in uniaxial compression; displacement-controlled loading with crosshead speed 5.33×10^{-2} mm/s, presented in [Figure 2](#).

when the displacement reaches a specific level; see [Figure 16](#). It predicts a stable postbuckling response that agrees with the experimental observations.

Two important observations about the buckling mode are apparent from the foregoing numerical and experimental results. First, the buckling mode is axisymmetric, and, second, the buckling begins near the ends of the tubes. We explain these observations as follows.

Axisymmetric buckling has only stretching in the hoop direction, whereas nonaxisymmetric buckling primarily involves bending in that direction. The energy required for either mode, that is, hoop direction stretching or hoop direction bending, is a function of tube thickness. As this increases, the energy required for stretching increases linearly. On the other hand, the bending energy varies quadratically with the thickness, making it increase more rapidly with thickness. For sufficiently thick tubes (roughly $R/t < 40$), the hoop bending energy exceeds the hoop membrane energy, and thus the buckling occurs in the lower energy axisymmetric mode [[Allan 1968](#)].

That buckling begins at the ends can be explained by the end boundary conditions and axisymmetric buckling localization theory [[Tvergaard 1983a](#)]. If the tubes were not constrained at the ends, then, as the load increases, the axial shortening would cause a radial expansion that is uniform along the axis (Poisson effect). However, because the tubes are constrained at both ends by friction, there arises an axisymmetric, radial shear stress which begins at the tube ends and decays rapidly away from the boundary. This additional shear stress triggers localized axisymmetric buckling at the boundaries. This behavior is observed in the quasistatic experiments and predicted by the finite element simulations.

6. Numerical simulation of hex-arrayed tube-buckling

To enhance energy absorption while keeping the system as light as possible, one may exploit the postbuckling interaction of adjacent tubes. As for a single tube, hex-arrayed tubes initially respond linearly to a compressive load. However, after they begin to buckle, they begin to interact with one another, enhancing the energy absorption of the structure.

How hex-arrayed tubes respond to a compressive load depends on their spacing. Here, we present the experimental and numerical results of dynamic compression tests of hex-arrayed tubes and document the effect of varying tube spacing, length, and thickness (for a fixed outer diameter).

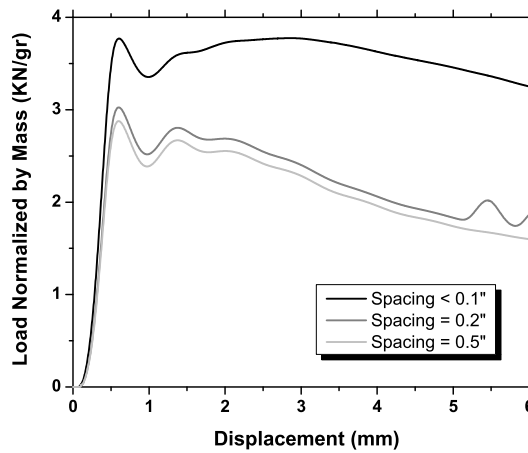


Figure 17. The numerical results of normalized load per mass with displacement variation of the sandwich plates for the hex-arrayed 3003 aluminum tubes compared at three different spacing levels, using Nemat-Nasser’s physics-based (PB) material model. Tube dimensions: OD = 15.9 mm; wall thickness = 1.65 mm; and length = 13.0 mm.

6.1. Computational results. Each tube has outer diameter 15.87 mm, wall thickness 1.65 mm, and height 13.0 mm ($R/t = 5$). All the simulations are performed with the same setup, using an impact speed of 32 m/s. Their fixed boundary conditions simulate welding the tubes to the plates. [Figure 17](#) compares the load histories for the three simulations. For all three tube spacings, they predict a buckling load per unit mass of approximately 3 KN/g, while the experiments show this value to be 2.6 KN/g. Although the numerical models qualitatively predict the experimental trends, the remaining quantitative discrepancy is not fully understood. It may be that the fabrication has introduced various imperfections in the samples [[Meissner 2004](#)], while the simulation assumes perfectly arranged hex-array structures.

The finite element model predicts that the tight structure (gaps < 0.1 inch) maintains the load level, perhaps because the tubes interact after buckling. The experiment shows the same effect. For less tight structures, with tube spacings of 0.2 inch and 0.5 inch, the load histories are almost the same, although the 0.2 inch one exhibits some postbuckling interaction. The finite element simulations predict lower buckling loads than for the tight structure, which is in good agreement with the experimental results; see [Figure 14](#). The simulations predict reasonably well how the overall behavior and the energy absorption depend on the tube spacing. [Figure 18](#) presents the predicted final deformed configuration of the tubes with 0.2 inch spacing; [Figure 19](#) shows the corresponding deformation sequences.

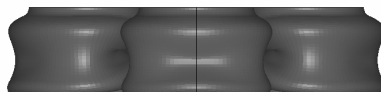


Figure 18. Final finite element configuration of the hex-arrayed 3003 aluminum tubes at maximum deformation; spacing equal to 0.2 inch, using Nemat-Nasser’s physics-based material model.

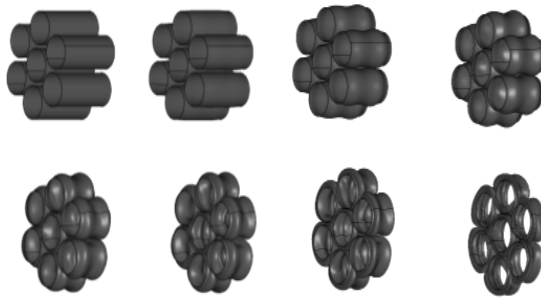


Figure 19. Sequence of numerical prediction of hex-arrayed tube structure buckling with 0.2 inch spacing, under dynamic loading.

6.2. Parametric study of hex-arrayed tube-buckling. We have simulated how the arrays respond to varying thickness and length, while keeping the outer diameter constant at 1.59 cm. To sensibly compare the results, we normalize the dissipated energy and the applied load by the mass of the system. All

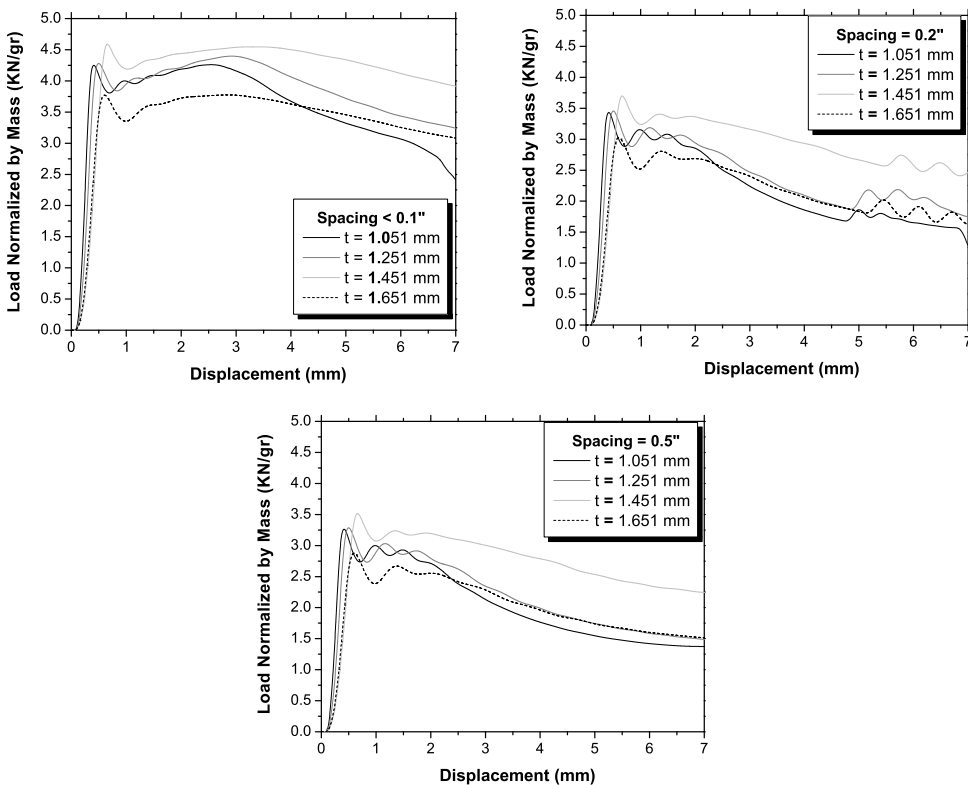


Figure 20. Effect of thickness on the normalized load per unit mass variation with displacement of the sandwich plates. The tubes have spacing less than 0.1 inch, equal to .02 inch, and equal to .05 inch. They have lengths 1.3 cm and outer diameter 1.59 cm.

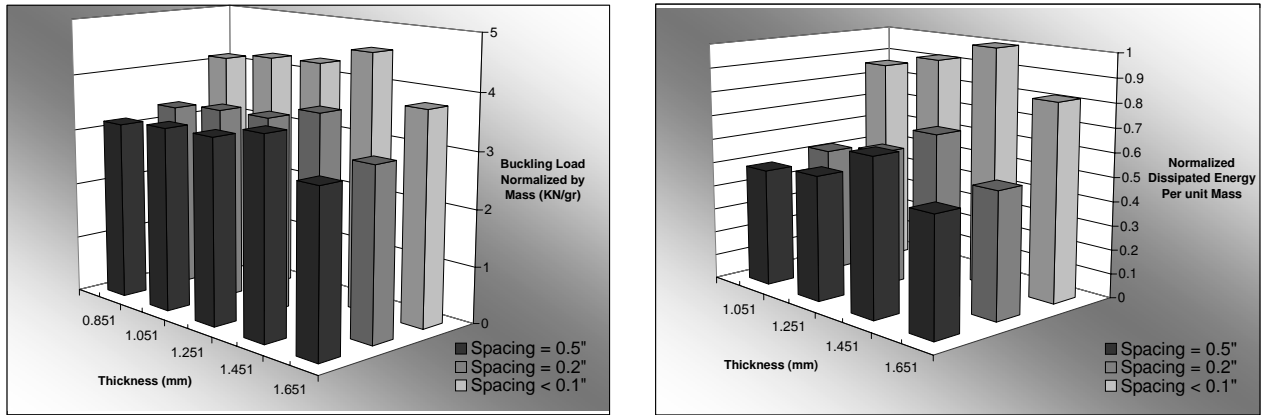


Figure 21. Buckling load and dissipated energy per unit mass of the hex-arrayed tube structure, normalized and plotted against varying thickness and spacing levels. The length of the tubes is 1.3 cm and the outer diameter is 1.59 cm.

simulations have the same fixed boundary conditions, with a 32 m/s impact velocity. We model aluminum 3003 using Nemat-Nasser’s PB model, presented in Section 2.

To analyze the effect varying tube thickness, we chose five different values of 0.851, 1.051, 1.251, 1.451, and 1.651 mm, while keeping the length at 1.30 cm and the outer diameter at 1.59 cm. For each thickness, we studied all three tube spacings considered in the previous section. Figure 20 shows the simulation results. Increasing the thickness from 1.051 to 1.451 mm causes an increase in the normalized load for all three tube spacings. However, further increasing the thickness from 1.451 to 1.651 mm does

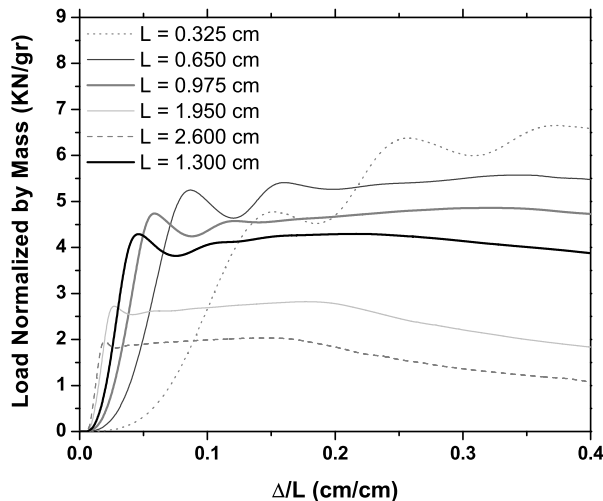


Figure 22. Variation of normalized load per unit mass of the hex-arrayed tube structure with deflection of unit length for tubes of different lengths and compact spacing (< 0.1 inch). The outer diameter of the 3003 aluminum tubes is 1.59 cm.

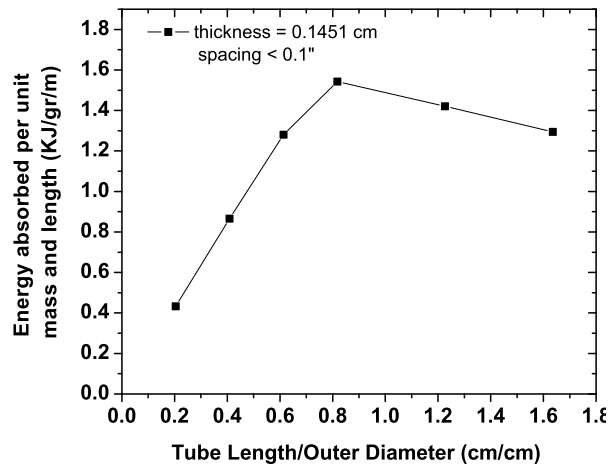


Figure 23. Variation of energy absorbed per unit mass and length of the hex-arrayed aluminum tube structure with different length to outer diameter ratios. The spacing is compact (< 0.1 inch) and the thickness is 0.145 cm.

not cause a significant drop in the normalized buckling load or the normalized dissipated energy. For comparison, we further rescale the normalized dissipated energies by the largest one, namely, that of the tightly spaced tubes with thickness 1.451 mm; see [Figure 21](#).

To analyze the effect of varying tube length, we choose various lengths L from 0.32 cm to 2.60 cm, while keeping a fixed outer diameter at 1.59 cm, the thickness at 1.451 mm, and a spacing less than 0.1 inch. The simulations show that, as L/R increases, the buckling mode changes from a single barrel in the middle to a double barrel at the ends. This change occurred as L went from 1.3 cm to 1.95 cm. [Figure 22](#) illustrates how the rescaled, normalized load varies with the deflection per unit length of the tubes. As length increases, starting from 0.325 cm, the absorbed energy (per unit mass per unit length) increases and reaches a maximum at 1.3 cm; however, increasing the length further does not seem to result in an increase in the absorbed energy (per unit mass, per unit length), as is illustrated in [Figure 23](#). Among the simulations conducted in this study, the hex-arrayed tube structure with an outer diameter to thickness $OD/t = 11$ and outer diameter to length $OD/L = 1.22$ showed the best energy-absorption performance.

7. Conclusions

We measured and simulated quasistatic buckling of single aluminum tubes and dynamic buckling of hex-arrayed aluminum tubes. The methods achieved excellent agreement in the buckling load, buckling mode, and the postbuckling behavior. The finite element calculations incorporate rate- and temperature-sensitive physics-based constitutive models for aluminum 3003 that we integrated into LS-DYNA using a J_2 -plasticity model and a radial-return algorithm.

The single tube experiments and simulations have confirmed that the buckling mode—that is, the deformation path of least resistance—depends on the geometrical ratios and the tube thickness. The

single tube initially buckled into an axisymmetric pattern near one end, and then, as the load level significantly dropped, continued into a diamond deformation mode.

The experiments and simulation of the hex-arrayed tube structures suggest that their energy absorption increases with a decrease in their spacing, due to postbuckling interaction between the adjacent tubes. Finally, we examined how varying the array's geometrical parameters affected their energy absorption.

References

- [Abramowicz and Jones 1984] W. Abramowicz and N. Jones, "Dynamic axial crushing of circular tubes", *Int. J. Impact Eng.* **2**:3 (1984), 263–281.
- [Alexander 1960] J. M. Alexander, "An approximate analysis of the collapse of thin cylindrical shells under axial loading", *Quart. J. Mech. Appl. Math.* **13** (1960), 10–15.
- [Allan 1968] T. Allan, "Experimental and analytical investigation of the behavior of cylindrical tubes subject to axial compressive forces", *J. Mech. Eng. Sci.* **2** (1968), 182–197.
- [Batterman 1965] S. C. Batterman, "Plastic buckling of axially compressed cylindrical shells", *AIAA J.* **3** (1965), 316–325.
- [Budiansky and Hutchinson 1966] B. Budiansky and J. W. Hutchinson, "A Survey of some buckling problems", *AIAA J.* **4** (1966), 1505–1510.
- [Gellin 1979] S. Gellin, "Effect of an axisymmetric imperfection on the plastic buckling of an axially compressed cylindrical shell", *J. Appl. Mech.* **46** (1979), 125–131.
- [Gerard 1962] G. Gerard, "On the role of initial imperfections in plastic buckling of cylinders under axial compression", *J. Aerosp. Sci. Technol.* **29** (1962), 744–745.
- [Hallquist 2001] J. O. Hallquist, *LS-DYNA Version 970: Theoretical manual*, Livermore: Livermore Software Technology Corporation, 2001.
- [Horton et al. 1966] W. H. Horton, S. C. Bailey, and A. M. Edwards, "Nonsymmetric buckle patterns in progressive plastic buckling", *Exp. Mech.* **23** (1966), 433–444.
- [Johnson et al. 1977] W. Johnson, P. D. Soden, and S. T. S. Al-Hassani, "Inextensional collapse of thin walled tubes under axial compression", *J. Strain Anal. Eng. Des.* **12** (1977), 317–330.
- [Karagiozova et al. 2000] D. Karagiozova, M. Alves, and N. Jones, "Inertia effects in axisymmetrically deformed cylindrical shells under axial impact", *Int. J. Impact Eng.* **24** (2000), 1083–1115.
- [Lee 1962] L. H. N. Lee, "Inelastic buckling of initially imperfect cylinder shells subject to axial compression", *J. Aerosp. Sci. Technol.* **29** (1962), 87–95.
- [Mamalis and Johnson 1983] A. G. Mamalis and W. Johnson, "The quasi-static crumpling of thin-walled circular cylinders and frusta under axial compression", *Int. J. Mech. Sci.* **25** (1983), 713–732.
- [Mamalis et al. 2003] A. G. Mamalis, D. E. Manolacos, M. B. Ioannidis, P. K. Kostazos, and C. Dimitriou, "Finite element simulation of the axial collapse of metallic thin-walled tubes with octagonal cross-section", *Thin-Walled Struct.* **41** (2003), 891–900.
- [Meissner 2004] J. Meissner, "Axially aligned cylindrical shell arrays as energy absorbing structures", Master's Thesis, UC San Diego, August 2004.
- [Nemat-Nasser 2004] S. Nemat-Nasser, *Plasticity a treatise on finite deformation of heterogeneous inelastic materials*, first ed., Cambridge University press, Cambridge, 2004.
- [Nemat-Nasser and Guo 2004] S. Nemat-Nasser and W. G. Guo, "Plastic flow of Al 3003 alloy over a wide range of strain rates and temperatures: experimental and modeling", 2004. unpublished work.
- [Nemat-Nasser et al. 2006] S. Nemat-Nasser, J. Choi, J. B. Isaacs, and D. W. Lischer, "Quasistatic and dynamic buckling of thin cylindrical shape memory shells", *J. Appl. Mech.* **73** (2006), 825–833. Special Volume on Current Trends in Mechanics, W.G. Khauss 2004 Symposium.
- [Nemat-Nasser et al. 2007] S. Nemat-Nasser, W. J. Kang, J. D. McGee, W. G. Guo, and J. B. Issacs, "Experimental investigation of energy-absorption characteristics of sandwich structures", *Int. J. Impact Eng.* **34**:6 (2007), 1119–1146.

- [Reid 1993] S. R. Reid, "Plastic deformation mechanisms in axially compressed metal tubes used as impact energy absorbers", *Int. J. Mech. Sci.* **12** (1993), 1035–1052.
- [Rule and Jones 1998] W. K. Rule and S. E. Jones, "A revised form for the Johnson-Cook strength model", *Int. J. Impact Eng.* **21**:8 (1998), 609–624.
- [Tennyson and Muggeridge 1969] R. C. Tennyson and D. B. Muggeridge, "Buckling of axisymmetric imperfect circular cylinder shells under axial compression", *AIAA J.* **7** (1969), 2127–2131.
- [Tvergaard 1983a] V. Tvergaard, "On the transition from diamond mode to an axisymmetric mode of collapse in cylindrical shells", *Int. J. Solids Struct.* **19**:10 (1983), 845–856.
- [Tvergaard 1983b] V. Tvergaard, "Plastic buckling of axially compressed circular cylindrical shells", *Thin-Walled Struct.* **1** (1983), 139–163.
- [Weingarten et al. 1964] V. I. Weingarten, E. J. Morgan, and P. Seide, "Elastic stability of thin-walled cylindrical and conical shells under axial compression", *AIAA J.* **3** (1964), 500–505.

Received 20 May 2007. Accepted 23 May 2007.

SIA NEMAT-NASSER: sia@ucsd.edu

Center of Excellence for Advanced Materials, Department of Mechanical and Aerospace Engineering, University of California San Diego, La Jolla, CA 92093-0416, United States

MAHMOUD REZA AMINI: mramini@starlite.ucsd.edu

Center of Excellence for Advanced Materials, Department of Mechanical and Aerospace Engineering, University of California San Diego, La Jolla, CA 92093-0416, United States

JEOM YONG CHOI: jjeomyong@posco.co.kr

POSCO Technical Research Laboratories, Pohang, Kyeongbuk, 790–785, Korea

JON ISAACS: JonIsaacs@aol.com

Center of Excellence for Advanced Materials, Department of Mechanical and Aerospace Engineering, University of California San Diego, La Jolla, CA 92093-0416, United States

AN APPROACH TO MODELING EXTREME LOADING OF STRUCTURES USING PERIDYNAMICS

PAUL N. DEMMIE AND STEWART A. SILLING

We address extreme loading of structures using peridynamics. The peridynamic model is a theory of continuum mechanics that is formulated in terms of integro-differential equations without spatial derivatives. It is a nonlocal theory whose equations remain valid regardless of fractures or other discontinuities that may emerge in a body due to loading. We review peridynamic theory and its implementation in the EMU computer code. We consider extreme loadings on reinforced concrete structures by impacts from massive objects. Peridynamic theory has been extended to model composite materials, fluids, and explosives. We discuss recent developments in peridynamic theory, including modeling gases as peridynamic materials and the detonation model in EMU. We then consider explosive loading of concrete structures. This work supports the conclusion that peridynamic theory is a physically reasonable and viable approach to modeling extreme loading of structures.

1. Introduction

In this paper, we address the extreme impact and explosive loading of structures using peridynamic theory, or *peridynamics*. The present paper is the first publication of results and developments in peridynamic theory to model extreme loading of large structures. Peridynamics is a theory of continuum mechanics that is formulated in terms of integro-differential equations without spatial derivatives [Silling 2000]. Conventional continuum-mechanics theory is formulated in terms of partial differential equations with spatial derivatives. However, these derivatives do not exist at discontinuities, and the conventional theory breaks down as a spatial discontinuity develops. Peridynamics replaces the spatial derivatives of conventional continuum-mechanics theory with integrals and assumes that particles in a continuum interact across a finite distance as in molecular dynamics. Therefore, an attractive feature of peridynamics is that its equations remain valid regardless of any fractures or discontinuities that may emerge in a structure due to loading. Implementation of peridynamics does not use stress intensity factors and does not require a separate law that tells cracks when and where to grow. Cracks emerge spontaneously as a result of the equations of motion and material model. They grow in whatever direction is energetically favorable for growth.

Although peridynamic theory is relatively new compared to conventional continuum-mechanics theory, its development is continuing and it has been applied to solve a number of problems. The method has origins in the work of Rogula [1982] and Kunin [1982] on nonlocal behavior in crystals.

Keywords: peridynamics, continuum mechanics, computational mechanics, solid mechanics, deformation, fracture, extreme loading.

Sandia National Laboratories is a multiprogram laboratory operated by Sandia Corporation, a Lockheed Martin Company, for the United States Department of Energy under contract DE-AC04-94AL85000.

[Silling \[2000\]](#) expanded and developed the model as a general way to formulate initial-boundary value problems in which the spontaneous occurrence of discontinuities is important. He proposed the term “peridynamic” from the Greek roots for “near” and “force”. He demonstrated that the reformulated approach permits the solution of fracture problems using the same equations either on or off the crack surface or crack tip without knowledge of the initial location of the crack. Since particles separated by a finite distance can interact with each other as in molecular dynamics, the theory is nonlocal. Although there are other nonlocal theories of continuum mechanics, they do not attempt to eliminate the spatial derivatives.

[Silling \[2003\]](#) described a numerical method for solving initial-value problems within peridynamic theory. Accuracy and numerical stability were addressed in [\[Silling and Askari 2005\]](#) This work also showed how to include nonhomogeneous materials, such as fiber-reinforced composite materials, as peridynamic materials.

[Silling et al. \[2003\]](#) applied peridynamics to study deformation of a peridynamic bar. Their solution exhibits features that are not present in the classical result but converges with the classical result in the limit of short-range forces. [Gerstle and Sau \[2004\]](#) and [Gerstle et al. \[2005\]](#) applied peridynamic theory to the quasistatic deformation of concrete. They illustrated the deformation and fracture of small plain concrete samples and the effect of using rebar reinforcement. [Silling and Bobaru \[2005\]](#) applied peridynamic theory to study stretching and tearing of membranes. They also studied string-like structures, similar to long molecules, that sustain tensile loads while interacting with each other through intermolecular and contact forces. Their work is an early effort to apply peridynamic theory at the nanoscale.

For several years, we have used peridynamic theory to investigate damage resulting from aircraft impacting buildings and other large structures made of reinforced concrete. In the present paper, we discuss this approach to modeling extreme loading of large structures. We also present some recent developments in peridynamics, which provide an approach to modeling loading from explosive detonations.

Since peridynamic theory is relatively new, we first review peridynamic theory. In [Section 2](#), we state the fundamental integro-differential equation of peridynamic theory and introduce the pairwise force function (PFF). The PFF is the force per unit volume squared between two particles. This interaction is called a bond. Constitutive properties of a material are given by specifying the PFF. Thus, in peridynamics, material response, damage, and failure are determined at the bond level. Bond properties can be derived from material properties including elastic modulus, yield properties, and fracture toughness [\[Silling 2000\]](#).

After discussing some properties of the PFF, we discuss the material models that we use for extreme-loading analyses. These materials are called proportional, microelastic or microplastic materials. For these materials, failure of a bond occurs when the stretch exceeds a value called the critical stretch.

In [Section 3](#), we discuss the numerical method used to solve the integro-differential equations of peridynamics in the EMU computer code. In this section, we also review accuracy and stability for explicit time integration. EMU is the first computer code that is based on the peridynamic theory of continuum mechanics.

[Section 4](#) contains a discussion of the EMU computer code. EMU is mesh free and Lagrangian. It uses explicit time integration to advance the solution in time and executes on parallel computers.¹

¹Information on EMU can be found at www.sandia.gov/emu/emu.htm.

In [Section 5](#), we consider impacts of aircraft into reinforced concrete structures. We first discuss a simulation of an experiment that was performed at Sandia National Laboratories. In the test, an F4-Phantom impacted a massive, essentially rigid reinforced concrete wall [[Sugano et al. 1993](#)]. Because of the strength of the target, there was no perforation of the target. In the second example, there is perforation. An aircraft impacts a cylindrical structure made of reinforced concrete. In this example, we demonstrate the ability of peridynamics to model deformation and fracture leading to perforation. The ability to model fracture in perforation problems is important since a target starts to weaken long before a penetrator gets through and the fracture growth process determines fragment properties.

We next focus on explosive loading. Before introducing the EMU detonation model, we describe modeling gases as peridynamic materials in [Section 6](#) since the detonation products are gases. How to model fluids as peridynamic materials is particularly important since the pairwise interactions through the linearized PFF imply a Poisson's ratio of $1/4$ [[Silling 2000](#)]. We describe the EMU detonation model in [Section 7](#).

In [Section 8](#), we consider explosive loading of a spherical shell and a large reinforced concrete structure containing water.

[Section 9](#) contains a summary and conclusions of this work. There, we also discuss current work and future directions in the development and applications of peridynamic theory and the EMU computer code.

2. Peridynamic theory and material modeling

Consider a peridynamic body that occupies a domain R as shown in [Figure 1](#).

In the peridynamic theory, the force density on a particle at point \mathbf{x} and time t is assumed to be given by

$$\rho(\mathbf{x}) \frac{d^2}{dt^2} \mathbf{u}(\mathbf{x}, t) = \iiint_R \mathbf{f}(\mathbf{u}(\mathbf{x}', t) - \mathbf{u}(\mathbf{x}, t), \mathbf{x}' - \mathbf{x}) dV' + \mathbf{b}(\mathbf{x}, t), \quad (1)$$

where $\rho(\mathbf{x})$ is the density at \mathbf{x} , \mathbf{x} and \mathbf{x}' are points in the reference configuration, t is the time, \mathbf{u} is the displacement vector, R is the domain of the body, \mathbf{f} is the pairwise force function, and \mathbf{b} is the

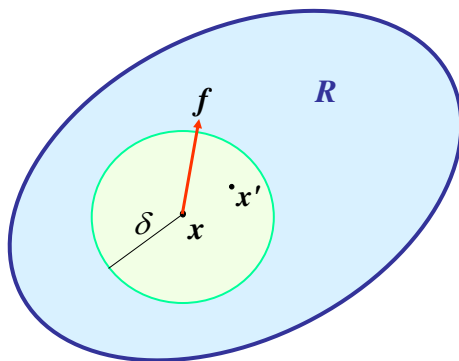


Figure 1. A peridynamic body occupying a domain R .

body-force density. (In Equation (1) and elsewhere, bold quantities are vectors unless stated otherwise.) The integral in Equation (1) is taken over the volume occupied by R . All functions are assumed to be sufficiently well behaved that the integral exists.

Equation (1) is the fundamental integro-differential equation of peridynamic theory. It is based on Newton's second law for all points within the domain of analysis. It does not contain any spatial derivatives. The specific force term is a functional depending on a vector-valued function, \mathbf{f} , called the pairwise force function (PFF). The PFF gives the force per unit volume squared on a particle at \mathbf{x} due to a particle at \mathbf{x}' . In conventional continuum-mechanics theory, this functional is the divergence of the stress tensor. All constitutive properties of a material are given by specifying the PFF.

Figure 1 shows a sphere $S_\delta(\mathbf{x})$ of radius δ centered at the point \mathbf{x} . It is convenient to assume that there is a distance δ such that the PFF function vanishes outside $S_\delta(\mathbf{x})$ for each point \mathbf{x} in the domain of analysis. The quantity δ is called the *horizon* since a particle cannot "see" a force beyond its horizon. This assumption is natural for the types of materials that are used for extreme-loading analysis as discussed below. It is also reasonable for forces that die off sufficiently rapidly or become shielded by intervening particles.

The appropriate value of δ depends on the physical nature of the application. At the nanoscale, it is determined by the distance over which physical interactions between atoms or molecules occur. At the macroscale, it is somewhat arbitrary since, for any given value of δ , the parameters in the PFF can be chosen to match the bulk-elastic properties of the material, as well as its most important fracture properties [Silling and Askari 2005]. However, in numerical modeling, typically δ is chosen to be three times the grid spacing. Values much smaller than this value result in undesirable grid effects such as cracks growing along the rows or columns of the grid. Values much larger than this may result in excessive wave dispersion and computational time.

Several properties of materials follow from the form of the PFF in (1). First, the dependence of \mathbf{f} on $\mathbf{x} - \mathbf{x}'$ implies that the materials are homogeneous. Here, we will not consider extensions of peridynamic theory for nonhomogeneous materials. Second, the materials have no memory of their deformation history. Modeling materials with memory is a potential area for future research and development of peridynamic theory. Perhaps the fractional calculus [Oldham and Spanier 1974] can be useful since the fractional calculus has been useful for rheology of materials with memory (see articles in [Hilfer 2000]).

Consider the functional dependence of PFF shown in (1). It is convenient to express the PFF in terms of the new set of variables, $\boldsymbol{\xi}$ and $\boldsymbol{\eta}$, where

$$\boldsymbol{\xi} = \mathbf{x}' - \mathbf{x} \quad \text{and} \quad \boldsymbol{\eta} = \mathbf{u}(\mathbf{x}', t) - \mathbf{u}(\mathbf{x}, t). \quad (2)$$

$\boldsymbol{\xi}$ is the relative position of particles at \mathbf{x} and \mathbf{x}' in the reference configuration and $\boldsymbol{\eta}$ is the difference in displacements at these points.

Figure 2 illustrates the relationship among the variables introduced thus far.

In this figure and elsewhere, $\mathbf{u}' = \mathbf{u}(\mathbf{x}', t)$. From this figure, $\boldsymbol{\eta} + \boldsymbol{\xi}$ is the relative position of the particles originally at \mathbf{x} , \mathbf{x}' in the deformed configuration.

In terms of the new variables $\boldsymbol{\eta}$ and $\boldsymbol{\xi}$, the PFF \mathbf{f} becomes

$$\mathbf{f}(\mathbf{u}(\mathbf{x}', t) - \mathbf{u}(\mathbf{x}, t), \mathbf{x}' - \mathbf{x}) = \mathbf{f}(\boldsymbol{\eta}, \boldsymbol{\xi}). \quad (3)$$

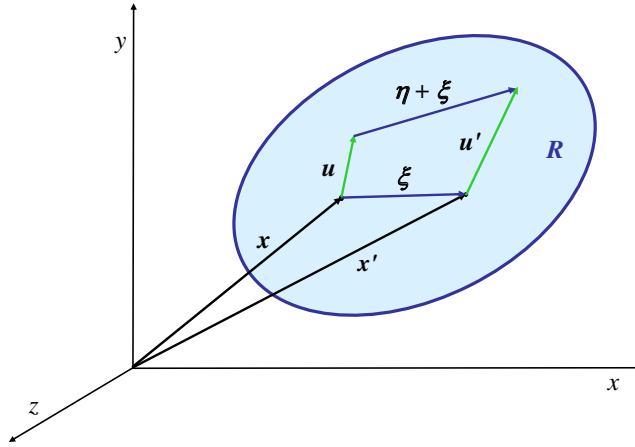


Figure 2. Relationships among the variables.

Newton’s laws not only lead to the fundamental equation of peridynamics but also imply another property of the PFF f . Newton’s third law states that the force on a particle at x due to a particle at x' must be the negative of the force on a particle at x' due to a particle at x . Therefore for (1) to satisfy Newton’s third law, $f(\eta, \xi)$ must satisfy

$$f(-\eta, -\xi) = -f(\eta, \xi), \quad \text{for all } \eta, \xi. \tag{4}$$

Thus, $f(\eta, \xi)$ is an odd function of (η, ξ) .

The next property of the PFF follows from the requirement to conserve angular momentum in the absence of external forces. If angular momentum were not conserved, then two particles initially at rest would move even in the absence of external forces. Thus, to ensure conservation of angular momentum, $f(\eta, \xi)$ must satisfy

$$(\eta + \xi) \times f(\eta, \xi) = 0, \quad \text{for all } \eta, \xi, \tag{5}$$

where “ \times ” is the cross product. This expression implies that the force between any two particles must be parallel to their current relative position. Therefore, (5) implies that $f(\eta, \xi)$ must have the functional form

$$f(\eta, \xi) = F(\eta, \xi)(\eta + \xi), \quad \text{for all } \eta, \xi, \tag{6}$$

where F is a scalar-valued function. Since $f(\eta, \xi)$ is an odd function of (η, ξ) , $F(\eta, \xi)$ must be an even function of (η, ξ) .

Gravity is important to determine the long-term consequences of impacts to structures. Before continuing the discussion of material modeling in peridynamics, we note that gravity is included in (1) as a body-force density. The body-force density for gravity, $\mathbf{b}_{\text{gravity}}$ is given by

$$\mathbf{b}_{\text{gravity}} = \rho(\mathbf{x})\mathbf{g}, \tag{7}$$

where \mathbf{g} is the acceleration vector due to gravity with magnitude $g = 9.814 \text{ m/s}^2$.

In the previous discussion, we showed that Newton’s third law and the physical requirement to conserve angular momentum in the absence of external forces imply that the PFF must be in the direction of the relative displacement in the deformed configuration as given by (6). Here, we develop the general

form of the PFF for materials that are used in loading analyses. Although many of these results were first published in [Silling 2000], we provide this short summary and discussion for completeness and to provide results that are used in Section 6 to model gases as peridynamic materials.

All constitutive properties of a material are given by specifying the PFF. Previously, we showed that the dependence of the PFF f on ξ implies that the material is homogeneous. If a material is isotropic, then there is a further restriction on the functional dependence of f . Proper behavior of f under the orthogonal rotation group in three dimensions implies that F in (6) must be invariant under this group. Hence, the scalar function F depends only on the length of η , the angle between η and ξ , and the length of ξ . However, we find it more convenient to use the length of $\eta + \xi$ rather than η . Therefore, for isotropic materials, the most general form for F is

$$F(\eta, \xi) = I(p, q, r), \quad \text{where } p = |\eta + \xi|, \quad q = \eta \cdot \xi, \quad \text{and } r = |\xi|, \tag{8}$$

where I is some scalar-valued function and “ \cdot ” is the dot product.

A peridynamic material is said to be *microelastic* if and only if there exists a scalar-valued function $w(\eta, \xi)$ such that

$$f(\eta, \xi) = \frac{\partial w}{\partial \eta}(\eta, \xi). \tag{9}$$

The function w is called the *micropotential*. It is important to realize that the derivatives in (9) are not the spatial derivatives that are to be avoided by using peridynamic theory.

The micropotential has units of energy per unit volume squared. It represents potential energy density associated with a bond. We may define a functional that for a displacement \mathbf{u} is the *local displacement energy density*,

$$W_u(\mathbf{x}, t) = \frac{1}{2} \iiint_R w(\mathbf{u}' - \mathbf{u}, \mathbf{x}' - \mathbf{x}) dV'. \tag{10}$$

Equation (10) is the energy density at the point \mathbf{x} and time t associated with a displacement \mathbf{u} of all the particles in domain R . The factor of $1/2$ is present since only half the energy is associated with each endpoint of the bond.

Integration of (10) over the body yields the *total macroscopic energy* functional. Silling [2000] showed that the time rate of change of the kinetic energy plus the time rate of change of the total macroscopic energy given by the integral of (10) over the body equals the work on the body done by external forces when the fundamental equation of peridynamics (1) is satisfied.

The most general form of the PFF f for a microelastic material is

$$f(\eta, \xi) = H(p, \xi)(\eta + \xi) \quad p = |\eta + \xi|, \tag{11}$$

where H is a scalar-valued function of (p, ξ) . In this case, there is a micropotential $w(p, \xi)$ such that

$$H(p, \xi) = \frac{1}{p} \frac{\partial w}{\partial p}(p, \xi). \tag{12}$$

The form of f in (11) implies that the force between any two points depends only on the distance between them in the deformed configuration. Thus, we may interpret a microelastic material as a material in which each two points is connected by a spring that, in general, may be nonlinear. If a microelastic material is isotropic, then (8) implies that H and w only depend on p and r , the magnitude of ξ .

The final specialization on the PFF that we will adopt is a further development of the notion that particles in microelastic materials may be considered to be connected by springs. We consider materials with a PFF having its magnitude proportional to the stretch s , where

$$s = \frac{p - r}{r}, \quad p = |\boldsymbol{\eta} + \boldsymbol{\xi}|, \text{ and } r = |\boldsymbol{\xi}|. \tag{13}$$

Materials having magnitudes proportional to the stretch are called *proportional* materials. The most general form of the PFF for proportional, microelastic materials is

$$\mathbf{f}(\boldsymbol{\eta}, \boldsymbol{\xi}) = \frac{g(s, r)}{p}(\boldsymbol{\eta} + \boldsymbol{\xi}), \tag{14}$$

where $g(s, r)$ is a piecewise linear function of s . The function g is called the *bond force* between two particles for a microelastic, proportional peridynamic material. Figure 3 shows the bond force dependence on bond stretch for such materials. This figure also shows the bond force for a *microplastic* material. The behavior of peridynamic microelastic and microplastic materials differ only on unloading. A microelastic material unloads reversibly back to zero stretch, while a microplastic material that is stretched beyond the elastic limit will retain some stretch when unloaded.

Figure 3 shows a linear dependence with nonzero slope in the elastic regime and constant bond force when the yield strength magnitude is exceeded in tension or compression. This figure also indicates bond failure at some value of bond stretch. Proportional peridynamic materials fail irreversibly when the stretch exceeds a value, s_c , called the *critical stretch*. Not only does the critical stretch define failure of a material, but it also assures the existence of a horizon for proportional materials. A microelastic, proportional material behaves reversibly as long as the stretch does not exceed the critical stretch.

Let $V_d(\mathbf{x}, t)$ denote the volume of the material that connected to \mathbf{x} by bonds that have been broken and $V_0(\mathbf{x})$ denote the volume of material initially connected to \mathbf{x} . Then the *damage* $D(\mathbf{x}, t)$ is defined by

$$D(\mathbf{x}, t) = V_d(\mathbf{x}, t)/V_0(\mathbf{x}). \tag{15}$$

3. Numerical method

To solve the fundamental peridynamics equation of motion, (1), the domain is discretized into a set of nodes, $\{\mathbf{x}_i\}$, as depicted in Figure 4. Each node has a known volume in the reference configuration. The nodes form a computational grid.

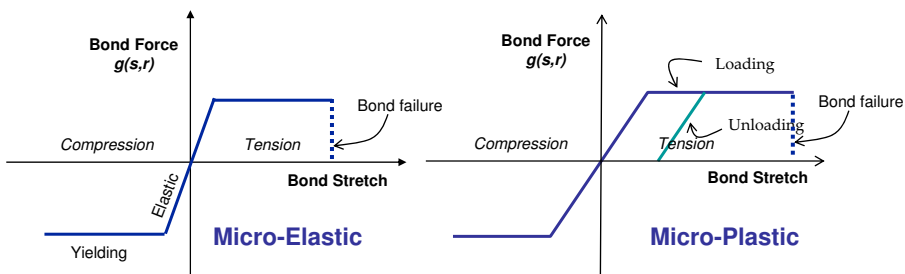


Figure 3. Bond force for microelastic and microplastic proportional materials.

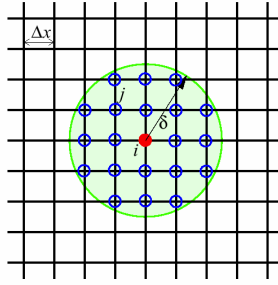


Figure 4. Computational grid.

The fundamental equation of motion (1) is replaced by a finite sum, which at time t_n is

$$\rho_i \frac{d^2}{dt^2} \mathbf{u}_i^n = \sum_p \mathbf{f}(\mathbf{u}_p^n - \mathbf{u}_i^n, \mathbf{x}_p - \mathbf{x}_i) V_p + \mathbf{b}_i^n, \tag{16}$$

where $\rho_i = \rho(\mathbf{x}_i)$, $\mathbf{u}_i^n = \mathbf{u}(\mathbf{x}_i, t_n)$, $\mathbf{b}_i^n = \mathbf{b}(\mathbf{x}_i, t_n)$, and V_p is the volume of node p . The sum is taken over all nodes within the horizon δ of x_i , $\{x_p : |x_p - x_i| < \delta\}$.

The acceleration term in (16) is approximated by an explicit central difference:

$$\mathbf{u}_i^n = \frac{\mathbf{u}_i^{n+1} - 2\mathbf{u}_i^n + \mathbf{u}_i^{n-1}}{(\Delta t)^2}, \tag{17}$$

where Δt is the constant time step. The error in (17) is well known to be second order in time [Silling and Askari 2005].

Silling and Askari [2005] investigated the accuracy of (16) with grid spacing and stability for a linearized PFF, where

$$\mathbf{f}(\boldsymbol{\eta}, \boldsymbol{\xi}) = \mathbf{C}(\boldsymbol{\xi})\boldsymbol{\eta}, \quad \text{where } \mathbf{C}(\boldsymbol{\xi}) = \frac{\partial \mathbf{f}(0, \boldsymbol{\xi})}{\partial \boldsymbol{\eta}}. \tag{18}$$

In (18), $\mathbf{C}(\boldsymbol{\xi})$ is called the *micromodulus*. The micromodulus is a second order tensor or 3×3 matrix. They showed that if the micromodulus and displacement \mathbf{u} are twice continuously differentiable, then (16) is second-order accurate in grid spacing. Otherwise, if there are discontinuities in \mathbf{C} or \mathbf{u} , (16) is first-order accurate in grid spacing. They also presented a stability criterion for the time step Δt , which states that the maximum time step is of order of the horizon. Hence, the maximum stable time step is limited by the horizon rather than the grid spacing. Alternative approaches to integrating the peridynamic equation of motion, along with some important mathematical properties of one-dimensional solutions, are discussed by Weckner and Abeyaratne [2005] and Emmrich and Weckner [2007].

4. The EMU computer code

EMU is the first computer code that is based on the peridynamic theory of continuum mechanics. It is written in Fortran 90 and executes on computers operating under Unix/Linux or Windows operating systems and on parallel computers using MPI (message passing interface). EMU is currently in the research and development stage and is being licensed to a few users.

The numerical method described in [Section 3](#) does not use elements, and there are no geometrical objects connecting the grid points. Hence, EMU is mesh free. There is no need for a mesh generator when modeling complex structures. Only the generation of grid points is required.

EMU is Lagrangian in the sense that each node contains a fixed amount of material. A body contains multiple nodes and may fragment if bonds between nodes are broken. However, the mass in each node remains constant.

EMU uses explicit time integration to advance the solution in time as discussed in [Section 3](#). Explicit time integration is a simple, reliable method. A stable time-step estimate was obtained by [Silling and Askari \[2005\]](#) for a linear PFF as given by (18). For nonlinear materials, a safety factor less than one may be applied to this stable time step to account for possible nonlinear material response that would make the estimated stable time step based on the linear analysis too large.

Execution of an EMU simulation requires a computational grid and an input file containing data to control execution, provide information on the grid geometry, and specify material properties. (An unpublished user's manual is available to licensed users of EMU.)

A computation grid in EMU can be defined in either of two ways, or any combination of the two. [Figure 5](#) shows an EMU problem containing two internally generated material regions and one externally generated grid. Everything outside the material regions is empty space.

For an internally generated grid, the code currently uses a lattice inside a rectangular box. The box containing the lattice includes several material regions, each region with a given material. There are various options for defining the shapes of these regions. A lattice site that is inside one of the material regions becomes a node. A lattice site that is not in any material region represents a void and is, in effect, not used during the calculation.

For an externally generated grid, one typically writes a separate program to generate the grid point coordinates and material numbers and place them into files that are processed during EMU execution.

A user writes an input file containing data to control execution, specify details of the grid geometry, and specify material properties. After the title on the first line of the input file, the input is keyword based. The keywords may be placed in any order. Any numerical input following a keyword is format-free and may extend to multiple lines. SI units are recommended for all dimensional quantities. Data to control

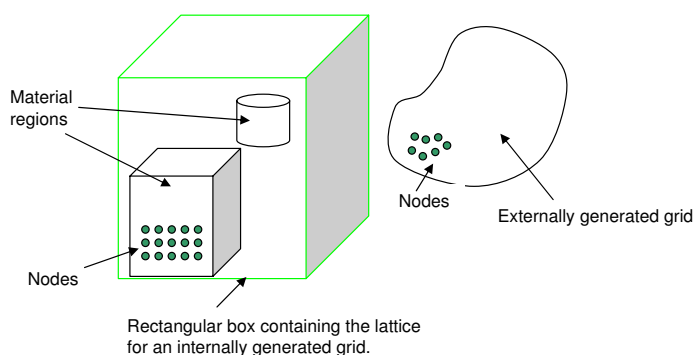


Figure 5. A computational grid containing two internally generated material regions and one externally generated region.

execution include time span or number of cycles for execution of a simulation, time-step safety factor, plot-dump frequency, and location of output files. Data to specify details of the grid geometry include grid spacing, horizon, and volume of a node for each material.

The details of the peridynamic material model are specified in the EMU input file. For each proportional, microelastic material, the user provides its density or total mass, yield strength, sound speed, and critical stretch. Alternately, material properties of microelastic materials may be specified by the penetrability as measured by Young's S-number [Young 1969]. Specific inputs give properties of fluids, gases, or explosive materials.

Initial and boundary conditions may be specified in the input file. Boundary conditions include fixed displacement or velocity and applied force. They are applied somewhat differently in the peridynamic method than in the classical approach. In peridynamics, boundary conditions are prescribed within a layer of finite thickness at the surface of a body. This layer must include some nodes in the computational grid. Forces at the surface of a body are applied as body force density \mathbf{b} in (1) within some layer under the surface.

In peridynamics as implemented in EMU, contact is treated using short-range repulsive forces that prevent nodes from getting too close. These short-range forces are independent of the positions of the nodes in the reference configuration, so that contact is treated in a consistent way even under large deformations. This approach is physical and avoids the need for defining contact surfaces as is required by many finite-element codes.

EMU is parallelized using MPI and executes on parallel computers. Parallelization was performed by allowing each processor to be responsible for a fixed region of space. Figure 6 illustrates this processor partitioning in two dimensions.

Figure 6 shows a grid surrounded by a margin region, which is the light blue shaded area. The regions of space owned by the eight processors in this example are separated by heavy red lines. Each processor region owns the nodes within its domain and needs information from nodes a distance equal to the horizon δ surrounding its domain. As the body deforms, nodes are permitted to migrate between processors. After each time step, the updated variables for nodes within a distance δ of a given processor are passed using MPI subroutines to be used during the following cycle. This parallelization technique

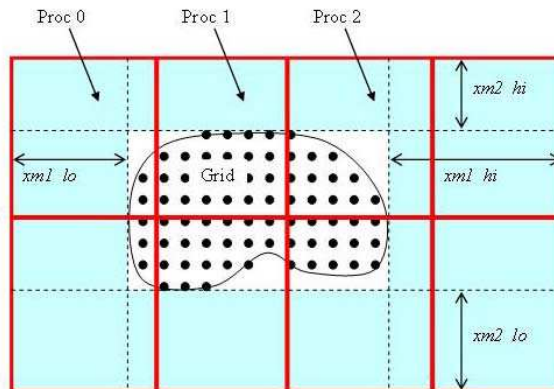


Figure 6. Computation grid and margin region partitioned among eight processors.

has the advantage of simplicity. However, load balancing is not optimal as seen in [Figure 6](#) since the two processors along the right boundary do not process any nodes. More sophisticated load balancing methods will be considered as part of future development of EMU to improve efficiency in problems involving large displacements.

A graphics postprocessor was written to produce output that can be viewed or further processed into many graphics formats, such as JPG or encapsulated postscript, using the RSCORS graphics system [[Padilla and Thompson 1984](#)]. Postprocessing software is also available to plot displacement histories and fragmentation histories and distributions.

5. Examples of large objects impacting concrete structures

We consider two examples of aircraft impacts into reinforced concrete structures to illustrate the capability of EMU to model extreme impacts.

In the first example, we simulated a test that was performed at Sandia National Laboratories [[Sugano et al. 1993](#)]. In the test, an F-4 Phantom aircraft impacted an massive, essentially rigid reinforced concrete wall. The primary purpose of the test was to determine the impact force as a function of time for the impact of an F-4 Phantom. Additional objectives of the test were to determine the crushing behavior of the aircraft, to determine if the engines broke away from the aircraft before their impact, and if so, to measure their impact velocity, and to record the dispersal of fuel after impact. Water was used instead of jet fuel for this test. The target was a block of reinforced concrete 3.6576 m thick in the direction of impact and 7.0104 m square perpendicular to the impact direction. It was mounted on a platform. The impact was perpendicular to the target at a speed of 215 m/s. The impacting mass of the aircraft and fuel surrogate was slightly more than 18,000 kg. The length of the F-4 is about 1.7678 m.

[Figure 7](#) shows a top and side view of materials in the EMU model at time zero and materials at 0.05 s and 0.09 s during the simulation of the experiment, and [Figure 8](#) shows damage to the structure. The damage at a node is given by (15). It represents the fraction of bonds that are broken between this node and all nodes initially having bonds with it.

In [Figure 7](#), the concrete is yellow and the rebar is green, the fuel is gold and the remaining colors are various parts of the aircraft. The simulation took about 36 minutes using 8 processors, and the time steps varied from 21 μ s to 36 μ s. The time simulated is about 0.09 s. The grid spacing is 0.229 m, and there are 36,244 nodes in the computational model.

There is no perforation of the target because of the target's strength. Only crush up of the aircraft occurs during the simulation, as was observed during the experiment.

[Figure 8](#) shows side and front views of damage to the target impacted by the F-4. We did not show damage to the aircraft in this figure. Only the concrete and its rebar reinforcement are shown in [Figure 8](#). This figure shows damage ranging from no damage (purple) to over 99% damage (orange). Although the target was not perforated, there is considerable damage on the impacted surface that extends to the interior. At 0.05 s, there is over 99% damage to a large part of the impacted surface, and by 0.09 s this damage leads to concrete falling away from the target.

[Figure 9](#) shows a penetrator impacting a target. This figure illustrates why peridynamics is useful in penetration analysis. In this figure, a penetrator (red) impacts at target (blue), fracture occurs, and fragments are emitted from the nonimpacted side of the target.

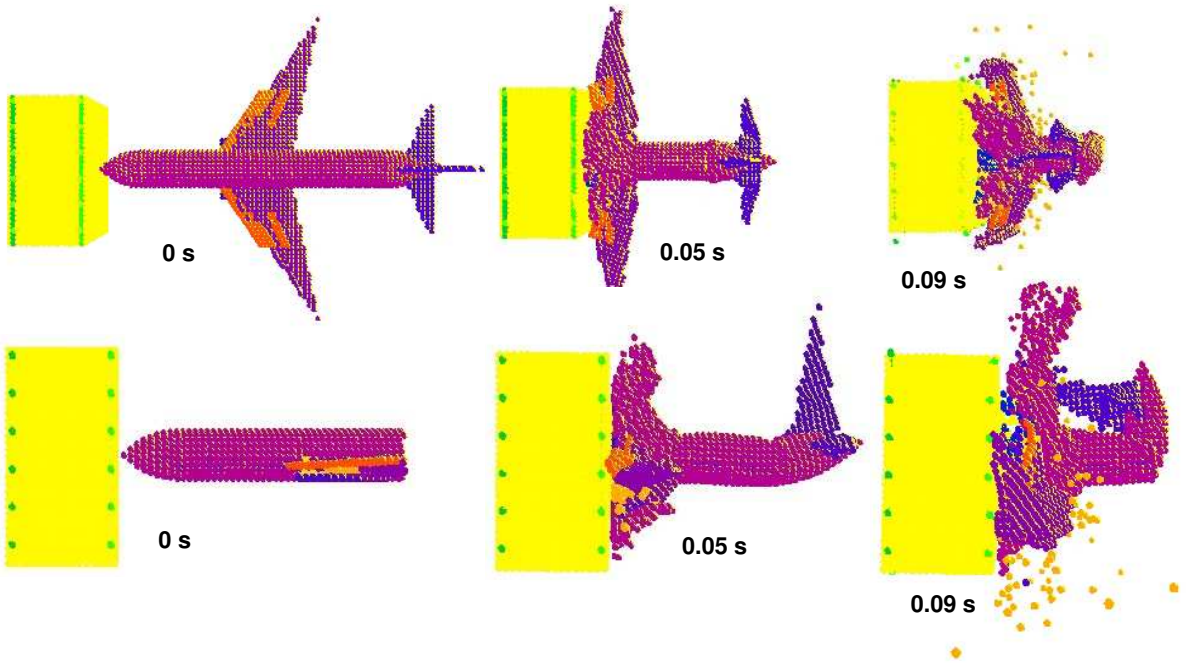


Figure 7. Top and side views of materials during F-4 impact simulation.

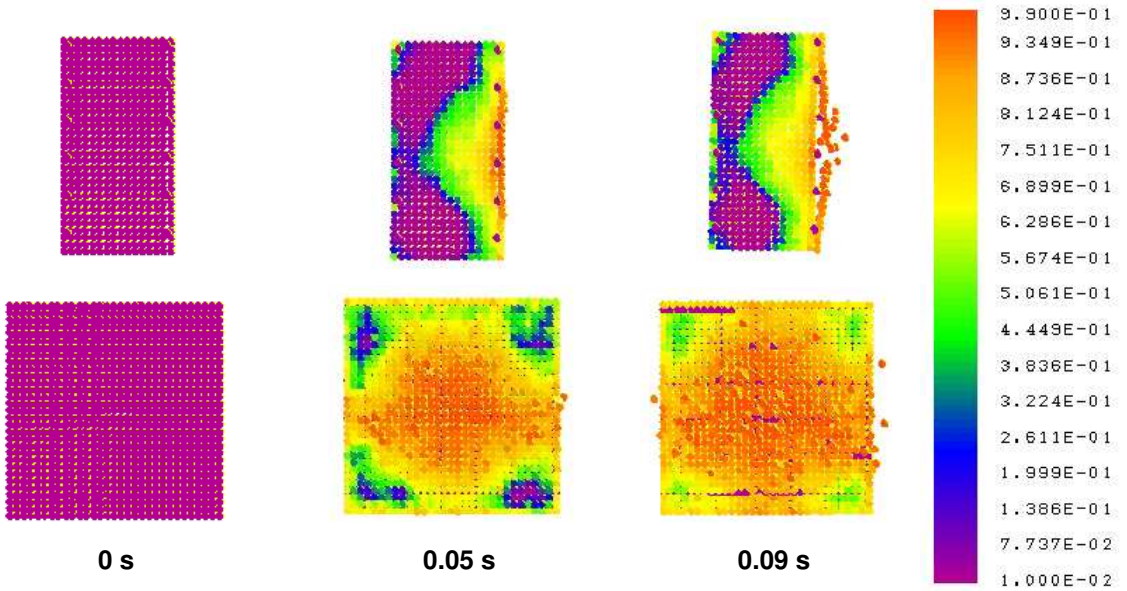


Figure 8. Side and front views of damage during F-4 impact simulation.

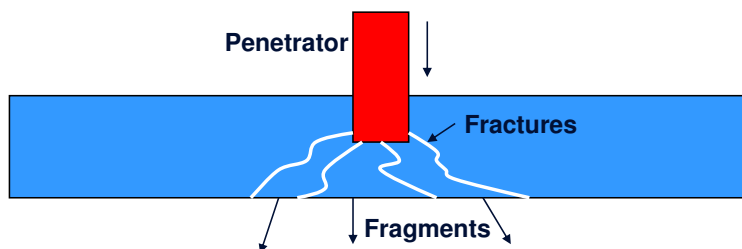


Figure 9. A penetrator impacting a target.

The ability to model fracture in perforation problems is important since fracture occurs before perforation occurs, as shown in [Figure 9](#), and a target starts to weaken long before a penetrator gets through. Furthermore, the fracture process determines fragment properties, and fragments leaving a target may damage structures separated from the initial target.

For another example of the capabilities of peridynamics, consider an aircraft impacting a cylindrical structure made of reinforced concrete. The main part of the structure is a reinforced concrete cylinder with an inside radius 19.812 m, height 27.432 m, and wall thickness 0.9144 m. Rebar is placed in hoops coaxial with the cylinder axis and vertically parallel to the cylinder axis. The rebar is embedded in the concrete inside its inner and outer surfaces. The rebar is #18 rebar with 0.3048 m spacing. Rebar was omitted in the roof of the structure for simplicity since the roof concrete is in compression. The roof is 0.9144 m thick. The structure includes a 9.525 mm steel liner that is the color yellow in [Figure 10](#) and coaxial with the concrete cylinder. The radius of the liner is 18.288 m. There is a 1.524 m annulus between the concrete and the steel liner.

[Figure 10](#) shows results from the EMU simulation of this scenario. In this figure, the concrete is yellow and green and the rebar is orange, and the remaining colors are various parts of the aircraft including the jet fuel. The time simulated is about 0.64 s. The simulation took about 26.5 h using 64 processors, and the time steps varied from 13 μ s to 20 μ s. The grid spacing is 0.229 m, and there are 580,624 nodes in the computational model.

[Figure 10](#) shows that before 0.17 s, the concrete wall is breached and the steel liner is deformed considerably. The breach in the concrete wall occurred soon after the hard parts of the aircraft, front landing gear, and center fuel tank (color green) impact the outer wall. By 0.64 s most of the aircraft is inside the structure. Only the tail end, parts of the wings, and some fuel from the wing tanks are not inside the structure. The center fuel tank remains intact.

[Figure 11](#) shows the progression of internal damage to the structure starting at 0.10 s. This figure shows only the front half of the structure so that a breach will not be obscured by the back of the structure. At 0.10 s, fracturing and cracks in the concrete are evident and over 99% of the bonds are broken near the impact location. Much failure occurs along the rebar. However, there is cracking in the concrete along diagonals beginning where rebars intersect. Damage appears to occur first in the rebar, and the rebar seems to fail completely before the concrete fails.

Although there is much damage at 0.10 s, the concrete and liner are not penetrated. There are a few small holes in the structure near the impact location. Breach of the concrete wall and liner occur before 0.18 s as the concrete continues to fracture and the liner is torn. After 0.34 s, the breach gets wider as

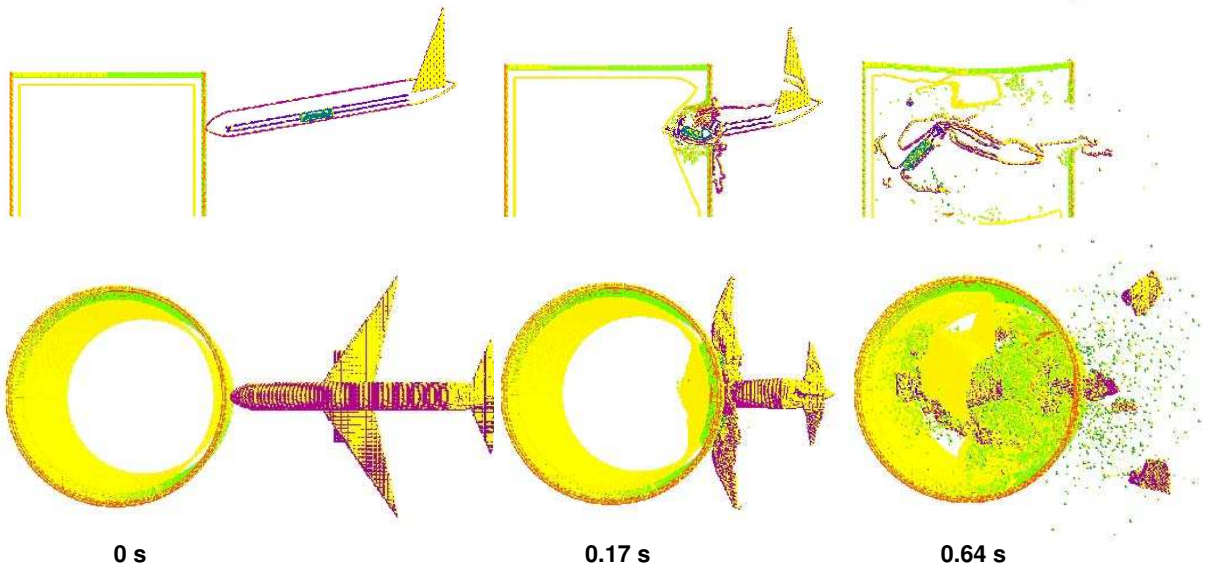


Figure 10. Side and top views of materials during simulation of an aircraft impacting a cylindrical concrete structure.

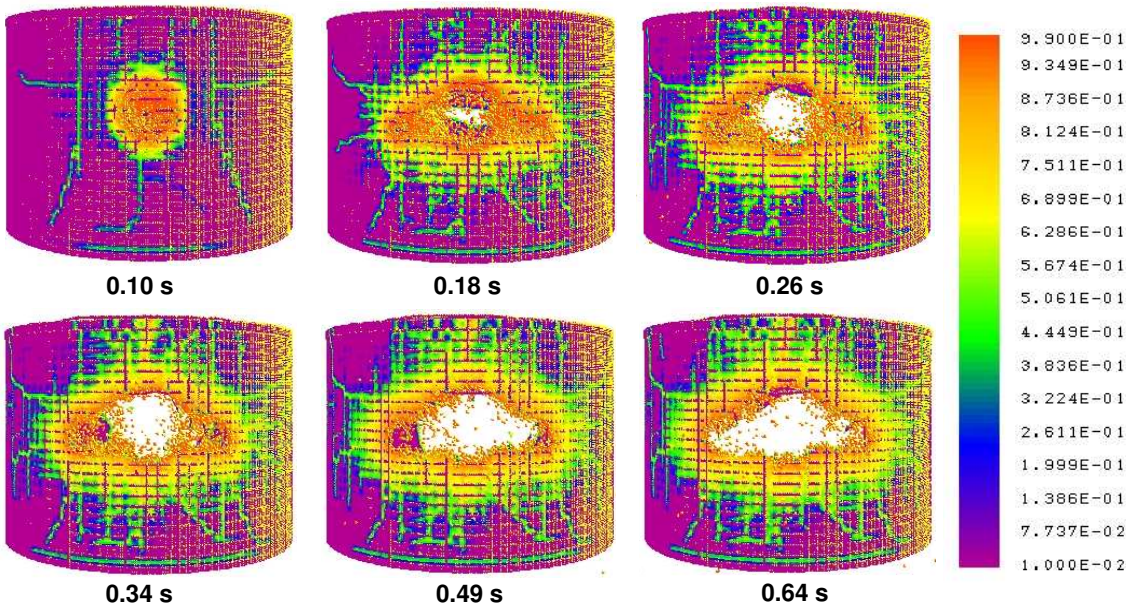


Figure 11. Damage to front of structure during simulation of an aircraft impact into a reinforced concrete structure.

parts of the wing penetrate and enter the structure. At the end of the simulation, over half of the front part of the structure is damaged.

The results in Figure 11 show the power of the peridynamics method in problems where deformation and fracture are expected. This figure shows the dynamic evolution of fracture with cracks emerging spontaneously as a result of the equations of motion and material model, and growing in whatever direction is energetically favorable for growth.

6. Gases as peridynamic materials

Since the detonation products in an explosion are gases, we must determine how to model gases as bond-based, peridynamic materials. In this section, we develop a general expression for the PFF of a gas. This expression depends on how the internal energy per unit volume of the gas changes with the expansion of the gas, X , where

$$X = \frac{v}{v_0} = \frac{\rho_0}{\rho}. \tag{19}$$

In (19), v and v_0 are the deformed and reference specific volumes of the gas, respectively, and ρ and ρ_0 are the deformed and reference densities, respectively. Implementation of a gas model requires approximating the expansion at a node from the undeformed and deformed bond lengths between this node and all gas nodes within its horizon. We provide the expression for the expansion that is presently used in EMU and complete this discussion of gases as peridynamic materials by developing the PFF for a gas.

To derive a general expression for the PFF of a gas, consider (9) and (10). From (9), the micropotential, w , may be written as

$$w(\mathbf{x}, t) = \int_{\eta_0}^{\eta(\mathbf{x}, t)} \mathbf{f}(\boldsymbol{\eta}, \boldsymbol{\xi}) \cdot d\boldsymbol{\eta}, \tag{20}$$

where η_0 is some fiducial state of stretch for evaluation of the micropotential. Since the integral (10) vanishes outside the horizon of \mathbf{x} , $H(\mathbf{x})$, (10) may be written using (20) as

$$W_u(\mathbf{x}, t) = \frac{1}{2} \iiint_{H(\mathbf{x})} \left[\int_{\eta_0}^{\eta(\mathbf{x}', t)} \mathbf{f}(\boldsymbol{\eta}, \boldsymbol{\xi}) \cdot d\boldsymbol{\eta} \right] dV_{\boldsymbol{\xi}}. \tag{21}$$

Let all the bonds be held fixed except for bond k at a given value of $\boldsymbol{\xi}$. Then, for an incremental stretch dp_k in bond k , (21) becomes dW , where

$$dW = \frac{1}{2} \mathbf{f} \cdot d\boldsymbol{\eta} \Delta V_{\boldsymbol{\xi}} = \frac{1}{2} \mathbf{f} \cdot d(\boldsymbol{\eta} + \boldsymbol{\xi}) \Delta V_{\boldsymbol{\xi}} = \frac{1}{2} f_k dp_k \Delta V_k. \tag{22}$$

In (22), f_k is the magnitude of the bond force per unit volume squared in bond k due to this incremental stretch dp_k in this bond, and $\Delta V_{\boldsymbol{\xi}}$ and ΔV_k are volume elements associated with bond k . The later two equalities follow since $\boldsymbol{\xi}$ is fixed under the stretch and \mathbf{f} is parallel to $\boldsymbol{\eta} + \boldsymbol{\xi}$ as stated in (6).

The quantity f_k in (22) is the PFF for a gas. This quantity can be expressed in terms of the expansion X as follows.

Changes in the energy per unit volume, dW , result from the stretch dp_k . Therefore, using the definition of dW and the chain rule, (22) may be written as

$$dW = \frac{\partial W}{\partial p_k} dp_k = \frac{dW}{dX} \frac{\partial X}{\partial p_k} dp_k \quad (23)$$

since W depends on p_k through its dependence on X .

Equating (22) and (23) and solving for f_k yields a general expression for the PFF of a gas

$$f_k = \frac{2}{\Delta V_k} \frac{dW}{dX} \frac{\partial X}{\partial p_k}. \quad (24)$$

The PFF can be obtained from (24) once the energy per unit volume, W , is known as a function of the expansion, X , and X is known as a function of the incremental stretches for all gas bonds within the horizon of a node.

There are many ways to approximate the expansion X . The present discussion describes the method currently implemented in EMU. Consider the ratio of the deformed density to the reference density. This ratio is $1/X$. We approximate the ratio of the deformed to reference density at a given node by

$$\frac{1}{X} = \left[\frac{1}{V} \sum_j \left(\frac{r_j}{p_j} \right)^m \Delta V_j \right]^{3/m}, \quad V = \sum_k \Delta V_k, \quad (25)$$

where the sum is taken over the nodes inside the horizon of the given node, $p_j = |\boldsymbol{\eta}_j + \boldsymbol{\xi}_j|$, $r_j = |\boldsymbol{\xi}_j|$, and ΔV_j is the reference volume of node j . We refer to the nodes inside the horizon of a given node as its family. Hence, V is the total reference volume of the family of the given node.

If $m = 1$ and the reference-node volumes are equal, (13) implies that the summation in (25) represents the cube of the average of the inverses of the one plus bond stretches within the family. For $m > 0$ with constant bond stretch s , (25) implies that the relative density $1/X$ is

$$\frac{1}{X} = \frac{1}{(1+s)^3}. \quad (26)$$

As expected, (26) shows that the density increases in compression ($s < 0$) and decreases in expansion ($s > 0$). The purpose of including $m \neq 1$ in (25) is to allow for the possibility that bonds of different length could sustain different forces even if the deformation is an isotropic expansion. This form can be helpful, for example, in preventing nodes in a numerical grid from getting so close to each other that they overlap.

For any m and equal reference-node volumes, (25) becomes

$$\frac{1}{X} = \left[\frac{1}{N} \sum_j \left(\frac{1}{(1+s_j)} \right)^m \right]^{3/m}, \quad s_j = \frac{p_j - r_j}{r_j}. \quad (27)$$

Since (27) represents the ratio of deformed to reference density, the more highly compressed bonds ($s_j < 0$) will have a larger contribution to the overall density ratio at a node for $m > 1$.

From Equation (25), the expansion X is

$$X = \left[\frac{1}{V} \sum_j \left(\frac{p_j}{r_j} \right)^{-m} \Delta V_j \right]^{-3/m}, \quad V = \sum_k \Delta V_k. \quad (28)$$

From (24) with this approximation for the expansion, the PFF for a gas is

$$f_k = \frac{6}{r_k V} \frac{dW}{dX} \left(\frac{p_k}{r_k} \right)^{-m-1} X^{1+m/3}. \quad (29)$$

If we identify W with the internal energy per unit volume of the gas, then (29) and knowledge of the dependence of W on the expansion X yield an expression for the PFF at node k .

From an axiomatic formulation of thermodynamics, such as found in [Callen 1960], the pressure is an intensive variable defined as minus the partial derivative of the internal energy with respect to a specific volume at constant entropy [Callen 1960, p. 31]. Therefore, the derivative in (29) is

$$\frac{dW}{dX} = -P, \quad (30)$$

which implies that the PFF for node k in a gas is

$$f_k = -\frac{6P}{r_k V} \left(\frac{p_k}{r_k} \right)^{-m-1} X^{1+m/3}. \quad (31)$$

Implementation of (31) requires knowledge of P as a function of X and a value for m . In the current version of EMU, a value of $m = 1$ is used. We have not investigated the consequences of using different values for m or using some alternate formulation of the expansion.

For many applications of interest, gases are rapidly expanding. Therefore, in the initial implementation of gas modeling in EMU, gases are treated as ideal gases undergoing an isentropic or adiabatic expansion. In this case, we can relate the pressure required in (31) to the expansion.

Consider an isentropic process from a state with volume and temperature (V_0, T_0) to a state with volume and temperature (V, T) . The change in entropy, ΔS , for an ideal gas between these states is given by

$$\Delta S = nR \ln \frac{V}{V_0} + nC_V \ln \frac{T}{T_0}, \quad (32)$$

where n is the number of moles of the gas, R is the gas constant (8.31 J/mol/K), and C_V is the molar specific heat at constant volume [Halliday et al. 2001, p. 487]. Setting $\Delta S = 0$ in (32) and using the ideal gas law ($PV = nRT$), we obtain the relation

$$PV^\gamma = P_0 V_0^\gamma, \quad (33)$$

where $\gamma = C_P/C_V$ is the ratio of molar specific heats and $C_P = C_V + R$ is the molar specific heat at constant pressure. Therefore, for an ideal gas, the pressure as a function of the expansion for an adiabatic expansion is given by

$$P = P_0 \left(\frac{V_0}{V} \right)^\gamma = P_0 X^{-\gamma}. \quad (34)$$

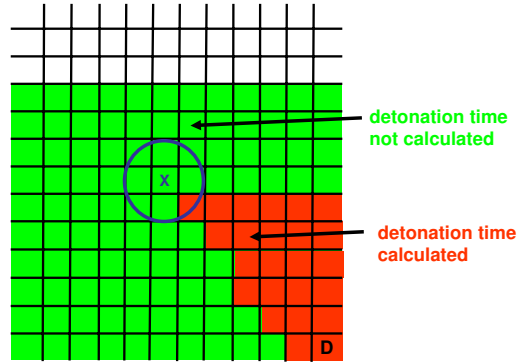


Figure 12. Huygen's construction procedure in two dimensions to calculate detonation times.

7. The peridynamic detonation model in EMU

A peridynamic detonation model was developed and implemented in the EMU computer code. The first component of the detonation model is the input. For each explosive material, the user provides the location of the detonation point (x_{det}) and time of detonation initiation (t_{det}) along with the density of the unreacted explosive (ρ_{un}) and the detonation speed (V_{det}). Multiple detonation points are permitted in the current version of EMU. For an ideal gas, the user may also specify the pressure (P_{CJ}), ratio of molar specific heats (γ), and detonation temperature (T_{CJ}) of the detonation-product gases. If the user does not specify these quantities, they are obtained from the following correlations:

$$P_{CJ} = \rho_{\text{un}}(V_{\text{det}})^2 [1.0 - 0.7125(\rho_{\text{un}}/1000)^{0.04}], \quad (35)$$

$$\gamma = 0.7125(\rho_{\text{un}}/1000) [1.0 - 0.7125(\rho_{\text{un}}/1000)^{0.04}], \quad (36)$$

$$T_{CJ} = 1643\gamma. \quad (37)$$

The units in (35), (36), and (37) are SI units; the ratio of molar specific heats (γ) is dimensionless [Cooper 1996, pp. 265, 79, and 156, respectively].

The next component of the detonation model is determining the detonation times at each node containing explosive material. These times are calculated during input processing using a Huygen's construction procedure. Since the detonation times are calculated during input processing, the method is called *program burn*. Figure 12 illustrates this procedure in two dimensions.

In Figure 12, the detonation is initiated in the node at the lower right cell labeled with a D. Detonation times have been calculated for the explosive material in the red cells and have not been calculated for the explosive material in the green cells. In this figure, the procedure started at the lower left and proceeded toward the right. After sweeping a row, the next row above is swept starting from the left. The procedure is currently in the green cell labeled with an X. While the idea of the construction is given by this discussion of Figure 12, the actual details differ somewhat during EMU execution since the nodes are not so well ordered in rows and columns as shown in this figure, and a node containing an explosive material may be owned by one processor and needed by another processor in the parallel implementation.

The detonation times are initially set to a large number. The construction proceeds by sweeping through the grid and examining at a given node X the detonation times of the nodes in a spherical

neighborhood of node X . If the node spacing is uniform with value Δq , then the radius of the spherical neighborhood is only slightly greater than $\sqrt{3}\Delta q$. Using this neighborhood radius ensures that the adjacent explosive nodes are not missed and that the detonation does not jump across a node that does not contain an explosive material. For any node X' in the neighborhood of node X , the detonation time for node X is the minimum of its detonation time and the detonation time of a node X' plus the time it takes the detonation to propagate from X' to X . This process continues until detonation times have been calculated for all explosive nodes. The Huygen's construction ensures that detonations propagate around obstacles and isolated regions of explosive material do not detonate.

When detonation occurs and the detonation products are ideal gases, the pressure of the gas is set to one half the Chapman–Jouguet pressure (P_{CJ}), which is given by (35) or specified by user input. To obtain the correct energy in the ideal-gas reaction products from the detonating explosive, the initial pressure must be set to one half the Chapman–Jouguet pressure. Once detonated, the gas expands adiabatically from this pressure. From (34), the pressure P at a time when the expansion is X is given by

$$P = \frac{1}{2}P_{CJ}\left(\frac{V_0}{V}\right)^\gamma = \frac{1}{2}P_{CJ}X^{-\gamma}. \quad (38)$$

With P given by (38), the PFF between gas nodes for an expansion X is given by (31).

The ideal gas law and (38) imply that the temperature T at a time when the expansion is X is

$$T = T_{CJ}\left(\frac{V_0}{V}\right)^{\gamma-1} = T_{CJ}X^{-\gamma+1}, \quad (39)$$

where T_{CJ} is given by (37) or specified by user input. The ratio of molar specific heats in (38) and (39) is given by (36) or specified by user input.

8. Examples of explosive loading of concrete structures

In this section, we illustrate the capability of EMU to model explosive loading by discussing two examples of explosive material detonating within concrete structures.

For the first example, consider a 0.05-m thick spherical concrete shell with an inside radius 0.25 m. The interior is filled with an explosive whose density is 1780 kg/m³ and detonation speed is 8590 m/s. The explosive is detonated at time zero at the center of the sphere. Although this structure is not large, this problem was used to debug the detonation model.

We simulated about 200 μ s of the explosion scenario. Using 2 processors, the simulation required about 0.76 h. The grid spacing is 0.01 m, and there are 133,185 nodes in the computational model.

Figure 13 is a cross section view of the materials at time zero and the calculated detonation times in the explosive. In the left graphic in this figure, the explosive is orange and the concrete is purple. The concrete is not reinforced. The detonation times in the right graphic vary from purple (less than 0.4 μ s) to orange (greater than 40 μ s). The calculated detonation times vary from 0 to about 35 μ s. The orange applies to the concrete, which is not an explosive material.

Since peridynamic theory does not use stresses in its formulation, stress and pressure are not output during a simulation. Although temperature plays no role in the current models in EMU, a temperature field was included in the data model for future developments. The temperature field can be used to observe the propagation of the detonation, since upon detonation, the temperature is given by (37) or

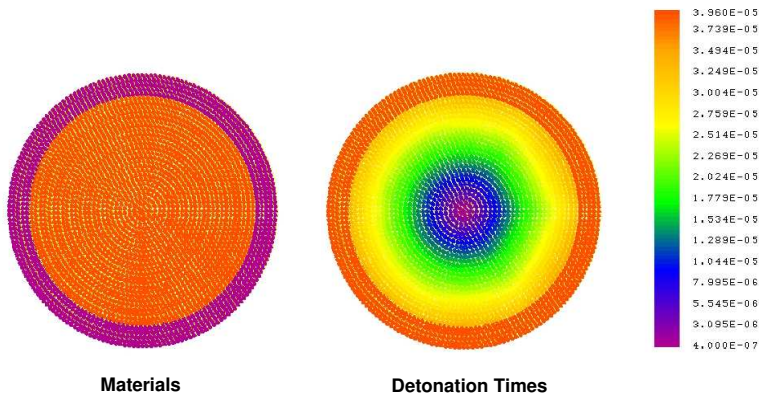


Figure 13. Materials at time zero and detonation times for exploding concrete shell.

user input and subsequently decreases during the adiabatic expansion as given by (39). Figure 14 shows temperatures calculated during the simulation of the explosion loading of the concrete shell.

Figure 14 shows the detonation propagating from shortly after initiation ($1.4 \mu\text{s}$) to $35 \mu\text{s}$ when all the explosive has detonated. The temperatures are in K.

At detonation, the temperature of the detonation products is about 4400 K. As the gas expands adiabatically, its temperature decreases as shown in the figure. The initial temperature of the concrete shell is 293 K. The temperature of the concrete will always be 293 K since there is no heat transfer mechanism

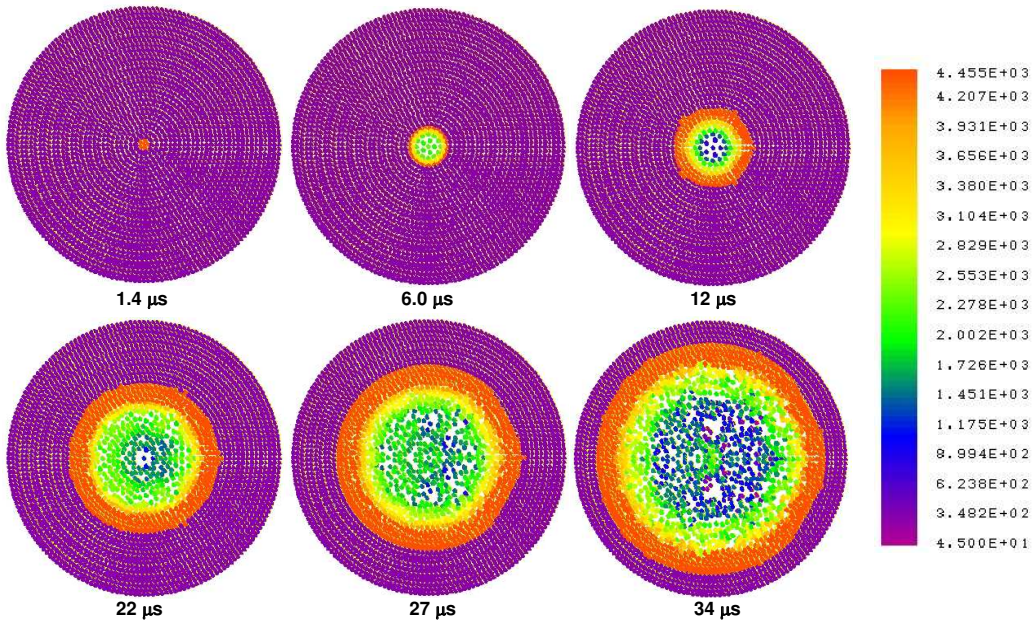


Figure 14. Temperatures showing propagation of the detonation for an exploding concrete shell.

in the current version of EMU. No distortion of the concrete shell is evident during the times shown in Figure 14. Later times must be shown to observe expansion and damage to the shell.

Figure 15 shows materials during the simulation. To observe voids and damage as the detonation propagates, this figure contains only a 2-cm slice about the center of the sphere. This figure shows materials and indicates the progression of damage to the shell during the simulation. The graphics at $13 \mu\text{s}$, $23 \mu\text{s}$, and $35 \mu\text{s}$ show voids produced as the gas expands.

The shell has not expanded much by the time the explosive is completely detonated at $35 \mu\text{s}$. However, by $43 \mu\text{s}$ there is some expansion of the shell, more at $65 \mu\text{s}$, and still more at $86 \mu\text{s}$. At $43 \mu\text{s}$ some gas has escaped through small cracks in the concrete. More fractures through the structure are evident at $65 \mu\text{s}$ and the concrete is completely fragmented by $86 \mu\text{s}$. Although the simulation extends to $200 \mu\text{s}$, well after the latest time shown in Figure 15, we do not show results from later times since these fragments just continue to expand outward.

For the second example, we consider a much larger structure. The structure is a rectangular parallelepiped made of reinforced concrete. The floor slab is 12.192 m by 15.850 m. The walls are placed on top of the slab and are 13.716 m high. The floor slab and walls are 1.8288 m thick. The floor slab is reinforced with #18 rebar at 0.3048-m spacing inside the lower and upper surfaces. The walls are reinforced with #18 rebar at 0.3048-m spacing inside the inner and outer surfaces. The rebar in the walls extends 0.3048 m into the floor slab. The structure is filled with water to a depth of 13.411 m. A cubic yard of explosive is placed on the floor at the middle of the bottom side of one wall. The explosive has a density of 1785.3 kg/m^3 and detonation speed of 8747 m/s. A cubic yard of this explosive has a mass of about 1365.0 kg. It is detonated at time zero at the center of the side in contact with the floor.

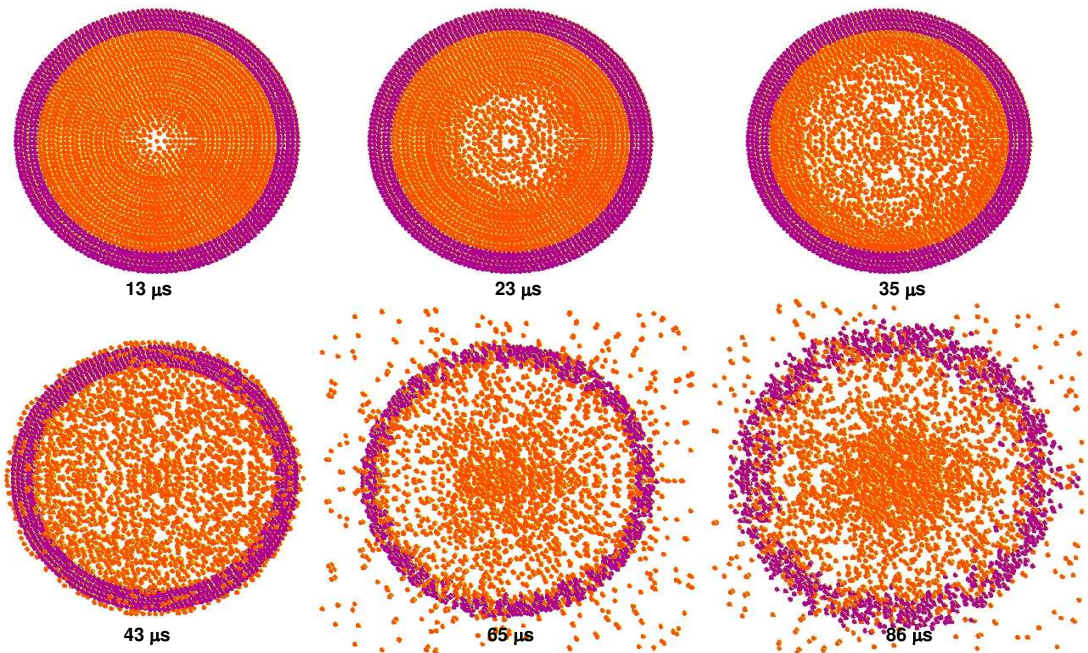


Figure 15. Materials during simulation of exploding concrete shell.

Figure 16 shows results from the EMU simulation of this scenario. In this figure, the concrete is green, the rebar is yellow, the liner is orange, the water is blue, and the explosive is purple. The view is a 0.5-m slice about a symmetry plane through the structure and explosive as shown in the graphic at time zero. The time simulated is about 9.8 ms. The simulation took about 1.52 h using 8 processors, and the time steps varied from $7.4 \mu\text{s}$ to $13.6 \mu\text{s}$. The grid spacing is 0.229 m, and there are 281,032 nodes in the computational model.

The explosive is completely detonated by 0.12 ms, and Figure 16 shows that the region containing the explosive is voided by 0.33 ms. By 1.0 ms, the liner near the initial location of the explosive is fragmented considerably, and by 1.9 ms the outer surface of the floor and concrete wall is slightly bulged near the detonation region. Concrete is leaving the outer surfaces by 2.8 ms as fracturing of the concrete continues. There is no evidence of the liner near the detonation region at this time.

By 4.4 ms, most of the structure is fractured and the detonation gases have reached the surface of the water. Progression of structure damage is evident at the later times shown in this figure at 4.8 ms, 5.3 ms, and 6.3 ms. At 4.8 ms, the liner has been completely removed. By 6.3 ms, all the walls shown in this figure are completely fragmented, and the water is essentially gone. The fragmented materials are dispersing.

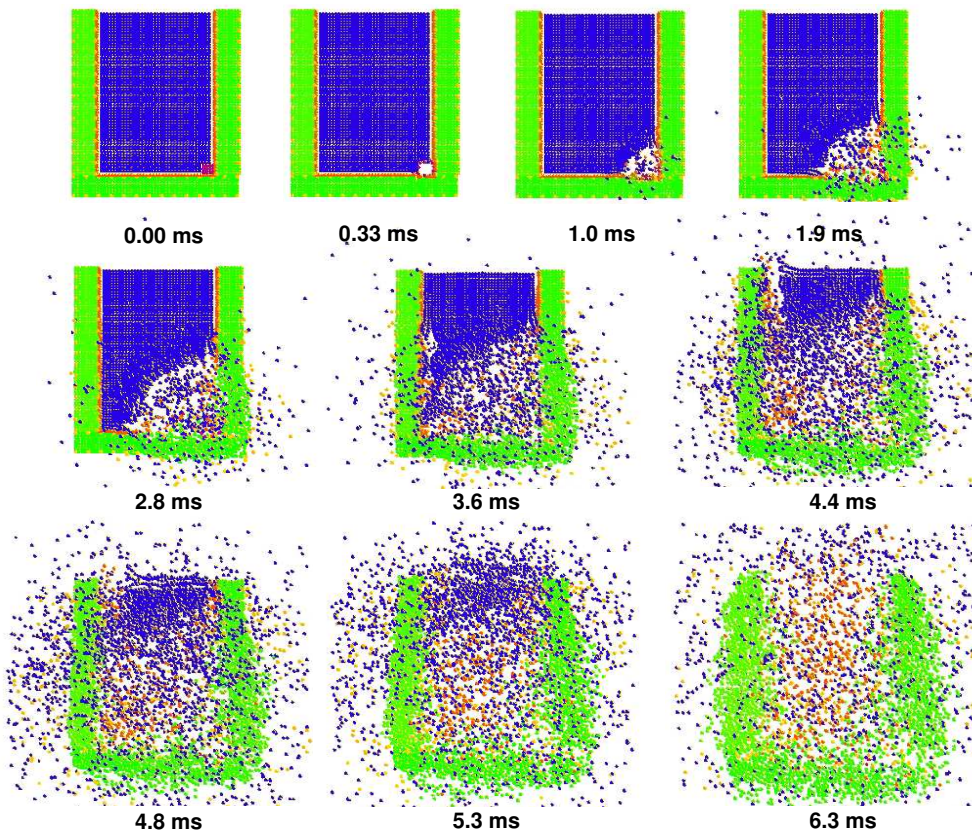


Figure 16. Materials during simulation of detonation within a concrete structure.

Figure 17 shows internal damage to a concrete wall and its rebar reinforcement during the simulation. The wall shown in this figure is adjacent to the explosive and is the wall to the right in Figure 16. No other materials are displayed to obscure the wall. This figure shows damage ranging from no damage (purple) to over 99% damage (orange).

The sequence of times begins at 0.12 ms when the explosive has completely detonated. The damage spreads until by 5.3 ms the bonds in the concrete have completely failed. The spontaneous emergence of cracks is particularly evident in this figure from 1.0 ms until the entire wall is totally fragmented by 5.3 ms. The orange lines in these figures are damage over 99% at the locations of the rebar. They imply that the rebar fails before the concrete.

9. Summary and conclusions

This paper addressed extreme loading of structures using peridynamics. We reviewed peridynamic theory and its implementation in the EMU computer code. The theory as implemented in EMU was illustrated with examples of extreme loadings on reinforced concrete structures by impacts from aircraft. While peridynamic theory has been extended to model composite materials, fluids, and explosives, we discussed only recent developments in modeling gases as peridynamic materials and the detonation model in EMU.

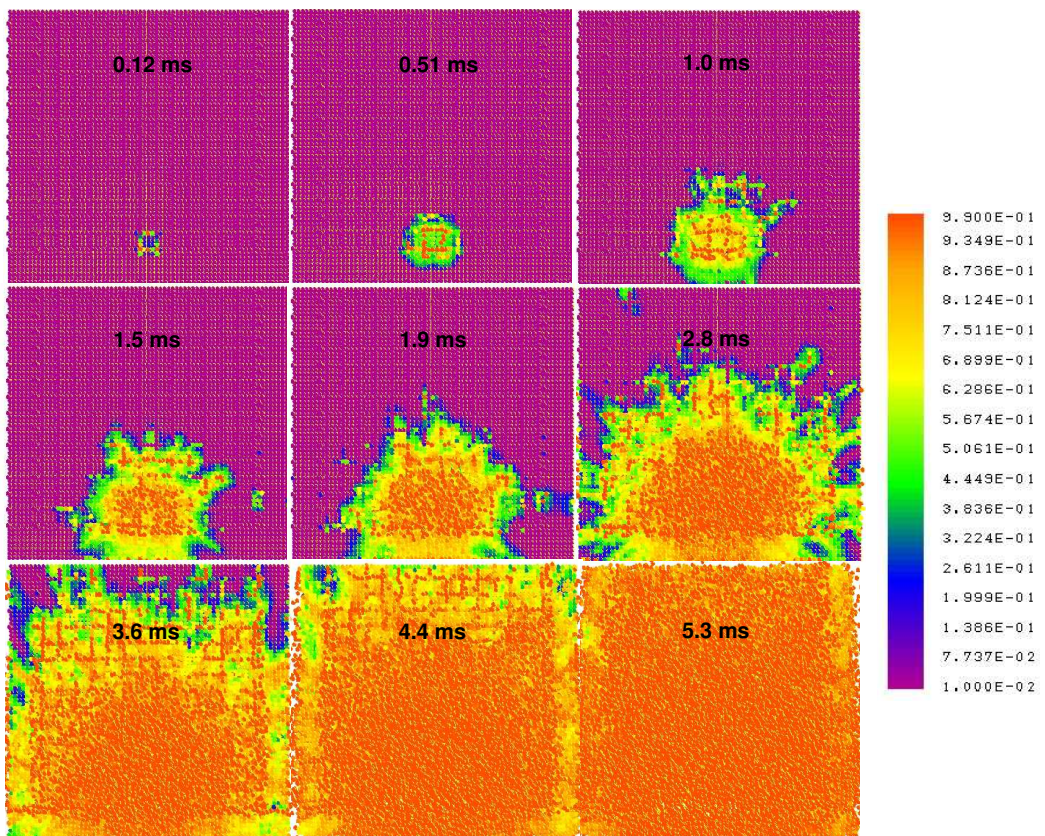


Figure 17. Damage to inside of wall adjacent to explosive.

Explosive loading of concrete structures was then illustrated. The examples illustrate the power of the peridynamics method in problems where deformation and fracture are expected. The work discussed in this paper supports the conclusion that peridynamic theory is a physically reasonable and viable approach to modeling extreme loading of structures from impacts and explosions.

Research and development in peridynamic theory is not completed. We are continuing our research on modeling fluids, composite materials, and explosives. Recently, we extended modeling of gas detonation products to include use of the JWL equation of state [Dobratz and Crawford 1985]. To improve confidence in EMU's capability to model extreme loading, a verification and validation process is being expanded. As the user base and number of code developers increase, attention is being given to software-engineering issues to maintain and distribute the code. There is a long history of constitutive model development to represent stress-strain and yield behavior. We are investigating how this wealth of information can be adapted to the peridynamics paradigm and implemented in EMU.

We envision future research and development addressing problems at both small scales and more encompassing, extreme loading macroscale scenarios. Nanoscale to continuum coupling may be possible using peridynamics with methods such as the embedded atom method [Daw et al. 1993].

Peridynamics has been demonstrated to be viable for analyzing fracture and failure due to loading at the macroscale. We visualize its being viable for analyzing failure at the microscale and nanoscale also. At the macroscale, we see the possibility of including more phenomenology such as fire, heat transfer, material degradation, etc. to provide a more comprehensive methodology for vulnerability assessment of critical structures.

References

- [Callen 1960] H. Callen, *Thermodynamics: an introduction to the physical theories of equilibrium thermostatics and irreversible thermodynamics*, Wiley, New York, 1960.
- [Cooper 1996] P. W. Cooper, *Explosives engineering*, Wiley-VCH, New York, 1996.
- [Daw et al. 1993] M. S. Daw, S. M. Foiles, and M. I. Baskes, "The embedded-atom method: a review of theory and applications", *Mater. Sci. Rep.* **9**:7-8 (1993), 251–310.
- [Dayal and Bhattacharya 2006] K. Dayal and K. Bhattacharya, "Kinetics of phase transformations in the peridynamic formulation of continuum mechanics", *J. Mech. Phys. Solids* **54**:9 (2006), 1811–1842.
- [Dobratz and Crawford 1985] B. M. Dobratz and P. C. Crawford, "LLNL explosives handbook: properties of chemical explosives and explosive simulants", Technical report, Lawrence Livermore National Laboratory, Livermore, CA., 1985.
- [Emmrich and Weckner 2007] E. Emmrich and O. Weckner, "Analysis and numerical approximation of an integro-differential equation modeling non-local effects in linear elasticity", *Math. Mech. Solids* **12**:4 (2007), 363–384. to appear.
- [Gerstle and Sau 2004] W. Gerstle and N. Sau, "Peridynamic modeling of concrete structures", pp. 949–956 in *Proceedings of the fifth international conference on fracture mechanics of concrete structures*, vol. 2, edited by L. Li et al., 2004. IAFRAMCOS.
- [Gerstle et al. 2005] W. Gerstle, N. Sau, and S. Silling, "Peridynamic modeling of plain and reinforced concrete structures", in *18th international conference on structural mechanics in reactor technology (SMiRT 18)*, Beijing, China, 2005. In SMiRT18-B01-2.
- [Halliday et al. 2001] D. Halliday, R. Resnick, and J. Walker, *Fundamentals of physics*, vol. 2, 6th ed., Wiley, New York, 2001.
- [Hilfer 2000] R. Hilfer (editor), *Applications of fractional calculus in physics*, edited by R. Hilfer, World Scientific, Singapore, 2000.
- [Kunin 1982] I. A. Kunin, *Elastic media with microstructure I*, Springer-Verlag, Berlin, 1982.

- [Oldham and Spanier 1974] K. B. Oldham and J. Spanier, *The fractional calculus: theory and applications of differentiation and integration to arbitrary order*, Academic, New York, 1974.
- [Padilla and Thompson 1984] G. Padilla and S. Thompson, *The RSCORS graphics system*, Albuquerque, NM: Sandia National Laboratories, 1984. SAND83-2639.
- [Rogula 1982] D. Rogula (editor), *Nonlocal theory of material media*, edited by D. Rogula, Springer, New York, 1982.
- [Silling 2000] S. A. Silling, “[Reformulation of elasticity theory for discontinuities and long-range forces](#)”, *J. Mech. Phys. Solids* **48**:1 (2000), 175–209.
- [Silling 2003] S. A. Silling, “Dynamic fracture modeling with a meshfree peridynamic code”, pp. 641–644 in *Computational fluid and solid mechanics*, edited by K. J. Bathe, Elsevier, Amsterdam, 2003.
- [Silling and Askari 2005] S. A. Silling and E. Askari, “[A meshfree method based on the peridynamic model of solid mechanics](#)”, *Comput. Struct.* **83**:17-18 (2005), 1526–1535.
- [Silling and Bobaru 2005] S. A. Silling and F. Bobaru, “[Peridynamic modeling of membranes and fibers](#)”, *Int. J. Nonlinear Mech.* **40**:2-3 (2005), 395–409.
- [Silling et al. 2003] S. A. Silling, M. Zimmermann, and R. Abeyaratne, “[Deformation of a peridynamic bar](#)”, *J. Elasticity* **73**:1-3 (2003), 173–190.
- [Sugano et al. 1993] T. Sugano, H. Tsubota, Y. Kasai, N. Koshika, S. Orui, W. A. von Riesenmann, D. C. Bickel, and M. B. Parks, “[Full-scale aircraft impact test for evaluation of impact force](#)”, *Nucl. Eng. Des.* **140**:3 (1993), 373–385.
- [Weckner and Abeyaratne 2005] O. Weckner and R. Abeyaratne, “[The effect of long-range forces on the dynamics of a bar](#)”, *J. Mech. Phys. Solids* **53**:3 (2005), 705–728.
- [Young 1969] C. W. Young, “Depth predictions for earth penetrating projectiles”, *J. Soil Mech. Found. Div.* **95**:SM3 (1969), 803–817.

Received 21 May 2007. Accepted 23 May 2007.

PAUL N. DEMMIE: pndemmi@sandia.gov

Multiscale Dynamic Material Modeling Department, Sandia National Laboratories, Box 5800 MS 1322, Albuquerque, NM 87185-1322, United States

STEWART A. SILLING: sasilli@sandia.gov

Multiscale Dynamic Material Modeling Department, Sandia National Laboratories, Box 5800 MS 1322, Albuquerque, NM 87185-1322, United States

PERFORMANCE AND FAILURE OF METAL SANDWICH PLATES SUBJECTED TO SHOCK LOADING

ASHKAN VAZIRI, ZHENYU XUE AND JOHN W. HUTCHINSON

The deflection and fracture of metal sandwich plates subjected to intense uniform impulsive pressure loads are studied for plates made of four steels representing a wide range of strength, strain hardening and ductility. Sandwich plates with both square honeycomb cores and folded plate cores are considered. The primary fracture modes of the sandwich plates are necking and subsequent tearing of the face sheets and webs and shear delamination of the core webs from the faces. Plates with square honeycomb cores have higher damage tolerance than those with folded plate cores in that they can withstand much larger loads above those at which the first signs of fracture appear. The trade-off between strength and ductility in plate performance is illustrated.

1. Introduction

All-metal sandwich plates perform better than solid plates of equal mass in resisting high intensity dynamic pressure loads, especially in water environments where sandwich construction benefits from fluid-structure interaction to reduce momentum transfer [Fleck and Deshpande 2004; Xue and Hutchinson 2004; Hutchinson and Xue 2005; Liang et al. 2007]. Whether the plate is monolithic or a sandwich, combinations of high ductility and high strength promote good performance. Assuming the material is sufficiently ductile to survive an intense blast, the ratio of maximum deflection δ to plate half-width L scales as [Xue and Hutchinson 2004]

$$\frac{\delta}{L} \propto \frac{I}{M\sqrt{\sigma_Y/\rho}}, \quad (1)$$

where I is the impulsive momentum/area transferred to the plate, ρ is the material density, σ_Y is the material yield stress, and M is the mass/area of the plate. To minimize δ/L for plates of a given M subjected to a given I , materials with high specific strength, σ_Y/ρ , are clearly preferred, assuming adequate ductility.

When metal plates are subjected to shock loading, various failure modes occur depending on the plate design and spatial details of the impulsive loading. For a solid plate, the two primary competing modes are failure at the supports and ductile tearing in the interior regions of the plate away from the supports. Failure at a support can be precipitated by tensile necking followed by ductile tearing, or it may take the form of a highly localized through-thickness shear failure [Nahshon et al. 2007]. Failure at supports and interior ductile tearing are also failure modes for face sheets of sandwich plates. Under intense impulsive loads, core webs will generally undergo extensive plastic buckling under compression or shear. In the

Keywords: sandwich plates, honeycomb core, folded plate core, strength, ductility, dynamic response.

This work has been supported in part by the ONR under grants N00014-02-1-0700 and GG10376-114934 and in part by the School of Engineering and Applied Sciences, Harvard University.

present context, buckling is regarded as a deformation mode and not a failure mode. However, extensive buckling can promote failure in either the core or the faces. Core failures occur as web tearing or as shear fracture at welded joints. Core failures do not necessarily imply ultimate failure since a sandwich plate can still have substantial residual strength afterward.

In this paper, we explore the role of material choice on plate performance against impulsive loads by evaluating failure modes and ultimate failure for two sandwich plate designs, one with a square honeycomb core and the other with a folded plate core. Four types of steel have been considered to delineate the roles of strength, strain hardening and ductility. The material description used here is based on the conventional J_2 plasticity constitutive relation with fracture imposed when the effective plastic strain reaches a critical value that may depend on the mean stress. This approach, coupled with element deletion when the failure criterion is met, has been widely used for finite element computations based on the early contributions to ductile fracture of [Hancock and Mackenzie \[1976\]](#) and subsequent work of [Johnson and Cook \[1983\]](#). We characterize steels by yield strength, strain hardening, and ductility as a function of mean-stress. We describe failure modes and compute deflections and maximum sustainable impulses.

2. Plates and loading specifications

Following several earlier studies [[Xue and Hutchinson 2004](#); [Vaziri et al. 2006](#); [Vaziri and Hutchinson 2007](#)], we model the plates as infinite in one direction and of width $2L$ in the other, with clamped conditions along the two edges. Solid plates have thickness h and mass/area $M = \rho h$. The two types of sandwich plates considered are shown in [Figure 1](#): one with a square honeycomb core and the other with a folded plate core running perpendicular to the clamped edges. [Figure 1](#) also depicts periodic units employed in the finite element models. Both core topologies have height H , web thickness t , and face sheet thickness h_f (the top and bottom faces of the sandwich plates have equal thickness). The square honeycomb core has web spacing B . The folded plate core has an inclination angle α such that the spacing of the folds is $B = t / \sin \alpha + H / \tan \alpha$. Denoting the relative density of the core (that is, the volume fraction of the core occupied by the webs) by f_c , we have

$$f_c = 2\frac{t}{B} - \left(\frac{t}{B}\right)^2, \quad \text{for the square honeycomb core,}$$

$$f_c = \frac{t}{t + H \cos \alpha}, \quad \text{for the folded plate core.}$$

The mass/area of the sandwich plate is $M = \rho(2h_f + f_c H)$. If L , M , and ρ are specified, the geometry of each of the sandwich plates is fully determined by f_c , H/L and B/H , or equivalently, by α rather than B/H for the folded plate core.

Following [[Rabczuk et al. 2004](#)] and [[Liang et al. 2007](#)], two types of clamped boundary conditions will be considered for the sandwich plates: *fully clamped*, where both faces and the webs are welded to rigid supports along the edges; and *periodic bottom clamping*, where only the bottom face is welded to rigid line-supports parallel to the plate. At the support, the top face and the webs are free to deflect in the direction normal to the support but are constrained against tangential displacement and rotation, in accord with periodic support conditions.

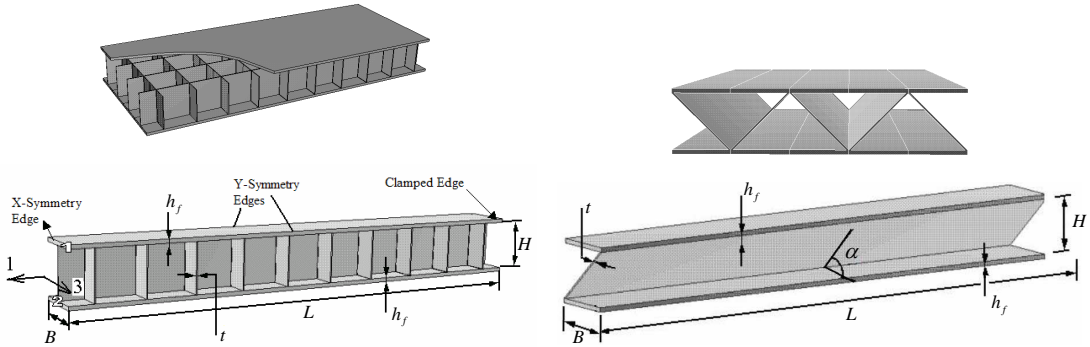


Figure 1. Schematic diagrams of metal sandwich plates configurations and the corresponding computational models for (left) square honeycomb sandwich plate and (right) folded sandwich plate. The width of the plates is $2L$.

The shock loading is modeled by applying a spatially uniform pressure history, $p(t) = p_0 \exp(-t/t_0)$ for $t > 0$, to the surface of the plate towards the blast (the top face), where p_0 and t_0 denote the peak over-pressure and decay time associated with shock. In all the calculations presented in this study, $t_0 = 10^{-4}$ s, which is representative of many blast loads and is very short compared to the overall response time of the plates. The impulse/area associated with the applied pressure history is $I = \int_0^\infty p dt = p_0 t_0$; to a good approximation, this is the momentum/area transferred to the plate because the impulse associated with the reaction forces at the supports is small over the period in which the shock acts. An alternative way to apply the loading is to assign the initial momentum/area I to the face of the sandwich towards the shock. However, [Vaziri and Hutchinson \[2007\]](#) have shown that the time-dependent pressure pulse gives more realistic predictions, especially for core crush since the crushing occurs early in the deformation history. The effect of fluid-structure interaction can be taken into account, at least approximately, by assigning values to I appropriate to the fluid medium and the mass/area of the face, according to the approach originally proposed for water blasts by [Taylor \[1963\]](#) and developed more fully for sandwich plates by [Liang et al. \[2007\]](#) and as extended recently by [Kambouchev et al. \[2006\]](#) to air blasts.

All calculations were carried out using ABAQUS/Explicit [[Hibbit, Karlsson and Sorensen Inc. 2001](#)]. Solid plates are modeled in plane strain and have ten elements through thickness. Full three-dimensional models are constructed for the sandwich plates based on periodic geometric units with detailed meshing of the core as reported more fully in [[Xue and Hutchinson 2004](#)] and [[Vaziri et al. 2006](#)]. At least four 8-node brick elements were employed through the thickness of each face sheet, which captures early stages of necking with acceptable fidelity. In the calculations, failed elements are removed using the approach available in ABAQUS.

3. Material specifications

Four steels have been selected to span a range of behaviors from a stainless steel (AL6XN) with intermediate yield strength, high strain hardening, and high ductility, to a high strength steel (HY80) with low strain hardening and modest ductility. Also considered are two intermediate strength steels with high ductility (DH36) and low ductility (AH36). The range of behaviors represented by these steels

is used to illustrate some of the critical issues underlying the role of material choice in plate design against impulsive loads. Tensile true stress-logarithmic strain curves for the four materials are presented in Figure 2, left. The effective plastic strain at failure $(\epsilon_{\text{eff}}^P)_C$ as a function of the triaxiality ratio σ_m/σ_e is plotted for three of the materials in Figure 2, right, where $\sigma_m = \sigma_{kk}/3$ is the mean stress, $\sigma_e = 3s_{ij}s_{ij}/2$ is the effective stress and s_{ij} is the stress deviator. Ductility data for HY80 was not available, but a parametric study will be conducted with this material using the fracture strain as a variable.

A difficulty that must be confronted in any study of this type is the lack of consistent sets of material data available for the different materials. This is even true for basic tensile stress-strain behavior where data incorporating strain-rate dependence is available for some materials and not for others. It is especially true that fracture data that expresses ductility as a function of mean stress is available for only a few materials. Moreover, such data depends on experimental procedures and inferences from specimen analysis that often vary from one investigator to another. In this study, we were forced to confront this difficulty. The data in Figure 2 were taken from various sources, as will now be described.

Young’s modulus, Poisson ratio, and the density of all the steel materials mentioned above are taken as $E = 200 \text{ GPa}$, $\nu = 0.3$, and $\rho = 7850 \text{ kgm}^{-3}$. The true stress-plastic strain response and the fracture locus for AH36 are taken from [Wierzbicki and Lee 2005]. For HY80 steel, the true stress-plastic strain response displayed in Figure 2, left, is representative of the material response at tensile strain rate of 100 s^{-1} as adopted from [Meyer et al. 2000]. Material strain rate dependence is not included for HY80. The tensile data for AL6XN was obtained from [Nahshon et al. 2007] and is similar to that given by [Nemat-Nasser et al. 2001]. For DH36, the Johnson and Cook [1983] plasticity model is employed for representing the stress-strain response of the material, as provided by [Nemat-Nasser and Guo 2003]. Neglecting temperature variations and assuming room temperature, the following relation obtains between the effective stress and effective plastic strain, ϵ_{eff}^P :

$$\sigma_e = 470 \text{ MPa} (1 + 1.5(\epsilon_{\text{eff}}^P)^{0.4}) (1 + 0.015 \ln(\dot{\epsilon}_{\text{eff}}^P/1 \text{ s}^{-1})),$$

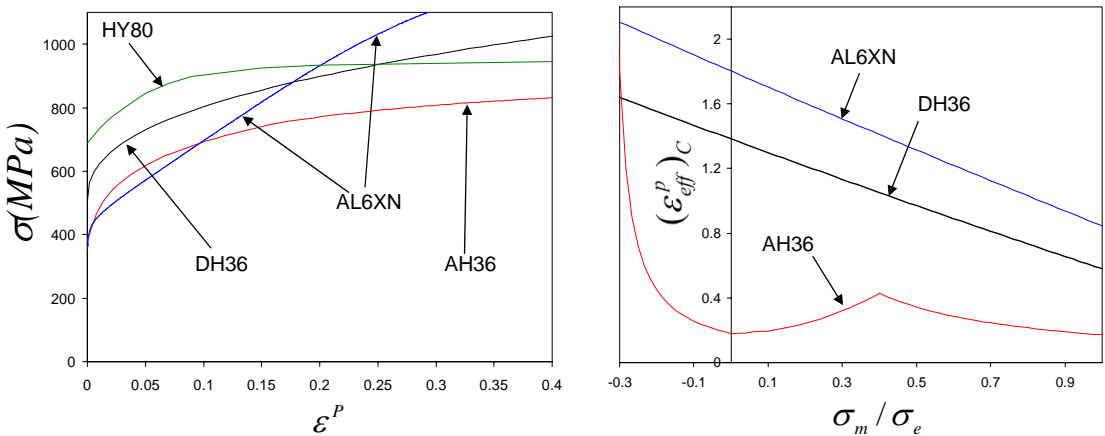


Figure 2. Left: true stress-plastic strain response of the four steels considered in this study. Right: failure locus for three of the four steels.

at the effective strain rate of $\dot{\epsilon}_{\text{eff}}^P$. The stress-strain curve for DH36 at the effective strain rate of

$$\dot{\epsilon}_{\text{eff}}^P = 100 \text{ s}^{-1}$$

is shown in Figure 2, left. The failure locus data for both DH36 and AL6XN are based on fitting experimental data (provided by Edward Johnson, private communication) to the Johnson–Cook shear failure model. Material strain rate dependence is only accounted for in calculations for DH36.

Figure 3 displays the center deflection (the maximum deflection) of solid plates made of the four steels as a function of the peak pressure imparted to the plate, p_0 , with impulse period fixed at $t_0 = 10^{-4}$ s. These plates have half-width $L = 1$ m and thickness $h = 20$ mm, corresponding to $M = 157 \text{ kg/m}^2$ and will serve as reference for comparison with equal weight sandwich plates. Over the range of p_0 plotted, the plates of AL6XN, DH36 and HY80 do not fail, because of the extensive ductility assumed for these materials (ductility limits for HY80 will be discussed later). However, plates of AH36 have a clear fracture limit associated with complete separation at edges by the supports. The sharp up-turn of the deflection of the plate made from AH36 just below the complete failure limit at $p_0 \cong 115$ MPa reflects the onset of fracture of the plate precipitated by necking at the plate edges. Once the peak pressure is large enough to cause necking, only slightly larger levels are required to detach the plate. Over the range of peak pressures plotted, a plate of HY80 deflects less than plates made of the other materials due to the higher strength of HY80 over the relevant range of strains (for example, 10 to 15%, as discussed later). The strain hardening and ductility of plates of DH36 and AL6XN ensure survivability to very large deflections, but their lower strength in the relevant range of strains gives rise to larger deflections at a given peak pressure.

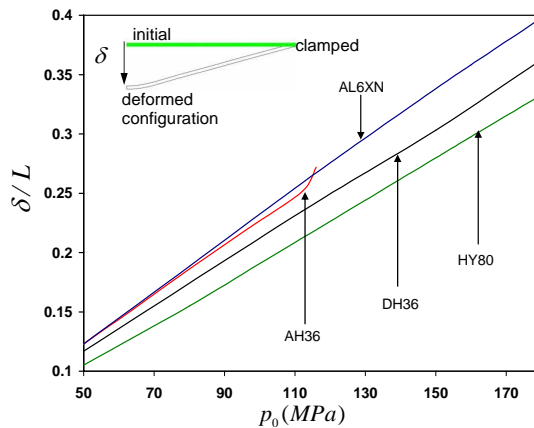


Figure 3. Normalized maximum deflection of solid plates of four steels of thickness 20 mm and width 2 m as a function of peak over-pressure p_0 associated with shock loading. The decay time associated with shock is $t_0 = 10^{-4}$ s. The curve corresponding to the plate made of AH36 is terminated at total failure, where the solid plate separates from the support and undergo free flight, $p_0 \sim 116$ MPa. No total failure is observed for solid plates made from DH36 and AL6XN in the range of peak over-pressure considered in this set of calculations. For HY80 no material failure criterion is incorporated and unlimited ductility has been assumed.

4. Competing fracture modes for sandwich plates of AH36 steel

In this section, we present detailed results on the deformation and failure modes of honeycomb and folded plate core sandwich plates for plates made of AH36 steel. This steel has been chosen for this purpose because the failure strain data is fully characterized and because its lower ductility compared to DH36 and AL6XN highlights the role of fracture limits. Most results have been determined with fully clamped boundary conditions, but a limited set of results will be presented for periodic bottom clamping. All plates have half-width $L = 1$ m and mass/area $M = 157$ kg m⁻². As mentioned above, the thickness of the solid plate having the same mass/area is 20 mm, and results for solid plates made from the four steels were presented in the previous section. The core thickness of both types of sandwich plates is fixed at $H/L = 0.1$, and the web spacing of the square honeycomb is fixed at $B/H = 1$ while the folded plate cores have $\alpha = 45^\circ$ such that $B/H \cong 1$. As noted in Section 2, the geometry of both types of sandwich plates is now prescribed by the relative density of the core. The stress-strain data and fracture locus of AH36 presented in Figure 2 were taken from [Wierzbicki and Lee 2005]; the initial yield strength is $\sigma_Y = 380$ MPa. Material strain-rate dependence is not included in the calculations.

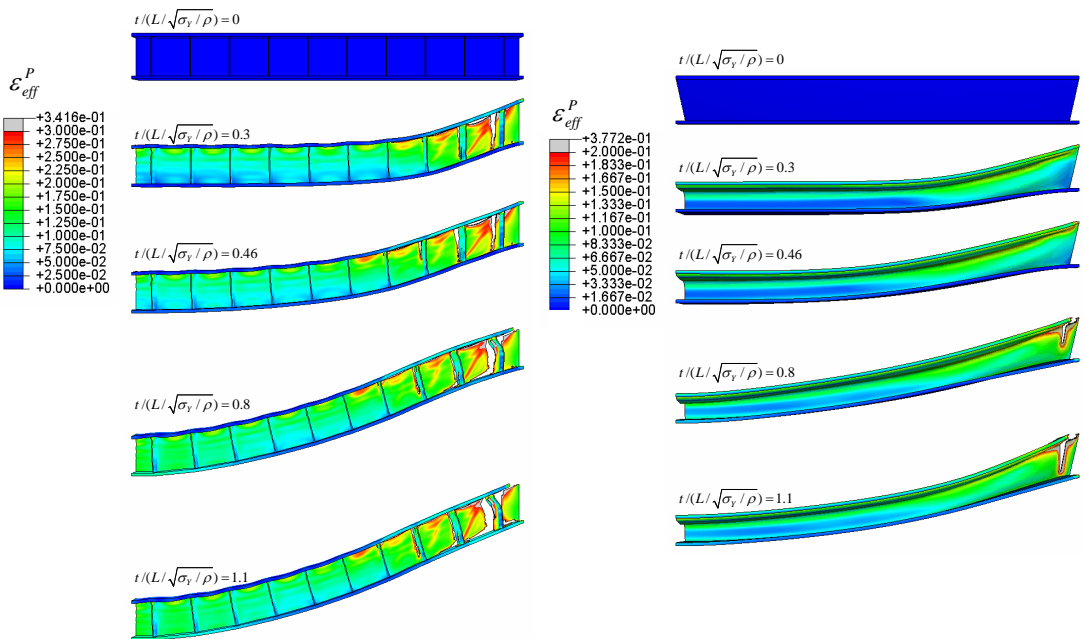


Figure 4. Successive views of the deformed profile at $t/(L/\sqrt{\sigma_Y/\rho}) = 0.0, 0.3, 0.46, 0.8, 1.1$ for (left) a square honeycomb sandwich plate subjected to $p_0 = 128$ MPa ($I/(M\sqrt{\sigma_Y/\rho}) \approx 0.364$) and (right) a folded sandwich plate subjected to $p_0 = 84$ MPa ($I/(M\sqrt{\sigma_Y/\rho}) \approx 0.238$). The sandwich plates have $M = 157$ kg/m², $f_c = 0.04$, $L = 1$ m. The decay time associated with shock is $t_0 = 10^{-4}$ s. Equivalent plastic strain field at each successive view is displayed. For both cases, there is no total failure of the sandwich plate since the bottom face remains intact.

4.1. Fully clamped support conditions. As reference for the present discussion, we note from Figure 3 that the clamped AH36 solid plate fails by necking, fracture, and finally detachment at the rigid supports at $p_0 \cong 115$ MPa ($I/(M\sqrt{\sigma_Y/\rho}) \approx 0.33$), corresponding to the maximum normalized deflection $\delta/L \approx 0.28$. Figure 4, left, presents successive views at various dimensionless times, $t/(L/\sqrt{\sigma_Y/\rho})$, of the sandwich plate with a square honeycomb core of relative density $f_c = 0.04$ subjected to a shock loading with $p_0 = 128$ MPa ($I/(M\sqrt{\sigma_Y/\rho}) \approx 0.364$). The contour map displays the equivalent plastic strain field at each stage of the response. Figure 4, right, presents the corresponding sequence of deformed states for the plate with a folded plate core with $f_c = 0.04$ and $p_0 = 84$ MPa ($I/(M\sqrt{\sigma_Y/\rho}) \approx 0.238$). For either plate, the applied pressure peaks just below the level required to completely fail the plate, defined as complete separation at the supports. The plate with the square honeycomb core undergoes relatively little core crush in the initial stage of deformation, but then it experiences intense shear in the core webs near the supports. Shear delamination cracks occur along the welds between webs and between the web and the face sheet. As deformation progresses, the top face undergoes tensile necking at the support and then fractures. The plate then comes to rest with the top face and most of the core separated from the support but with the bottom face sheet still intact. For the sandwich plate with the folded plate core, the response differs in several respects, including the occurrence of more extensive core crushing in the first stage and the near-simultaneous failure of the web and the top face sheet at the support. Here, again, the loading intensity is such that the plate comes to rest before the bottom face fails. Fracture begins

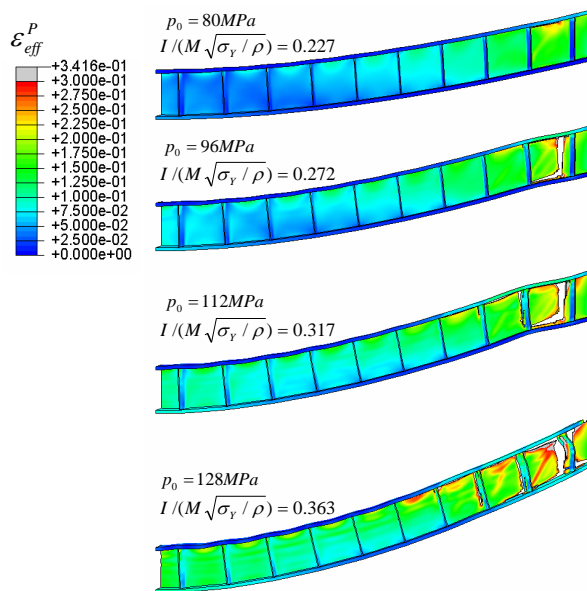


Figure 5. Deformed configurations and the equivalent plastic strain fields of a square honeycomb sandwich plate with the relative core density of, $f_c = 0.04$, subjected to loads of various intensities. The sandwich plates has $M = 157$ kg/m² and $L = 1$ m. The decay time associated with shock is $t_0 = 10^{-4}$ s. The equivalent plastic strain field at each deformed configuration is displayed. Even at the highest intensity shown, the bottom face remains intact.

substantially earlier in the plates with the square honeycomb core than in those with the folded plate, due to failures in the core. Nevertheless, the early core fractures are evidently benign: the plate withstands much larger deflections and peak pressures without complete failure.

Figure 5 shows the crack tolerance of the square honeycomb core sandwich plates. The same plate ($f_c = 0.04$) is subjected to four loads of increasing intensity. The figure displays the effective plastic strain distribution and cracks in the plate after it has come to rest. At the lowest loading intensity, plastic shearing occurs in a web near the support and a shear crack has just begun to emerge at the top face sheet. At an impulse that is 20% higher, the crack extends across the web from the top to the bottom face. At the next higher load the crack has spread along the bottom face in the web. At the highest impulse, which is 60% above that causing the first cracks, the top face has detached from the support, but the bottom face remains attached.

Figure 6 reveals the role of the relative density of the core, f_c , for various cases with the same mass/area $M = 157 \text{ kg m}^{-2}$. At left, the figure shows the deformed state of the plates with the square honeycomb core, where each has been subjected to an impulse with $p_0 = 96 \text{ MPa}$ ($I/(M\sqrt{\sigma_Y/\rho}) \approx 0.272$). At right are the deformed plates with the folded cores; here the impulse had $p_0 = 84 \text{ MPa}$ ($I/(M\sqrt{\sigma_Y/\rho}) \approx 0.238$). Of the plates with a square honeycomb core, the one with the lowest relative density ($f_c = 0.02$) sustains the largest core crush, and it undergoes extensive shear failure at the core/face weld line. The square honeycomb core plate with the highest relative density ($f_c = 0.08$) undergoes very little core crush, but it nearly fails at the supports. The plate with $f_c = 0.04$ deflects least and exhibits only localized fracture of the core web near the support. The folded-core plate with the lowest relative density ($f_c = 0.02$)

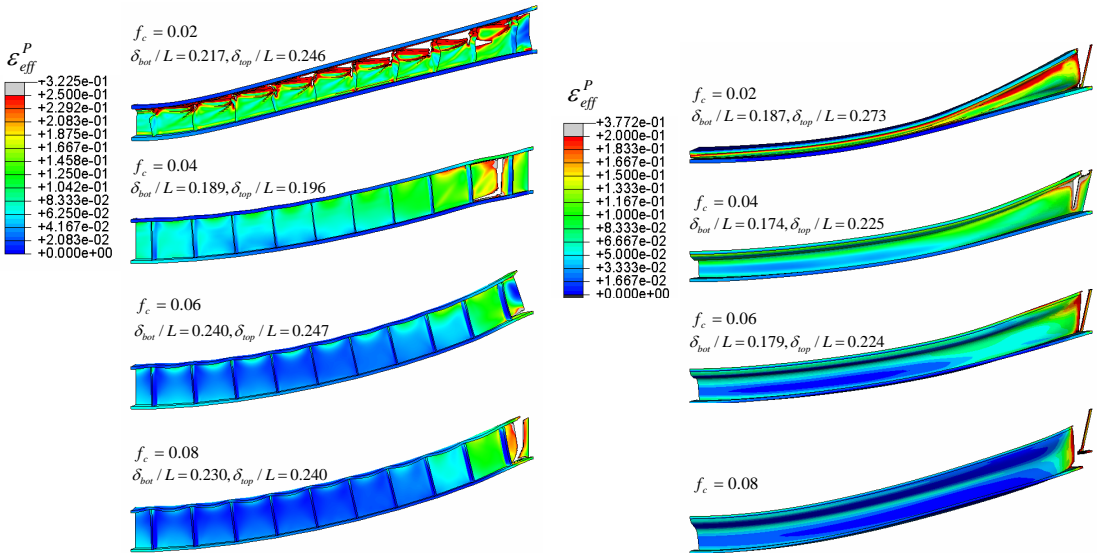


Figure 6. Deformed configurations and the equivalent plastic strain fields of (left) square honeycomb sandwich plates with various core densities subjected to $p_0 = 96 \text{ MPa}$ ($I/(M\sqrt{\sigma_Y/\rho}) = 0.272$) and (right) folded sandwich plates with various core densities subjected to $p_0 = 84 \text{ MPa}$ ($I/(M\sqrt{\sigma_Y/\rho}) = 0.238$). The sandwich plates have $M = 157 \text{ kg/m}^2$ and $L = 1 \text{ m}$. The decay time associated with the loading is $t_0 = 10^{-4} \text{ s}$.

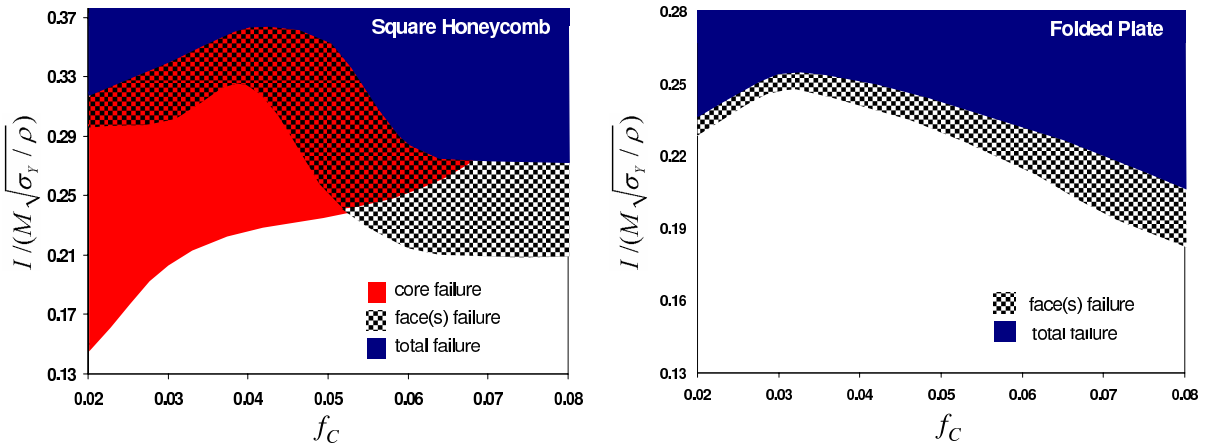


Figure 7. Failure map for square honeycomb and folded sandwich plates as dependent on the relative density of the core. The sandwich plates have $M = 157 \text{ kg/m}^2$ and $L = 1 \text{ m}$. The decay time associated with the loading is $t_0 = 10^{-4} \text{ s}$.

is completely crushed and fails almost completely at the support. Of all the plates with folded-plate cores, only the one with the highest relative density $f_c = 0.08$ fails completely. The plates with cores of intermediate relative density ($f_c = 0.04$ and $f_c = 0.06$) perform comparably at this level of impulse.

Figure 7 gives failure maps for the sandwich plates as a function of normalized impulse intensity and relative core density. As before, the plates share mass/area $M = 157 \text{ kg m}^{-2}$. In constructing this map, onset of core failure is recognized when the total length of shear delamination becomes equal to the core height. Core failure for the folded-core plates occurs after the failure of the top face at the supports. It is lumped into the total failure region of the plot where the bottom face also fails. By contrast, the honeycomb-core plates have a wide band of core failure if $f_c < 0.06$ at impulse levels well below failure of the two faces. As described above, the sandwich plates fail completely under uniform impulse when both faces and core webs have separated from the supports.

Companion maps in Figure 8 show the maximum deflection of the bottom face sheet. The maximum normalized impulse that can be sustained without total failure is $I/(M\sqrt{\sigma_Y/\rho}) \approx 0.368$ ($p_0 = 130 \text{ MPa}$) for the honeycomb-core plate and $I/(M\sqrt{\sigma_Y/\rho}) \approx 0.258$ ($p_0 = 91 \text{ MPa}$) for the folded-core plate. The largest bottom plate deflections that can be sustained without total failure are $\delta/L \cong 0.3$ for the honeycomb and $\delta/L \cong 0.15$ for the folded.

4.2. Role of support conditions — fully clamped versus periodic clamping of bottom face. In this section, a limited set of calculations is presented to study how the edge boundary conditions of a metal sandwich plate affect its overall performance and failure under high intensity loading. We consider square honeycomb and folded sandwich plates made from AH36 steel with relative core density of $f_c = 0.04$. Two idealized boundary conditions are considered.

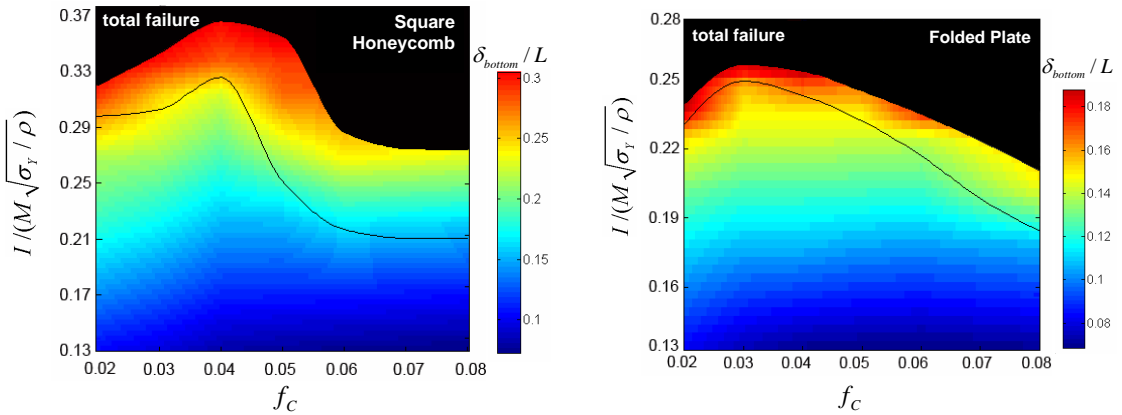


Figure 8. Normalized maximum deflection of the bottom face of (left) square honeycomb sandwich plates and (right) folded sandwich plates as a function of the loading intensity and the relative density of the core. The sandwich plates have $M = 157 \text{ kg/m}^2$ and $L = 1 \text{ m}$. The decay time associated with the loading is $t_0 = 10^{-4} \text{ s}$. The black solid line in each plot corresponds to the top face failure as depicted also in Figure 7.

- (i) *Fully clamped.* As above, the edges of both faces and the core webs are welded to rigid supports at the plate ends.
- (ii) *Periodic clamping.* The bottom face is welded to rigid supports of zero width. The top face and core webs are free to move perpendicularly to the plate (zero shear traction) but are constrained tangentially.

For both support conditions, Figure 9 displays how the maximum center deflection of each face sheet depends on the normalized loading intensity. The plate has the square honeycomb core. Figure 10 presents similar plots for the sandwich plate with the folded plate core. For comparison, the figure includes the response of the fully clamped solid plate of equal mass from Figure 3. In the fully clamped case, failure of the bottom face constitutes total failure. For periodic clamping, the top face and core webs have not failed when the bottom face tears away at the support. Nevertheless, the damage is extreme when the bottom face fails, and more intense loadings would produce proportionally much larger deflections. For this reason, we believe that the relevant range of intensities has been plotted for periodic clamping.

The plots in Figures 9 and 10 reveal that the support conditions significantly influence how metal sandwich plates respond and fail under high intensity loading. Sandwich plates with periodic clamping experience extensive core crushing at the support. For square honeycomb sandwich plates, the top and bottom faces have comparable center deflections, as relatively little core crushing occurs in the core away from the supports. By contrast, for folded core sandwich plates, the top face sheet undergoes significantly larger center deflections than the bottom face due to core crushing at early stages of deformation. For both types of sandwich plates, the bottom face sheet undergoes significant local stretching which leads to tearing at relatively low intensities of shock load. This effect is more pronounced for the folded sandwich plate, as revealed by comparing the deformed configurations at right in Figures 9 and 10. It is

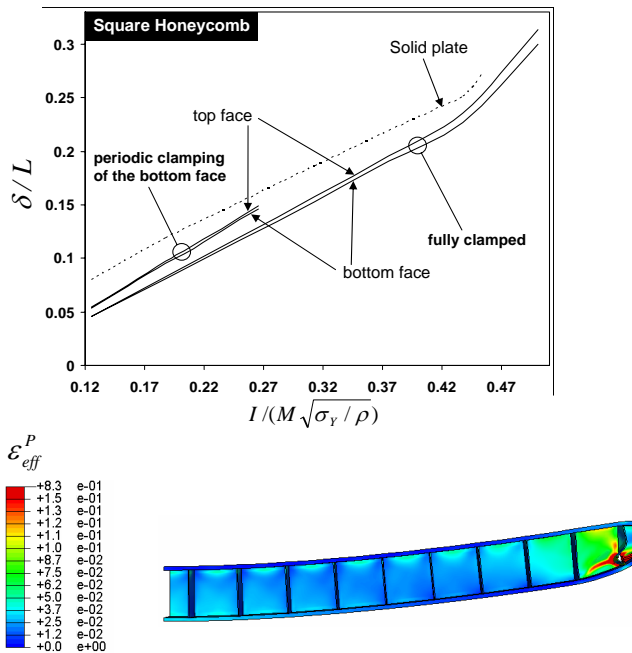


Figure 9. Top: normalized maximum deflection of the solid plate from Figure 2. Normalized maximum deflection of the top and bottom faces of the square honeycomb sandwich plate with $f_c = 0.04$ versus the imparted normalized momentum. Results are shown for two sets of boundary conditions: fully clamped and periodic clamping of the bottom face. The curves are terminated at failure. Bottom: deformed configurations of the square honeycomb sandwich plates with periodic clamping of the bottom face subjected to normalized momentum, $I/(M\sqrt{\sigma_Y/\rho}) = 0.181$. The plate has $M = 157 \text{ kg/m}^2$ and $L = 1 \text{ m}$.

noteworthy that the difference between the shock load intensities that cause the two sandwich types to fail is considerably smaller when they are periodically clamped than when they are fully clamped.

Both sets of boundary conditions are idealized in that they assume the plates are welded to immovable supports. It is likely that more realistic modeling of the small support movement may postpone failure of the faces at the supports and allow for larger load intensities to be sustained, particularly for the periodic clamping where support width may be an important factor. The spread of the results in Figures 9 and 10 with support conditions emphasizes that support design is a critical component of effective sandwich plate designs.

5. Comparative performance of sandwich plates made from four steels

In this section, the influence of material properties on the overall response and failure of metal sandwich plates is investigated by considering sandwich plates made from the four steels characterized in Section 3: AH36, DH36, AL6XN and HY80. As emphasized in Section 3, we had to make compromises in conducting this study because of the limited available data. Of the four steels, DH36 is characterized

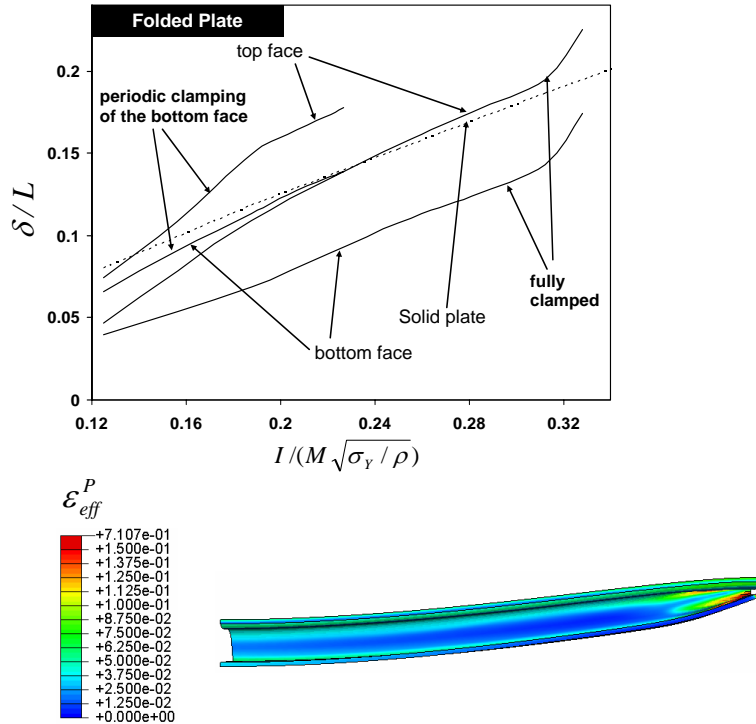


Figure 10. Top: normalized maximum deflection of the solid plate from Figure 2. Normalized deflection of the top and bottom faces of the folded sandwich plate with $f_c = 0.04$ versus the imparted normalized momentum. Results are shown for two sets of boundary conditions: fully clamped and periodic clamping of the bottom face. The curves are terminated at failure. Bottom: deformed configurations of the plates with periodic clamping of the bottom face subjected to normalized momentum, $I/(M\sqrt{\sigma_Y/\rho}) = 0.164$. The plate has $M = 157 \text{ kg/m}^2$ and $L = 1 \text{ m}$.

most completely, and it is the only one for which the strain-rate dependence was incorporated. Concerns about the accuracy of the fracture criteria used for the individual steels have also been noted in Section 3. With these caveats in mind, the comparative study highlights important connections between material properties and plate performance under intense shock loading.

Two specific plate geometries will be considered in this section: the fully clamped sandwich plates analyzed in Section 4 with the square honeycomb core and the folded plate core. Both have relative core density $f_c = 0.04$. The plate dimensions and loading are precisely as specified in Section 4—only the material is varied.

Figure 11 presents plots of the deflections of the top and bottom faces at the center of the plate as a function of the peak pressure. The left group shows result each of the four steels arranged in plates with a square honeycomb core; at right is the same for folded plate cores. The deflection curves terminate at the peak pressure associated with total failure of the plate, as described earlier. The ductility of DH36 and AL6XN (compare Figure 2, right) is sufficiently large that no failure occurs in either of the two types of plates over the range of blast pressures plotted. By contrast, the limited ductility of AH36 (at least as

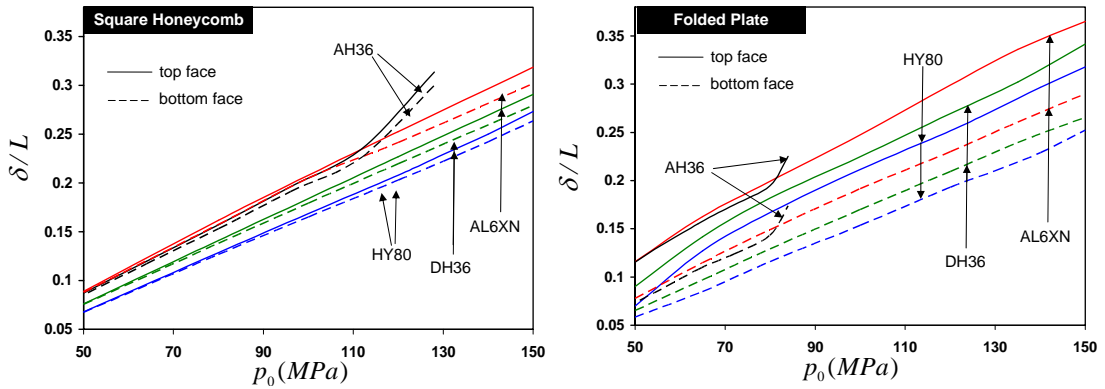


Figure 11. Normalized maximum deflection of top and bottom faces of (left) the square honeycomb and (right) folded sandwich plates with $f_c = 0.04$ for four steels. The results for HY80 assume unlimited ductility. The plates are fully clamped with $M = 157 \text{ kg/m}^2$ and $L = 1 \text{ m}$.

assumed for the purposes of this study) leads to failure within the range of blast pressures considered. With no ductility limits assumed for HY80, there is no failure over the range plotted.

Figure 11 also brings out the connection between the strength of the steel and the magnitude of the deflection. At a given peak pressure of the shock loading, plates made from the higher strength steels, HY80 and DH36, sustain smaller deflections than the two lower strength steels, as the scaling relation Equation (1) would suggest. The stretching strength of the faces is important in limiting the deflection, and the effective plastic strain occurring over most of the faces is under 10% for much of the range of deflections shown in Figure 11. Thus, it is the strength of the materials for strains below about 10% that determines the deflection differences seen in Figure 11. That the flow strength of AL6XN exceeds even that of HY80 at strains above 20% (Figure 2, right) reflects the high strain hardening and extensive ductility of AL6XN but has little influence in reducing the overall deflection. For the same reason, strength enhancement due to material rate sensitivity for strains below about 10% is the most important in influencing the deflection. Material rate-dependence for DH36 plays a relatively small role in determining the overall deflection. The elevation in flow stress for a strain rate on the order of 100 s^{-1} , which is relevant to the dynamic plate response, is only about 5% above that associated with low strain rates, with deflection reductions scaling as in Equation (1).

Further insight into failure development in the HY80 sandwich plates is provided by Figure 12, top, which presents the effective plastic strain, averaged through the face thickness at the point along the top face where it is largest, as a function of the shock peak pressure. The corresponding result for the solid plate having the same mass is also included. These results have been computed assuming unlimited ductility for the HY80. For peak pressures below 120 MPa, the maximum plastic strain in the top face of the square honeycomb core plate occurs at the support, and the magnitude is close to that of the solid plate. Plastic shear strains in the core webs are considerably larger than the strains in the top face at this stage. For $p_0 > 120 \text{ MPa}$, the location of the maximum plastic strain in the face shifts inward from the support (Figure 12, bottom left). There is an associated steep increase in the maximum strain caused by increasing blast intensity associated with necking at this location. The critical location for the face

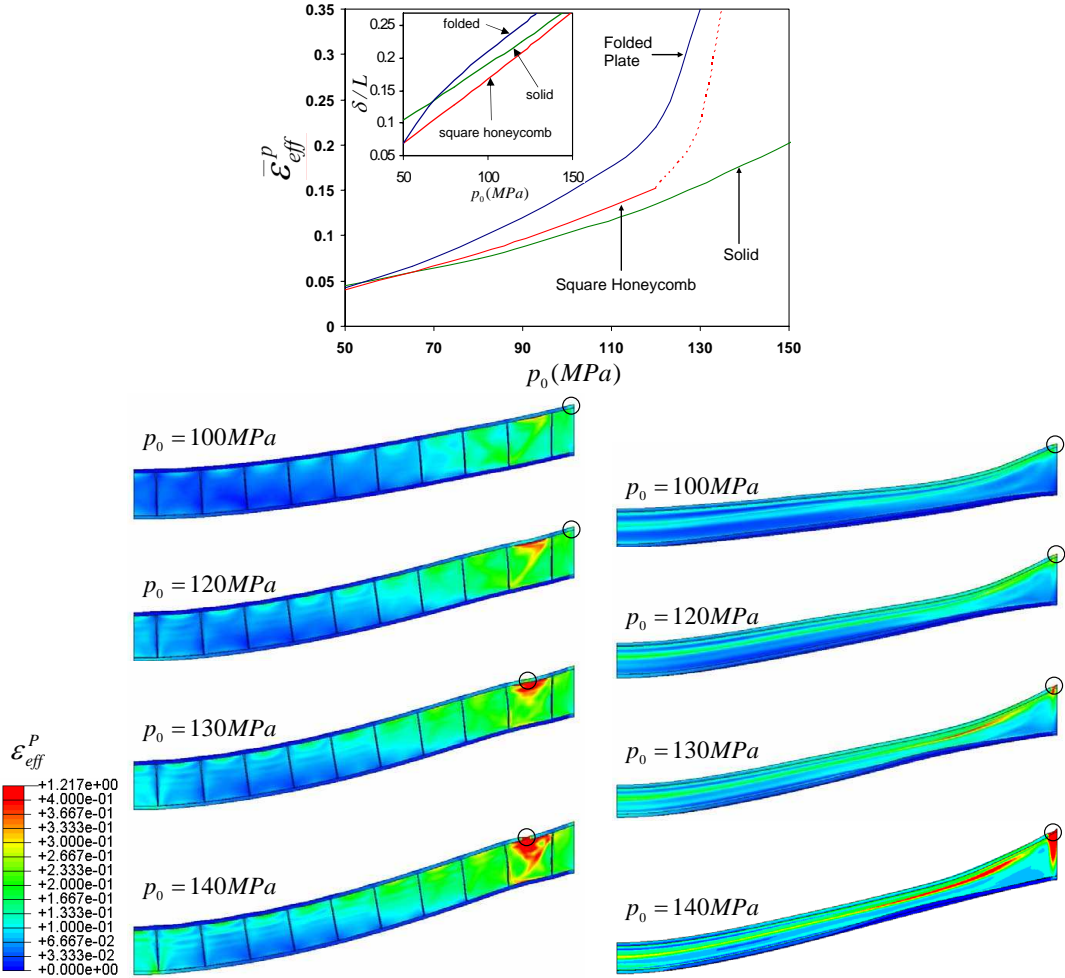


Figure 12. Strains in plates of HY80 and $f_c = 0.04$ computed assuming unlimited ductility. Top: effective plastic strain averaged through the thickness of the top face sheet at the location where it is the maximum. The result for the solid plate is included. The decay time associated with the loading is $t_0 = 10^{-4}$ s. The inset shows the normalized deflection as a function of the load intensity. Bottom left and right: deformed configurations of the square honeycomb and folded sandwich plates at various levels of peak over-pressure. The location of maximum equivalent plastic strain in the top face is indicated by black circles on each deformed configurations. The plates have $M = 157 \text{ kg/m}^2$ and $L = 1 \text{ m}$.

of the folded core sandwich plate is at the support (Figure 12, bottom right), where necking sets in at approximately the same loading intensity as for the square honeycomb plate. Intense plastic shearing also occurs in the core webs of this plate.

To illustrate the role of ductility for HY80, a series of studies has been carried out for the square honeycomb plate analyzed in Figure 12, top and bottom left, (with $f_c = 0.04$) treating the fracture strain $(\epsilon_{eff}^P)_c$ as a parameter. As mentioned earlier in the paper, fracture data on HY80 was not available. As a

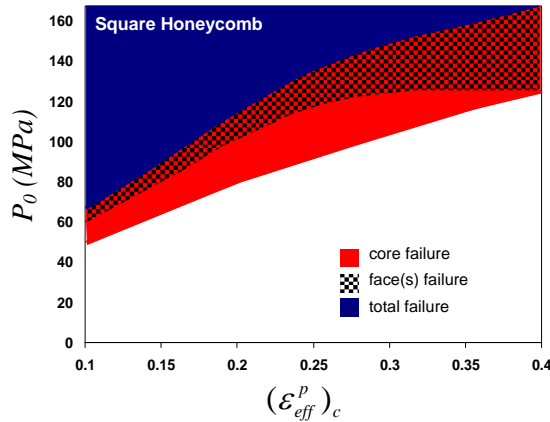


Figure 13. The failure map for HY80 as dependent on the critical effective plastic strain at fracture. $(\varepsilon_{\text{eff}}^P)_c$ is taken to be independent of mean stress. Square honeycomb core plates with $M = 157 \text{ kg/m}^2$, $L = 1 \text{ m}$ and $f_c = 0.04$.

high-strength steel, HY80 is expected to have limited ductility and its fracture strain is likely to depend on stress triaxiality. In the present simulations, $(\varepsilon_{\text{eff}}^P)_c$ will be taken as independent of triaxiality given the absence of data, but we will comment on what effect it might have had in what follows. A fracture diagram delineating core fractures, top face failure, and total failure as a function of blast intensity p_0 is shown in Figure 13 for fracture strains $(\varepsilon_{\text{eff}}^P)_c$ ranging from 0.1 to 0.4.

For the lowest fracture strain, $(\varepsilon_{\text{eff}}^P)_c = 0.1$, the plate undergoes total failure at a surprisingly low intensity ($p_0 \cong 70 \text{ MPa}$). The sequence of events leading to total failure is shear failure where the core webs are joined to the top face, followed by progressive failure of the top face, and finally necking and tearing of the bottom face at the sheet. The sequential nature of the failure significantly reduces the maximum intensity the plate can withstand compared with a prediction computed by assuming no intermediate failures and by applying the critical strain criterion to the bottom face (compare Figure 12). Thus, for example, if the critical strain in shear (a low triaxiality stress state) were much higher than 0.1, then the core webs would not fail first in shear and the maximum sustainable pressure would likely be considerably larger than $p_0 \cong 70 \text{ MPa}$. In Figure 13, a HY80 fracture strain, $(\varepsilon_{\text{eff}}^P)_c \cong 0.35$, is required to sustain intensities in the upper range of those plotted in Figure 11, that is, $p_0 \cong 140 \text{ MPa}$. A fracture strain this large seems unlikely for steels with the high strength and low strain hardening of HY80. Another feature of note in Figure 13 is that top face failure becomes independent of fracture strain for $(\varepsilon_{\text{eff}}^P)_c > 0.25$, implying necking localization itself constitutes failure. In addition, for $(\varepsilon_{\text{eff}}^P)_c > 0.4$, the top face fails before the core fractures.

6. Conclusions

Sandwich plates made of four steels and subjected to impulsive pressure loads have been simulated to learn how plate deflection and the fracture modes depend on load intensity. The materials range from relatively low strength steels with high strain hardening and ductility to high strength steels with low strain hardening. As emphasized in the paper, some of the fracture properties obtained from the literature

for the materials may be suspect. Whether hypothetical or not, the fracture properties serve to illustrate the trade-off between strength and ductility in the design of high performance steel sandwich plates. In particular, high strength reduces plate deflections and is beneficial as long as fracture does not occur. However, face sheets of high strength steel with low strain hardening, such as HY80, are susceptible to necking as they stretch, which is followed soon thereafter by face sheet tearing. By contrast, plates made of DH36 steel are not as strong as those of HY80 and deflect somewhat more in the range of load intensities in which both plates survive. Due to their extensive ductility, plates of DH36 and AL6XN did not fail over the range of deformations and load intensities considered here.

This paper has emphasized fractures that develop in a plate subjected to a single blast load and examined their extent as a function of blast intensity. It did not study the residual capacity of the plate after it has been damaged; however, the methods used here are capable of addressing the residual strength and blast resistance.

The damage tolerance appears to differ between plates with square honeycomb cores and those with folded plate cores (Figure 7). Local fractures and delaminations of the honeycomb web occur at load intensities well below the intensity that causes total failure of the plate. On the other hand, in plates with folded plate cores, the core fractures in a narrow range of load intensities just below the intensity at total failure. For a material with fracture properties such as those assumed for AH36 steel, the honeycomb-core plates can sustain significantly more load intensity than those with folded plate cores. In this connection, it is important to recognize that the load intensity applied to the plate, as measured here by either the peak pressure p_0 or the impulse/area, doesn't account for any fluid-structure interaction. Thus, for water blasts, it is generally not valid to make a direct comparison between square honeycomb and folded plate core performances based on the same p_0 since fluid-structure interaction for the two cores is different.

A limited study of the role of support conditions has been conducted by comparing behavior under fully clamped conditions with those where the plate is a periodic unit that is supported only at the bottom face away from the blast. The results suggest that the latter means of support is more susceptible to fracture and cannot sustain as much load intensity as the fully clamped plate, at least to the point where the bottom face fails. The most important conclusion to be drawn from this limited comparison is that support details are very important in the design of sandwich plates against intense dynamic loads.

References

- [Fleck and Deshpande 2004] N. A. Fleck and V. S. Deshpande, "The resistance of clamped sandwich beams to shock loading", *J. Appl. Mech. (Trans. ASME)* **71** (2004), 386–401.
- [Hancock and Mackenzie 1976] J. W. Hancock and A. C. Mackenzie, "On the mechanisms of ductile failure in high-strength steels subjected to multi-axial stress states", *Journal of Mechanics and Physics of Solids* **24** (1976), 1471–69.
- [Hibbit, Karlsson and Sorensen Inc. 2001] Hibbit, Karlsson and Sorensen Inc., *ABAQUS/Explicit User's Manual*, Hibbit, Karlsson and Sorensen Inc., 2001. Version 6.0.
- [Hutchinson and Xue 2005] J. W. Hutchinson and Z. Xue, "Metal sandwich plates optimized for pressure impulses", *Int. J. Mech. Sci.* **47** (2005), 545–569.
- [Johnson and Cook 1983] G. R. Johnson and W. H. Cook, "A constitutive model and data for metals subjected to large strains, high strain rates and high temperatures", pp. 541–547 in *Proceedings of 7th International Symposium On Ballistics*, Netherlands, 1983.
- [Kambouchev et al. 2006] N. Kambouchev, L. Noels, and R. Radovitzky, "Compressibility effects in fluid-structure interaction and their implications on the air-blast loading of structures", *J. Appl. Phys.* **100** (2006), 063519.

- [Liang et al. 2007] Y. Liang, A. V. Spuskanyuk, S. E. Flores, D. R. Hayhurst, J. W. Hutchinson, R. M. McMeeking, and A. G. Evans, “The response of metal sandwich panels to water blasts”, *J. Appl. Mech. (Trans. ASME)* **74** (2007), 81–99.
- [Meyer et al. 2000] L. W. Meyer, L. Krüger, and F. F. Hahn, “Influence of pre-deformation and strain rate on the flow behavior of HY80 steel”, pp. 295–300 in *Pressure vessels and piping*, vol. 414, Emerging technologies in fluids, structures and fluid/structure interactions **1**, 2000.
- [Nahshon et al. 2007] K. Nahshon, M. G. Pontin, A. G. Evans, J. W. Hutchinson, and F. W. Zok, “Dynamic shear rupture of steel plates”, *Journal of Mechanics of Materials and Structures* (2007). In press.
- [Nemat-Nasser and Guo 2003] S. Nemat-Nasser and W. Guo, “Thermomechanical response of DH-36 structural steel over wide range of strain rates and temperatures”, *Mech. Mater.* **35** (2003), 1023–1047.
- [Nemat-Nasser et al. 2001] S. Nemat-Nasser, D. P. Kihl, and W. Guo, “Thermomechanical response of AL-6XN stainless steel over a wide range of strain rates and temperatures”, *Journal of Mechanics and Physics of Solids* **49** (2001), 1823–1846.
- [Rabczuk et al. 2004] T. Rabczuk, J. Y. Kim, E. Samaniego, and T. Belytschko, “Homogenization of sandwich structures”, *Int. J. Numer. Methods Eng.* **61** (2004), 1009–1027.
- [Taylor 1963] G. I. Taylor, “The pressure and impulse of submarine explosion waves on plates”, pp. 287–303 in *The scientific papers of Sir Geoffrey Ingram Taylor, volume III: aerodynamics and the mechanics of projectiles and explosions*, edited by G. K. Batchelor, Cambridge University Press., 1963.
- [Vaziri and Hutchinson 2007] A. Vaziri and J. W. Hutchinson, “Metal sandwich plates subject to intense air shocks”, *Int. J. Solids Struct.* **44** (2007), 2021–2035.
- [Vaziri et al. 2006] A. Vaziri, Z. Xue, and J. W. Hutchinson, “Metal sandwich plates with polymeric foam-filled cores”, *Journal of Mechanics of Materials and Structures* **1** (2006), 95–128.
- [Wierzbicki and Lee 2005] T. Wierzbicki and Y. W. Lee, “Fracture prediction of thin plates under localized impulsive loading. Part II: discing and petalling”, *Int. J. Impact Eng.* **31** (2005), 1277–1308.
- [Xue and Hutchinson 2004] Z. Xue and J. W. Hutchinson, “A comparative study of impulse-resistant metallic sandwich plates”, *Int. J. Impact Eng.* **30** (2004), 1283–1305.

Received 23 May 2007. Accepted 23 May 2007.

ASHKAN VAZIRI: avaziri@seas.harvard.edu

School of Engineering and Applied Sciences, Harvard University, Cambridge, MA 02138, United States
www.seas.harvard.edu/~avaziri

ZHENYU XUE: xue@esag.harvard.edu

School of Engineering and Applied Sciences, Harvard University, Cambridge, MA 02138, United States

JOHN W. HUTCHINSON: hutchinson@husm.harvard.edu

School of Engineering and Applied Sciences, Harvard University, Cambridge, MA 02138, United States
<http://www.seas.harvard.edu/hutchinson/>

COMPUTATIONAL MODELING OF TUNGSTEN CARBIDE SPHERE IMPACT AND PENETRATION INTO HIGH-STRENGTH-LOW-ALLOY (HSLA)-100 STEEL TARGETS

COSTAS G. FOUNTZOULAS, GEORGE A. GAZONAS AND BRYAN A. CHEESEMAN

The current investigation tested the existing material models of tungsten carbide and HSLA-100 steel by comparing available published experimental data, such as the depth and diameter of the impact crater, against the corresponding simulated results. Lagrange and smoothed particle hydrodynamics (SPH) simulations were carried out using an axisymmetric model of the tungsten carbide (WC) projectile and the HSLA-100 target. The Lagrange simulation predicted the crater diameter accurately. The SPH simulation efforts predicted the crater diameter with acceptable accuracy (within 15%) for impact velocities ranging from 830 to 2550 m/s. However, the SPH simulations failed to predict the crater depth for impact velocities greater than 1.5 km/s. The current paper will detail the results of parametric studies conducted using various existing models in an attempt to simulate the observed damage and the efforts to improve the simulation prediction of the experimental data.

1. Introduction

Impact and penetration problems include but are not limited to, armor and antiarmor development, personnel armor, vehicle protection, and analysis of weapon design. Multiple physical phenomena are involved during penetration, such as fracture, failure, residual stresses, and friction heating. Sufficient knowledge of the material response to these dynamic phenomena and consequent development of material models which can depict accurately the behavior of the materials are required for the design of efficient structures under high rate loadings. However, to include underlying physics in the model is a difficult task. In reality, since empirical and analytical approaches cannot capture all of these phenomena, numerical simulation has become a necessary tool for the study of these phenomena. Smoothed particle hydrodynamics (SPH) is a meshless Lagrangian technique, and can model large material shear flows and material fracture more robustly. The deficiencies of the conventional finite element methods involve large mesh distortions and mesh-size sensitivity. Furthermore, the production of large local inelastic flow and material cracking during the penetration process generate irrecoverable mesh distortions. The mesh-size sensitivity problem stems from the inability of conventional continuum constitutive models to treat material softening during failure. Meshless methods, such as SPH, applied to penetration problems have achieved only limited success due to an inherent tensile instability and inability to reproduce low-order polynomials. However, recent advances in meshless technology have addressed these shortcomings, and have overcome many other difficulties in failure simulation, boundary conditions, and efficiency (see www.ca.sandia.gov/8700/projects/content.php?cid=100).

Keywords: computational modeling, Lagrange, smoothed particle hydrodynamics (SPH), meshless particles, AUTODYN, tungsten carbide, HSLA-100 steel, impact.

HSLA-100 steel is an improved weldability steel, which has been used to replace high strength alloy steels in a number of applications, including aircraft carriers, cruisers, and submarines. Modern warships, surface combatants and submarines, require high strength steel plate in increasing portions of the hull structure for weight reduction, better stability, increased payload, increased mobility, and survivability [Czyryca et al. 2003]. According to Czyryca et al. [2003],

Nearly half of the total Department of Defense requirement for alloy and armor steel plate is used in naval shipbuilding. In service, naval ship structures are subjected to a complex spectrum of loads and environments, and the structural steels and welding materials used in hull fabrication must demonstrate high fracture toughness for these extreme conditions. The routine dynamic loads in service include wave loading, sea slap, slamming, vibration, cargo buoyancy, and aircraft landing. Thus, the key requirements for naval shipbuilding steels are not only strength, weldability, and toughness at low temperature under shock events, but are also driven by economics, in order to keep an affordable ship acquisition cost.

HSLA-100 is a high yield strength, high toughness, and improved weldability steel, used as an alternative to quenched and tempered alloy steels [Martineau et al. 2004]. Tungsten carbide (WC) accounts for about 65% of tungsten consumption in the USA each year (see www.mii.org/Minerals/phototung.html).

It is combined with cobalt as a binder to form the so-called cemented carbides, which are used in cutting and wear applications. Most of these carbides have characteristically high hardness, good electrical and thermal conductivity, and high stability. These properties account for the principal applications: structures resistant to chemical reaction, uses in which wear resistance is of major importance, and high-temperature radiant-energy sources. The brittleness of carbides, however, has prevented their use as single-phase materials in highly stressed structural applications and has led to the development of metal-bonded composites (cemented carbides or cermets); see www.itia.org.uk/tungsten/tungsten_facts.html.

Ceramics are materials that possess characteristics such as low density, high hardness, and high compressive strength which make them ideal for use in light weight armor; however, ceramics are also brittle and have a low tensile strength, which complicates the design of such systems. Numerous experimental investigations have been performed since the 1960s to develop an understanding of the behavior of ceramics under high velocity impact and the behavior of the failed ceramic under high pressures [Wilkins et al. 1969; Shockey et al. 1990].

Recently, there has been interest in developing the capability to simulate the ballistic response of WC, which is widely used as a hard core in projectiles [Wilkins et al. 1969]. The cemented carbide utilized in [Burkins 2003] and in this analysis is comprised of 93% WC and 6% cobalt (the metallic binder). The modeling challenge lies in the ability to accurately represent the behavior of the WC core material. Several studies have been performed recently involving the impact of WC spheres on a variety of different target materials and thicknesses, and over a wide range of velocities [Williams 1995; Grady 1999]. However, few studies appear to have been performed on high velocity impact of HSLA steels. Martineau et al. [2004] examined experimentally and numerically the residual stress in the target HSLA material as a result of the WC sphere impact and subsequent cratering. The residual stress was examined because of its possible effect on the ability of armor or turbine blades to survive multiple impacts or to survive future service loads when the original impact event did not cause total failure.

The current investigation will test the existing material models of tungsten carbide and HSLA-100 steel by comparing available published experimental data [Martineau et al. 2004], such as the depth and diameter of the impact crater, against the corresponding simulated results. The simulation will use exclusively the SPH method for the WC projectile, and SPH and Lagrange methods for the HSLA-100 target. The response of the target to the impact will be analyzed by both discretization methods, SPH and Lagrange, for all the impact velocities in an effort to study the effect of these methods on the simulation accuracy. The commercially available finite element code, AUTODYN [2004], will be used to simulate impact and penetration of HSLA-100 targets by WC projectiles. The contribution and sensitivity of the selected material parameters on the accuracy of the solution when compared to the experimentally determined results will be discussed in detail.

Details of the impact experiments have been reported by Martineau et al. [2004], and are summarized in Table 1. The 51 mm thick plate material was prepared by hot-cross-rolling. It was austenized at 900°C for 75 min and then water quenched. The tungsten carbide spheres were purchased from Machining Technologies, Inc. in Elmore, Ohio. The 6.35 mm diameter spheres, Grade 25, were composed of 94% WC with 6% a cobalt binder. The steel plate was impacted normal to the plate by the small diameter spheres with velocities ranging from 830–2550 m/s. For this study, the accuracy of the material models which were used to simulate the impact process will be established by comparing the simulated depth and width of the crater against the ones measured relative to the planar surface of the plate.

2. Numerical simulations

These twelve experiments were simulated using the nonlinear commercial analysis software AUTODYN [2004]. AUTODYN is a uniquely versatile explicit analysis tool for modeling the nonlinear dynamics

Velocity (km/s)	Grady Spall		Mott Stochastic Failure		Experimental	
	Diameter	Depth	Diameter	Depth	Diameter	Depth
0.83	6.3	6.01	7.55	5.38	6.35	4.57
0.97	7.18	7.18	7.92	5.32	6.60	5.59
0.98	7.44	7.24	8.00	5.55	6.53	5.46
1.27	8.6	8.21	8.38	7.31	7.49	7.09
1.28	8.67	8.55	8.67	7.38	7.29	6.86
1.50	9.2	8.9	9.32	8.84	8.00	8.51
1.81	10.4	10.1	10.66	11.19	8.92	8.79
1.91	11.08	10.48	11.19	11.86	9.27	8.53
2.15	12.0	11.3	11.82	12.98	9.91	8.41
2.22	13.22	11.4	12.00	13.11	10.03	8.64
2.46	13.9	11.73	12.56	12.48	10.87	9.5
2.55	13.34	11.81	13.14	13.62	11.43	9.6

Table 1. Impact velocity and resulting simulation crater diameter and depth (in mm) compared to the experimental data by Martineau et al. [2004]. The target was discretized using the SPH method.

of solids, fluids, gas and their interactions. We have successfully used AUTODYN software for the modeling of impact of metallic and ceramic targets.

Using the geometry detailed above, an axisymmetric model was generated for the analysis of the WC projectile and the HSLA-100 target. The HSLA-100 target was discretized using both methods, SPH with a particle size of 0.125 mm, and Lagrange with element size of 0.5 mm, respectively. The sphere was discretized using SPH with a particle size of 0.125 mm. The HSLA-100 target was modeled for all simulations using a shock equation of state (EOS) [Martineau et al. 2004], a Zerilli–Armstrong strength model [Hanson 2003], and a Johnson–Cook (equivalent plastic strain to failure) model using constants derived from the experimental results of Chae and Koss [2004]. Fitting constants to this data resulted in $D_1 = 0.0$, $D_2 = 4.8$, $D_3 = -2.7$, $D_4 = 0.01$, and $D_5 = 0.0$. The WC was modeled using a polynomial EOS [Holmquist et al. 2005], and a Johnson–Cook strength and failure model using constants from [Holmquist et al. 2005]. Nevertheless, initial results were disappointing; the WC appeared to fragment prematurely, and the results underestimated the depth-of-penetration (DOP) by 9% and overestimated the crater diameter by 50% at an impact velocity of 0.83 km/s. We then attempted to improve predictions of the WC fragmentation behavior by increasing the dynamic yield stress from $Y = 3$ GPa [Hanson 2003] to the value $Y = 4.95$ GPa reported in [Normandia 2004], and by evaluating two additional failure models: the Grady spall model, which was initially developed for spall in ductile metals [Grady and Kipp 1997], and the principal tensile failure strain model, with crack softening and stochastic failure [Mott 1947]. A summary of the constitutive properties of the HSLA-100 plate and the tungsten carbide spheres is given in Table 2. Analytical expressions of the material models are given in Appendix A.

The Grady spall model relates the spall stress S in the ceramic to the dynamic yield stress and failure strain, $S = (2\rho c^2 Y \varepsilon_c)^{1/2}$, where ρ is the mass density, $c^2 = E/\rho$ is the square of the wave speed in the material, and E is the modulus of elasticity of the material. We tried to improve the dynamic fragmentation behavior of the WC by using a larger value than the dynamic yield stress of $Y = 4.95$ GPa reported in [Normandia 2004], Young’s modulus 620 GPa [Hanson 2003], and $\varepsilon_c = 0.0027$. Hence,

Material	Description	Value	Units
HSLA plate	Density, ρ	7.842	g/cm ³
	Shear modulus	76.3	GPa
	Elastic modulus	197.0	GPa
	Yield stress	103	MPa
	Poisson’s ratio	0.29	
	Grüneisen γ	2.17	
WC spheres	Density, ρ	14.77	g/cm ³
	Shear modulus	396	GPa
	Bulk modulus	362	GPa
	Yield stress	495	MPa
	Principal tensile failure strain	0.001	
	Fracture energy	40.32	J/m ²

Table 2. Constitutive properties for the HSLA-100 plate and WC spheres.

the derived spall stress $S = 4$ GPa is only about 10% larger than the value reported by Grady [1999]; we note that Martineau et al. [2004] report failure strains of $\varepsilon_c = 0.015$ for WC, but this value would predict unrealistically high spall stresses in the WC (using the equation above). The spall stress S is then equated to the local maximum principal stress necessary for failure in AUTODYN.

The Mott stochastic failure model [Mott 1947] as implemented in AUTODYN is a probabilistic failure model used to simulate an initial flaw distribution (heterogeneity) in the material; we randomized the principal strain-to-failure in the ceramic about $\varepsilon_c = 0.001$, with stochastic variance $\xi = 100$, and crack-softening with fracture energy $G_f = 40.3$ J/m².

2.1. SPH method. The results of the simulations, where the HSLA-100 target was discretized by the SPH, are summarized in Table 1; despite the rather sophisticated modifications to the models of the failure behavior of the ceramic relative to that reported in [Martineau et al. 2004], the results did not correlate well with the experimental observations.

Figures 1 and 2 compare the simulation results of the crater diameter and depth to the experimentally obtained values with increasing impact velocity.

Both modeling efforts result in premature tungsten carbide failure. In general, the calculated penetration depth and crater diameter are overestimated when compared to the experimentally obtained values. The relationship between crater depth and experimental velocity is much more linear in numerical predictions than indicated by the experimental data. Martineau et al. [2004] also observed a similar trend of the crater evolution versus the impact velocity using LS-DYNA. They used a less sophisticated material and failure model for their simulations, but with qualitatively similar results. Figure 1 shows that for impact velocities from 830 to 2550 m/s both failure modeling approaches overpredicted the crater diameters by about 15%.

Velocity (km/s)	Grady Spall		Mott Stochastic Failure		Experimental	
	Diameter	Depth	Diameter	Depth	Diameter	Depth
0.83	6.26	4.31	5.4	4.44	6.35	4.57
0.97	6.82	5.58	6.	5.89	6.60	5.59
0.98	6.82	6.	5.84	5.94	6.53	5.46
1.27	7.58	7.13	7.	7.78	7.49	7.09
1.28	7.8	8.41	7.04	7.78	7.29	6.86
1.50	8.16	8.53	8.00	9.05	8.00	8.51
1.81	9.04	8.59	8.24	9.13	8.92	8.79
1.91	9.3	9.21	9.1	9.18	9.27	8.53
2.15	10.38	8.64	9.74	10.33	9.91	8.41
2.22	10.56	8.64	10.8	10.72	10.03	8.64
2.46	10.56	9.51	10.9	10.6	10.87	9.5
2.55	11.58	9.87	11.82	10.34	11.43	9.6

Table 3. Impact velocity and resulting simulation crater diameter and depth (in mm) compared to the experimental data by Martineau et al. [2004]. The target was discretized using the Lagrange method.

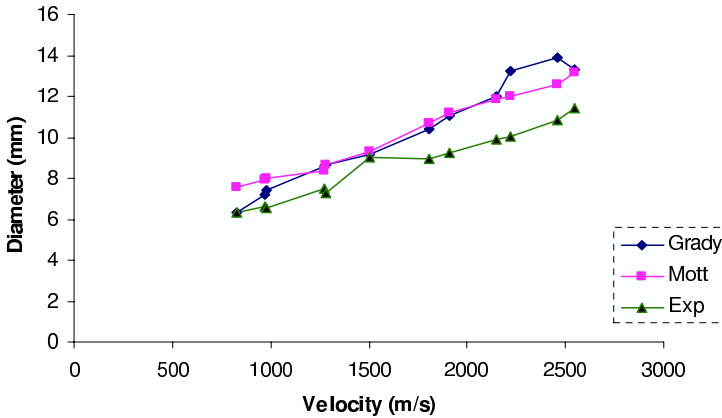


Figure 1. Comparison of crater diameter versus velocity for experimental data and numerical models, using SPH target discretization.

Figure 2 shows that the Mott failure model more closely predicted the DOP at velocities less than 1.5 km/s, but the Grady spall model performed better at velocities greater than 1.5 km/s. However, at the maximum impact velocity of 2.55 km/s, the Grady spall model overpredicted the DOP by 23%, whereas the Mott failure model overpredicted the DOP by 40%; this discrepancy is perhaps due to the fact that the published values were developed for the core of an armor piercing projectile, which is also composed of WC-6% Co, but may possess a different statistical strength, surface finish, and flaw/inclusion distribution than the WC-6% Co sphere utilized in the experiments being studied here. Indeed, more recent experimental efforts utilizing WC-6% Co spheres from a different manufacturer have resulted in the spheres fracturing at lower velocities than the velocities used in this paper [Fountzoulas et al. 2005]. Neither failure model was able to simulate the relative leveling-off of the penetration depth

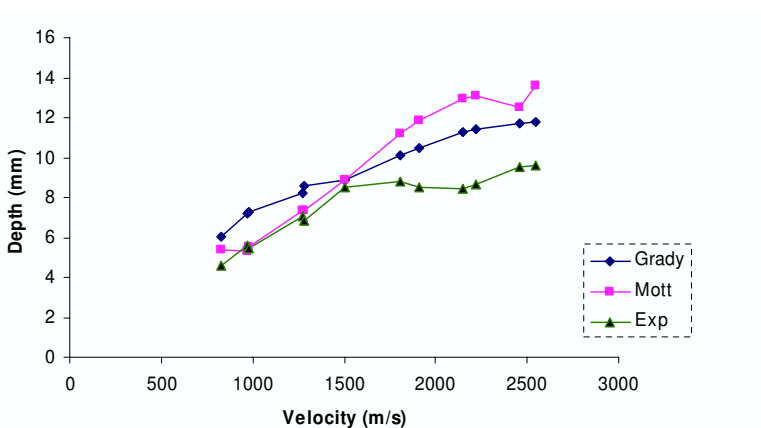


Figure 2. Comparison of crater depth versus velocity for experimental data and numerical models, using SPH target discretization.

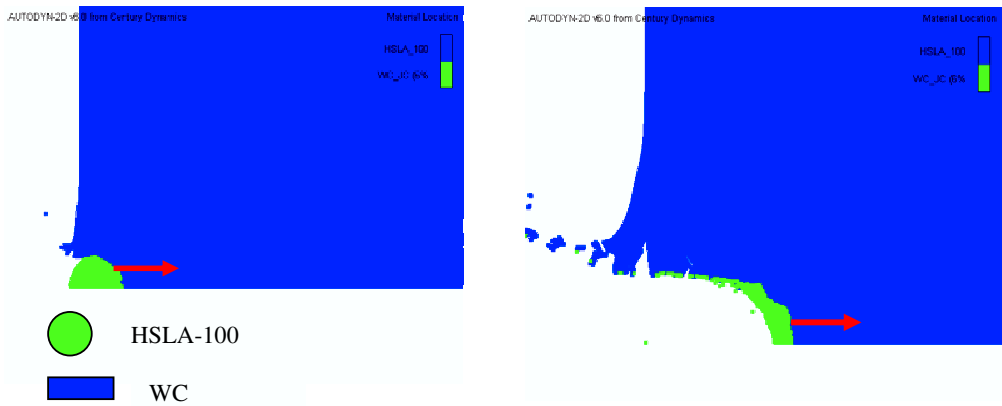


Figure 3. Impact at 830 m/s 22 μ s (left). Impact at 2550 m/s, 22 μ s (right).

between 1500–2250 m/s (Figure 2). Furthermore, this discrepancy may be attributed to the fact that the SPH method is employed mostly for ceramics simulation rather than ductile materials, such as metals.

Figure 3 shows the penetration of the HSLA-100 target at 22 μ s for impact velocities of 830 and 2550 m/s. For the 2550 m/s impact velocity the simulation predicts disintegration of the WC sphere impactor and the region around the crater lip beginning to spall.

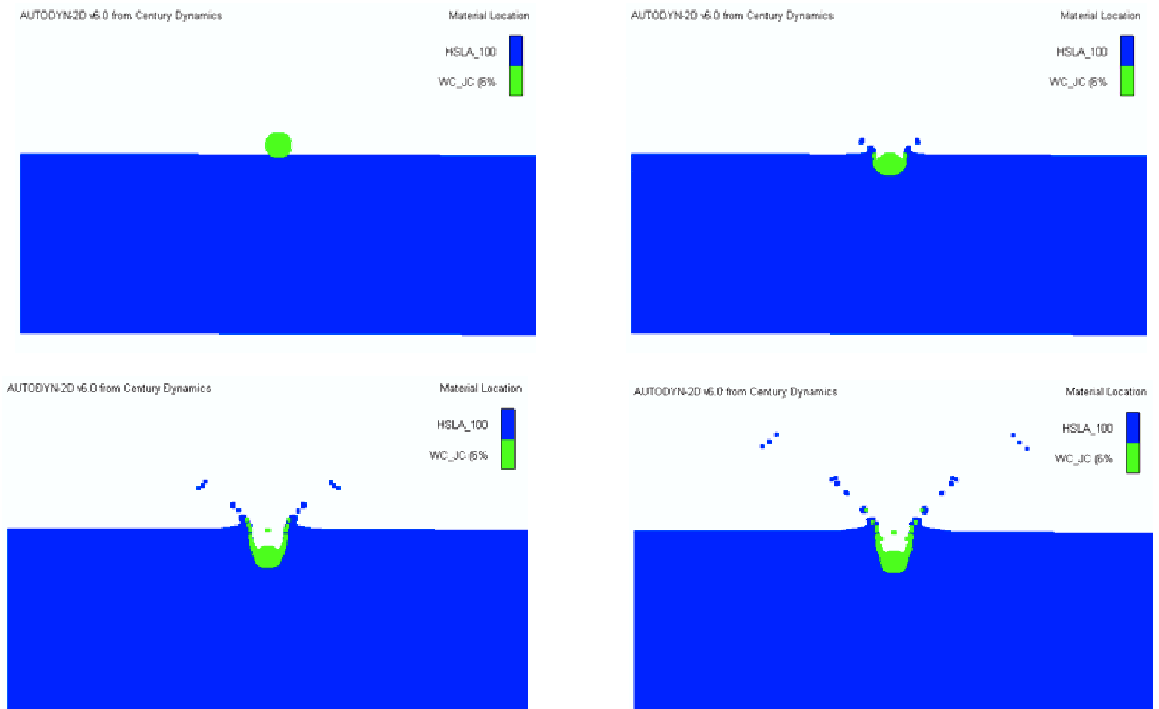


Figure 4. Section of the SPH elements illustrating projectile erosion and target penetration at 0 μ s (upper left), 4 μ s (upper right), 11 μ s (lower left), and 22 μ s (lower right).

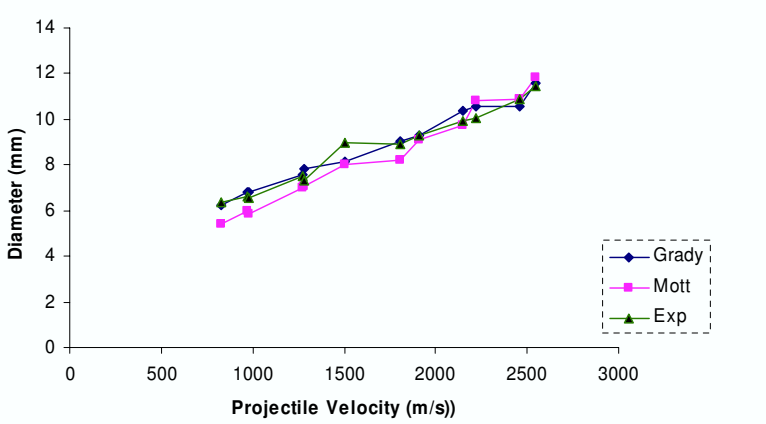


Figure 5. Comparison of crater diameter versus velocity for experimental data and numerical models, using Lagrangian discretization.

Figure 4 illustrates the erosion of the WC projectile and the penetration of the HSLA-100 target, using principal strain with crack softening and stochastic variation as the failure model of the target, for an impact velocity 1810 m/s.

2.2. Lagrangian method. The HSLA-100 target was discretized using the Lagrangian method with 0.5 mm element size. The results of the Lagrangian simulations are summarized in Table 3. As Figure 5 shows, the correlation of the simulation results and the experimental data for the crater diameter is excellent. The correlation of the simulation results and the experimental data for the crater depth is excellent for all velocities using the Grady failure model (Figure 6). However, as also illustrated in Figure 6, the Mott failure model did not result in similar excellent correction for the all impact velocities when compared to the crater diameter simulation results. Although the simulation results overestimate the crater depth for all the impact velocities, they are in reasonable agreement for impact velocities up

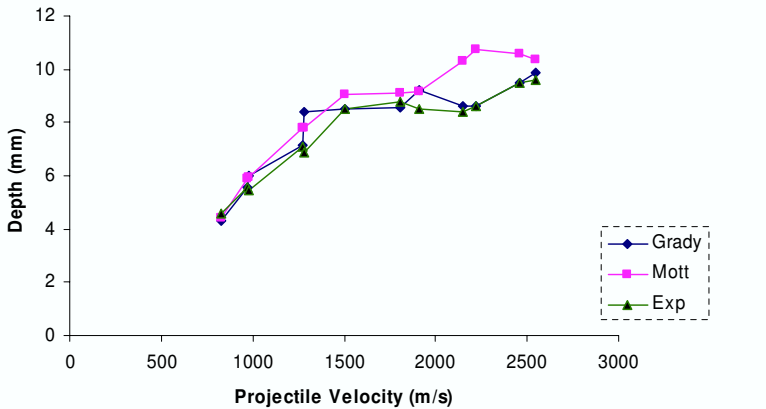


Figure 6. Comparison of crater depth versus velocity for experimental data and numerical models, using Lagrangian discretization.

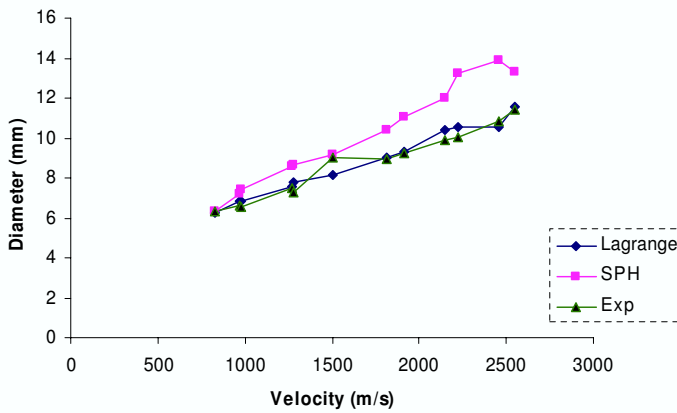


Figure 7. Comparison of experimental data for crater diameter with simulation results using SPH and Lagrangian discretization methods for steel target for Grady failure model for WC projectile

to 1810 m/s. As observed in both Figures 5 and 6, for impact velocities above 1810 m/s the simulation predictions overestimate the crater depth. However, it is worth mentioning that the experimental leveling-off of the penetration depth is followed by the Lagrange simulation method, unlike the SPH method.

The simulation differences between the SPH and Lagrange methods for both failure models of HSLA-100 target Grady criterion and Mott are illustrated in Figures 7–11. The Lagrange element erosion issue was overcome by turning on the *prevent erosion of degenerate cells* and *retain inertia or eroded nodes* option of the AUTODYN commercial software.

Figure 11 shows the erosion of the WC projectile and the penetration of the HSLA-100 target, using principal strain with crack softening and stochastic variation as the failure model of the target, for impact velocity 1810 m/s.

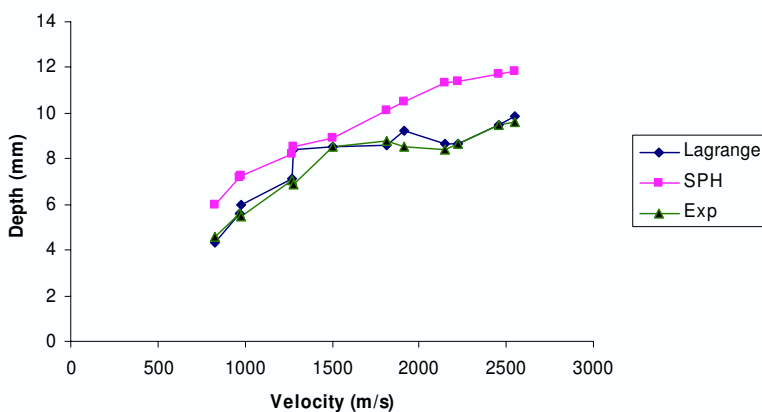


Figure 8. Comparison of experimental data for the crater depth with simulation results using SPH and Lagrangian discretization methods for steel target for Grady failure model for WC projectile.

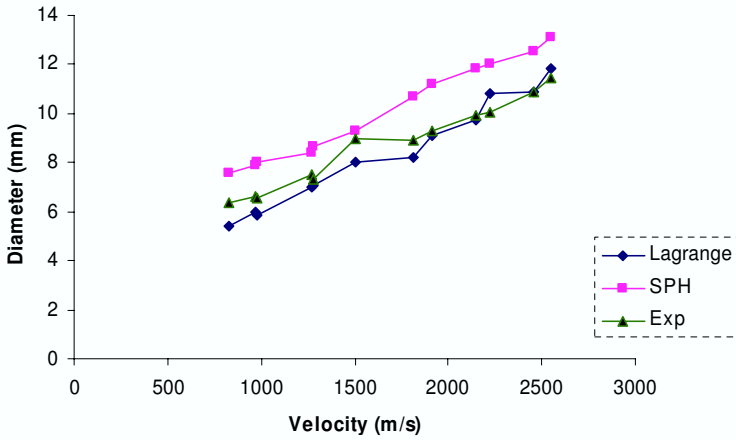


Figure 9. Comparison of experimental data for the crater diameter with simulation results using SPH and Lagrangian discretization methods for steel target for Mott stochastic variation failure model and principal strain for WC projectile.

3. Discussion

The ballistic behavior of an HSLA-100 target impacted by a WC sphere was simulated by discretizing it with two different methods, Lagrange and SPH. The SPH method, although it has been used successfully for ballistic simulation of ceramic materials, did not produce as accurate results as the Lagrangian method. The Grady failure model reproduced the experimental data of the crater diameter and depth more accurately for both the Lagrangian and SPH methods. The Lagrangian method reproduced the experimental data accurately, with the exception of the Mott failure, which showed small deviation from

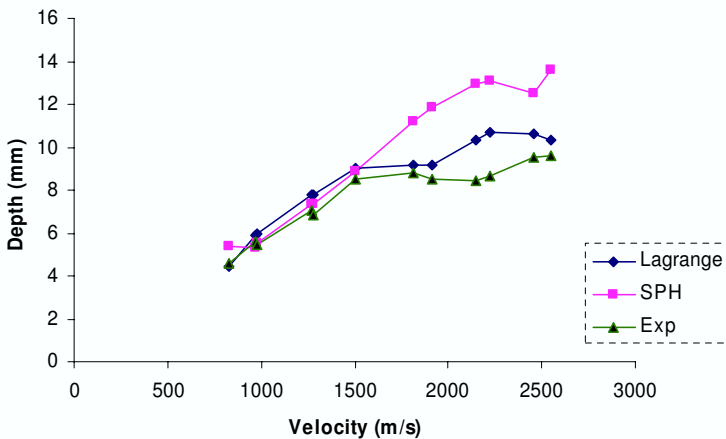


Figure 10. Comparison of experimental data for the crater depth with simulation results using SPH and Lagrangian discretization methods for steel target for Mott stochastic variation failure model and principal strain for WC projectile.

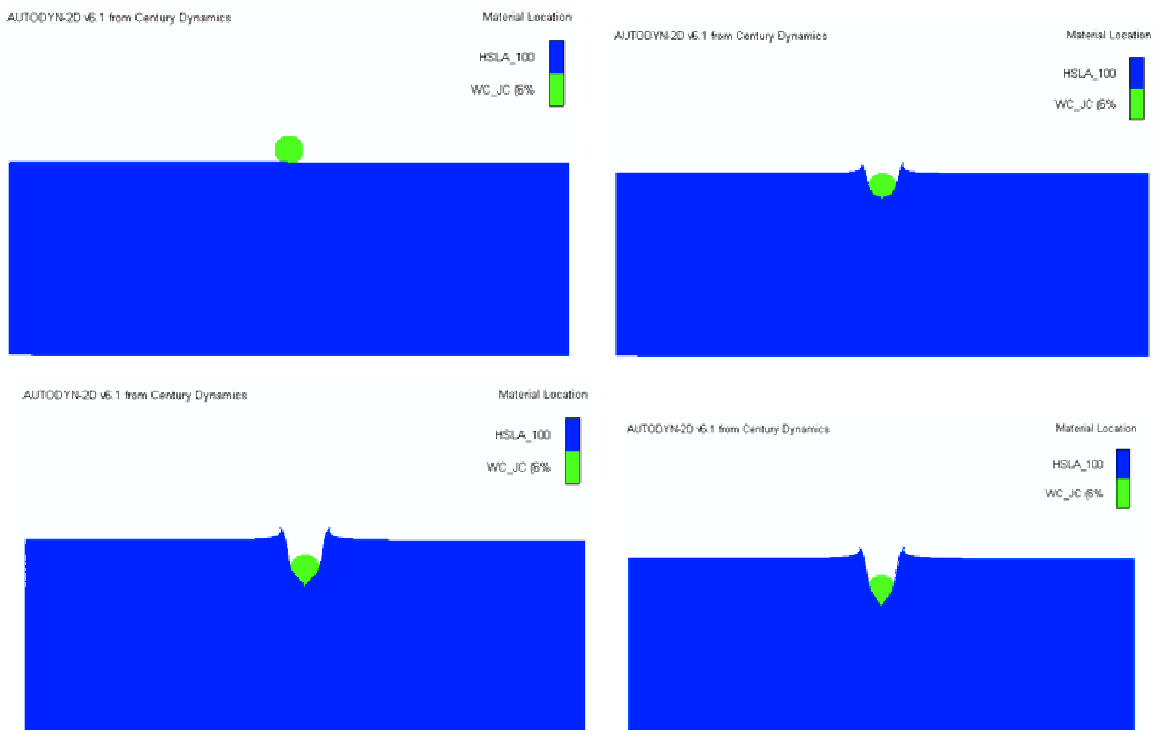


Figure 11. Section of the Lagrange elements illustrating projectile erosion and target penetration at $0 \mu\text{s}$ (upper left), $4 \mu\text{s}$ (upper right), $11 \mu\text{s}$ (lower left), and $22 \mu\text{s}$ (lower right).

the experimental data. To the authors' knowledge, targets meshed by the SPH method exhibit enhanced sensitivity to spall relative to targets meshed with the Lagrange method. The small deviation of the simulated values from the experimental values (Figures 5–10) may be attributed to: (a) an accurate material model for the WC; and (b) the parameters of the constitutive properties of the HSLA-100 target Johnson–Cook (equivalent plastic strain to failure) model were derived from the experimental results of [Chae and Koss \[2004\]](#) through interpolation of their experimental values. However, we believe that the derived constants resulted in a reasonably accurate failure model, and they did not contribute to the disagreement between the simulated and experimental data of the crater diameter and depth. Until the behavior of the tungsten carbide utilized in these sphere impact experiments can be accurately modeled, the current study on the applicability of the existing tungsten carbide strength and failure models to high velocity impact will remain incomplete.

However, a few salient points can be drawn. Although the Lagrangian method predicted the experimental values of the crater diameter and depth more accurately than the SPH method, the SPH method does reproduce accurately the failure of the ductile materials within acceptable statistical error. Precise knowledge of the HSLA-100 yield strength, mainly a function of manufacturing and heat treatment, is a significant factor in accurate simulation. Since the Zerilli–Armstrong strength model is limited by the strain-rate at which the maximum dislocation velocity is reached, prior knowledge of that strain-rate

is of great importance for accurate prediction of the target failure. The simulation results have shown that none of the WC failure models appear well calibrated for impact velocities over the entire range investigated (830 to 2550 m/s). However, the prediction of the leveling-off of the penetration depth is a convincing indication that the Lagrange discretization, in conjunction with the Grady failure model, is the indicated method of predicting the failure of HSLA-100 steel impacted by a tungsten carbide sphere. Finally, [Hanson \[2003\]](#) concludes that the Zerilli–Armstrong constitutive model does not account for the plastic behavior of HSLA-100 steel to better than 10%, and we are not aware of any detailed studies of the dynamic failure behavior of HSLA-100 steel which could, in part, be responsible for the discrepancies between the experimental and computed results reported herein.

4. Conclusion

This paper has illustrated some of the difficulties involved in modeling the complex fragmentation behavior of a tungsten carbide sphere impacting an HSLA-100 plate. The computational investigation tested some existing material and failure models of tungsten carbide and HSLA-100 steel by comparing available published experimental data, such as the depth and diameter of the impact crater, with simulation results. Generally speaking, the Lagrange discretization of the HSLA-100 plate utilizing the Grady failure model predicted the crater depth and diameter accurately. A finer particle size for the SPH method would not have necessarily predicted the experimental data more accurately, since SPH mesh convergence studies have shown that penetration depth is a nonmonotonic function of particle size. The Lagrangian discretization method in conjunction with recent WC strength and WC failure models produced accurate agreement over the entire range of impact velocities investigated. However, previous work [[Fountzoulas et al. 2005](#)] that investigated the ability of existing computational models of WC spheres impacting confined SiC targets also concluded that more accurate WC failure models are needed if we are to make accurate predictions at high impact velocities.

Appendix A

Zerilli–Armstrong model The constitutive equation of this model is based on the dislocation theory mechanics [[Thompson 2006](#)]. This model attempts to better describe material behavior, as well to extrapolate beyond the strain-rates and temperatures seen in experiments.

Their constitutive model consists of a thermal and an a-thermal part, and introduces grain-size dependence.

$$\sigma = \sigma_{\text{thermal}} + \sigma_{\text{athermal}} + kl^{1/2}, \quad (\text{A.1})$$

where

$$\sigma_{\text{thermal}} = B \exp(\beta T). \quad (\text{A.2})$$

The thermal stress is the stress necessary to overcome thermally activated dislocation barriers. Thus, it increases as the strain-rate increases and decreases as the temperature increases. For FCC metals, the thermal activation energy is dependent on dislocation interactions. Since the dislocation density increases as the strain increases, the thermal portion of the stress is dependent on the strain, as well as the strain-rate and temperature.

$$\sigma_{\text{thermal-FCC}} = c_2 \varepsilon^{1/2} \exp(-c_3 T + c_4 T \ln \dot{\varepsilon}) \quad (\text{A.3})$$

$$\sigma_{\text{thermal-BCC}} = c_1 \exp(-c_3 T + c_4 T \ln \dot{\epsilon}) \quad (\text{A.4})$$

The final constitutive equation for BCC metals is shown in Equation (A.5), where σ_0 accounts for the grain size and initial yield strength,

$$\sigma = \sigma_0 + c_1 \epsilon^n + c_1 \exp(-c_3 T + c_4 T \ln \dot{\epsilon}). \quad (\text{A.5})$$

Of note is that the Zerilli–Armstrong equations cannot be used for strain rates at which the maximum dislocation velocity is exceeded. Thus, the limit of extrapolation is the strain-rate at which the maximum dislocation velocity is reached.

A.1 Johnson–Cook failure model Failure accumulation in the Johnson–Cook model does not directly degrade the yield surface [Johnson and Cook 1985; Kay 2003]. The model defines the strain at fracture as

$$\epsilon_{\text{failure}} = [D_1 + D_2 \exp(D_3 \sigma^*)][1 + D_4 \ln(\dot{\epsilon}^*)][1 - T_5^*], \quad (\text{A.6})$$

where σ^* is the ratio of the pressure to the effective stress, that is,

$$\sigma^* = \text{Pressure}/\sigma_{\text{eff}}. \quad (\text{A.7})$$

Fracture occurs in the Johnson–Cook model when the damage parameter D exceeds 1.0. The evolution of D is given by the accumulated incremental effective plastic strains divided by the current strain at fracture as

$$D = \Sigma \epsilon_{\text{eff}}^P / \epsilon_{\text{failure}}. \quad (\text{A.8})$$

During the calculation, element stresses are all set to zero, and remain equal to zero when the fracture criteria is evoked for a specific element.

The first set of brackets in the Johnson–Cook fracture model are intended to represent the observation that the strain to fracture decreases as the hydrostatic tension increases. The second set of brackets in the strain to failure expression represent the effect of an increased strain rate on the material ductility, while the third set of brackets represent the effect of thermal softening on the material ductility.

A.2 The Grady spall criterion An estimate of the critical spall stress of a ductile material can be made using the following formula due to Grady,

$$S = (2\rho c^2 Y \epsilon_f)^{1/2}, \quad (\text{A.9})$$

where ρ is the density, c the bulk sound speed, Y the yield stress, and ϵ_f is a critical strain failure usually set to 0.15 [AUTODYN 2004; Grady and Kipp 1997].

This spall stress is calculated for each cell at each cycle, thus including the local conditions in the cell. The calculated spall stress is used as the local maximum principal stress failure criterion in the cell.

A.3 Stochastic failure The materials have inherent microscopic flaws, and these flaws are where the failure and cracking initiate. An approach to reproducing this numerically is to randomize the failure stress/strain for the material [Johnson and Cook 1985]. Therefore, each cell in the numerical model will

have a different failure strain, thus creating weak spots in the material. A Mott distribution is used to define the variance in failure stress/strain, as defined by

$$P = 1 - \exp[-(C/\gamma)e^{\gamma\epsilon}], \quad (\text{A.10})$$

where P is the probability of fracture; and C and γ are constants. The constant C is calculated at failure stress/strain probability equal to 0.5, and γ is defined by the user. The distribution type of P is defined by the value of γ ; it can be either fixed, the same each type a part is filled, or random. The Mott distribution can be applied to most failure models.

Acknowledgement

The authors wish to express their wholehearted gratitude to the reviewers whose productive criticism and suggestions made this paper better and more complete.

References

- [AUTODYN 2004] ANSYS, Inc., *AUTODYN theory manual*, Southpointe 275 Technology Drive Canonsburg, PA: ANSYS, Inc., 2004.
- [Burkins 2003] M. Burkins, "An evaluation of 14.5 mm AP surrogate projectiles", Presented at the Ground Vehicle Survivability Symposium, 2003.
- [Chae and Koss 2004] D. Chae and D. A. Koss, "[Damage accumulation and failure of HSLA-100 steel](#)", *Mater. Sci. Eng.* **366**:2 (2004), 299–309.
- [Czyryca et al. 2003] E. J. Czyryca, D. P. Kihl, and R. DeNale, "[Meeting the challenge of higher strength, lighter warships](#)", *Amptiac Q.* **7**:3 (2003), 63–70.
- [Fountzoulas et al. 2005] C. G. Fountzoulas, M. J. Normandia, J. C. LaSalvia, and B. A. Cheeseman, "Numerical simulations of silicon carbide tiles impacted by tungsten carbide spheres", 22nd International Symposium on Ballistics, 14–18 November 2005.
- [Grady 1999] D. E. Grady, "[Impact failure and fragmentation properties of tungsten carbide](#)", *Int. J. Impact Eng.* **23**:1 (1999), 307–317.
- [Grady and Kipp 1997] D. E. Grady and M. E. Kipp, "[Fragmentation properties of metals](#)", *Int. J. Impact Eng.* **20**:1-5 (1997), 293–308.
- [Hanson 2003] K. Hanson, "[Inference of material-model parameters from experimental data](#)", LANL, 12 May 2003, Available at <http://www.lanl.gov/home/kmh>.
- [Holmquist et al. 2005] T. J. Holmquist, G. R. Johnson, and W. A. Gooch, "Modeling the 14.5 mm BS41 projectile for ballistic impact computations", Presented at the 2nd International Conference on Computational Ballistics, 18–20 May 2005.
- [Johnson and Cook 1985] G. R. Johnson and W. H. Cook, "[Fracture characteristics of three metals subjected to various strains, strain rates, temperatures and pressures](#)", *Eng. Fract. Mech.* **21**:1 (1985), 31–48.
- [Kay 2003] G. Kay, "Failure modeling of Titanium 6Al-4V and aluminum 2024-T3 with the Johnson-Cook material model", Technical report, Washington, DC, 2003. DOT/FAA/AR-03/57.
- [Martineau et al. 2004] R. L. Martineau, M. B. Prime, and T. Duffey, "[Penetration of HSLA-100 steel with tungsten carbide spheres at striking velocities between 0.8 and 2.5 km/s](#)", *Int. J. Impact Eng.* **30**:5 (2004), 505–520.
- [Mott 1947] N. F. Mott, "Fragmentation of shell cases", pp. 300–308 in *Proceedings of the Royal Society of London*, vol. 189, Series A, Mathematical and Physical Sciences **1018**, 1947.
- [Normandia 2004] M. J. Normandia, "[Impact response and analysis of several silicon carbides](#)", *Int. J. Appl. Ceram. Technol.* **1**:3 (2004), 226–234.

- [Shockey et al. 1990] D. A. Shockey, A. H. Marchand, S. R. Skaggs, G. E. Cort, M. W. Burkett, and R. Parker, “[Failure phenomenology of confined ceramic targets and impacting rods](#)”, *Int. J. Impact Eng.* **9**:3 (1990), 263–275.
- [Thompson 2006] A. C. Thompson, “High strain rate characterization of advanced high strength steels”, MS Thesis, University of Waterloo, Waterloo, Ontario, Canada, 2006.
- [Wilkins et al. 1969] M. L. Wilkins, C. F. Cline, and C. A. Honodel, “Light Armor”, Technical report UCRL-71817, Lawrence Radiation Laboratory, Livermore, CA, July 23 1969.
- [Williams 1995] A. E. Williams, “[The effect of phase changes on target response](#)”, *Int. J. Impact Eng.* **17**:4-6 (1995), 937–947.

Received 27 Jun 2007. Accepted 21 Aug 2007.

COSTAS G. FOUNTZOULAS: cfount@arl.army.mil

U.S. Army Research Laboratory, Weapons and Materials Directorate, 2800 Powder Mill Rd, Adelphi, MD 20783-1197, United States

GEORGE A. GAZONAS: gazonas@arl.army.mil

U.S. Army Research Laboratory, Weapons and Materials Directorate, 2800 Powder Mill Rd, Adelphi, MD 20783-1197, United States

BRYAN A. CHEESEMAN: bcheesem@arl.army.mil

U.S. Army Research Laboratory, Weapons and Materials Directorate, 2800 Powder Mill Rd, Adelphi, MD 20783-1197, United States

DEFORMATION AND FRACTURE MODES OF SANDWICH STRUCTURES SUBJECTED TO UNDERWATER IMPULSIVE LOADS

L. F. MORI, S. LEE, Z. Y. XUE, A. VAZIRI, D. T. QUEHEILLALT,
K. P. DHARMASENA, H. N. G. WADLEY, J. W. HUTCHINSON AND H. D. ESPINOSA

Sandwich panel structures with thin front faces and low relative density cores offer significant impulse mitigation possibilities provided panel fracture is avoided. Here steel square honeycomb and pyramidal truss core sandwich panels with core relative densities of 4% were made from a ductile stainless steel and tested under impulsive loads simulating underwater blasts. Fluid-structure interaction experiments were performed to (i) demonstrate the benefits of sandwich structures with respect to solid plates of equal weight per unit area, (ii) identify failure modes of such structures, and (iii) assess the accuracy of finite element models for simulating the dynamic structural response. Both sandwich structures showed a 30% reduction in the maximum panel deflection compared with a monolithic plate of identical mass per unit area. The failure modes consisted of core crushing, core node imprinting/punch through/tearing and stretching of the front face sheet for the pyramidal truss core panels. Finite element analyses, based on an orthotropic homogenized constitutive model, predict the overall structural response and in particular the maximum panel displacement.

1. Introduction

Structures that combine high stiffness, strength, and mechanical energy absorption with low weight, are widely used in a variety of aerospace, automotive, and Naval applications. Metallic sandwich panels with various light weight core topologies have attracted significant interest for shock mitigation in general and the mitigation of underwater propagated shocks in particular.

As a first step toward understanding the mechanical behavior of these types of sandwich structures, [Chiras et al. \[2002\]](#) and [Rathbun et al. \[2004\]](#) conducted quasistatic experiments and numerical simulations of the compressive and shear response of truss core panels with a tetragonal lattice topology. These studies identified an asymmetric structural response between compression loaded trusses collapsing by buckling and those placed in tension failing by fracture (usually near nodes). [Rathbun et al. \[2004\]](#) measured the behavior of tetrahedral truss sandwich panels in shear and bending. [Deshpande and Fleck \[2001\]](#) measured the collapse responses of truss core sandwich beams in 3-point bending and obtained upper bound expressions for the collapse loads. [Wallach and Gibson \[2001b\]](#) analyzed the elastic moduli and the uniaxial and shear strengths of a three-dimensional truss geometry. Other studies have addressed the role of structural core defects [[Wallach and Gibson 2001a](#)]. These studies were then used to motivate optimal design [[Wicks and Hutchinson 2001](#); [Rathbun et al. 2005](#)] and to develop continuum constitutive models [[Xue and Hutchinson 2004b](#)]. Their compressive behavior has been measured by many groups and summarized and compared with honeycombs in [[Wadley 2006](#)].

Keywords: fluid-structure interaction, sandwich structures, dynamic plasticity.

The dynamic behavior of cores used in sandwich structures has also been extensively investigated. [Vaughn et al. \[2005\]](#) and [Vaughn and Hutchinson \[2006\]](#) performed numerical simulations of truss cores and quantified the effect of microinertia on load carrying capacity. [Lee et al. \[2006\]](#) analyzed the dynamic compressive behavior of pyramidal truss cores and showed that the material strain rate hardening and microinertia effects make significant contributions to the total energy absorbed by a core. A transition in failure mode with deformation rate was experimentally identified and numerically analyzed. The role of deformation rate on the crushing response of square honeycomb cores has been addressed theoretically by [Xue and Hutchinson \[2005\]](#) and for both folded plate and pyramidal truss cores by [Vaziri and Xue \[2007\]](#).

Extensive investigations of the fluid structure interaction (FSI) associated with shock impingement on a plate in both air and water were also pursued. The eventual application of these concepts will require full scale computational simulations. However, much computational power is required to conduct a complete fully core-gridded finite element analysis. Homogenized constitutive models are therefore being developed and implemented in finite element frameworks. [Xue and Hutchinson \[2003; 2004a\]](#) modeled circular truss cores sandwich plates subjected to uniformly distributed impulses with finite elements. The study extended the classical work of [Taylor \[1963\]](#) relating the far-field momentum to the momentum imparted to plates. The simulation results were then compared to those of solid plates made of the same material and having the same weight per unit area. They concluded a well-designed sandwich plate can sustain significantly larger impulses for a given maximum deflection. Moreover the analysis showed that, if the blast is under water, the fluid-structure interaction reduces the momentum transmitted to the sandwich plate by as much as a factor of two. Indeed, the fluid-structure interaction is predicted to enhance the performance of sandwich plates relative to solid plates under intense shocks even in air, in which the effects are thought not to be as significant as for water borne shocks [[Vaziri and Hutchinson 2007](#)].

[Xue et al. \[2005\]](#) proposed a homogenized constitutive model that incorporates rate-dependence arising from material rate-dependence and microinertial effects. The model was used with finite elements to represent the behavior of square honeycomb sandwich plates [[Xue et al. 2005](#)], folded plate and pyramidal truss cores [[Vaziri and Xue 2007](#)], and hexagonal honeycomb cores [[Mohr et al. 2006](#)] subjected to quasistatic and dynamic loads. [Rabczuk et al. \[2004\]](#) developed a homogenization method for sandwich structures using a quasicontinuum approach that takes into account buckling of the core; this model shows good agreement with fully discretized models for shell interlaced cores. [Qiu et al. \[2004; 2005a\]](#) developed an analytical model for the deformation response of clamped circular sandwich plates subjected to shock loading in air and in water. This model was verified using finite elements in [[Qiu et al. 2003](#)] and then used to define a systematic design procedure [[Fleck and Deshpande 2004a](#)].

[Liang et al. \[2007\]](#) used an analytic model based on the relative time scales for core crushing and water cavitation to evaluate the mechanical performance of different core topologies. The work highlighted the importance of core crushing strength for exploiting the benefits of fluid-structure interaction. [Xue and Hutchinson \[2005\]](#) developed a continuum model for high-rate deformation of square honeycomb cores and demonstrated that this is an effective core for sandwich plates because it combines excellent crushing strength and energy absorption with good out-of-plane stiffness and strength and in-plane stretching resistance. They also [[Xue and Hutchinson 2004a](#); [Hutchinson and Xue 2005](#)] extended the work by [Fleck and Deshpande \[Fleck and Deshpande 2004b; Deshpande and Fleck 2005\]](#) and addressed the

problem of the minimum weight design of square honeycomb plates of given span that must sustain a uniformly distributed impulse. They argued that optimally designed sandwich plates could sustain water shocks that were two to three times larger than monolithic plates of the same mass and material. Further studies [Vaziri et al. 2007] investigated fracture modes of square honeycomb sandwich plates showing that the primary fracture modes are necking and subsequent tearing of the face sheets and webs, and shear delamination of the core webs from the faces. Vaziri et al. [2006] showed that there is no considerable advantage or disadvantage in filling the core interstices by low-density polymeric foams for structural purposes. Therefore, it is possible to exploit the multifunctional advantages offered by polymeric foam-filled cores, such as acoustic and thermal insulation, with only a minor weight penalty.

While all these analytical and computational models have been developed, experimental analysis of the structural behavior under blast loading is still limited. Radford et al. [2005] used Al foam projectiles fired from a gas gun at high velocities against stainless steel square honeycomb core sandwich panels. Although this technique produces pressure pulses representative of shock interactions caused by explosions [Radford et al. 2005; Qiu et al. 2005b; Rathbun et al. 2006], it cannot simulate the fluid-structure interaction (FSI), which is especially relevant for underwater explosions [Vaziri and Hutchinson 2007]. Hutchinson and Xue [2005], Liang et al. [2007] and Tilbrook et al. [2006] showed that much of the advantage of sandwich plates over solid plates subjected to underwater blast comes from the FSI and that optimal designs are highly dependant on the details of this interaction. Wave propagation in water and associated cavitation phenomena, which play an important role in FSI, make analytical and numerical modeling quite complex. Thus it is necessary to perform realistic FSI experiments to validate, calibrate, and develop models that take them into account. Wadley and his collaborators have investigated the structural response of lattice cores to shock loading in water and air [Dharmasena et al. 2007a; 2007b; Wadley et al. 2007a; 2007b]. The experiments confirm very significant reductions in the transmitted shock pressure and reduced panel deflections.

In this paper, a recently developed water shock tube technique similar to the one developed by Deshpande et al. [2006] is used to measure the dynamic structural response under a realistic, although scaled, fluid-structure interaction with a water borne shock [Espinosa et al. 2006]. Using this experimental setup, the dynamic performance of sandwich panels with honeycomb and pyramidal core topologies is compared with that of solid plates made of the same material under the same boundary conditions. Liang et al. [2007] introduced several performance metrics: the back-face deflection, the tearing susceptibility of the faces, and the loads transmitted to the supports. In this article, the performance of the different structures is compared in terms of the dynamic back-face deflection and the panel fracture modes. After describing the experimental technique and the design of the specimens, the experimental results for each kind of structure are presented; failure mechanisms in the sandwich panels are identified by exploring not only the maximum deflection but also the deformation history and the presence of fracture on the face sheets after the test. The experimental investigation is complemented by numerical simulations using a detailed computation model of the experimental setup. The model includes separate components representing the water column, tube, piston and sandwich plates, as will be described later. The core materials were modelled using a constitutive model, developed by Xue et al. [2005], for plastically orthotropic materials which allows for modelling nonuniform hardening and softening behavior in stressing in different directions. The validity of this constitutive model for simulating and predicting the structural response of sandwich plates underwater blast loading has been investigated by comparing the

experimental measurements and simulation predictions. The developed model was used to gain insight into the mechanism of deformation and the mechanics of sandwich plates subjected to underwater shock loading.

2. Methods

2.1. Experimental approach. A novel experimental methodology incorporating fluid-structure interaction (FSI) effects was recently developed [Lee 2005; Espinosa et al. 2006]. The set-up is a highly instrumented scaled model designed to characterize the underwater blast impulsive loading of structures and to identify their failure by means of real time measurements of deflection profiles, deformation histories, and fracture. In the FSI setup, a water chamber made of a steel tube is incorporated into a gas gun apparatus (Figure 1). A scaled structure is fixed at one end of the steel tube and a water piston seals the other end. A flyer plate impacts the water piston and produces an exponentially-decaying pressure history in lieu of blast loading caused by explosive detonation. The pressure induced by the flyer plate propagates and imposes an impulse to the structure (panel specimen), whose response elicits water cavitation. The performance of the set-up was assessed by conducting calibration experiments and by subjecting solid stainless steel panels to impulsive water loading. Pressure sensors were employed to record pressure histories. The experimental measurements confirmed that the FSI setup can generate an exponentially decaying pressure history. Shadow moiré and high speed photography were also used to record in real time the full field out-of-plane deformation profile of the solid panel [Lee 2005; Espinosa et al. 2006].

In this investigation the same setup has been employed. Stainless steel panel structures with square honeycomb and pyramidal truss cores were subjected to water borne shocks and assessed against monolithic plates using a maximum panel deflection metric. The mass per unit area of the sandwich structures is determined by the face sheet thickness and the core density. The tested sandwich panels had a relative density of 4% (see Table 1).

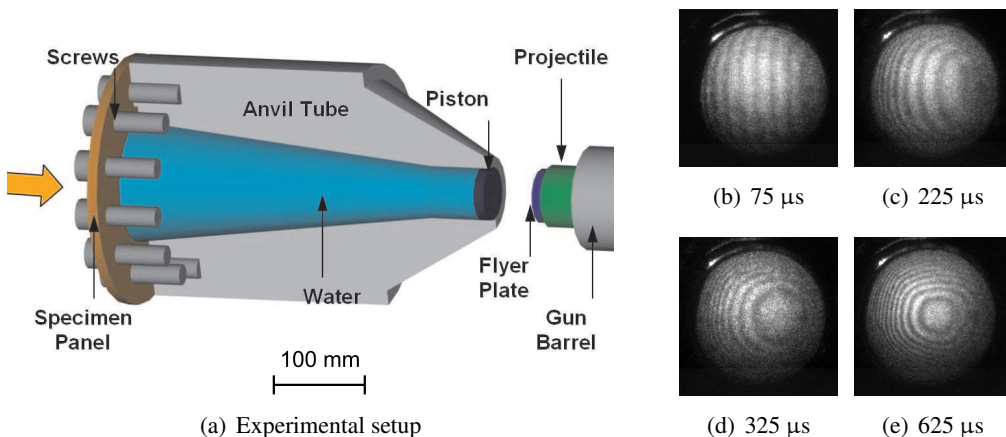


Figure 1. (a) Configuration of fluid-structure interaction (FSI) experimental setup. (b)–(e) Sequence of high-speed images obtained by shadow moiré.

Structure type	Core relative density	Mass per unit area, kg/m ²	Thickness, mm
Monolithic plate	100%	14.55	1.85
Square honeycomb sandwich	4.0%	14.00	13.97
Pyramidal truss sandwich	4.5%	13.78	12.75

Table 1. Properties of the edge clamped test specimens.

For each experiment, three loading parameters are of interest: the water pressure just ahead of the specimen panel, p_0 , the characteristic decay time, t_0 , and the far-field applied impulse, I_0 . The incident transient load can be idealized as an exponentially decaying pressure given by:

$$p = p_0 \cdot e^{-t/t_0},$$

where p_0 is the peak water pressure measured in water just in front of the specimen panel and t_0 is a characteristic decay time [Smith and Hetherington 1994]. In the FSI setup, the peak pressure is governed by the projectile impact velocity, the acoustic impedance of the piston and the fluid, and by the experimental geometry (see Figure 1):

$$p_0 = V_0 \cdot \left(\frac{D_i}{D} \right)^2 \cdot \frac{s \cdot f}{s + f}, \tag{1}$$

where V_0 is the impact velocity, f and s are the acoustic impedances of the fluid and of the solid respectively, and D and D_i are the diameters of the water tube at the specimen and impact locations, respectively. Equation (1) has been derived using wave propagation theory with the assumption of linearity for the water equation of state [Espinosa et al. 2006]. Likewise, the time constant t_0 is obtained from evolving the nondimensional pressure profile in time:

$$\frac{p}{p_0} = e^{-t_n/t_0} = \left[\frac{s - f}{s + f} \right]^n, \quad n = 0, 1, 2, \dots$$

In this equation, n is the number of wave reverberations in the flyer plate and t_n is the corresponding elapsed time. The far-field impulse I_0 per unit area is given by

$$I_0 = \sum_{n=0}^{\infty} p_0 \left[\frac{s - f}{s + f} \right]^n \Delta t \approx p_0 \cdot t_0,$$

where Δt is the time required for the elastic longitudinal wave to twice traverse the flyer plate [Espinosa et al. 2006].

To compare structures with different core geometries and materials, it is useful to employ the nondimensional impulse defined by Xue and Hutchinson [2004a] as

$$\hat{I} = \frac{I_0}{\bar{M} \cdot \sqrt{\sigma_y/\rho}},$$

where I_0 is the impulse per unit area previously defined, \bar{M} the panel mass per unit area, σ_y the uniaxial tensile yield stress, and ρ the density of the specimen material.

Quantity	Symbol	Unit	Value
Young's modulus	E	GPa	200
Poisson's ratio	ν	–	0.3
Density	ρ_0	kg/m ³	7900
Melting temperature	T_{melt}	K	1673
Room temperature	T_{room}	K	293
Specific heat capacity	c	J/(kg · K)	440
Coefficient of thermal expansion	α	μm/(m · K)	17.3
Fitting parameter A	A	MPa	310
Fitting parameter B	B	MPa	1000
Fitting parameter n	n	–	0.65
Fitting parameter c	c	–	0.07
Fitting parameter $\dot{\epsilon}_0$	$\dot{\epsilon}_0$	s ⁻¹	1.00
Fitting parameter m	m	–	1.00

Table 2. Material properties and Johnson–Cook parameters for AISI 304 stainless steel used in the numerical analyses.

3. Experimental results

3.1. Honeycomb panels.

3.1.1. Specimen geometry. The square honeycomb sandwich panels were fabricated from 304 stainless steel alloy, with an approximate composition of 67Fe-10Ni-20Cr-2Mn-1Si (wt%). The material properties for AISI 304 stainless steel are reported in Table 2. A slotted metal sheet assembly approach was used for fabrication [Wadley et al. 2003; Cote et al. 2004; Zok et al. 2004a; Wadley 2006]. Figure 2 schematically illustrates the fabrication sequence. First, a two dimensional profile was generated with a laser on a sheet metal strip incorporating the slots needed for the interlocking strip assembly and with allowances for bending the top and bottom flanges. The flanges were then bent at 90° to the core web. Finally, the core was assembled by slip fitting the laser cut and bent strips to form a square grid pattern. The core consisted of an assembly of 0.254 mm thick strips spaced 12.7 mm apart to form a 23 cell × 23 cell square grid (300 mm × 300 mm). A vacuum brazing method was used to bond 0.635 mm thick 304 stainless steel face sheets to the core to form the sandwich structure. The assemblies were vacuum brazed at an initial base pressure of ~ 13 mPa. They were heated at 10 °C/min to 550 °C, held for 1 h (to volatilize the binder), then heated to the brazing temperature of 1050 °C, where they were held for 60 min at this temperature before furnace cooling at ~ 25 °C/min to ambient. A braze alloy with a nominal composition of Ni-22.0Cr-6.0Si, wt.% (Nicrobraz[®] 31) was applied by spraying one side of the face sheet with a mixture of the braze powder and a polymer binder (Nicrobraz[®] 520 cement) which were both supplied by Wall Colmonoy (Madison Heights, WI).

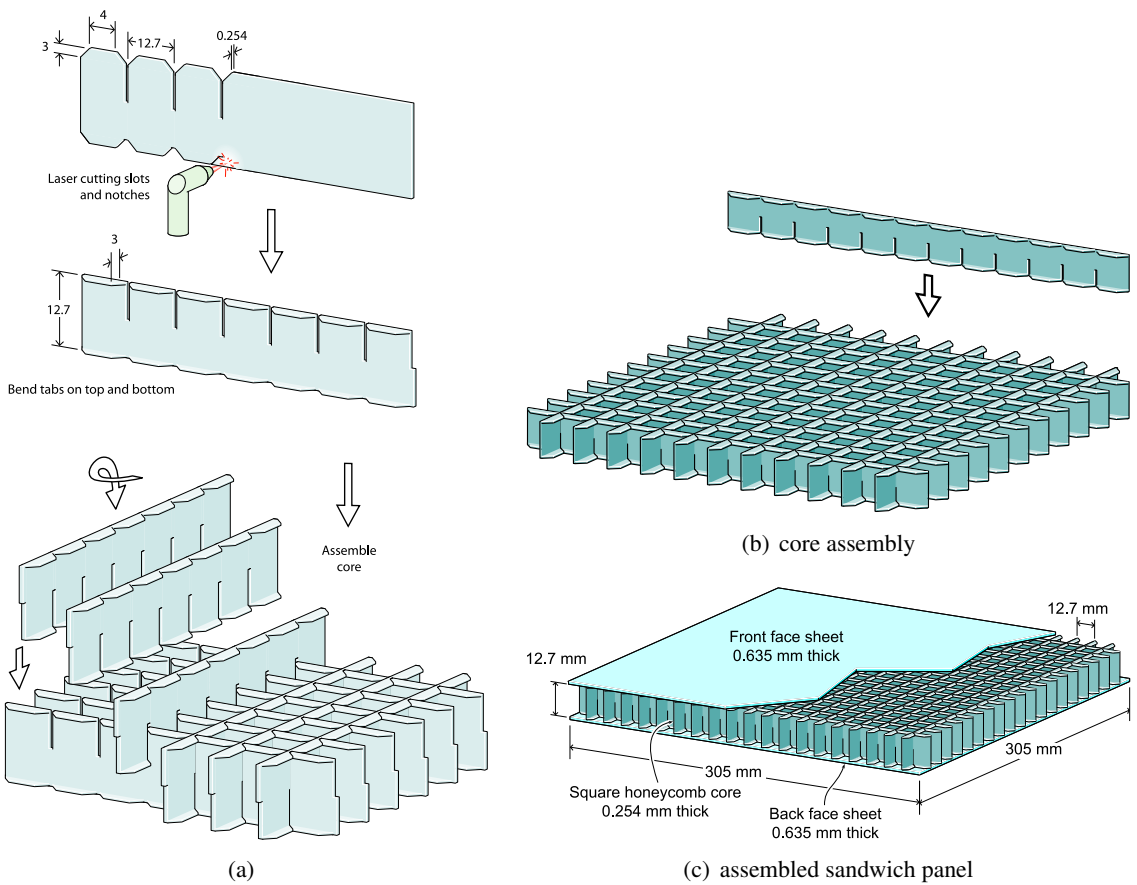


Figure 2. Fabrication of the square honeycomb sandwich panel by a transient liquid phase bonding process. All dimensions are in millimeters.

The panels were then machined to round specimens 305 mm in diameter (see Figure 3). The total thickness of the sandwich panels was 13.97 mm and the relative density of the core ρ_{cr} was 4%; the mass per unit area of the sandwich panels was 14.0 kg/m^2 . To clamp the panels in the periphery, 12 through holes were machined and ring spacers were inserted to prevent core crushing during the clamping process. The specimens were clamped using a steel ring and 12 high strength screws.

Three experiments were conducted on the panels with projectile impact velocities between 175 m/s and 314 m/s. The results are summarized in Table 3. Details for the case with impact velocity of 272 m/s are given next.

3.1.2. Test results: case with impact velocity of 272 m/s. The peak pressure p_0 was 70.6 MPa; the characteristic decay time t_0 was $25.8 \mu\text{s}$; the corresponding applied impulse I_0 was $30.16 \text{ N} \cdot \text{s}$ and the nondimensional applied impulse \hat{I} was 1.234. The maximum deflection measured by shadow moiré, δ_{\max} , was 29.62 mm and, thus, the nondimensional maximum deflection δ_{\max}/L was 0.389. The final strain of the core in the middle of the sample was $\varepsilon_f = 26.8\%$.

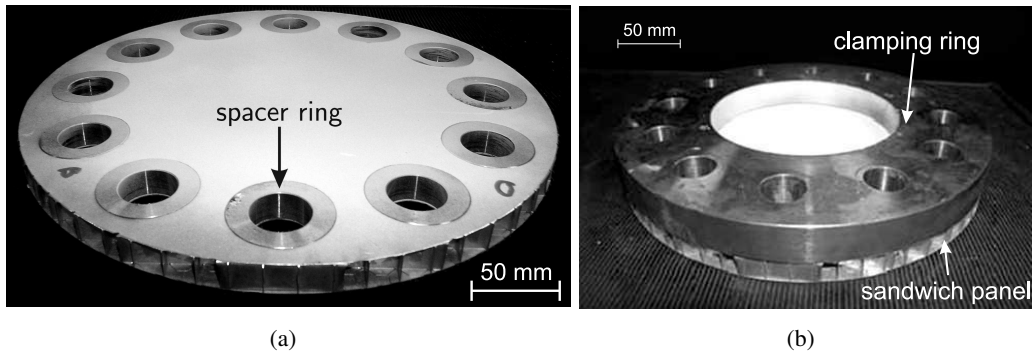


Figure 3. AISI 304 stainless steel panel with square honeycomb core. (a) Solid-ring spacers were employed to prevent core crushing while fastening the clamping ring. (b) A steel ring was employed to clamp the sandwich panel to the anvil tube with 12 screws. The test panel shown above is 305 mm in diameter and 13.97 mm thick.

Figure 4 shows the shadow moiré images between 25 μ s and 625 μ s after the wave front reached the specimen. The deflection along the diameter of the specimen obtained by processing the shadow moiré fringe patterns at different time instances is given in Figure 4i. Although no direct measurement of the back face velocity was performed, it is possible to compute an average velocity from the recorded history of the panel center position.

Figure 5 shows images of the honeycomb sandwich panel after the test. Square-grid imprints on both face sheets (see Figure 5a, b) are observed. The imprints on the face sheets are the result of the high crushing strength of the square honeycomb core. As discussed later, this phenomenon is characteristic of all the sandwich structures with a strong core. As observed in previous studies [Espinosa et al. 2006], the FSI configuration employing bolts to achieve a clamped boundary condition allows some in-plane

Structure type	Monolithic plate	Sandwich square honeycomb core			Sandwich pyramidal truss core
Impact velocity, V_0 , m/s	315	175	272	314	307
Flyer plate thickness, t_f , mm	4.75	4.76	4.83	4.83	4.83
Water pressure, p_0 , MPa	81.7	45.3	70.6	81.5	79.7
Characteristic decay time, t_0 , μ s	25.3	25.4	25.8	25.8	25.8
Final core strain, ϵ_f	—	1.7%	26.8%	7.1%	11.3%
Dimensionless applied impulse, \hat{I}	0.882	0.939*	1.234*	0.931	0.925
Dimensionless maximum deflection, δ_{max}/L	0.391	0.297	0.389	0.299	0.299
Normalized maximum deflection, $(\delta_{max}/L)_N$	0.391	0.279	0.278	0.283	0.285
Improvement	—	29%	29%	28%	27%
Damage on the face sheets	no damage		imprints		punctures/cracks

Table 3. Performances of blast-resistant structures with fixed boundary condition.

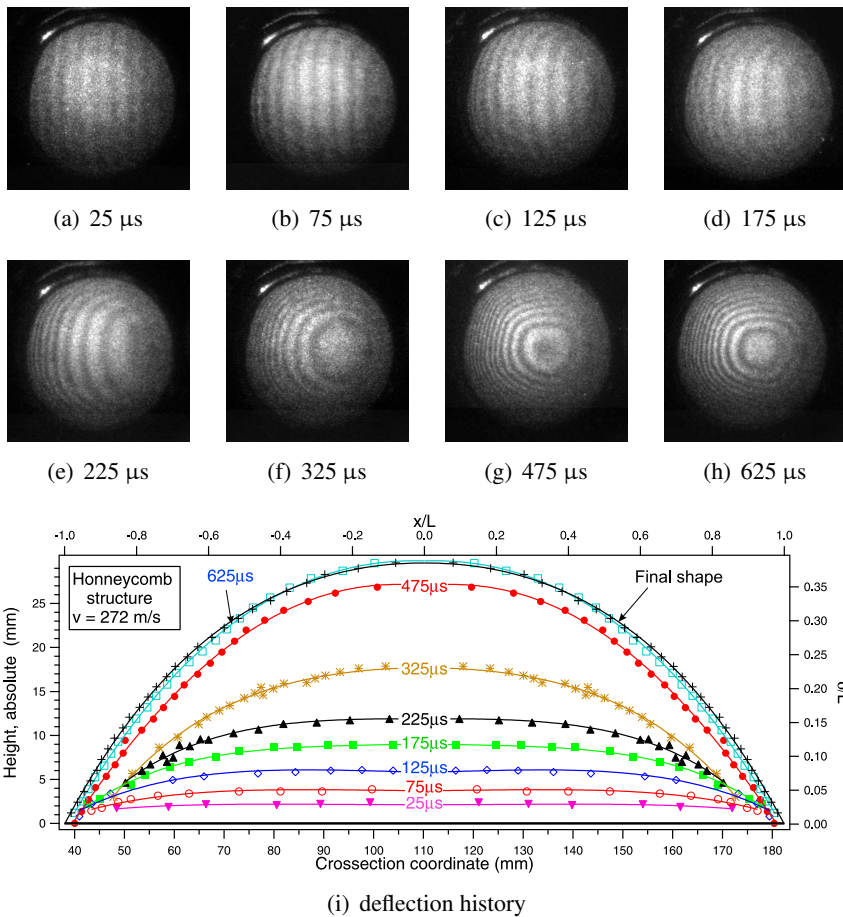


Figure 4. (a)–(h) High-speed camera images showing shadow moiré fringes for the AISI 304 stainless steel panel with square honeycomb core at different time intervals, and (i) deflection along the diameter of the specimen plate measured by shadow moiré. $t = 0 \mu\text{s}$ corresponds to the arrival of the shock at the specimen location.

deformation of the sample at the boundary. Evidence of slippage and hole ovalization is reported in Figure 5d.

3.1.3. Test results: comparison of the three experiments. The three experiments that were conducted on the square honeycomb sandwich plates differ both in the speed of the projectile and on the geometry of the projectile. The external wall of the PMMA flyer holder was 8.5 mm-thick for the tests at 175 m/s and 272 m/s while it was 1.5 mm-thick for the test at 314 m/s. The additional impulse, for the cases of thicker holder tubes, was computed multiplying the compressive strength of PMMA, the cross-sectional area of the holder wall, and the time duration of the compressive stress wave propagation through the holder wall in the axial direction (for additional details see [Lee 2005]). With this correction, the tests at 175 m/s and at 314 m/s have almost the same nondimensional impulse (0.939 and 0.931) and in fact the final deflection is very similar (22.6 mm and 22.8 mm).

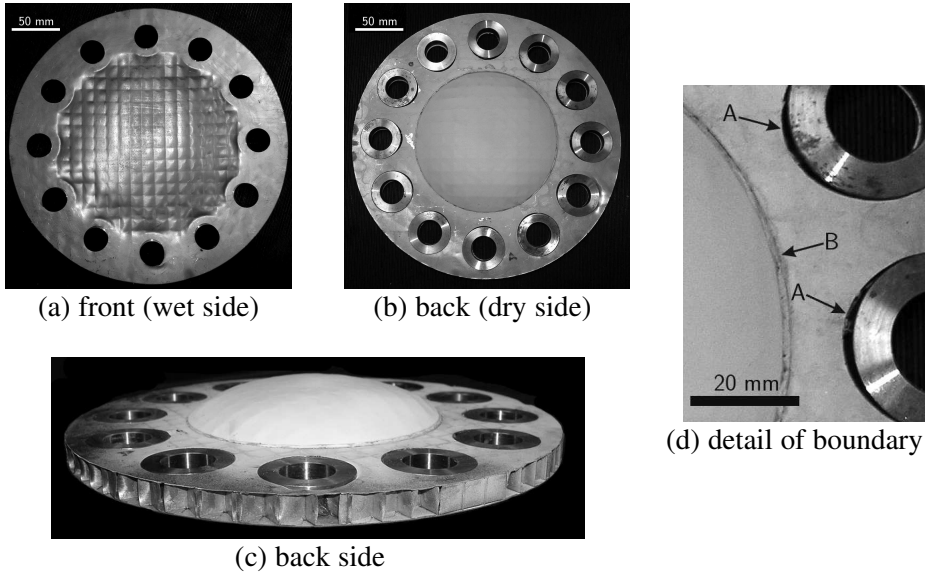


Figure 5. AISI 304 stainless steel honeycomb sandwich panel after the blast loading. (a), (b), and (c) show the front and the back of the plate while (d) shows details of hole ovalization (A) and slippage (B).

After the tests, the samples subjected to nondimensional impulses of $\hat{I} = 1.234$ and $\hat{I} = 0.939$ were cut in half by water-jet machining and are shown in Figure 6. On both cases significant core crushing close to the boundary is observed. However, the amount of core crushing in the center of the panel is very different. Only the largest impulse resulted in significant plastic buckling of the core webs in the center of the section panel (Figure 6b); the core buckled from the front (wet) side as shown in Figure 6e. The postmortem front and back face sheet profiles along the diameter of the panel subjected to a nondimensional impulse of $\hat{I} = 1.234$ are shown in Figure 7.

3.2. Pyramidal lattice panels.

3.2.1. Specimen geometry. Solid truss pyramidal lattice structures were fabricated via a folding operation that bends a diamond perforated sheet to create a single layer of trusses arranged with a pyramidal topology [Zok et al. 2004b; Queheillalt and Wadley 2005; McShane et al. 2006; Radford et al. 2006; Biagi and Bart-Smith 2007; Cote et al. 2007]. Briefly, the process consisted of punching a metal sheet to form a periodic diamond perforation pattern, folding node row by node row using a paired punch and die tool set, and then brazing this core to solid face sheets to form the sandwich structure. Figure 8 schematically illustrates this process. A solid truss structure with a core relative density of 4.5% was made from 304 stainless steel by the process described above. The sheet thickness $t = 1.52$ mm, truss width $w = 1.52$ mm, and the truss length $l = 17$ mm. The inclination angle $\omega = 45^\circ$ and the face sheet thickness was 0.635 mm, resulting in a pyramidal lattice with square cross section trusses and a desired relative density.

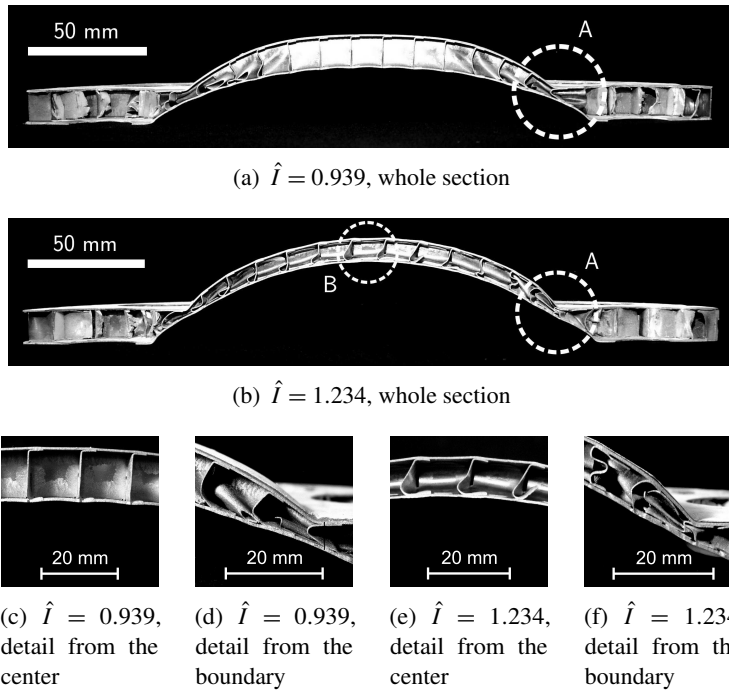


Figure 6. Cross-section of AISI 304 stainless steel honeycomb sandwich panels after blast loading. For the case of $\hat{I} = 0.939$, (a) core crushing occurs at the periphery, while for the case of $\hat{I} = 1.234$ (b) core crushing at both periphery (A) and center (B) occurs. (c)–(d) report core details for the lower impulse case and (e)–(f) for the higher impulse case.

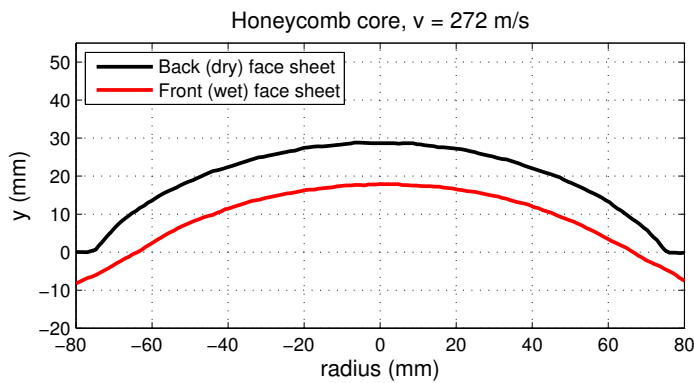


Figure 7. Postmortem profile of front and back face sheets along the diameter of the AISI 304 stainless steel panel with square honeycomb core subjected to a nondimensional impulse of $\hat{I} = 1.234$.

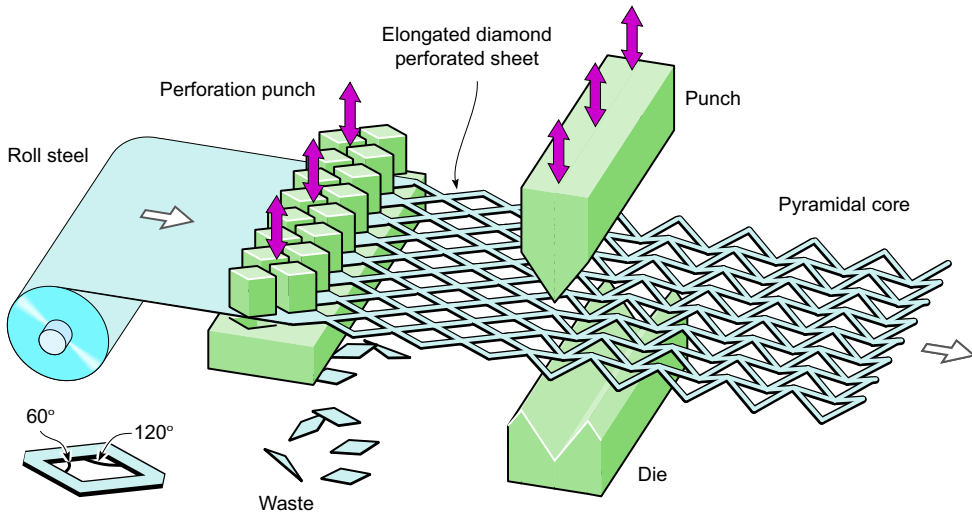


Figure 8. Fabrication of the pyramidal lattice core.

AISI 304 stainless steel panels with pyramidal truss cores were made by brazing the core to the face sheets. The brazing cycle for the truss core was the same as that previously described for the square honeycomb panels. The plates were then machined like the honeycomb panels to achieve the same boundary conditions. The overall thickness of the panels was 12.75 mm, the core relative density was 4.5% and the mass per area was 13.78 kg/m². The material properties for AISI 304 stainless steel are reported in [Table 2](#).

3.2.2. Test results. The sandwich panel was tested at an impact velocity of 307 m/s using a flyer thickness of 4.83 mm and a PMMA flyer holder tube with wall thickness of 1.5 mm. This resulted in a peak pressure p_0 of 79.7 MPa and a characteristic decay time t_0 of 25.8 μ s. The corresponding applied impulse I_0 was 37.47 N \cdot s and the nondimensional applied impulse \hat{I} was 0.925. The maximum deflection δ_{\max} was 22.79 mm, and thus the nondimensional maximum deflection δ_{\max}/L was 0.299. The final strain of the core in the middle of the sample was $\varepsilon_f = 11.3\%$.

Figures 9a–9h show fringe patterns, obtained by shadow moiré and high speed photography, at eight time instances between 93 μ s and 793 μ s after the wave front reached the specimen. The corresponding panel deflections along the diameter of the specimen are shown in [Figure 9i](#).

Several distinct failure modes were observed in this experiment, as seen in [Figures 10](#) and [11](#). Shear-off occurred at truss apexes on the front face sheet (wet side), ([Figure 10a](#), [c](#), and [e](#)). This failure mode is of main concern in sandwich panels with thin front face sheets and strong cores. On the other hand, the back face sheet partially sheared off at the supporting edge of the clamped boundary in [Figure 10d](#) and [f](#). Ovalization of the holes and even fracture of the face sheet in the back was also observed in [Figure 10b](#) and [d](#). The observed phenomena can be related to the influence of the boundary conditions and core properties.

After the experiment, the panel was sectioned and imaged as shown in [Figure 11](#). Clearly, significant collapse of the pyramidal truss core is observed in the boundary region. The observed plastic buckling of the trusses is consistent with buckling modes at intermediate strain rates (see [[Lee et al. 2006](#)]). By

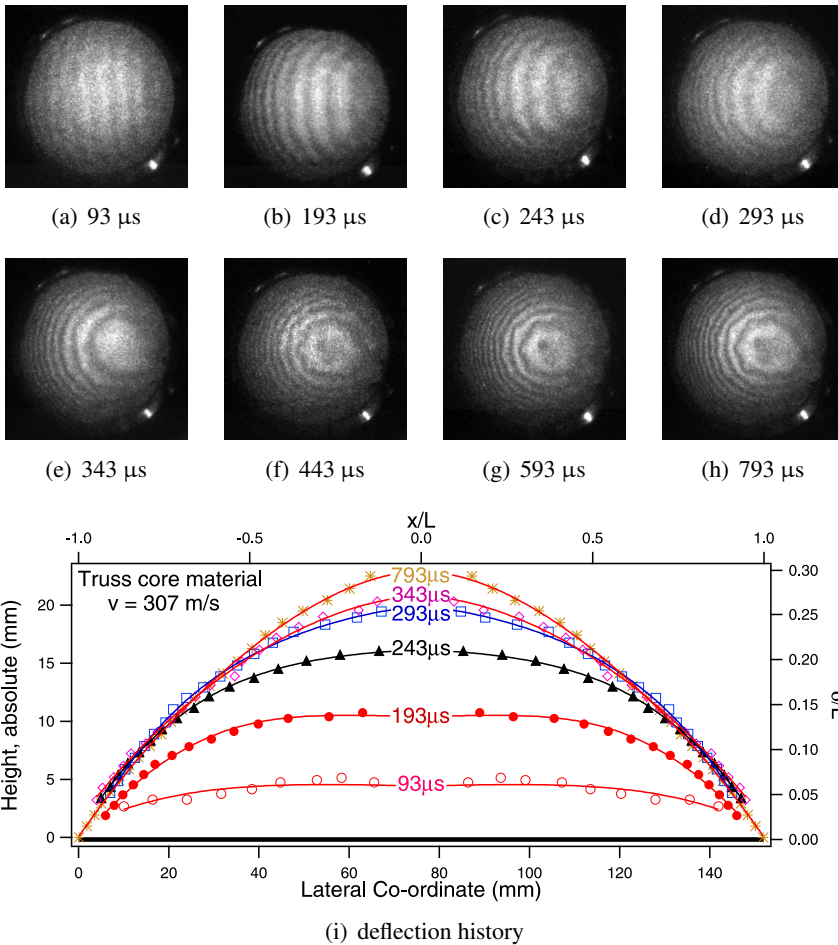


Figure 9. High-speed camera images of shadow moiré fringes for the AISI 304 stainless steel panel with pyramidal truss core at different time intervals (a)–(h), and deflection along the diameter of the specimen plate measured by shadow moiré (i). $t = 0 \mu\text{s}$ corresponds to the arrival of the shock at the specimen location.

contrast, the core in the center of the specimen is almost undeformed, as shown in Figure 11a. The postmortem front and back face sheets profiles along the diameter of the panel are reported in Figure 12.

4. Comparison of Performances

As previously stated, comparison of performances is based on the nondimensional impulse \hat{I} and the measured nondimensional maximum deflection δ_{max}/L . Since the experiments were performed at slightly different nondimensional impulses, all the results were referenced to one experiment. We chose the monolithic panel as our reference case such that any improvement by the sandwich topology automatically emerges. To scale the maximum deflection with impulse, we used the fact that nondimensional deflection

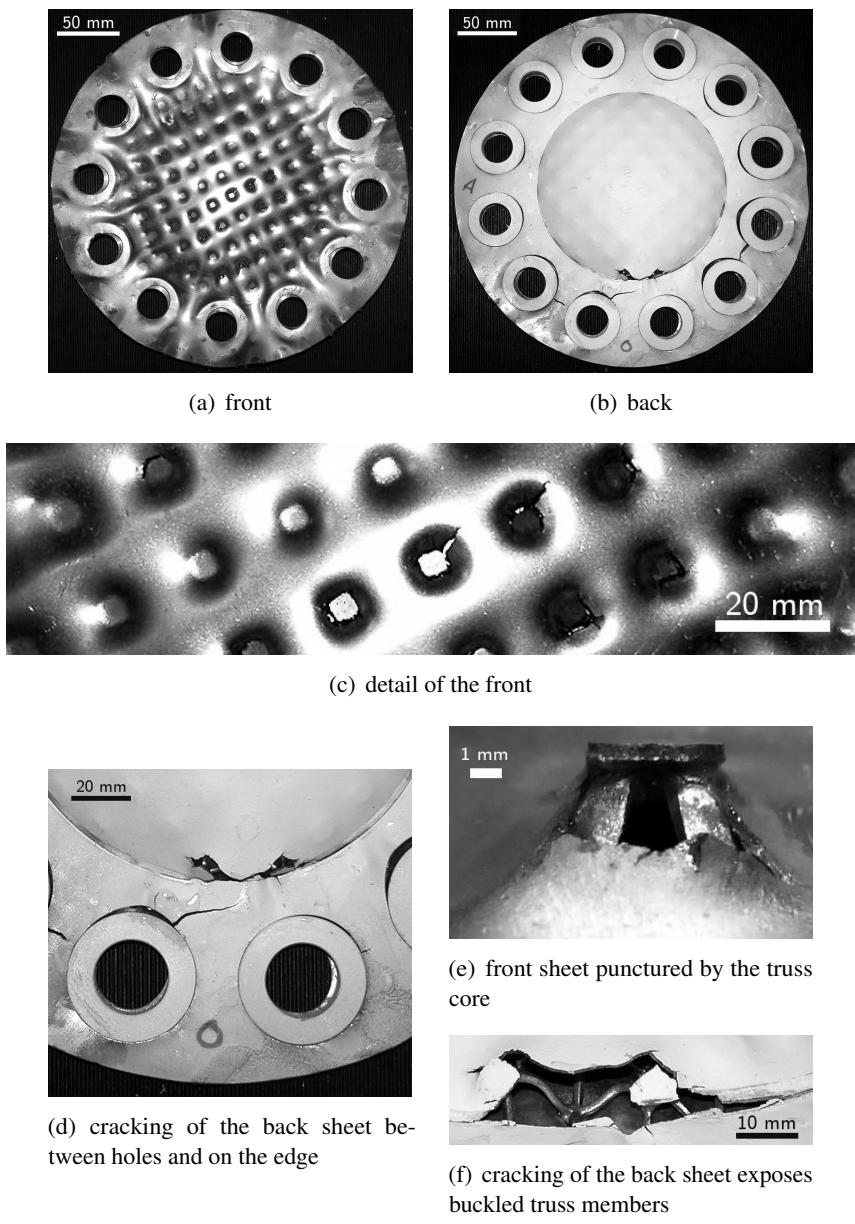


Figure 10. AISI 304 stainless steel sandwich panel with pyramidal truss core after blast loading. (a) and (b) show the front and the back of the plate; (c) and (e) show details observed in (a). (d) and (f) show fracture features.

and impulse follow a linear relationship [Xue and Hutchinson \[2004a\]](#). Then, the normalized maximum deflection is given by

$$(\delta_{\max}/L)_N = I_{nf} \cdot (\delta_{\max}/L)$$

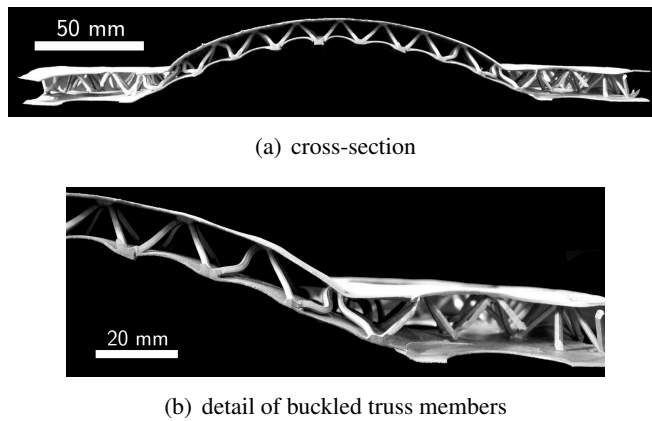


Figure 11. Cross-section of AISI 304 stainless steel sandwich panel with pyramidal truss core after blast loading.

where I_{nf} is the impulse normalization factor defined as $I_{nf} \stackrel{\text{def}}{=} \frac{\hat{f}_{\text{monolithic}}}{\hat{f}}$.

The calculations and improvements are reported in Table 3. Both honeycomb and pyramidal truss cores exhibit an improvement of about 30%, with the pyramidal truss core presenting significant localized damage and loss of impermeability.

5. Numerical simulations

Finite element calculations using ABAQUS/Explicit 6.4–1 [2003] were carried out to mimic the response of the sandwich plates. As shown in Figure 13, an axisymmetric model of the experimental set up was developed.

The material of the anvil tube is wrought AISI 4340 steel, that of the specimen plate is AISI 304 stainless steel, and that of the piston and flyer plate is heat-treated AISI 4140 steel. For the anvil tube the strain hardening law $\sigma = K \cdot \varepsilon^n$ is used. For AISI 4340 steel an elastic-perfectly plastic model is used. The material properties and the strain hardening law parameters for the wrought AISI 4340 steel and for heat-treated AISI 4140 steel are given in Table 4. The anvil tube and the piston were modeled with 4-node axisymmetric elements with reduced integration. The von Mises criterion was adopted to model steel yielding.

The water was modeled as a hydrodynamic material and the following Mie–Grüneisen equation of state with a linear Hugoniot relation was used

$$p = \frac{\rho_0 \cdot c_0^2 \cdot \eta}{(1 - s_1 \cdot \eta)^2} \cdot \left(1 - \frac{\Gamma_0 \cdot \eta}{2} \right) + \Gamma_0 \cdot \rho_0 \cdot E_m, \quad u_s = c_0 + s_1 \cdot u_p.$$

A tensile pressure was made to correspond to water cavitation at room temperature. The material properties used in the simulation are listed in Table 5. The water was modeled with 3-node axisymmetric elements. Adaptive meshing was employed to prevent excessive element distortion in the water and a contact algorithm was incorporated to avoid penetration of steel surfaces. The amplitudes and overall

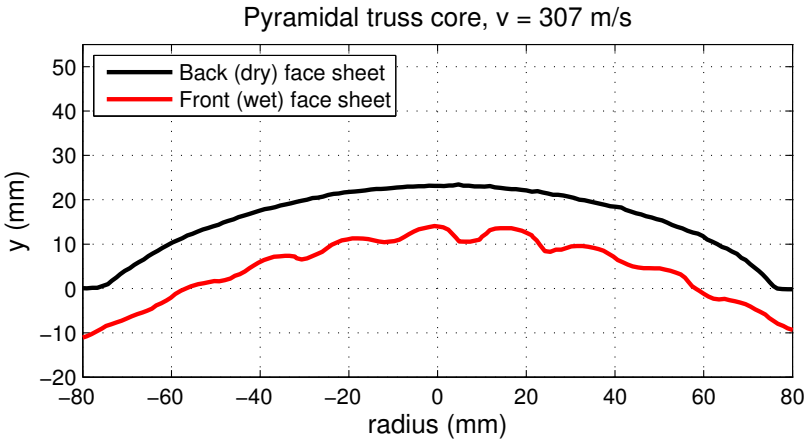


Figure 12. Postmortem profile of front and back face sheets along the diameter of the AISI 304 stainless steel panel with pyramidal truss core subjected to a nondimensional impulse of $\hat{I} = 0.925$.

Quantity	Symbol	Unit	AISI 4340 steel	AISI 4140 steel
Young's modulus	E	GPa	205	205
Poisson's ratio	ν	–	0.29	0.29
Density	ρ_0	kg/m ³	7850	7850
Yield stress	σ_0	MPa	470	1000
Hardening coefficient	K	MPa	470	1615
Hardening exponent	n	–	0	0.09

Table 4. Material properties and strain hardening coefficients for wrought AISI 4340 steel and for heat-treated AISI 4140 steel used in the numerical analyses.

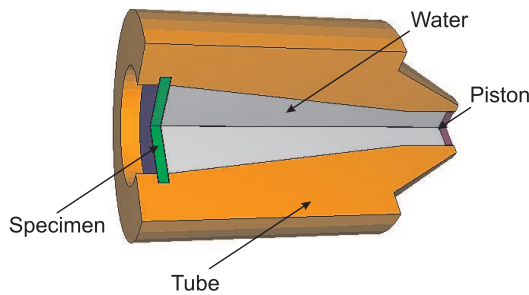


Figure 13. Schematic diagram of finite element model.

Quantity	Symbol	Unit	Water
Density	ρ_0	kg/m ³	958
Sound speed	c_0	m/s	1490
EOS coefficient	s_1	–	1.92
Grüneisen coefficient	Γ_0	–	0.1

Table 5. Material properties and parameters for the Mie–Grüneisen equation of state used for the water in the numerical analyses.

trends of pressure histories predicted by the model are in agreement with those measured in experiments [Espinosa et al. 2006].

The sandwich panels are made of stainless steel 304. The face sheets of the sandwich panel were meshed with 4-node axisymmetric elements with reduced integration. The Johnson–Cook plasticity model was adopted to model their elastic-plastic behavior. According to this model, the flow stress σ_y is given by

$$\sigma_y = \left[A + B \cdot \left(\varepsilon_p^{eq} \right)^n \right] \cdot \left(1 + c \cdot \ln \dot{\varepsilon}^* \right) \cdot \left[1 - \left(T^* \right)^m \right],$$

where

$$\dot{\varepsilon}^* \stackrel{\text{def}}{=} \frac{\dot{\varepsilon}_p^{eq}}{\dot{\varepsilon}_0}, \quad T^* \stackrel{\text{def}}{=} \frac{T - T_{\text{room}}}{T_{\text{melt}} - T_{\text{room}}},$$

ε_p^{eq} and $\dot{\varepsilon}_p^{eq}$ are equivalent plastic strain and equivalent plastic strain rate, respectively; T is the material temperature, T_{room} is the room temperature, and T_{melt} is the melting temperature of the material; A , B ,

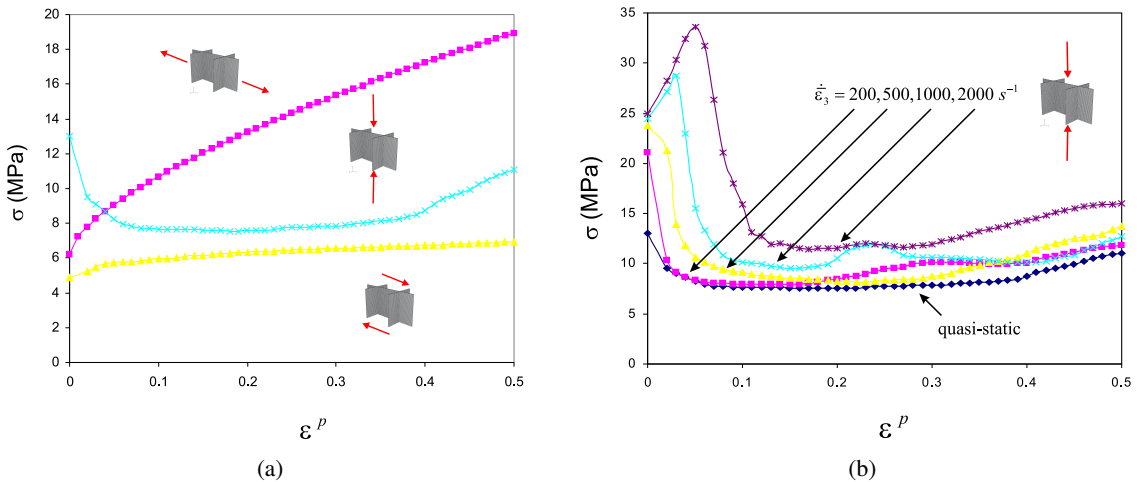


Figure 14. (a) True stress-plastic strain response of the square honeycomb core under three basic loading histories as computed using a three dimensional unit cell model. (b) Crushing response of the square honeycomb at various overall strain rates.

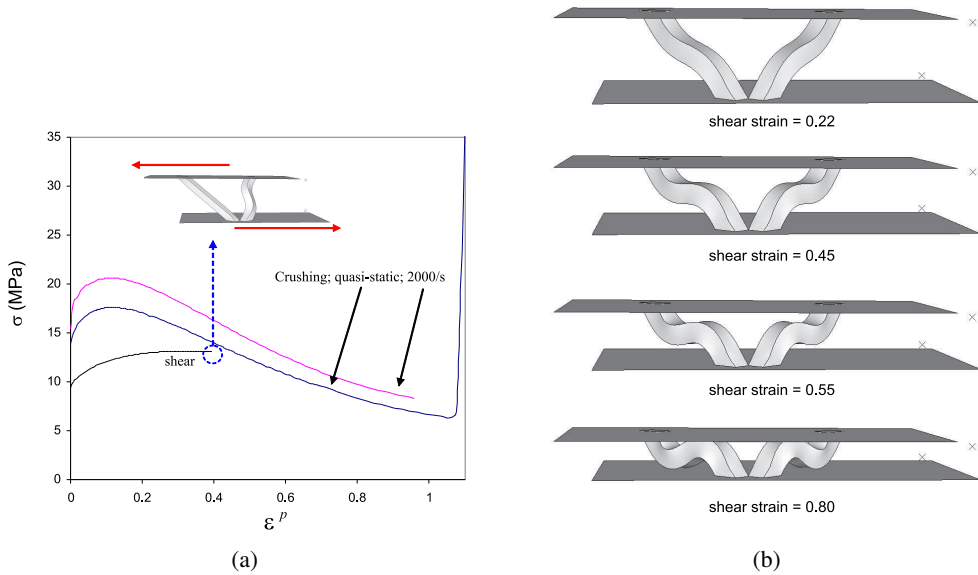


Figure 15. (a) True stress-plastic strain response of the square truss core under crushing and out of plane shearing as computed using the three dimensional unit cell model. The response of the truss core under a crushing rate of 2000/s is also depicted. Inset: deformed configuration of the truss core under out-of-plane shear at strain = 0.4. (b) Deformed configurations of the truss core under crushing at various level of crushing (true) strain.

n , c , $\dot{\epsilon}_0$, and m are Johnson–Cook parameters determined by fitting experimental stress-strain curves as a function of strain rate and temperature. The material properties and the identified Johnson–Cook parameters for the AISI 304 stainless steel are listed in Table 2. The computational model of the core consists of a homogenized material using the orthotropic constitutive model developed by Xue et al. [2005]. Four-node axisymmetric elements with reduced integration were used for the core. The inputs to this constitutive model are rate-dependent stress-strain responses of the metal core under six fundamental loading histories. These inputs were calculated using full three-dimensional unit cell models of the two tested cores: square honeycomb and pyramidal truss. The unit cell calculations do not take into account any imperfection. The boundary conditions applied to the unit cell on the edges of the core webs are consistent with symmetry and periodicity. The details of the calculations are similar to those reported in [Xue et al. 2005; Vaziri and Xue 2007; Vaziri and Hutchinson 2007; Mohr et al. 2006]. The dimensions employed in the unit cell calculations were obtained from measurements on the tested panels.

Figure 14a shows the response of the square honeycomb core under crushing, out-of-plane shear, and in-plane stretching when deformed in the quasistatic regime. When the core is deformed at high strain rates, both material rate dependence and inertia effects could significantly alter its response. This effect is significant specifically under crushing where a combination of inertial resistance and delay in buckling leads to a significant enhancement in the crushing resistance of the core [Xue and Hutchinson 2005]. The response of the square honeycomb core under crushing at different strain rates are quantified in Figure

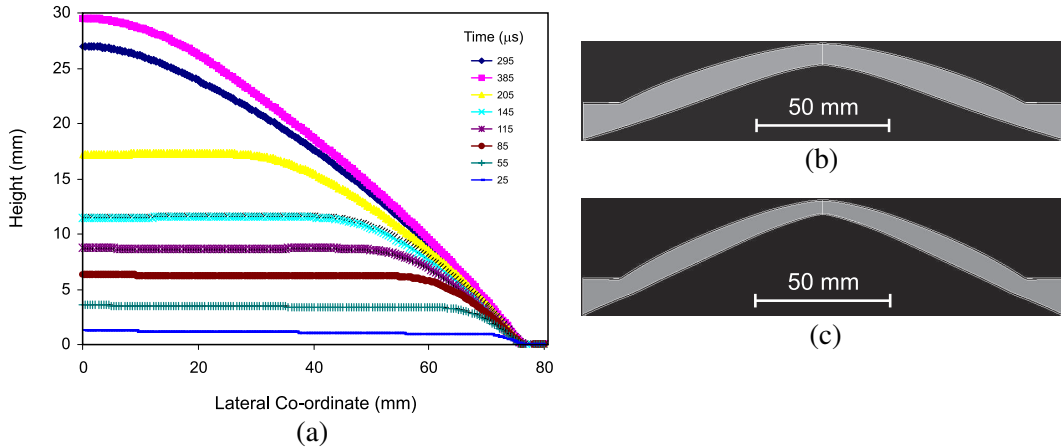


Figure 16. (a) Computed history of deformation of the dry-face sheet for the square honeycomb core sandwich panel (experimental results shown in Figure 4). (b) The final configuration of the square honeycomb core sandwich panel for the loading case $\hat{I} = 0.939$; experimental results are shown in Figure 6a. (c) The final configuration of the core sandwich panel for the loading case $\hat{I} = 1.234$; experimental results are shown in Figure 6b.

14b. These curves were directly input into the homogenized model to represent core behavior. All the calculations presented here incorporate the effect of deformation rate on core crushing. Its effect does not appear significant (see Figure 14b), in agreement with our previous studies [Xue et al. 2005; Vaziri and Xue 2007]. Similar calculations were carried out to quantify the response of the pyramidal truss core under three basic loading histories. The results of these calculations are summarized in Figure 15. For further discussion on deformation of pyramidal truss cores, see [Vaziri and Xue 2007].

In the computational model of the set up, the sandwich plate was taken to be perfectly bonded to the tube with an effective radius of 74 mm at its outer edge. The effect of the boundary condition will be discussed later. Frictionless contact was assumed at all other interfaces. The initial impulse per unit area \bar{I} applied to the piston was experimentally measured. In the computational model, the impulse is simplified as a uniformly distributed velocity $v = \bar{I}/\rho h$ suddenly applied through the entire piston, where ρ and h denote the density and height of the piston.

6. Numerical results and discussion

The computed deflection histories of the dry side of the sandwich panel along its radial direction are shown in Figures 16a and 18a for the sandwich plates with square honeycomb core and pyramidal truss core. The corresponding experimental measurements are shown in Figures 4i and 9i. The maximum deflection history obtained with the FEM model is reported in Figures 17a and 19a for the sandwich plates with square honeycomb core and pyramidal truss core. Figure 19a shows an excellent agreement between numerical and experimental results. Figure 20 reports the comparison between the experimental result and the numerical prediction for the final shape of both types of sandwich structures. The difference in height between the prediction and the experimental result is less than 7% for the pyramidal truss core

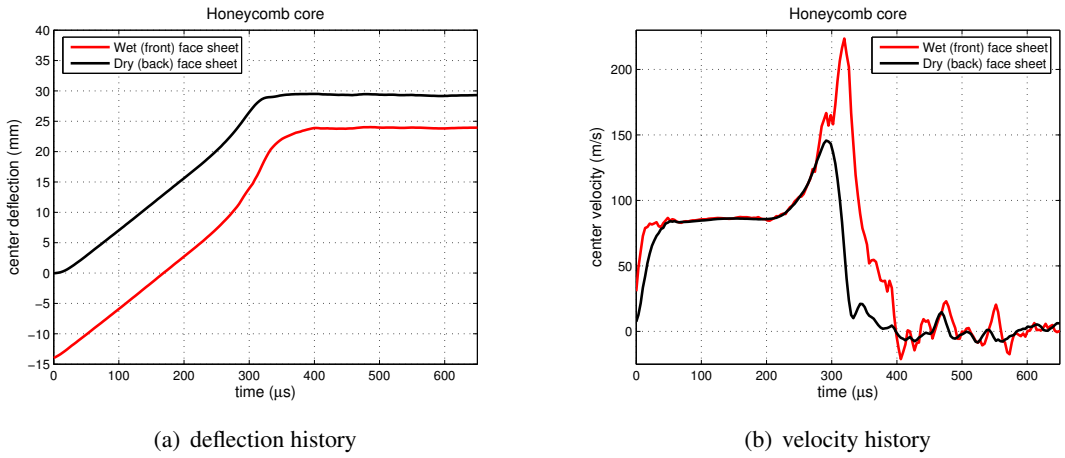


Figure 17. (a) Computed history of the maximum deflection of the dry-face and the wet face sheets for the square honeycomb core sandwich panel. (b) Computed history of the velocity of the center of the dry and wet face sheets after the Savitzky–Golay filter.

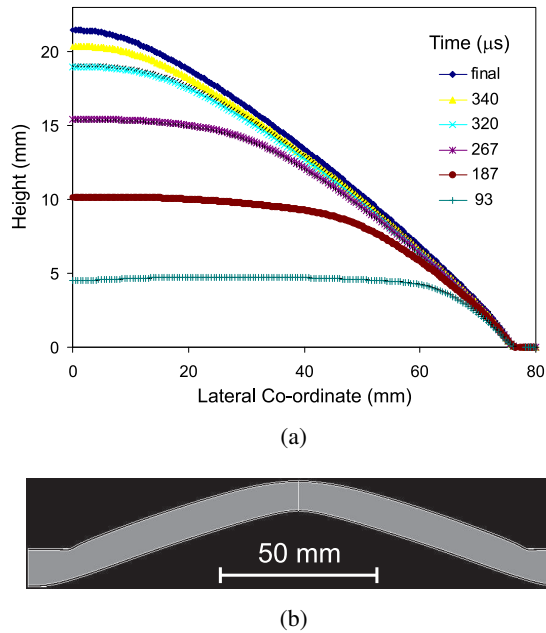


Figure 18. (a) Computed history of deformation of the dry-face sheet for the pyramidal truss core sandwich panel; experimental results are shown in Figure 9. (b) The final configuration of the pyramidal truss core sandwich panel; experimental results are shown in Figure 11.

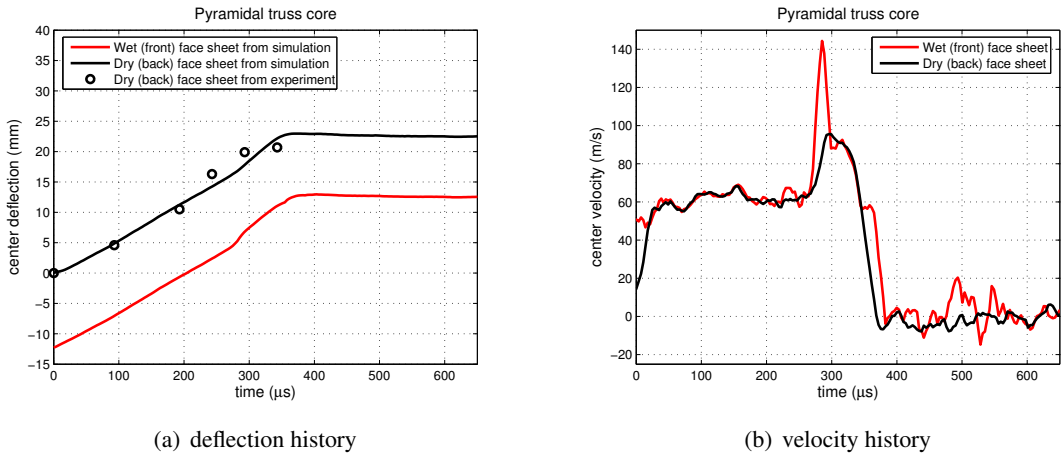


Figure 19. (a) Computed and experimental history of the maximum deflection of the dry-face and the wet face sheets for the pyramidal truss core sandwich panel. (b) Computed history of the velocity of the center of the dry and wet face sheets after the Savitzky–Golay filter.

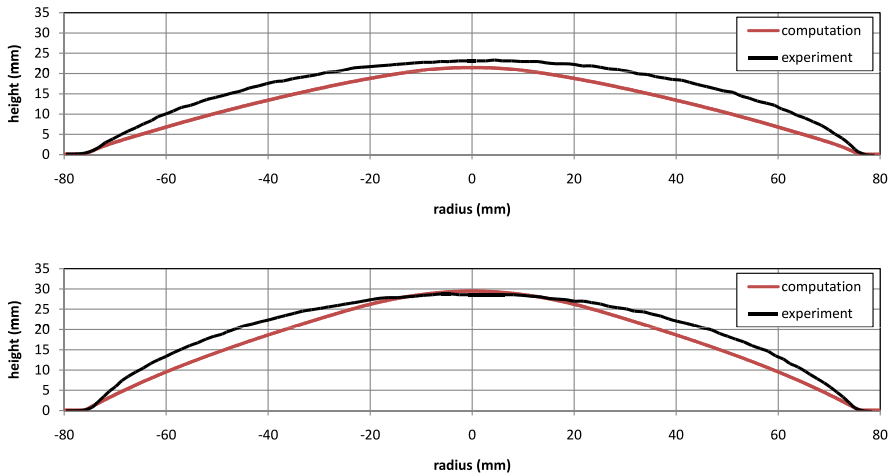


Figure 20. Comparison between the numerical prediction and the experimental result for the final shape of the pyramidal truss core sandwich (top) and the square honeycomb core sandwich (bottom).

and less than 3% for the square honeycomb. The velocity history of the center of the plate obtained with the FEM model is reported in Figure 17. Due to numerical errors of the FEM simulations, the velocity histories were noisy and so they were smoothed with a Savitzky–Golay filter on a frame of 10 points and with a polynomial of the third degree [Savitzky and Golay 1964]. The predicted deflection history profiles are in agreement with the corresponding experimental measurements. In particular, the

maximum deflection is captured very well by the computational model. A minor inconsistency between the numerical simulations and the experimental measurements is the time for the plate to attain a particular deformed shape. One possible reason is that the homogenization method fails to capture the full wave propagation process very accurately and slightly underpredicts the time interval required to achieve a given deformation. Figures 16b and 16c display the computed final deformed configuration of the sandwich panels with honeycomb cores for two impulses. Likewise, Figure 18b shows the computed final configuration for the case of pyramidal core. The results reveal a very good agreement between the experimental observations and numerical predictions, except that the crushing deformation of the sandwich panels around the edge is less in the numerical prediction. Noteworthy is that the 12 through holes machined on the panels, to achieve clamping, weaken the sandwich core locally and effectively act as imperfections. Since this feature was not accounted for in the numerical simulations, the local level of crushing observed experimentally was not reproduced by the simulations. Likewise, Figure 10 illustrates that tearing occurs on the face sheets of the sandwich panel with pyramidal truss cores in the clamped region. By contrast, the simulations did not account for fracture or rupture of the face sheets. Models capable of simulating fracture of metal sandwich plates are currently under development [Vaziri et al. 2007] and can be employed in the analysis of the experimental data in future studies. Due to the nature of the homogenization method, the numerical simulations also could not capture the local bending of the wet face due to shock loading at early stages of deformation. This local behavior is more pronounced for the panel with the truss core. Despite these limitations, the overall and maximum deflection are captured by the model in the spirit of its formulation.

7. Conclusions

A water shock tube has been used to investigate the fluid-structure interaction between water borne shock fronts and stainless steel sandwich panels with either honeycomb or pyramidal lattice cores of identical relative density. Tests have been conducted at impulse levels sufficient to initiate some of the panel failure modes. The panel deflections and back face velocity have been measured and compared with results obtained for monolithic panels of the same mass per unit area. A finite element modeling method has been used to investigate the basic deformation mechanisms of the core constituents and to predict the overall panel response to impulsive loading. We find that:

- (i) The back face deflections of sandwich panels with specific mass of 14 kg/m^2 subjected to impulse loading in the $1 - 2 \text{ kPa} \cdot \text{s}$ range are approximately 30% less than those observed in solid panels of identical mass per unit area.
- (ii) The difference in response partly resulted from reduced impulse acquired by the sandwich panels due to beneficial fluid-structure interactions. The simulations indicate that only a fraction of the far field impulse is transmitted to the structure.
- (iii) The sandwich panels were also able to exhibit some core crushing (between 1.7 and 26.8% depending on core type and applied impulse) which also contributed to a reduction in FSI and energy dissipation.
- (iv) The two core structures investigated underwent similar back (dry) face deflections. However, their front (wet) side deformation patterns were influenced by spacial distribution of nodal contacts with

the underlying core. The larger contact area for the honeycomb core resulted in slightly less face sheet stretching and tearing during the dynamic dishing of the panels.

- (v) The resistance to face sheet tearing during impulse loading is clearly sensitive to the detailed design of the core-face sheet nodal contacts. Further work should explore approaches for reducing the fracture susceptibility of the various candidate topologies.

Acknowledgments

This research was supported by the Office of Naval Research through MURI grant no. 123163–02–N00014–02–1–0700 to Harvard University, University of California at Santa Barbara, and Northwestern University (Program Manager Dr. R. Barsoum) and grant no. N00014–01–1–1051 to the University of Virginia (Program Managers Dr. S. Fishman and Dr. D. Shifler).

References

- [ABAQUS/Explicit 6.4–1 2003] ABAQUS/Explicit 6.4–1, *User's Manual*, ABAQUS Inc., 2003.
- [Biagi and Bart-Smith 2007] R. Biagi and H. Bart-Smith, "Imperfection sensitivity of pyramidal core sandwich structures", *International Journal of Solids and Structures* **44**:14-15 (2007), 4690–4706.
- [Chiras et al. 2002] S. Chiras, D. R. Mumm, A. G. Evans, N. Wicks, J. W. Hutchinson, K. Dharmasena, H. N. G. Wadley, and S. Fichter, "The structural performance of near-optimized truss core panels", *International Journal of Solids and Structures* **39** (2002), 4093–4115.
- [Cote et al. 2004] F. Cote, V. S. Deshpande, N. A. Fleck, and A. G. Evans, "The out-of-plane compressive behavior of metallic honeycombs", *Materials Science and Engineering A* **380** (2004), 272–280.
- [Cote et al. 2007] F. Cote, R. Biagi, H. Bart-Smith, and V. S. Deshpande, "Structural response of pyramidal core sandwich columns", *International Journal of Solids and Structures* **44**:10 (2007), 3533–3556.
- [Deshpande and Fleck 2001] V. S. Deshpande and N. A. Fleck, "Collapse of truss core sandwich beams in 3-point bending", *International Journal of Solids and Structures* **38**:36–37 (2001), 6275–6305.
- [Deshpande and Fleck 2005] V. S. Deshpande and N. A. Fleck, "One-dimensional response of sandwich plates to underwater shock loading", *Journal Of The Mechanics And Physics Of Solids* **53**:11 (November 2005), 2347–2383.
- [Deshpande et al. 2006] V. S. Deshpande, A. Heaver, and N. A. Fleck, "An underwater shock simulator", *Proceedings of the Royal Society A: Mathematical, Physical and Engineering Sciences* **462**:2067 (2006), 1021–1041.
- [Dharmasena et al. 2007a] K. P. Dharmasena, D. T. Queheillalt, H. N. G. Wadley, Y. Chen, P. Dudt, D. Knight, Z. Wei, and A. G. Evans, "Dynamic response of a multilayer prismatic structure to impulsive loads incident from water", *International Journal of Impact Engineering* (2007). Accepted.
- [Dharmasena et al. 2007b] K. P. Dharmasena, H. N. G. Wadley, Z. Y. Xue, and J. W. Hutchinson, "[Mechanical response of metallic honeycomb sandwich panel structures to high intensity dynamic loading](#)", *International Journal of Impact Engineering* (2007). In press.
- [Espinosa et al. 2006] H. D. Espinosa, S. Lee, and N. Moldovan, "A Novel Fluid Structure Interaction Experiment to Investigate Deformation of Structural Elements Subjected to Impulsive Loading", *Experimental Mechanics* **46**:6 (2006), 805–824.
- [Fleck and Deshpande 2004a] N. A. Fleck and V. S. Deshpande, "The Resistance of Clamped Sandwich Beams to Shock Loading", *Journal of Applied Mechanics* **71**:3 (2004), 386–401.
- [Fleck and Deshpande 2004b] N. A. Fleck and V. S. Deshpande, "The resistance of clamped sandwich beams to shock loading", *Journal Of Applied Mechanics-Transactions Of The ASME* **71**:3 (May 2004), 386–401.
- [Hutchinson and Xue 2005] J. W. Hutchinson and Z. Y. Xue, "Metal sandwich plates optimized for pressure impulses", *International Journal Of Mechanical Sciences* **47**:4–5 (April-May 2005), 545–569.

- [Lee 2005] S. Lee, *Dynamic Failure of Blast-Resistant Structures Subjected to Impulsive Loading*, Ph.D. thesis, Northwestern University, Evanston, IL, USA, December 2005.
- [Lee et al. 2006] S. Lee, F. Barthelat, J. W. Hutchinson, and H. D. Espinosa, “Dynamic failure of metallic pyramidal truss core materials: Experiments and modeling”, *International Journal of Plasticity* **22**:11 (2006), 2118–2145.
- [Liang et al. 2007] Y. Liang, A. V. Spuskanyuk, S. E. Flores, D. R. Hayhurst, J. W. Hutchinson, R. M. McMeeking, and A. G. Evans, “The Response Of Metallic Sandwich Panels To Water Blast”, *Journal of Applied Mechanics* **74**:1 (2007), 81–99.
- [McShane et al. 2006] G. J. McShane, D. D. Radford, V. S. Deshpande, and N. A. Fleck, “The response of clamped sandwich plates with lattice cores subjected to shock loading”, *European Journal of Mechanics — A/Solids* **25** (2006), 215–229.
- [Mohr et al. 2006] D. Mohr, Z. Y. Xue, and A. Vaziri, “Quasi-static punch indentation of a honeycomb sandwich plate: Experiments and Constitutive Modeling”, *Journal of Mechanics of Materials and Structures* **1**:3 (2006), 581–604.
- [Qiu et al. 2003] X. Qiu, V. S. Deshpande, and N. A. Fleck, “Finite element analysis of the dynamic response of clamped sandwich beams subject to shock loading”, *European Journal Of Mechanics A-Solids* **22**:6 (November-December 2003), 801–814.
- [Qiu et al. 2004] X. Qiu, V. S. Deshpande, and N. A. Fleck, “Dynamic response of a clamped circular sandwich plate subject to shock loading”, *Journal Of Applied Mechanics-Transactions Of The ASME* **71**:5 (September 2004), 637–645.
- [Qiu et al. 2005a] X. Qiu, V. S. Deshpande, and N. A. Fleck, “Impulsive loading of clamped monolithic and sandwich beams over a central patch”, *Journal Of The Mechanics And Physics Of Solids* **53**:5 (May 2005), 1015–1046.
- [Qiu et al. 2005b] X. Qiu, V. S. Deshpande, and N. A. Fleck, “Impulsive loading of clamped monolithic and sandwich beams over a central patch”, *Journal of the Mechanics and Physics of solids* **53** (2005), 1015–1046.
- [Queheillalt and Wadley 2005] D. T. Queheillalt and H. N. G. Wadley, “Pyramidal lattice truss structures with hollow trusses”, *Materials Science and Engineering A* **397** (2005), 132–137.
- [Rabczuk et al. 2004] T. Rabczuk, J. Y. Kim, E. Samaniego, and T. Belytschko, “Homogenization of sandwich structures”, *International Journal For Numerical Methods In Engineering* **61** (2004), 1009–1027.
- [Radford et al. 2005] D. D. Radford, V. S. Deshpande, and N. A. Fleck, “The use of metal foam projectiles to simulate shock loading on a structure”, *International Journal of Impact Engineering* **31** (2005), 1152–1171.
- [Radford et al. 2006] D. D. Radford, N. A. Fleck, and V. S. Deshpande, “The response of clamped sandwich beams subjected to shock loading”, *International Journal of Impact Engineering* **32** (2006), 968–987.
- [Rathbun et al. 2004] H. J. Rathbun, Z. Wei, M. Y. He, F. W. Zok, A. G. Evans, D. J. Sypeck, and H. N. G. Wadley, “Measurement and Simulation of the Performance of a Lightweight Metallic Sandwich Structure With a Tetrahedral Truss Core”, *Journal of Applied Mechanics* **71**:3 (2004), 368–374.
- [Rathbun et al. 2005] H. J. Rathbun, F. W. Zok, and A. G. Evans, “Strength optimization of metallic sandwich panels subject to bending”, *International Journal of Solids and Structures* **42**:26 (2005), 6643–6661.
- [Rathbun et al. 2006] H. J. Rathbun, D. D. Rodford, Z. Y. Xue, M. Y. He, J. Yang, V. Deshpande, N. A. Fleck, J. W. Hutchinson, F. W. Zok, and A. G. Evans, “Performance of metallic honeycomb-core sandwich beams under shock loading”, *International Journal of Solids and Structures* **43** (2006), 1746–1763.
- [Savitzky and Golay 1964] A. Savitzky and M. J. E. Golay, “Smoothing and differentiation of data by simplified least squares procedures”, *Analytical Chemistry* **36**:8 (1964), 1627–1639.
- [Smith and Hetherington 1994] P. D. Smith and J. G. Hetherington, *Blast and ballistic loading of structures*, Butterworth-Heinemann, Oxford, November 1994.
- [Taylor 1963] G. I. Taylor, *The scientific papers of G. I. Taylor*, vol. III, Chapter The pressure and impulse of submarine explosion waves on plates, pp. 287–303, Cambridge University Press, Cambridge, 1963.
- [Tilbrook et al. 2006] M. T. Tilbrook, V. S. Deshpande, and N. A. Fleck, “The impulsive response of sandwich beams: analytical and numerical investigation of regimes of behaviour”, *Journal of the Mechanics and Physics of Solids* **54**:11 (2006), 2242–2280.

- [Vaughn and Hutchinson 2006] D. G. Vaughn and J. W. Hutchinson, “Bucklewaves”, *European Journal of Mechanics A-Solids* **25**:1 (2006), 1–12.
- [Vaughn et al. 2005] D. G. Vaughn, J. M. Canning, and J. W. Hutchinson, “Coupled plastic wave propagation and column buckling”, *Journal of Applied Mechanics* **72**:1 (2005), 139–146.
- [Vaziri and Hutchinson 2007] A. Vaziri and J. W. Hutchinson, “Metallic sandwich plates subject to intense air shocks”, *International Journal of Solids and Structures* **44**:1 (2007), 2021–2035.
- [Vaziri and Xue 2007] A. Vaziri and Z. Y. Xue, “[Mechanical behavior and constitutive modeling of metal cores](#)”, *Journal of Mechanics of Materials and Structures* **2**:9 (2007), 1743–1760. In press.
- [Vaziri et al. 2006] A. Vaziri, Z. Y. Xue, and J. W. Hutchinson, “Metal sandwich plates with polymeric foam-filled cores”, *Journal of Mechanics of Materials and Structures* **1**:1 (2006), 95–128.
- [Vaziri et al. 2007] A. Vaziri, Z. Y. Xue, and J. W. Hutchinson, “Performance and failure of metal sandwich plates subject to shock loading”, *Journal of Mechanics of Materials and Structures* (2007). In press.
- [Wadley 2006] H. N. G. Wadley, “Multifunctional periodic cellular metals”, *Philosophical Transactions of the Royal Society A* **364** (2006), 31–68.
- [Wadley et al. 2003] H. N. G. Wadley, N. A. Fleck, and A. G. Evans, “Fabrication and structural performance of periodic cellular metal sandwich structures”, *Composite Science & Technology* **63** (2003), 2331–2343.
- [Wadley et al. 2007a] H. N. G. Wadley, K. P. Dharmasena, Y. Chen, P. Dudd, D. Knight, R. Charette, and K. Kiddy, “[Compressive response of multilayered pyramidal lattices during underwater shock loading](#)”, *International Journal of Impact Engineering* (2007). In press.
- [Wadley et al. 2007b] H. N. G. Wadley, K. P. Dharmasena, D. T. Queheillalt, Y. Chen, P. Dudd, D. Knight, K. Kiddy, Z. Xue, and A. Vaziri, “Dynamic compression of square honeycomb structures during underwater impulsive loading”, *Journal of Mechanics of Materials and Structures* (2007). In press.
- [Wallach and Gibson 2001a] J. C. Wallach and L. J. Gibson, “Defect sensitivity of a 3D truss material”, *Scripta Materialia* **45**:6 (2001), 639–644.
- [Wallach and Gibson 2001b] J. C. Wallach and L. J. Gibson, “Mechanical behavior of a three-dimensional truss material”, *International Journal of Solids and Structures* **38** (2001), 7181–7196(16).
- [Wicks and Hutchinson 2001] N. Wicks and J. W. Hutchinson, “Optimal truss plates”, *International Journal of Solids and Structures* **38**:30–31 (2001), 5165–5183.
- [Xue and Hutchinson 2003] Z. Y. Xue and J. W. Hutchinson, “Preliminary assessment of sandwich plates subject to blast loads”, *International Journal Of Mechanical Sciences* **45**:4 (April 2003), 687–705.
- [Xue and Hutchinson 2004a] Z. Y. Xue and J. W. Hutchinson, “A comparative study of impulse-resistant metal sandwich plates”, *International Journal of Impact Engineering* **30**:10 (November 2004), 1283–1305.
- [Xue and Hutchinson 2004b] Z. Y. Xue and J. W. Hutchinson, “Constitutive model for quasi-static deformation of metallic sandwich cores”, *International Journal For Numerical Methods In Engineering* **61** (2004), 2205–2238.
- [Xue and Hutchinson 2005] Z. Y. Xue and J. W. Hutchinson, “Crush dynamics of square honeycomb sandwich cores”, *International Journal for Numerical Methods in Engineering* **65** (2005), 2221–2245.
- [Xue et al. 2005] Z. Y. Xue, A. Vaziri, and J. W. Hutchinson, “Non-uniform constitutive model for compressible orthotropic materials with application to sandwich plate cores”, *Computer Modeling in Engineering & Sciences* **10**:1 (2005), 79–95.
- [Zok et al. 2004a] F. W. Zok, H. Rathbun, M. He, E. Ferri, C. Mercer, R. M. McMeeking, and A. G. Evans, “Structural performance of metallic sandwich panels with square honeycomb cores”, *Philosophical Magazine* **85** (2004), 3207–3234.
- [Zok et al. 2004b] F. W. Zok, S. A. Waltner, Z. Wei, H. J. Rathbun, R. M. McMeeking, and A. G. Evans, “A protocol for characterizing the structural performance of metallic sandwich panels: application to pyramidal truss cores”, *International Journal of Solids and Structures* **41** (2004), 6249–6271.

Received 5 Aug 2007. Accepted 6 Aug 2007.

L. F. MORI: lapo.mori@gmail.com

Department of Mechanical Engineering, Northwestern University, Evanston, IL 60208, United States

S. LEE: sungsoo.f.lee@gmail.com

Department of Mechanical Engineering, Northwestern University, Evanston, IL 60208, United States

Z. Y. XUE: xue@deas.harvard.edu

School of Engineering and Applied Sciences, Harvard University, Cambridge, MA 02138, United States

A. VAZIRI: avaziri@deas.harvard.edu

School of Engineering and Applied Sciences, Harvard University, Cambridge, MA 02138, United States

D. T. QUEHEILLALT: dtq2j@virginia.edu

Department of Materials Science and Engineering, University of Virginia, 140 Chemistry Way, Charlottesville, VA 22904, United States

K. P. DHARMASENA: kumar@virginia.edu

Department of Materials Science and Engineering, University of Virginia, 140 Chemistry Way, Charlottesville, VA 22904, United States

H. N. G. WADLEY: haydn@virginia.edu

Department of Materials Science and Engineering, University of Virginia, 140 Chemistry Way, Charlottesville, VA 22904, United States

J. W. HUTCHINSON: jhutchin@fas.harvard.edu

School of Engineering and Applied Sciences, Harvard University, Cambridge, MA 02138, United States

H. D. ESPINOSA: espinosa@northwestern.edu

Department of Mechanical Engineering, Northwestern University, Evanston, IL 60208, United States

DYNAMIC FAILURE OF CLAMPED CIRCULAR PLATES SUBJECTED TO AN UNDERWATER SHOCK

SOHRAB KAZEMAHVAZI, DARREN RADFORD, VIKRAM S. DESHPANDE AND NORMAN A. FLECK

Clamped circular copper plates have been subjected to exponentially decaying underwater blast waves with peak pressures in the range 10 MPa to 300 MPa and decay constants varying between 0.05 ms to 1.1 ms. The deformation and failure modes were observed by high-speed photography. For the thin plates considered in this study, the failure modes were primarily governed by the peak pressures and were reasonably independent of the blast wave decay constant. Three modes of deformation and failure were identified. At low pressures, the plates undergo bending and stretching without rupture (mode I). At intermediate pressures a range of tensile tearing modes were observed, from petalling failures to tearing at the supports with increasing blast pressures. These tearing modes are referred to as mode II failures. At the highest pressures investigated here, the plate tears at the supports in a manner that is reminiscent of a *shear-off* failure. This failure is labeled as mode III. Scanning electron micrographs of the failure surfaces showed that in all cases, the local failure mechanism was tensile necking. Finite element (FE) simulations employing a local shear failure criterion are used to model the rupture of the material. Appropriately calibrated FE models capture all failure modes with sufficient fidelity.

1. Introduction

Military and commercial ship structures require adequate strength and ductility to survive an underwater explosion. This need has stimulated considerable recent interest in investigating the underwater blast response of metallic monolithic and sandwich structures, see for example [Fleck and Deshpande 2004; Xue and Hutchinson 2003]. Local failure of these metallic structures under dynamic loading is a major design constraint: typically, failure occurs at the supports or at the junction between the sandwich core and faces of a sandwich structure [Radford et al. 2005; Rathbun et al. 2006].

Recent assessments of steel sandwich panels subject to underwater blast exemplify the tendency for rupture at the supports [Liang et al. 2006]. Shortly after arrival of the pressure wave, much of the wet face acquires an uniform velocity. However, small portions of the wet face remain stationary: at the supports, and at the attachment points to the core. Plastic strains concentrate within the wet face adjacent to these stationary locations. Rupture occurs when the plastic strain reaches a critical value (say 20%), causing the wet face to tear.

Experiments on impulsively loaded clamped beams have revealed a range of deformation and failure modes [Menkes and Opat 1973; Nurick and Shave 2000]. At low value of impulse I , the beams plastically bend and stretch without rupture (mode I). At intermediate I , plate stretching is followed by tensile rupture at the supports (mode II). And at high I , shear failure occurs at the supports with negligible plastic deformation in the remainder of the beam (mode III).

Keywords: dynamic fracture, petalling, underwater blast, FE simulation.

Recent theoretical studies by Lee and Wierzbicki [2005a; 2005b] have analyzed the so-called discing and petalling failure modes in impulsively loaded clamped plates. These tensile tearing modes are reminiscent of the mode II failure modes for impulsively loaded beams. On the other hand, Balden and Nurick [2005] have reported an experimental and numerical investigation into the so-called shear rupture modes (mode III) of impulsively loaded clamped circular plates. Systematic experimental studies, along with appropriate high speed photography, are required to elucidate the deformation modes and the range of failure mechanisms of dynamically loaded clamped plates.

The primary aims of this study are:

- (i) to investigate the sensitivity of failure mode of monolithic plates to the level of underwater blast pressure and to the decay time of the blast waves.
- (ii) to determine the ability of finite element (FE) calculation to predict the observed failure modes.

We report a combined experimental and numerical study on the failure modes of clamped copper plates subjected to an underwater blast. In Section 2 the experimental method is described, based on the underwater shock simulator of [Deshpande et al. 2006]. The observed failure mechanisms are elucidated by high-speed photography, and are discussed in Section 3. The observed failure modes are then used to construct failure regime maps for the clamped copper plates. A limited set of finite element simulations of the failure of the copper plates are reported in Section 4 and are compared with observation.

2. Experimental protocol

2.1. Summary of the water shock tube apparatus and the Taylor fluid-structure interaction analysis.

Deshpande et al. [2006] have developed a shock simulator for the underwater shock loading of materials and test structures within the laboratory. The tube is capped at one end by the test structure and by a piston at the other end. The piston is struck by a steel projectile, as sketched in Figure 1. Pressure pulses that decay exponentially with time t are generated in the water. Similar to realistic underwater blasts, these pulses have the form

$$p = p_o e^{-t/\theta}, \quad (1)$$

where p_o is the peak pressure and θ is the decay constant. The apparatus is capable of generating peak pressures in the range 10–300 MPa with decay times ranging from 0.05 ms to 1.5 ms. The peak pressure and the decay time are adjusted independently by varying the projectile velocity and mass, respectively. In particular, using one-dimensional linear wave theory, Deshpande et al. [2006] have shown that (p_o, θ) are related to the projectile mass per unit area m_p and velocity v_o by

$$p_o = \rho_w c_w v_o \quad (2a)$$

and

$$\theta = \frac{m_p}{\rho_w c_w}, \quad (2b)$$

where ρ_w is the density of water and c_w is the speed of sound in water. Good agreement was observed between the measured pressure pulses and these simple analytical predictions.

In the present study, a water shock tube is used to load a clamped circular copper plate of mass per unit area m_f . The momentum transmitted to the plate can be estimated using the one-dimensional fluid-structure interaction analysis of [Taylor 1941] for an underwater pressure pulse of the form of Equation

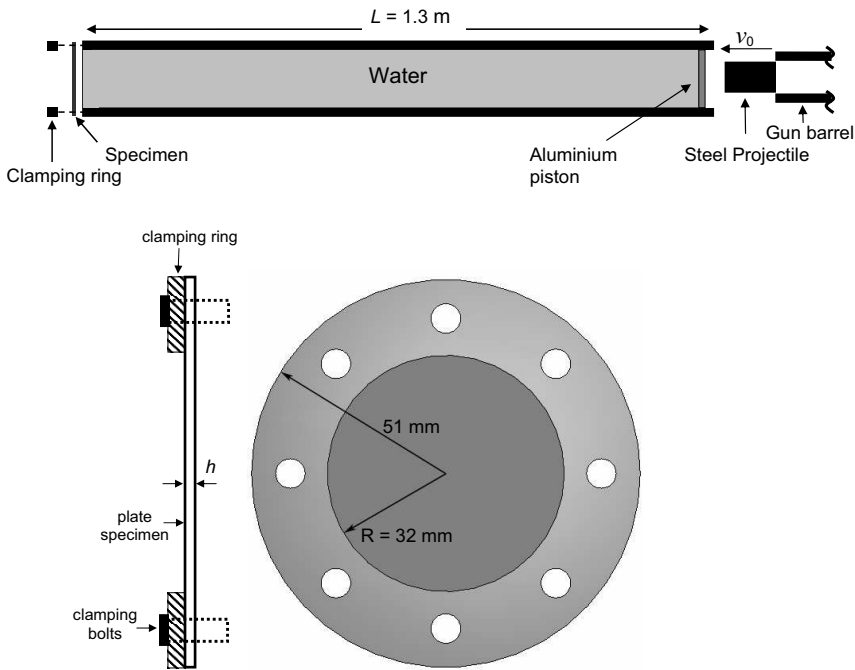


Figure 1. Schematic of the water shock tube experimental set-up, not to scale (above). Sketch of the copper plate test specimen along with the side view of the clamping arrangement (below).

(1) impinging on a free standing plate. When this pressure wave hits a stationary rigid plate at normal incidence, it imparts an impulse

$$I_o = 2 \int_0^{\infty} p_o e^{-t/\theta} dt = 2 p_o \theta \tag{3}$$

to the plate. The factor of two arises in Equation (3) due to full reflection of the pressure wave. If, instead, the pressure wave impacts a free-standing plate, the imparted impulse is less than I_o , and can be estimated as follows. When the pressure wave strikes a free standing plate, it sets the plate in motion and is partly reflected. Cavitation of the water occurs when the pressure at the interface between the plate and the fluid drops to zero; this occurs a time τ_c after initial impingement given by

$$\frac{\tau_c}{\theta} = \frac{1}{\psi - 1} \ln \psi, \tag{4}$$

where $\psi \equiv \rho_w c_w \theta / m_f$. The momentum per unit area I_{trans} transmitted into the plate up to the instant of cavitation is given by

$$I_{trans} = I_o \zeta, \tag{5a}$$

where

$$\zeta \equiv \psi^{\psi/(1-\psi)}. \tag{5b}$$

We shall investigate the failure modes of the clamped plate as a function of both the peak blast wave pressure p_o and the Taylor fluid-structure interaction parameter ψ .

2.2. Specimen configuration. Clamped circular copper plates of diameter 102 mm and thicknesses $h = 0.08$ mm and 0.25 mm were tested using the water shock tube sketched in [Figure 1](#). Eight equally spaced clearance holes for M8 bolts were drilled into the copper plates on a pitch circle of radius 41 mm, to enable clamping of the copper plate onto the end the water tube ([Figure 1](#)). To facilitate this an annular steel ring was used, of thickness 10 mm, inner radius 32 mm, and outer radius 51 mm. Thus, the effective radius of the clamped plate was $R = 32$ mm.

The water column is located in a steel tube of length $L = 1.3$ m, internal diameter $\phi = 64$ mm and wall thickness $w = 19$ mm. The tube is capped at one end by a 6 mm thick aluminum piston and at the opposite end by the copper specimen. The piston has an O-ring seal and contains a bleed valve to ensure that air is not trapped in the water column, as detailed by [Deshpande et al. \[2006\]](#). Dynamic loading is achieved by firing steel circular cylinders of diameter $d = 28.5$ mm and mass in the range 0.2 kg to 5 kg at the piston of the water tube. The water tube is aligned such that the projectile strikes the piston centrally and normally. The projectiles are accelerated using a gas gun of barrel length 4.5 m and inner diameter 28.5 mm. No sabot is employed and bursting of copper shim diaphragms forms the breach mechanism of the gas gun. The projectile velocity ranges from 10 ms^{-1} to 180 ms^{-1} , measured at the exit of the barrel using laser-velocity gates. The pressure transient in the water tube was measured using a high frequency piezoelectric pressure sensor. This pressure transducer, with an in-built charge amplifier, is specifically designed for shock tube and blast wave measurements. It has a dynamic measurement range of 0 to 300 MPa, a rise time of less than $1 \mu\text{s}$, and a resonant frequency above 500 kHz.

2.3. Test protocol. As discussed in [Section 2.1](#) above, the peak pressure and the decay time of the pressure transients in the shock tube were controlled by varying the projectile velocity and mass, respectively. Experiments were designed to span a range of peak pressures p_o and fluid-structure interaction parameter ψ for each plate thickness. High-speed photographic sequences of the dry face of the copper plates were taken using a Hadland 790 camera, thereby allowing for direct observation of the sequence of deformation and failure modes of the plates.

2.4. Material properties. The uniaxial tensile response of the copper used to manufacture the circular plate specimens was measured at a nominal strain rate of 10^{-3} s^{-1} , and the true tensile stress versus logarithmic plastic strain curve is plotted in [Figure 2](#). We denote this curve by $\sigma_0(\varepsilon^P)$. The measured 0.2% offset yield strength σ_Y was 220 MPa, and ultimate tensile strength $\sigma_{UTS} = 320$ MPa occurred at a tensile failure strain $\varepsilon_f \approx 22\%$.

[Lindholm \[1964\]](#) investigated the sensitivity of the stress-strain response of copper to plastic strain rate $\dot{\varepsilon}^P$ over the range $10^{-3} \text{ s}^{-1} < \dot{\varepsilon}^P < 10^4 \text{ s}^{-1}$. Their data suggest that the dynamic strength σ_d versus plastic strain ε^P of the copper used in the present study can be written in the form

$$\sigma_d(\varepsilon^P) = q(\dot{\varepsilon}^P) \sigma_0(\varepsilon^P), \quad (6)$$

where $\sigma_0(\varepsilon^P)$ is the uniaxial stress-strain curve of the present investigation at $\dot{\varepsilon}^P = 10^{-3} \text{ s}^{-1}$, as plotted in [Figure 2](#). The multiplying factor $q(\dot{\varepsilon}^P)$ denotes the ratio of the stress at an applied strain-rate $\dot{\varepsilon}^P$ to the stress at an applied strain rate $\dot{\varepsilon}^P = 10^{-3} \text{ s}^{-1}$. The stress versus strain histories measured by [Lindholm](#)

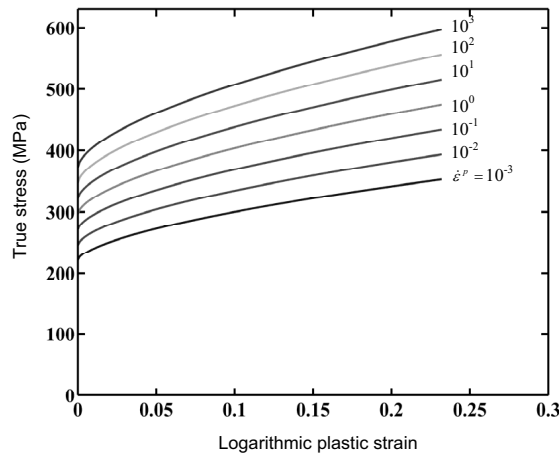


Figure 2. Measured uniaxial tensile response of the copper at an applied plastic strain rate $\dot{\varepsilon}^p = 10^{-3} \text{ s}^{-1}$. Estimated tensile stress versus strain histories for the copper at selected higher values of the applied strain-rate are also included using data from [Lindholm 1964].

[1964] indicate that q is reasonably independent of the magnitude of plastic strain ε^p . The estimates in Equation (6) of true tensile stress versus logarithmic plastic strain at selected values of $\dot{\varepsilon}^p$ are included in Figure 2.

3. Summary of experimental findings

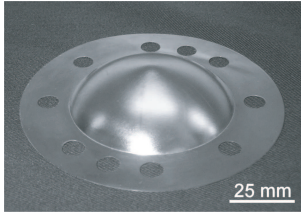
Results are described in detail for the $h = 0.25 \text{ mm}$ copper plates subjected to water blasts with a decay constant $\theta = 0.05 \text{ ms}$ (Taylor fluid-structure interaction parameter $\psi = 31$). Subsequently, we compare these findings with those for other values of ψ and for the $h = 0.08 \text{ mm}$ plate.

3.1. Failure modes of the $h = 0.25 \text{ mm}$ with $\psi = 31$. Post-test photographs of the $h = 0.25 \text{ mm}$ copper plates are shown in Figure 3. These specimens were subjected to water blasts of decay constant $\theta = 0.05 \text{ ms}$ and a range of peak pressures p_o . The deformation and failure modes are subdivided into three modes, consistent with the classification system of [Menkes and Opat 1973].

At low blast pressures ($p_o \leq 35 \text{ MPa}$), the plate undergoes plastic bending and stretching but no failure is observed (Figure 3a). This is the dishing mode, and is referred to as *mode I*. High speed photography revealed that the deformation mode involves plastic hinges traveling from the periphery to the center of the plate, followed by stretching and bending of the plate in a manner similar to the quasistatic deformation mode of a clamped circular plate under uniform transverse pressure. This deformation history supports several theoretical predictions [Wang and Hopkins 1954; Florence 1966].

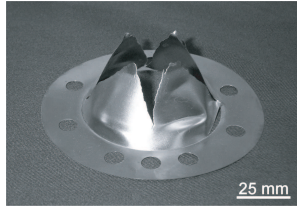
At intermediate blast pressures, a variety of tensile failure modes of the plates are triggered (Figure 3b). These are labeled as *mode II* failures, wherein the plates assume a dome-shaped final profile with failure at the center and/or periphery. In particular, the following modes were observed:

(a) Mode I



$p_0 = 34 \text{ MPa}$ ($w_B = 16.8 \text{ mm}$)

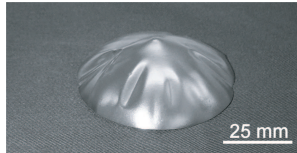
(b) Mode II



$p_0 = 64 \text{ MPa}$

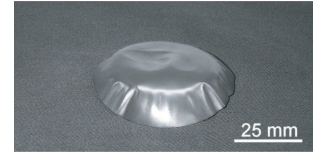


$p_0 = 88 \text{ MPa}$



$p_0 = 130 \text{ MPa}$

(c) Mode III



$p_0 = 137 \text{ MPa}$



$p_0 = 173 \text{ MPa}$

Figure 3. Post-test photographs of the $h = 0.25 \text{ mm}$ copper plates subjected to $\theta = 0.05 \text{ ms}$ water blasts for a range of peak pressures p_o . The deformation and failure modes have been divided into three modes motivated by the classification system introduced by [Menkes and Opat \[1973\]](#). The final mid-span deflection of the plate in mode I is marked for (a).

- (i) at $p_o = 64 \text{ MPa}$, the plate fails by the formation of four petals. We shall show subsequently that this failure is initiated by the onset of tearing at the center of the plate;
- (ii) with increasing blast pressure, failure initiates at the center of the plate but the petals do not fully develop. Tearing at the supports intervenes ($110 \text{ MPa} < p_o < 120 \text{ MPa}$);
- (iii) at higher pressures ($130 \text{ MPa} < p_o < 135 \text{ MPa}$) the plate tears at the inner periphery of the annular clamps, with no failure at the center of the plate.

For the highest pressures investigated here ($p_o \geq 137 \text{ MPa}$), the plate tears off the supports before the traveling hinges have reached the center of the plate, and the final deformed shape of the plates resembles a flat-topped dome with failure at the periphery ([Figure 3c](#)). This mode is reminiscent of the *shear-off mode III* as identified by [Menkes and Opat \[1973\]](#). Here we arbitrarily define mode III failures as those cases where the plates cleanly tears at the supports with the traveling hinges not reaching the mid-span of the plate, giving rise to the flat-topped final deformed profiles of the plates ([Figure 3c](#)).

3.2. High speed photographic sequences of the failure modes for the $h = 0.25 \text{ mm}$ plates with $\psi = 31$.

High speed photographic sequences of the deformation and failure modes of the plates are included

in Figures 4–6 for increasing values of the blast pressure p_o . In each of the photographic sequences traveling hinges initiate at the supports and travel towards the mid-span of the plate. At $p_o = 64$ MPa (Figure 4), a mode II failure initiates at the mid-span immediately after the traveling hinges coalesce there. Petalling of the plates is evident, with the resulting outburst of the water. In Figure 5 ($p_o = 130$ MPa), we observe that the plate tears off from the supports prior to the traveling hinges reaching mid-span. Note that wrinkling of the plates near the supports at $t = 50 \mu s$ indicates that the plate has detached from the supports. However, the hinges continue to travel towards the mid-span after the plate has separated from the supports, as evidenced by the photographs for $t > 50 \mu s$ and the final deformed shape. For this level of blast pressure the plate only acquires a uniform velocity after the traveling hinges have coalesced at mid-span. At a blast pressure $p_o = 173$ MPa (Figure 6), the plate again tears from the supports at $t = 50 \mu s$. After circumferential tearing has completed, the hinges remain very close to the supports, and the plate acquires a final, spatially uniform velocity. The final deformed shape of the plate is reminiscent of the shear-off mode III of [Menkes and Opat 1973].

3.3. Examination of fracture surfaces. The plates failed either at mid-span after coalescence of traveling plastic hinges or at the supports. The macroscopic failure modes are shear-off near the supports and petalling by tensile necking. It is instructive to determine whether the microscopic mode of failure (tension versus shear) is the same as that suggested by the macroscopic mode. In order to address this, scanning electron micrographs of the failure surfaces of the plates subjected to blast pressures $p_o = 64$ MPa and 173 MPa ($\psi = 31$) are shown in Figures 7 and 8, respectively. It is concluded from the micrographs that the local failure mechanism is tensile necking, regardless of whether the macroscopic mode is petalling (at $p_o = 64$ MPa) or shear-off ($p_o = 173$ MPa). We conclude that the thin copper plates fail by local tensile necking over the entire range of blast pressures considered.

3.4. Failure mechanism maps. Consider a clamped circular plate of radius R and thickness h made from a rigid, ideally plastic material of yield strength σ_Y and density ρ_f . This plate is subjected to a spatially uniform underwater blast of the form of Equation (1). Following Fleck and Deshpande [2004] we can argue that the response can be temporally decoupled into two stages. First, in a fluid-structure interaction phase, the plate acquires a momentum I_{trans} as given by analysis of [Taylor 1941]. Subsequent loading by the water is neglected and the second phase of the response reduces to the classical problem of an impulsively loaded clamped plate as analyzed (for small deflections) by Wang and Hopkins [1954]. The relevant nondimensional groups governing the deformation of the plate are

- (i) the aspect ratio of the plate $\frac{R}{h}$, and
- (ii) the nondimensional transmitted impulse $\frac{I_{trans}}{(h\sqrt{\rho_f\sigma_Y})}$.

For the large values of ψ considered in this study, the Taylor estimate (Equation (5)) for the transmitted impulse reduces to

$$I_{trans} \approx \frac{2\rho_f h p_o}{\rho_w c_w}, \tag{7}$$

independent of the value of θ . This suggests that the deformation and failure of the plates are only dependent on the peak pressure of the blast p_o and independent of the decay constant θ . We shall gauge the validity of this prediction by experimentally probing the failure modes of the plates for a decay constant in the range $0.05 \text{ ms} \leq \theta \leq 1.1 \text{ ms}$.

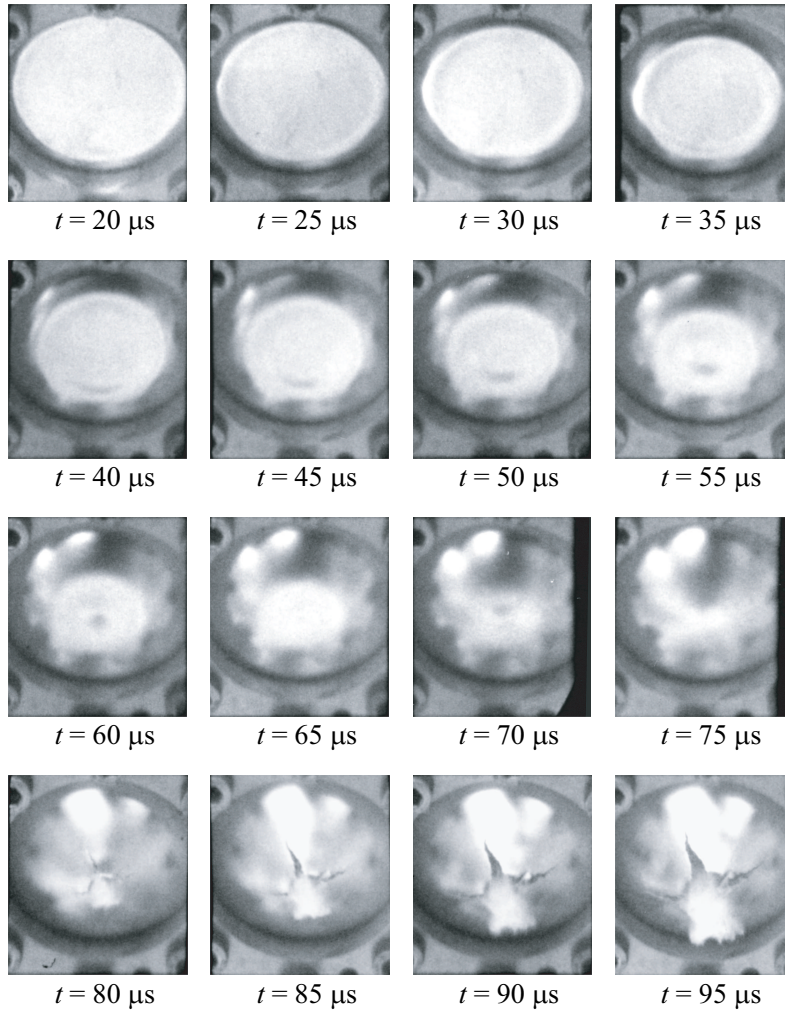


Figure 4. High-speed photographic sequence (exposure time $4 \mu\text{s}$) of the $h = 0.25 \text{ mm}$ copper plate subjected to a blast with a peak pressure $p_o = 64 \text{ MPa}$ and decay constant $\theta = 0.05 \text{ ms}$ (mode II: petalling failure). Time after the arrival of the shock is indicated for each frame.

The response of the plates can be determined in terms of four independent nondimensional groups: R/h , ρ_f/ρ_w , p_o/σ_{UTS} , and $h/(c_w\theta)$. With ρ_f/ρ_w held fixed in this study we plot maps using axes of the peak blast pressure normalized by the ultimate tensile strength of the copper, p_o/σ_{UTS} , and the normalized plate thickness, $h/(c_w\theta)$, for two values of R/h corresponding to the $h = 0.25 \text{ mm}$ and 0.08 mm plates investigated here. The observed failure modes of the copper plates are summarized in maps in [Figure 9](#) for the $h = 0.25 \text{ mm}$ ($R/h = 128$) and 0.08 mm ($R/h = 400$) plates, respectively. The maps were generated as follows. For each plate thickness, experiments were performed for a fixed value of θ and increasing values of p_o . The failure modes (according to the classification system of [Section 3.1](#)) were determined by post-test examination of the specimens. The procedure was repeated for selected

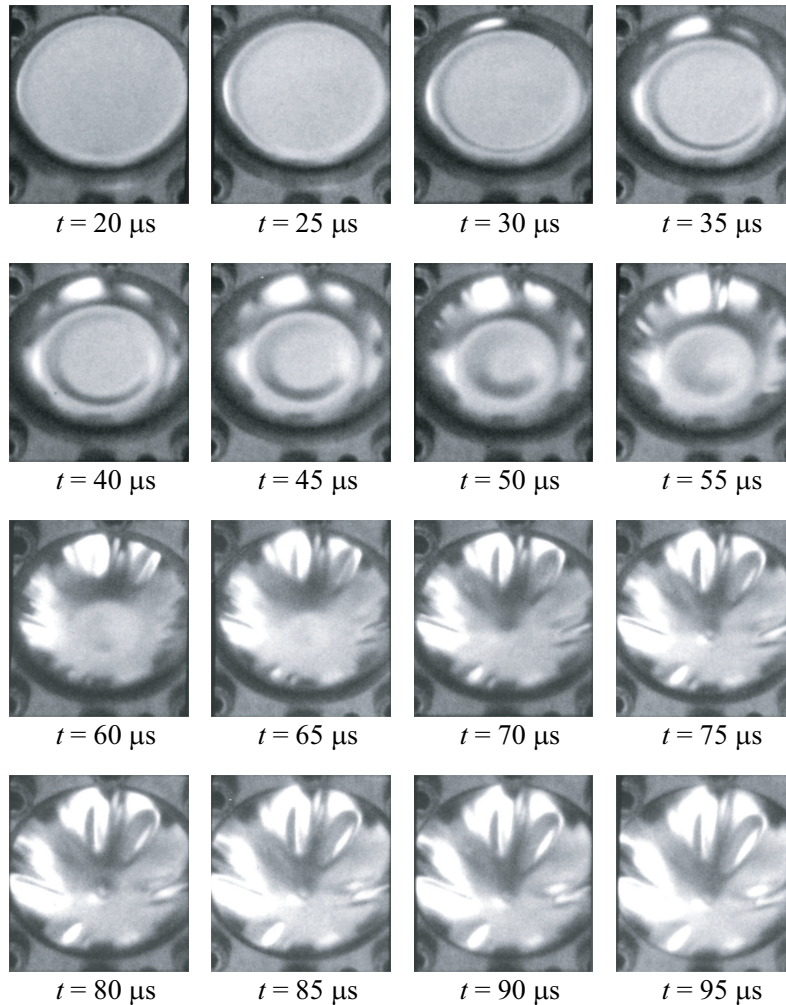


Figure 5. High-speed photographic sequence (exposure time $4 \mu\text{s}$) of the $h = 0.25 \text{ mm}$ copper plate subjected to a blast with a peak pressure $p_o = 130 \text{ MPa}$ and decay constant $\theta = 0.05 \text{ ms}$ (mode II: support failure). Time after the arrival of the shock is indicated for each frame.

values of the decay constant θ for each plate thickness. The boundaries between the modes are included on the figures.

The following deductions are made from the failure mechanism maps:

- (i) For both plate thicknesses and for all values of θ considered here, the failure mode switches from mode I through to mode III with increasing p_o .
- (ii) In line with the expectations outlined at the beginning of [Section 3.4](#), the failure modes are primarily a function of the peak pressure p_o , and are only weakly depend upon the value of the wave decay constant; upon increasing θ by nearly two orders of magnitude, the peak pressure to transit from mode II to mode III decreases by only a factor of two.

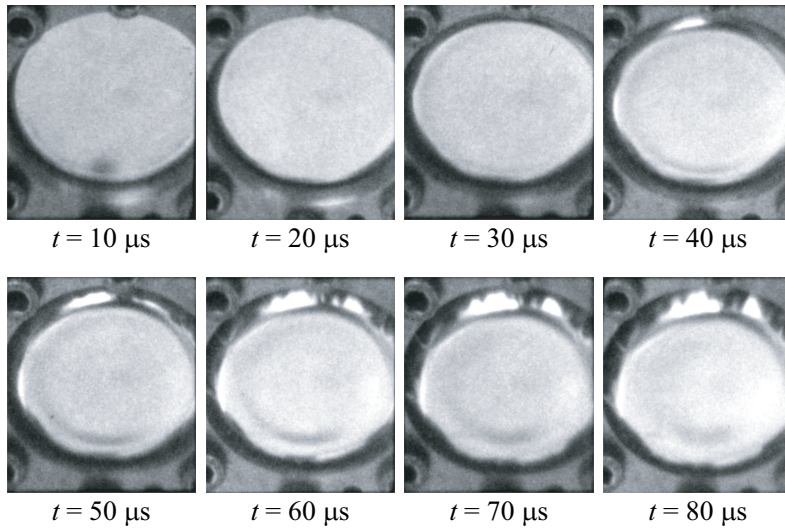


Figure 6. High-speed photographic sequence (exposure time $4 \mu\text{s}$) of the $h = 0.25 \text{ mm}$ copper plate subjected to a blast with a peak pressure $p_o = 173 \text{ MPa}$ and decay constant $\theta = 0.05 \text{ ms}$ (mode III support failure). Time after the arrival of the shock is indicated for each frame.

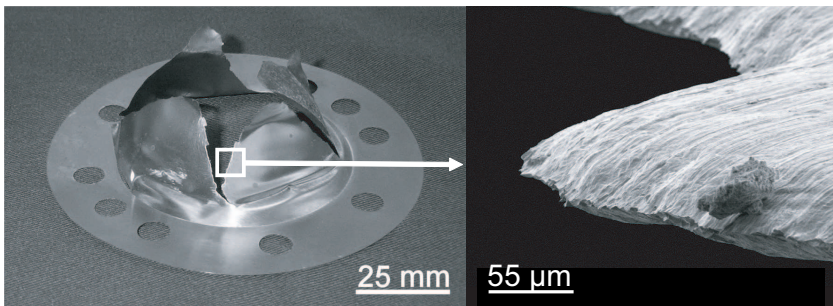


Figure 7. Scanning electronic micrographs of the failed surface of the $h = 0.25 \text{ mm}$ copper plate subjected to a blast with a $p_o = 64 \text{ MPa}$ and decay constant $\theta = 0.05 \text{ ms}$.

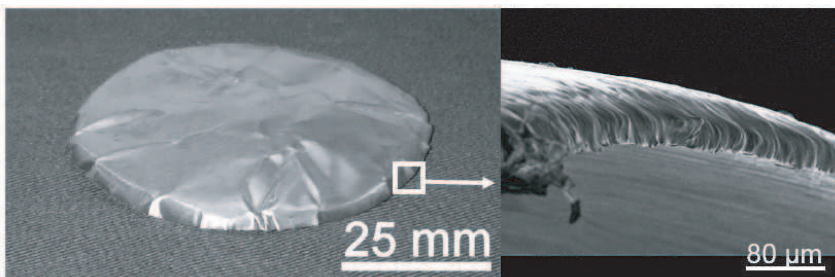


Figure 8. Scanning electronic micrographs of the failed surface of the $h = 0.25 \text{ mm}$ copper plate subjected to a blast with a $p_o = 173 \text{ MPa}$ and decay constant $\theta = 0.05 \text{ ms}$.

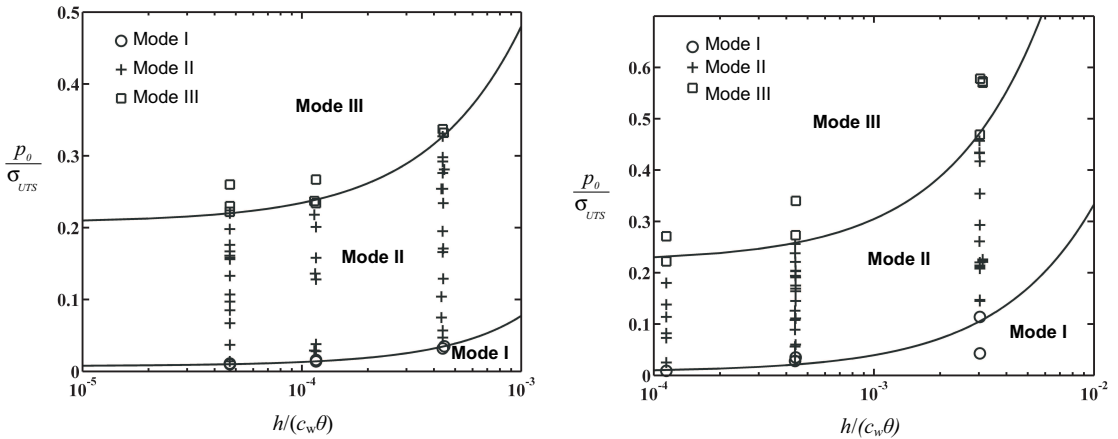


Figure 9. The regimes of dominance of the observed three modes of deformation and failure are indicated on a map of normalized peak pressure and nondimensional plate thickness for the $h = 0.25$ mm ($R/h = 128$) (above) and $h = 0.08$ mm ($R/h = 400$) (below) copper plates.

We also note that the failure mechanism maps for both the plate thicknesses ($R/h = 128$ and 400) are very similar. This suggests that, at least for $R/h \geq 128$, the plate aspect ratio does not significantly affect the failure modes of the copper plates. It is concluded that the blast pressure dictates the operative failure mode.

4. Numerical investigation of the failure modes

We proceed to present a limited numerical investigation into the failure modes of the copper plates. The aim is to determine the capability of a finite element model in capturing the range of failure modes observed in the experiments described above. Attention is restricted to the choice $h = 0.25$ mm subjected to underwater blasts with decay constant $\theta = 0.05$ ms ($\psi = 31$).

4.1. Finite element model. Finite element calculations of the response of the clamped plates were performed using the explicit time integration version of the commercial finite element package ABAQUS. The circular plates of radius $R = 32$ mm were modeled using three-dimensional 4-noded quadrilateral shell elements (of type S4R in ABAQUS notation) with 5 integration points through the thickness of the elements. In most of the calculations, the elements were of approximate in-plane dimension $30 \mu\text{m} \times 90 \mu\text{m}$ near the center of the plate (57600 elements in total); the effect of mesh size upon the predicted deformation and failure response is discussed below in Section 4.3. The boundary conditions were as follows. The circular plate was clamped along its periphery with all displacement and rotational degrees of freedom constrained to zero. The experimental results presented in Section 3 suggest that it is acceptable to decouple the fluid-structure interaction phase from the stretching and bending phases of the plate response. Hence we did not explicitly model the fluid-structure interaction phase. Instead, the estimate of [Taylor 1941] was employed to determine the blast momentum transmitted into the plate. We

assumed that the blast imparts a spatially uniform velocity

$$v_o = \frac{2p_o\theta\xi}{\rho_f h} \quad (8)$$

to the plate. This velocity was applied as an initial velocity boundary condition to the entire plate and the subsequent deformation and failure were determined by the finite element method.

4.2. Assumed constitutive description for the copper. The copper was modelled as a J2-flow theory rate dependent solid of density $\rho_f = 8960 \text{ kgm}^{-3}$, Young's modulus $E = 105 \text{ GPa}$, and Poisson ratio $\nu = 0.34$. The uniaxial tensile true stress versus equivalent plastic strain curves at plastic strain-rates $10^{-3} \text{ s}^{-1} \leq \dot{\varepsilon}^p \leq 10^4 \text{ s}^{-1}$ were tabulated in ABAQUS using the data of Figure 2. In addition, it was assumed that the copper lost all strength at a material point when the effective plastic strain ε^p attained the tensile failure strain in a quasistatic tension test $\varepsilon_f = 0.22$. For simplicity, this failure strain is assumed to be independent of strain-rate and stress triaxiality¹. Formally, the failure criterion is expressed in terms of damage parameter ω , defined as

$$\omega = \int_0^t \frac{d\varepsilon^p}{\varepsilon_f}. \quad (9)$$

Failure occurs when $\omega = 1$, whereupon the failed element is deleted from the calculation.

We emphasize that the assumed failure criterion contains no material length, and consequently the predictions of the numerical simulations are inherently mesh-size dependent (see [Needleman and Tvergaard 1994; Gullerud et al. 2000]). The mesh size w , coupled with the failure strain, dictates the amount of localized deformation that occurs on the fracture plane, and the displacement jump across the critical element is analogous to the critical displacement in a cohesive zone formulation. Thus, for an ideally plastic material with a yield strength σ_Y , the intrinsic mode I crack tip toughness K_{IC} is given as $K_{IC} \sim \sqrt{Ew\sigma_Y\varepsilon_f}$ (w being the element width), as discussed by Nahshon et al. [2007]. Thus with $w = 90 \mu\text{m}$ and $\sigma_Y = 220 \text{ MPa}$, this implies that the assumed fracture toughness $K_{IC} \approx 22 \text{ MPa m}^{1/2}$, which is consistent with a wide body of experimental data for copper. In addition to its role in determining toughness, the mesh size governs the resolution of the predicted strain distribution adjacent to the crack tip. Consequently, the selected mesh must be sufficiently fine to ensure adequate strain resolution, yet be of sufficient size to give a realistic toughness.

4.3. Illustration of mesh size dependence of the failure predictions. A scoping study of the failure of circular plates subjected to impulsive loads was performed in order to investigate the effect of mesh size on the failure predictions. To simplify the calculations we considered an axisymmetric FE model of a clamped circular copper plate of radius $R = 32 \text{ mm}$ and thickness $h = 0.25 \text{ mm}$. The FE model comprised 2 noded axisymmetric shell elements (SAX1 in the ABAQUS notation), and the element size w was varied from 0.03 mm to 1.0 mm. All degrees of freedom were constrained at the plate periphery at radial distance $r = R$. The plate was given a spatially uniform initial velocity v_o in the axial direction. For a given mesh size w , v_o was increased in steps of 5 ms^{-1} , and the critical velocity v_{crit} at which failure of the plate at the supports first occurs was determined from the FE calculations.

¹Very low hydrostatic stresses are generated in these thin plates and hence it is considered reasonable to neglect the effect of stress triaxiality on ε_f .

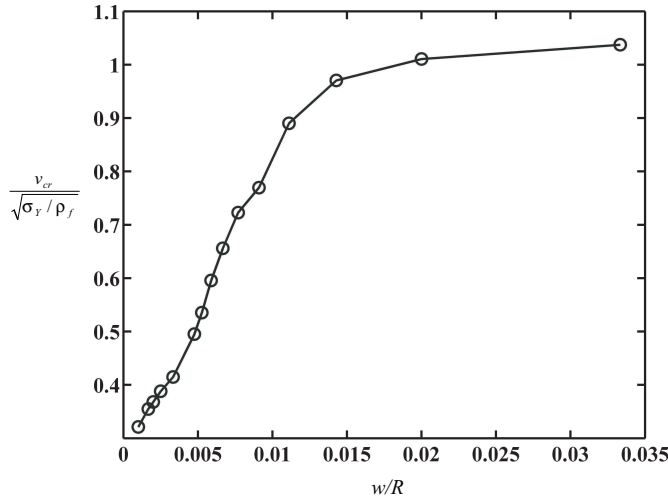


Figure 10. Illustration of the mesh dependence of predictions. Axisymmetric FE predictions of the normalized velocity at which the $h = 0.25$ mm copper plate first fails at the supports as a function of the normalized mesh size.

The normalized critical velocity $v_{crit}/\sqrt{\sigma_Y/\rho_f}$ is plotted in [Figure 10](#) as a function of the normalized mesh size w/R . Here, $\sigma_Y = 220$ MPa is the quasistatic yield strength of copper. We observe that v_{crit} increases monotonically with increasing w for all mesh sizes investigated here. This is rationalized by recalling that the toughness of the copper in the FE model scales with w . It is emphasized that no independent measurements of the toughness were made in order to determine the appropriate value of w . Rather, we choose a mesh size to ensure agreement with the experimentally observed failure modes over the entire range of pressures investigated here.

4.4. Numerical results. We proceed to show comparisons between the FE predictions and experimental observations of the failure of the $h = 0.25$ mm copper plates subjected to an underwater blast with decay constant $\theta = 0.05$ ms ($\psi = 31$). As mentioned above, in the FE calculations, the fluid-structure interaction was not modeled explicitly and the initial velocity, as given by [Equation \(8\)](#), was imparted to the plate for each value of the peak blast pressure p_o .

FE predictions of the time sequences of the deformation of the plates subjected to blast pressures $p_o = 84$ MPa and 170 MPa are given in [Figures 11](#) and [12](#), respectively. For the choice $p_o = 84$ MPa the calculated failure mode of petalling resembles the observed mode in [Figure 5](#). However, the predicted value of required pressure level for petalling is about 20% higher than the measured value. This discrepancy may be due to: (i) the FE calculations neglect additional fluid loading after first cavitation, and (ii) the failure model employed in the FE calculations overestimates the material toughness at low values of the blast pressures. Moreover, unlike in the experiments, the petals in the FE calculations do not reach the plate periphery. Recall that the element sizes in the FE calculation increases towards the plate periphery, resulting in an increase in the material toughness towards the periphery. Thus, the petals in the FE calculation are arrested at approximately $r = R/2$ in the FE calculations.

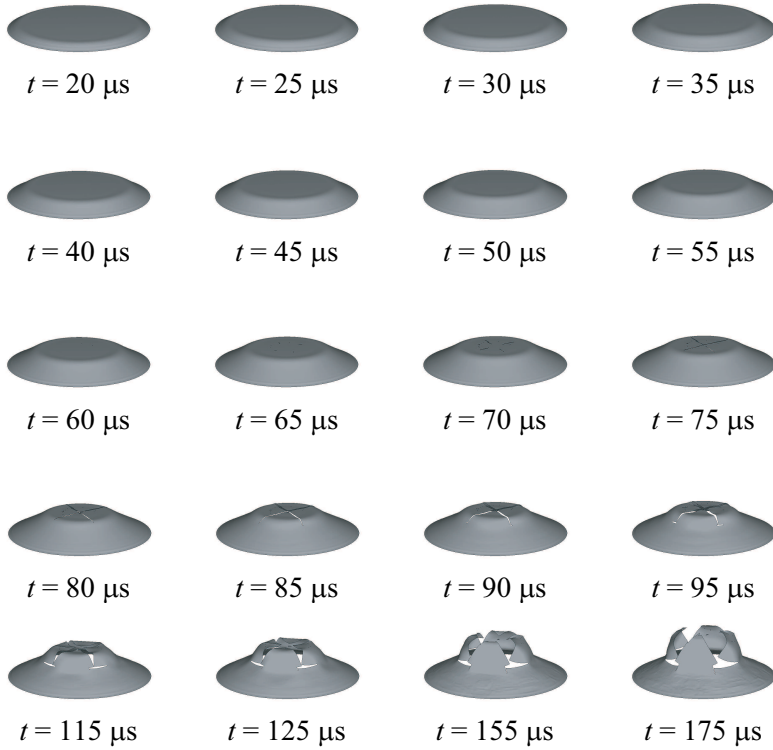


Figure 11. FE predictions of the evolution of the deformation and failure of the $h = 0.25$ mm copper plate subjected to a blast with a peak pressure $p_o = 84$ MPa and decay constant $\theta = 0.05$ ms. The petalling failure mode (mode II) similar to the observations (Figure 4) is predicted.

The FE prediction for (mode III) at $p_o = 170$ MPa is in good qualitative agreement with the observed response at $p_o = 173$ MPa; compare Figures 6 and 12. Failure at the periphery of the plate is evident in both cases.

Comparisons between the observed and FE predictions of the final deformed shapes of the copper plates subjected to a range of blast pressures are included in Figure 13. These comparisons indicate that over the whole range of pressures investigated here, reasonable agreement between the observed and FE predictions of failure modes is obtained. It is worth noting that the FE predictions have sufficient fidelity to capture the wrinkling of the plates near the failure surfaces for the $p_o = 125$ MPa and $p_o = 170$ MPa.

5. Concluding remarks

A water shock tube has been employed to investigate the deformation and failure modes of clamped circular copper plates of radius 32 mm and thicknesses 0.08 mm and 0.25 mm. The plates were subjected to blast waves with peak pressures in the range 10 MPa to 120 MPa and decay constants varying between 0.05 ms to 1.1 ms. The deformation and failure modes were observed via high-speed photography.

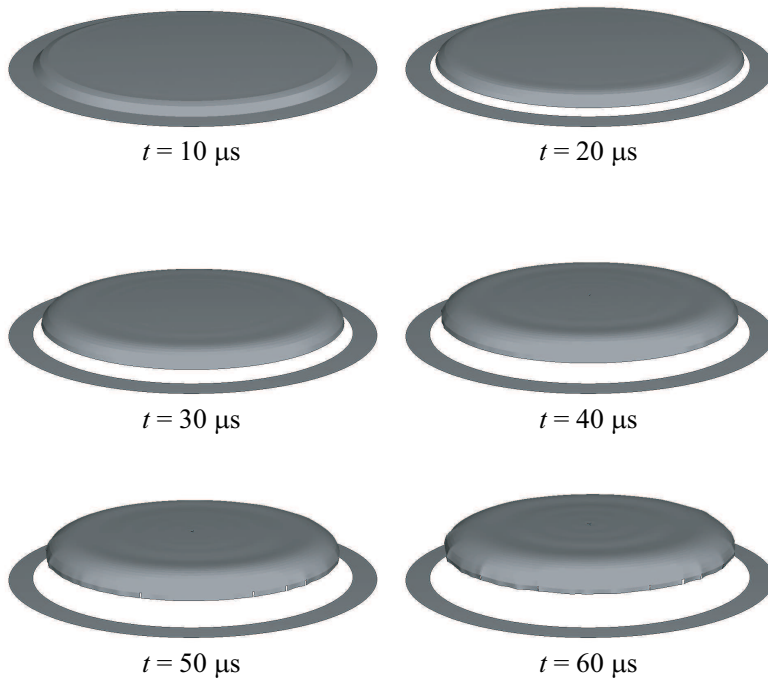


Figure 12. FE predictions of the evolution of the deformation and failure of the $h = 0.25$ mm copper plate subjected to a blast with a peak pressure $p_o = 170$ MPa and decay constant $\theta = 0.05$ ms. Support failure with negligible deformation of the plate (mode III) similar to the observations (Figure 6) is predicted. The clamped portion of the plate is sketched in to clearly illustrate failure.

For the thin plates considered in this study, the failure modes were primarily governed by the peak pressures and were relatively insensitive to the blast wave decay constant. Three modes of deformation and failure were identified. At low pressures, plastic bending and stretching of the plates occurred with no observable failures (mode I). At moderate pressures, the plates assume a dome-shaped final profile with failure at the mid-span and/or periphery. This is termed mode II failure. At the highest pressures investigated here mode III failure occurs: the plate tears at the supports while remaining almost flat. Consequently, the final deformed profile of the plates resembles a flat-topped dome with failure at the periphery. This mode is reminiscent of the shear-off failure reported by [Menkes and Opat \[1973\]](#). Scanning electron micrographs of the failure surfaces showed that in all cases, the local failure mechanism was tensile necking.

A limited number of finite element (FE) calculations were performed to investigate the fidelity of such simulations to capture the observed deformation and failure modes. A simple critical shear strain failure criterion was employed to model material rupture. As there is no intrinsic length scale in the failure criterion, the simulations are mesh size dependent: the mesh size combined with the material properties dictates the material toughness in such an approach. With an appropriate calibration of the mesh size, the FE calculations captured all the observed failure modes to sufficient fidelity.

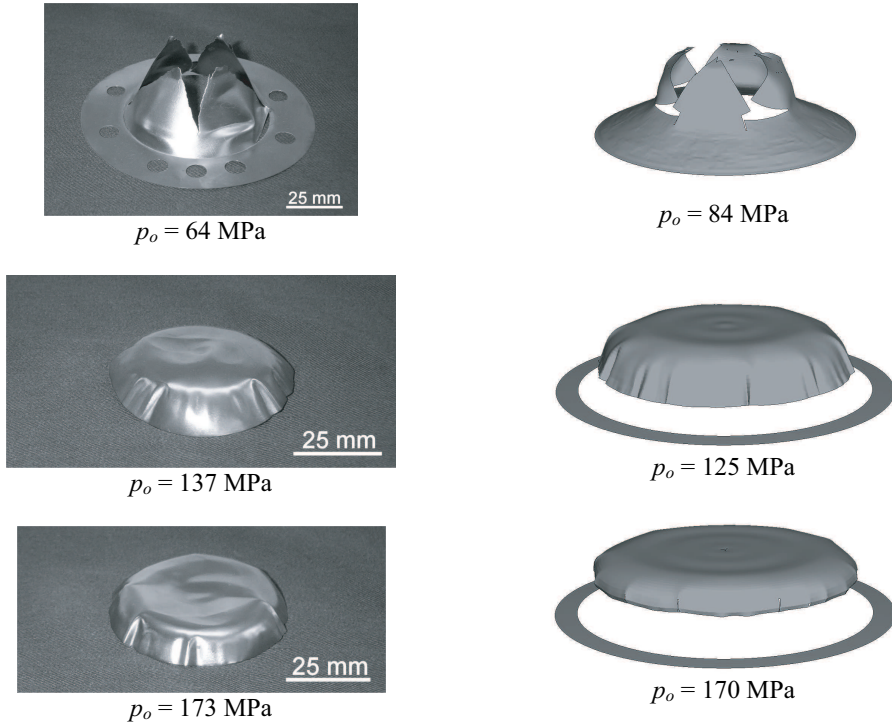


Figure 13. Comparisons between the observed and FE predictions of the final deformed shapes of the $h = 0.25 \text{ mm}$ copper plates subjected to a range of blast pressures with a decay constant $\theta = 0.05 \text{ ms}$. The clamped portions of the plates are sketched in for the $p_o = 125 \text{ MPa}$ and $p_o = 170 \text{ MPa}$ calculations to clearly illustrate the failure.

Acknowledgements

The authors are grateful to ONR for their financial support through USONR IFO grant number N00014-03-1-0283 on The Science and Design of Blast Resistant Sandwich Structures and to the Isaac Newton Trust, Trinity College Cambridge.

References

- [Balden and Nurick 2005] V. H. Balden and G. N. Nurick, “Numerical simulation of the post-failure motion of steel plates subjected to blast loading”, *Int. J. Impact Eng.* **32** (2005), 14–34.
- [Deshpande et al. 2006] V. S. Deshpande, A. Heaver, and N. A. Fleck, “An underwater shock simulator”, *Proc. R. Soc. Lon. Ser-A* **462** (2006), 1021–1041.
- [Fleck and Deshpande 2004] N. A. Fleck and V. S. Deshpande, “Shock resistance of sandwich beams”, *J. Appl. Mech. (Trans. ASME)* **71** (2004), 386–401.
- [Florence 1966] A. L. Florence, “Circular plate under a uniformly distributed impulse”, *Int. J. Solids Struct.* **2** (1966), 37–47.
- [Gullerud et al. 2000] A. S. Gullerud, X. Gao, B. Dodds Jr., and R. Haj-Ali, “Simulation of ductile crack growth using computational cells: numerical aspects”, *Eng. Fract. Mech.* **66** (2000), 65–92.
- [Lee and Wierzbicki 2005a] Y.-W. Lee and T. Wierzbicki, “Fracture prediction of thin plates under localized impulsive loading. part I: dishing”, *Int. J. Impact Eng.* **31** (2005a), 1253–1276.

- [Lee and Wierzbicki 2005b] Y.-W. Lee and T. Wierzbicki, “Fracture prediction of thin plates under localized impulsive loading. part II: discing and petalling”, *Int. J. Impact Eng.* **31** (2005b), 1277–1308.
- [Liang et al. 2006] Y. Liang, A. V. Spuskanyuk, S. E. Flores, D. R. Hayhurst, J. W. Hutchinson, R. M. McMeeking, and A. G. Evans, “Response of metallic sandwich panels to water blasts”, *J. Appl. Mech. (Trans. ASME)* (2006). In Press.
- [Lindholm 1964] U. S. Lindholm, “Some experiments with the split Hopkinson pressure bar”, *J. Mech. Phys. Solids* **12** (1964), 317–335.
- [Menkes and Opat 1973] S. B. Menkes and H. J. Opat, “Tearing and shear failure in explosively loaded clamped beams”, *Exp. Mech.* **13** (1973), 480–486.
- [Nahshon et al. 2007] K. Nahshon, M. G. Pontin, A. G. Evans, J. W. Hutchinson, and F. W. Zok, “Dynamic shear rupture of steel plates”, *Journal of the Mechanics of Materials and Structures* **This issue** (2007).
- [Needleman and Tvergaard 1994] A. Needleman and T. Tvergaard, “Mesh effects in the analysis of dynamic ductile crack growth”, *Eng. Fract. Mech.* **47** (1994), 75–91.
- [Nurick and Shave 2000] G. N. Nurick and G. C. Shave, “The deformation and tearing of thin square plates subjected to impulsive loads- an experimental study”, *Int. J. Mech. Sci.* **18** (2000), 99–116.
- [Radford et al. 2005] D. D. Radford, N. A. Fleck, and V. S. Deshpande, “The response of clamped sandwich beams subjected to shock loading”, *Int. J. Impact Eng.* **32** (2005), 968–987.
- [Rathbun et al. 2006] H. J. Rathbun, D. D. Radford, Z. Xue, M. Y. He, J. Yang, V. S. Deshpande, N. A. Fleck, J. W. Hutchinson, F. W. Zok, and A. G. Evans, “Performance of metallic honeycomb-core sandwich beams under shock loading”, *Int. J. Solids Struct.* **43** (2006), 1746–1763.
- [Taylor 1941] G. I. Taylor, “The pressure and impulse of submarine explosion waves on plates”, pp. 287–303 in *The scientific papers of G. I. Taylor*, vol. III, Cambridge University Press, 1963, 1941.
- [Wang and Hopkins 1954] A. J. Wang and H. G. Hopkins, “On the plastic deformation of built-in circular plates under impulsive load”, *J. Mech. Phys. Solids* **3** (1954), 22–37.
- [Xue and Hutchinson 2003] Z. Xue and J. W. Hutchinson, “Preliminary assessment of sandwich plates subject to blast loads”, *Int. J. Mech. Sci.* **45** (2003), 687–705.

Received 5 Sep 2007. Accepted 7 Sep 2007.

SOHRAB KAZEMAHVAZI: sohrabk@kth.se
Cambridge University Engineering Department, Trumpington Street, Cambridge, CB2 1PZ, United Kingdom

DARREN RADFORD: radfordd@aecl.ca
Cambridge University Engineering Department, Trumpington Street, Cambridge, CB2 1PZ, United Kingdom

VIKRAM S. DESHPANDE: vsd@eng.cam.ac.uk
Cambridge University Engineering Department, Trumpington Street, Cambridge, CB2 1PZ, United Kingdom

NORMAN A. FLECK: naf1@eng.cam.ac.uk
Cambridge University Engineering Department, Trumpington Street, Cambridge, CB2 1PZ, United Kingdom

DYNAMIC COMPRESSION OF SQUARE HONEYCOMB STRUCTURES DURING UNDERWATER IMPULSIVE LOADING

HAYDN N. G. WADLEY, KUMAR P. DHARMASENA, DOUG T. QUEHEILLALT, YUNGCHIA CHEN,
PHILIP DUDT, DAVID KNIGHT, KEN KIDDY, ZHENYU XUE AND ASHKAN VAZIRI

Significant reductions in the fluid structure interaction regulated transfer of impulse occur when sandwich panels with thin (light) front faces are impulsively loaded in water. A combined experimental and computational simulation approach has been used to investigate this phenomenon during the compression of honeycomb core sandwich panels. Square cell honeycomb panels with a core relative density of 5% have been fabricated from 304 stainless steel. Back supported panels have been dynamically loaded in through thickness compression using an explosive sheet to create a plane wave impulse in water. As the impulse was increased, the ratio of transmitted to incident momentum decreased from the Taylor limit of 2, for impulses that only elastically deformed the core, to a value of 1.5, when the peak incident pressure caused inelastic core crushing. This reduction in transmitted impulse was slightly less than that previously observed in similar experiments with a lower strength pyramidal lattice core and, in both cases, was well above the ratio of 0.35 predicted for an unsupported front face. Core collapse was found to occur by plastic buckling under both quasistatic and dynamic conditions. The buckling occurred first at the stationary side of the core, and, in the dynamic case, was initiated by reflection of a plastic wave at the (rigid) back face sheet-web interface. The transmitted stress through the back face sheet during impulse loading depended upon the velocity of the front face, which was determined by the face sheet thickness, the magnitude of the impulse, and the core strength. When the impulse was sufficient to cause web buckling, the dynamic core strength increased with front face velocity. It rose from about 2 times the quasistatic value at a front face initial velocity of 35 m/s to almost 3 times the quasistatic value for an initial front face velocity of 104 m/s. The simulations indicate that this core hardening arises from inertial stabilization of the webs, which delays the onset of their buckling. The simulations also indicate that the peak pressure transmitted to a support structure from the water can be controlled by varying the core relative density. Pressure mitigation factors of more than an order of magnitude appear feasible using low relative density cores. The study reveals that for light front face sandwich panels the core strength has a large effect upon impulse transfer and the loading history applied to support structures.

1. Introduction

Metallic sandwich panels with cellular cores have attracted significant attention for dynamic energy absorption and impact mitigation [Baker et al. 1998; Fleck and Deshpande 2004; 2005; Hutchinson and Xue 2005; Deshpande et al. 2006; Rathbun et al. 2006; Dharmasena et al. 2007b; Liang et al. 2007]. During impact with rigid objects, they reduce damage to the structures they protect by core crushing and face sheet stretching at pressures significantly less than those created when an equivalent solid is

Keywords: sandwich panels, honeycomb cores, impulse loading, cellular structures.

impacted. When sandwich panel structures are impulsively loaded in water, additional mitigation is possible because of beneficial fluid structure interactions (FSI) with thin face sheets [Fleck and Deshpande 2004; Hutchinson and Xue 2005].

The origin of the FSI enhancement arises from a reduction in the reflection coefficient of a normally incident shock front with a solid structure. The pressure pulse from a detonation in water exhibits a sharp rise to a peak pressure and is followed by a slower decay [Cole 1948]. The pressure, $p(t)$, can be written

$$p(t) = p_0 e^{-t/t_0},$$

where p_0 is the peak pressure, t is time measured from the peak in pressure and t_0 is a characteristic time constant. The impulse per unit area, I_0 , transported by the pressure pulse through the fluid is given by

$$I_0 = \int_0^{\infty} p(t) dt = p_0 t_0.$$

Taylor [1963] showed that in the linear (acoustic) fluid propagation limit, the pressure pulse is totally reflected at the surface of a rigid structure, or one with very heavy face sheets. The impulse I transmitted to the structure is then twice that of the incident pulse. An extension of Taylor's theory for FSI in air blasts, which accounts for nonlinear compressibility and finite shock behavior, was recently proposed [Kambouchev et al. 2006] and employed to assess the performance of all-metal sandwich plates under high intensity air shocks [Vaziri and Hutchinson 2007]. In this the reflection coefficient depends upon the peak pressure, and can reach a value of 8 for ideal gases, and higher values when dissociation occurs.

When an unsupported thin (light) panel or a sandwich panel with thin faces and a very weak core is impulsively loaded in water, the front face sheet can move away from the impulse, and the transmitted pressure and impulse are then less than the Taylor prediction [Taylor 1963; Fleck and Deshpande 2004; Hutchinson and Xue 2005]. The effect is strongest for water borne impulses. In the acoustic limit, the transmitted impulse I when a core has no strength depends only upon the thickness of the front face sheet, the density of the material it is made of, and the decay time (t_0) of the pulse, as

$$I = 2I_0 q^{q/(1-q)}, \quad (1)$$

where

$$q = \frac{\rho_w c_w}{\rho h_f} t_0,$$

in which ρ_w is the density of and c_w the speed of sound in the acoustic medium, and ρ is the density and h_f the thickness of the face sheet. The mass per unit area of the face sheet, m_f , is the ρh_f product. The ratio $\rho_w c_w / m_f$ is an important dimensionless quantity which controls the impulse transferred to a plate structure. For very heavy plates, Equation (1) gives Taylor's result, but for thinner plates, large reductions in impulse can occur. For example, a 5 mm thick, 304 stainless steel plate loaded in water has $m_f = 40 \text{ kg/m}^2$, $\rho_w = 1000 \text{ kg/m}^3$, and $c_w = 1400 \text{ m/s}$. If $t_0 = 0.1 \text{ ms}$, $q = 3.5$, and the impulse transmitted from water to such a face sheet is only 0.35 times that of the incident pulse.

In sandwich panels with strong cores, front face sheet motion is resisted by the core [Xue and Hutchinson 2006; Liang et al. 2007]. Recent measurements of the impulse transmitted into fully back supported sandwich panels with pyramidal lattice cores and 4.8 mm thick stainless steel face sheets indicate the

transmitted to incident impulse ratio is increased (from 0.35 for a free 5 mm thick plate) to ~ 1.4 during underwater impulsive loading [Wadley et al. 2007a]. This is significantly less than the Taylor result for the rigid plate of the same mass per unit area as the sandwich panel. This result indicates that even when the face sheet thickness is held constant, considerable changes in the impulse transferred to a back supported structure can result from variations to the core crush resistance.

Recent analytical and numerical studies of edge supported panels subjected to dynamic loading have confirmed that core crushing during distributed impulsive loading does affect impulse transfer [Baker et al. 1998; Fleck and Deshpande 2004; 2005; Hutchinson and Xue 2005; 2006; Rathbun et al. 2006; Tilbrook et al. 2006; Dharmasena et al. 2007b; Liang et al. 2007; McShane et al. 2007]. This crushing behavior depends upon the cell topology, the material used to construct the cells, and the volume fraction of cell material (the core relative density, $\bar{\rho}$) [Tilbrook et al. 2006; McShane et al. 2007]. Numerous sandwich panel core topologies have been investigated, including simple I cores [Liang et al. 2007], various honeycombs [Xue and Hutchinson 2004; 2006; Dharmasena et al. 2007b], (prismatic) corrugations [Xue and Hutchinson 2004; Dharmasena et al. 2007a; McShane et al. 2007], and lattice truss structures [Wadley et al. 2007a; Wei et al. 2007a]. Examples of these are schematically illustrated in Figure 1. These theoretical assessments are being complimented with a variety of experiments designed to probe the dynamic crush response of cellular structures. This required development of experimental methods for the fabrication of sandwich panels from high ductility alloys [Tilbrook et al. 2006; McShane et al. 2007]. Honeycombs with cell dimensions in the 10 mm range can be made using a slotted sheet method followed by transient liquid phase bonding [Wadley et al. 2003; Wadley 2006]. The corrugations and lattices shown in Figure 1 can be made using sheet folding methods (in the latter case using a perforated metal sheet) [Wadley et al. 2003; Wadley 2006].

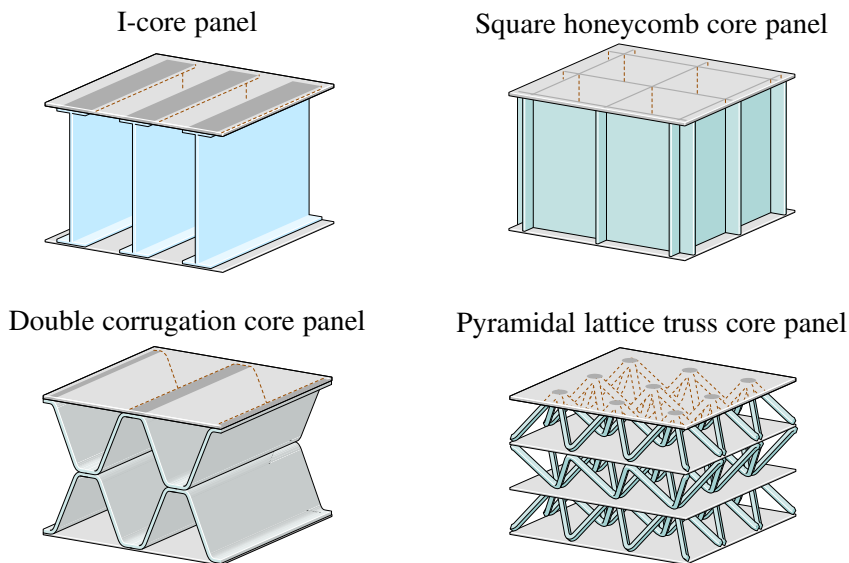


Figure 1. Cellular core topologies.

Several experimental techniques can be utilized to investigate the dynamic mechanical response of sandwich panel structures [Radford et al. 2005; Lee et al. 2006a; 2006b; Rathbun et al. 2006; Dharmasena et al. 2007b; Mori et al. 2007; Wadley et al. 2007a]. These include Kolsky bar methods [Lee et al. 2006a; 2006b] and gas gun experiments using metal foam projectiles [Radford et al. 2005; Rathbun et al. 2006] and other impactors [Lee et al. 2006a; 2006b; Mori et al. 2007]. These have been coupled with high speed photography to observe core crush mechanisms over a wide range of strain rates and incident pressures [Radford et al. 2005; Lee et al. 2006a; 2006b; Rathbun et al. 2006; Mori et al. 2007]. Recent water shock tube experiments have also been conducted on small scale metallic test structures with either stochastic foam [Radford et al. 2005; Deshpande et al. 2006], pyramidal lattice [Lee et al. 2006a; Mori et al. 2007], or square honeycomb [Rathbun et al. 2006; Mori et al. 2007] core topologies. These have enabled the dynamic response of sandwich panel structures to be examined as a function of the front face velocity (core crushing rate). All of these experiments indicate significant elevations of the quasistatic core strength once the front face velocity is increased above about 20 m/s [Deshpande et al. 2006].

Experimental assessments of the core dynamic compressive strength of sandwich panels can also be made using a novel explosive test technique, in which an explosive sheet is detonated inside a water column positioned on top of a well supported sandwich panel [Wadley et al. 2007a]. The response of the sandwich panel to the water borne impulse is then controlled by the charge mass, the charge to sample (standoff) distance, and the FSI which defines the momentum transferred to the structure [Fleck and Deshpande 2004; Hutchinson and Xue 2005; Liang et al. 2007]. The momentum transferred to the front face of the sandwich panels in these tests depends in part upon the face sheet mass per unit area [Hutchinson and Xue 2005; Liang et al. 2007]. As the momentum is acquired, the face sheet is quickly accelerated to a peak velocity. The characteristic time for this is governed by the decay constant of the exponentially decreasing pressure pulse [Cole 1948]. Movement of the front face compresses the core; the front face is decelerated by the dynamic resistance force of the core and eventually brought to rest. This resisting pressure can be measured at the back face, providing a good estimate of the core's dynamic compressive strength.

Finite element models (FEM) have been used to investigate the mechanisms of core crushing during dynamic loading [Qiu et al. 2003; Rabczuk et al. 2004; Xue and Hutchinson 2004; Xue et al. 2005; Tilbrook et al. 2006; Liang et al. 2007; McShane et al. 2007; Vaziri and Xue 2007]. The inelastic deformation of the axially loaded webs in a honeycomb panel begins by propagation of a plastic wave down the plate. If the back of the structure can support stress, reflection of the wave at the bottom face sheet can cause a buckle to form near the bottom face sheet [Vaughn and Hutchinson 2006]. Dynamic core hardening then results from three mechanisms: inertial resistance (to acceleration) of the core mass, inertial stabilization against web buckling, and material strain rate hardening of the webs [Xue and Hutchinson 2006]. The FEM analyses indicate that the three effects combine to dissipate the kinetic energy acquired by an impulsively loaded sandwich panel structure.

The energy absorbed during the crushing of a square honeycomb lattice increases with the critical buckling strain and is therefore sensitive to the mode of web collapse [Xue and Hutchinson 2006]. This depends upon the web thickness, width and height (which also establish the cell size and relative density), and the tangent modulus of the web material. Moreover, combining with an eigenvalue analysis, Xue and Hutchinson [2006] have also conducted a set of computations to systematically explore the effects of initial imperfection on the dynamic response of square honeycomb cores. They concluded that the

velocity imparted to the front face also plays a significant role in governing the buckling mode of web collapse such that the higher the velocity the shorter the buckling wavelength.

These studies reveal that the effective crush strength of a honeycomb core structure is a strong function of the velocity of the front face during dynamic loading. For small crush strains, motion of the front face is resisted by the reaction forces created when a plastic wave is propagated along the straight webs. If strain hardening effects are weak, and therefore ignored, the dynamic strength of the core in the nonbuckling regime is governed by the core's dynamic yield stress, σ_{YD}^c . In the plastic yield region of core crushing, this can be estimated by

$$\sigma_{YD}^c \cong \sigma_{YD} \bar{\rho},$$

where σ_{YD} is the dynamic yield strength of the alloy and $\bar{\rho}$ is the relative density of the core defined as the volume fraction of the core occupied by the material. The dynamic strength of 304 stainless steel at the loading rates of interest is not more than 20% higher than that measured quasistatically [Stout and Follansbee 1986].

At higher impulses, web buckling is the dominant deformation mode. The analysis of honeycomb web buckling from [Xue and Hutchinson 2006] led to the approximate relation between the dynamic yield strength and core density

$$\sigma_{YD}^c \cong \left[1 + \left(\frac{E_t}{E} \right)^{1/2} \left(\frac{v_f}{c_{el} \varepsilon_Y} - 1 \right) \right] \sigma_Y \bar{\rho}, \quad (2)$$

where E_t is the linear hardening tangent modulus (measured quasistatically), E is the Young's modulus, c_{el} is the elastic wave speed, v_f is the front face (crush) velocity, and σ_Y and ε_Y are the yield strength and strain of the alloy, respectively. Equation (2) indicates that for fixed E and $\bar{\rho}$, it is beneficial to use alloys with high E_t . Austenitic stainless steels exhibit this characteristic.

Here we use a simple corrugation method to fabricate square honeycomb sandwich panel structures from a high ductility, high tangent modulus 304 stainless steel [Stout and Follansbee 1986], explained in Section 2. In Section 3, the quasistatic compression response of the core has been measured and found to be approximately three times stronger than the recently tested pyramidal lattice structures made from the same alloy [Wadley et al. 2007a]. It therefore provides an opportunity to experimentally assess the role of core strength (via a change in topology) upon impulse transmission during explosive loading. Test panels with identical thickness face sheets to those of the pyramidal lattice were subjected to a range of impulsive loads by varying the stand off distance between the test structure and a planar explosive source (see Section 3). The backside pressure-time waveforms of the fully back supported test structures were then monitored as they dynamically collapsed. Similar experiments were conducted with solid cylinders to determine the incident impulse. A complementary numerical modeling study investigated various aspects of the mechanical response of square honeycomb cores under this high intensity loading. A 3-dimensional finite element model of the experimental setup was constructed, and is described in detail in Section 4.1. The material models used in the computational schemes to represent the behavior of the water column and sandwich panel material are discussed in Section 4.2. In Section 4.3, a finite element hydrocode analysis was carried out to predict the pressure applied to the panel due to the underwater explosion. Finally, in Section 4.4, a simplified finite element unit cell model was used to investigate the effect of core relative density upon the dynamics of the square honeycomb core. These

finite element calculations were carried out using the commercially available software ABAQUS/Explicit. Experimental and numerical results are presented in Section 5 followed by a discussion of the results. The study confirms significant, front face velocity dependent core strengthening in square honeycomb structures. However, even though the dynamic honeycomb core strength is more than three times that of pyramidal lattices, the impulse transferred to heavily loaded panels is only increased slightly. The transmitted pressure appears controllable over wide ranges by varying the core density.

2. Sandwich panel fabrication

A sheet bending and brazing method was used to fabricate square honeycomb core sandwich panels from 304 stainless steel (see Figure 2). The core was fabricated by periodically bending 0.76 mm thick, 99 mm wide steel sheet to create a corrugated structure with a 90° bend angle. The peak to peak corrugation height was approximately 22 mm. Twelve of these corrugated panels were spot welded to create a square honeycomb block. A brazing paste (Wall Colmonoy, Microbraz 51 alloy) was applied along the contact edges. This assembly was placed between a pair of 4.8 mm thick, 304 stainless steel face plates which had been spray coated with the same brazing alloy powder carried in a polymer binder. Four structures were placed in a vacuum furnace and subjected to a high-temperature brazing treatment. The thermal cycle consisted of heating at 10° C/min to 550° C, holding for 20 minutes (to volatilize and remove the polymer binder), then further heating to 1050° C for 60 minutes at a base pressure of $\sim 10^{-4}$ torr before furnace cooling to ambient temperature at $\sim 25^\circ$ C/min. After brazing, 203 mm diameter cylindrical samples were cut using a wire electro discharge machine to obtain the circular test samples for quasistatic and dynamic testing. A photograph of one of the test structures is shown in Figure 3.

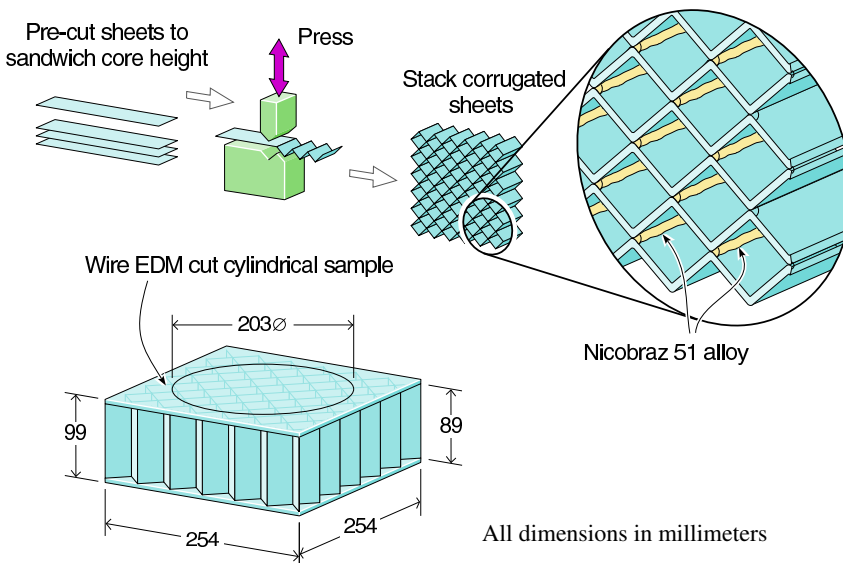


Figure 2. Square honeycomb core and sandwich panel fabrication process.

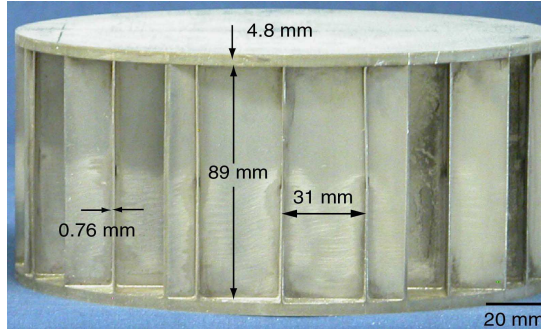


Figure 3. 304SS square honeycomb “dynocrusher” test sample.

The relative density, $\bar{\rho}$, of a square honeycomb structure can be calculated from the ratio of the metal to unit cell volumes (see [Figure 4](#)),

$$\bar{\rho} = \frac{t(2l - t)}{l^2} \cong 2\frac{t}{l}.$$

For the samples fabricated here, $h = 89$ mm, $l = 31$ mm, and $t = 0.76$ mm. This gives a core relative density of $\sim 5\%$.

3. Quasistatic compression and impulse loading tests

3.1. Alloy mechanical properties. The fabrication process resulted in a core made of annealed 304 stainless steel. The yield strength and strain hardening characteristics of this alloy are sensitive to its thermal history so the uniaxial stress strain response of similarly heat treated alloy specimens was measured according to ASTM E8-01 specifications at a strain rate of 10^{-4} s^{-1} . The elastic modulus and 0.2% offset yield strength were 203 GPa and 176 MPa, respectively. The strain hardening was well approximated by a bilinear fit to the true stress strain data up to a strain of 20%. The tangent modulus in this strain region was ~ 2.1 GPa.

3.2. Quasistatic compression. One sandwich panel sample was loaded in uniaxial compression at a strain rate of $5 \times 10^{-4} \text{ s}^{-1}$; its normalized stress strain response is shown in [Figure 5a](#). The specimen

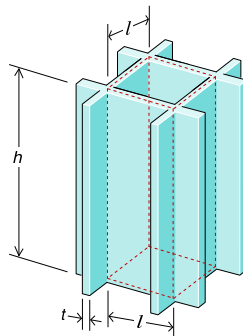


Figure 4. Square honeycomb core unit cell.

exhibited a peak strength of 12 MPa coincident with the onset of web buckling (marked by the first arrow). Two additional buckles were formed at strains of $\sim 25\%$ and $\sim 50\%$ before the core began to harden rapidly at a strain of $\sim 70\%$. The first buckling event occurred near the bottom (stationary) end of the sample. **Figure 5b** shows a cross section of the fully compressed sample. The onset of hardening at a strain of 70% resulted from the impingement of the three buckles in each honeycomb web.

3.3. Dynamic loading tests. The dynamic response of the square honeycomb structures was determined using the explosive test technique schematically illustrated in **Figure 6**. The test procedures were identical to those previously reported [Wadley et al. 2007a]. Each test sample was placed on a specimen tray resting on four high strength steel columns to which strain gauges were attached as shown. Prior calibrations in a mechanical testing frame were used to convert the strain gauge signals to average pressure measured at the back face of the specimen. Suitable band pass filtering techniques were used to increase the signal to noise ratio. A steel cover plate was positioned over the specimen such that the top sample face was flush with the top surface of the cover plate. A 0.9 m diameter cardboard cylinder (and plastic liner) was then placed over the cover plate and filled with water. A 20.3 cm \times 20.3 cm \times 0.1 cm explosive sheet was then positioned in the water at standoff distances $H = 25.4$ cm, 15.2 cm, or 10.2 cm above the top sample surface. An analysis of the test and effects of the reverberations in the support columns upon the results is presented elsewhere [Dharmasena et al. 2007a; Wei et al. 2007a].

3.4. Dynamic test calibration. The dynamic pulse loading system was calibrated using a solid 6061-T6 aluminum alloy cylinder whose outer dimensions were identical to the sandwich panel specimens. The

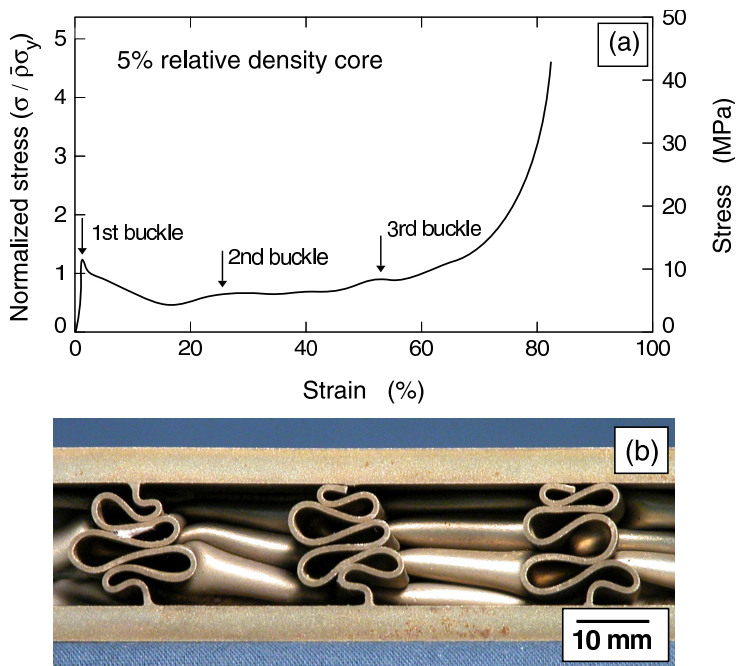


Figure 5. (a) Quasistatic response of 5% relative (core) density square honeycomb sample. (b) Compressed sample after quasistatic test.

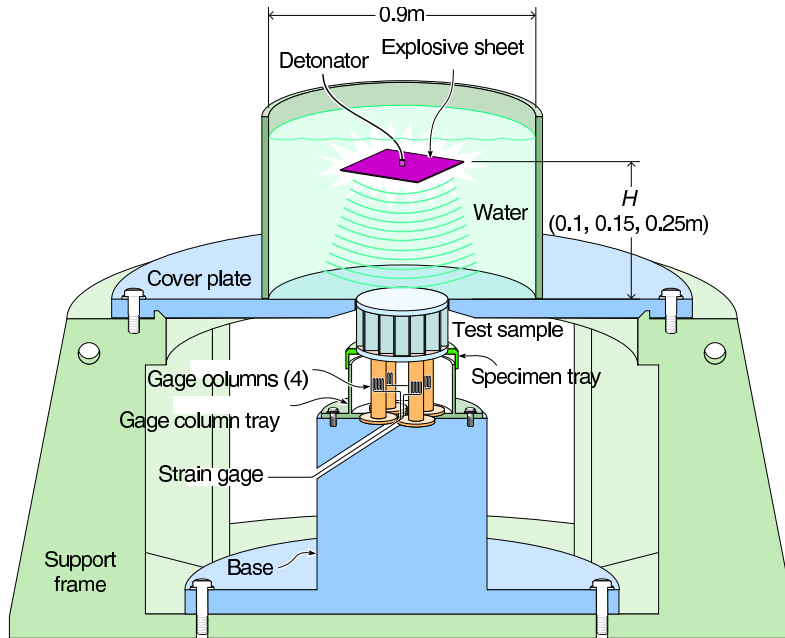


Figure 6. “Dynocrusher” test configuration.

“dry” side pressure for each test was obtained from the average of the four pressures converted from the strain gage signals. Each of the pressure-time traces for the four load column signals was very similar in amplitude and time response. The transmitted impulses were calculated by time integration of the pressure-time waveforms. The “dry” side pressure versus time response and the transmitted impulse per unit area waveforms for the different standoff distances have been reported elsewhere [Dharmasena et al. 2007a; Wadley et al. 2007a]. The peak pressure and transmitted impulses for the three standoffs are summarized in Table 1.

4. Finite element simulations

4.1. Finite element model of the experimental setup. A computational model of the experimental setup was developed to mimic the experiments performed on the dynamically loaded square honeycomb panels, and to study various aspects of the mechanical response of the sandwich panel core. A schematic illustration of the model is shown in Figure 7. In the model, the water, face sheets, specimen tray, and four gage columns were fully meshed using eight-node linear brick elements with reduced integration. Each

Standoff distance (cm)	Peak pressure (MPa)	Transmitted impulse (kPa·s)
25.4	27	6
15.2	40	9.9
10.2	52	11.8

Table 1. Effect of standoff on the transmitted pressure and impulse for solid cylinders.

face sheet was discretized with two elements through the thickness. The honeycomb core walls were meshed using four-node shell elements with finite membrane strains. Five section integration points with Simpson's integration rule were used in each shell element. Fifty elements were uniformly distributed through the core thickness. The core webs were perfectly welded to the face sheet at the corresponding connections. The contact between the bottom surface of the sandwich panel and the top surface of the specimen tray was taken to be frictionless. As suggested by [Wei et al. 2007a; 2007b], the support base beneath the gage columns was modeled as a parallel spring and dashpot pair capable of capturing its elasticity and energy dissipation in terms of its overall response. The top surface of each gage column was perfectly bonded to the specimen tray, while the bottom surface of each gage column was tied to a rigid surface connected to the spring-dashpot pair. The bottom ends of the spring and dashpot were fixed. The base, the spring, and the dashpot were allowed to move only vertically, with no transverse displacements and rotations allowed.

4.2. Material properties. The water was modeled as an acoustic medium, with a bulk modulus set to 2.05 GPa and a density of 998.23 kg/m^3 [Abaqus 2005]. To model fluid cavitation during reflection of a waterborne impulse with the structure a cavitation pressure was simply set as zero, such that the fluid undergoes free volume expansion when the pressure reaches zero. The sandwich panel was made of a stainless steel alloy having a density of 7900 kg/m^3 and a Poisson ratio of 0.3. In the simulations, the Mises criterion was adopted to model yielding of the material. The true stress (σ) versus true strain (ϵ)

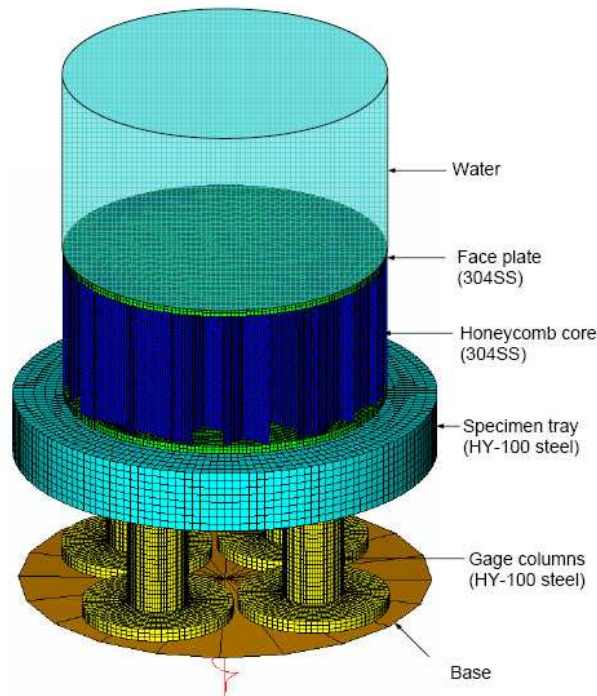


Figure 7. Finite element model representation of the “dynocrusher” test.

relation for the steel was taken to be bilinear for each value of plastic strain-rate, $\dot{\varepsilon}_p$, as

$$\sigma = \begin{cases} E\varepsilon, & \varepsilon \leq \frac{\sigma_Y}{E} \left(1 + \left(\frac{\dot{\varepsilon}_p}{\dot{\varepsilon}_0} \right)^m \right), \\ \sigma_Y \left(1 + \left(\frac{\dot{\varepsilon}_p}{\dot{\varepsilon}_0} \right)^m \right) + E_t \left(\varepsilon - \frac{\sigma_Y}{E} \left(1 + \left(\frac{\dot{\varepsilon}_p}{\dot{\varepsilon}_0} \right)^m \right) \right), & \varepsilon > \frac{\sigma_Y}{E} \left(1 + \left(\frac{\dot{\varepsilon}_p}{\dot{\varepsilon}_0} \right)^m \right). \end{cases}$$

Here, $E = 203$ GPa, $\sigma_Y = 176$ MPa, and $E_t = 2100$ MPa. Dynamic measurements on stainless steels are well represented using the values $\dot{\varepsilon}_0 = 4.916 \text{ s}^{-1}$ and $m = 0.154$. The specimen tray and the gage columns were made of HY100 steel. Since the specimen tray and all the gage columns undergo elastic deformation only, their mechanical behavior was specified by linear elasticity with elastic modulus of 205 GPa, a Poisson ratio of 0.3, and a density of 8000 kg/m^3 . All the materials were assumed to be sufficiently ductile that no fracture needed to be taken into account.

In order to calibrate the coefficients of the spring and dashpot, additional finite element simulations were performed for the reference tests, where solid 6061-T6 aluminum alloy cylinders were used as the specimens, as described in [Section 4.2](#). The solid cylinders were fully meshed using eight-node linear brick elements with reduced integration. A density of 2713 kg/m^3 and a Poisson ratio of 0.33 were used for the aluminum alloy cylinder simulations. In addition, its rate dependent stress strain relation was specified by

$$\sigma = \begin{cases} E^{Al} \varepsilon, & \varepsilon \leq \frac{\sigma_Y^{Al}}{E^{Al}}, \\ \left(\frac{E^{Al} - E_t^{Al}}{E^{Al}} \sigma_Y^{Al} + E_t^{Al} \varepsilon \right) \left(1 + \left(\frac{\dot{\varepsilon}_p^{Al}}{\dot{\varepsilon}_0^{Al}} \right)^m \right), & \varepsilon > \frac{\sigma_Y^{Al}}{E^{Al}}, \end{cases}$$

where the elastic modulus $E^{Al} = 70$ GPa, the initial yield strength $\sigma_Y^{Al} = 241$ MPa, the tangent modulus $E_t^{Al} = 188$ MPa, $\dot{\varepsilon}_0 = 163000 \text{ s}^{-1}$, and $m = 1.75$. Other components of the test system were modeled in the same way as discussed before. The calibration procedure for identifying the system compliance is similar to that detailed in [\[Wei et al. 2007b\]](#). As described in [Section 4.2](#), three calibration tests were performed with the solid cylinders. For a given spring stiffness and dashpot viscosity, the finite element prediction of the transmitted pressure history was compared with the corresponding experimental data. By adjusting the spring stiffness and the dashpot viscosity, the amplitudes of the transmitted signal and echoes and the time intervals of the echoes were reasonably matched. A spring stiffness of 10 GN/m and dashpot viscosity of $1 \text{ MN}\cdot\text{s/m}$ were found to approximately represent the system compliance.

4.3. Hydrocode analysis of the pressure history in water. The pressure fields in the fluid and at the specimen-water interface following detonation of an explosive sheet were calculated using a fully coupled Euler–Lagrange finite element hydrocode [\[Wardlaw and Luton 2000; Wardlaw et al. 2003\]](#). The code allowed the analysis of shock propagation through a fluid medium using an Eulerian solver and then coupled it to the structural response of the solid target using a Lagrange code. Since the explosive sheet was relatively thin (1 mm), and high spatial and temporal gradients of pressure existed in the fluid medium, a fine Eulerian mesh in the direction of the target was used. The Euler run was started with 0.2 mm cells in the explosive sheet thickness direction and 0.4 mm divisions in the other two directions (in the plane parallel to the explosive sheet). The explosive sheet was specified by its geometry, the

explosive’s material properties, and by the detonation velocity using the Jones–Wilkins–Lee equations of state for shock calculations [Wardlaw and Luton 2000; Wardlaw et al. 2003]. The pressure loading on a rigid wall, representing the front surface of the solid cylinder, was calculated at four locations along the radial direction measured from the shortest distance of impact of the blast wave.

The time sequences of pressures at various radial distances for standoff distances 25 cm, 15 cm, and 10 cm are shown in Figure 8. They show the pressure at the rigid sample surface as the wave front underwent reflection. These pressure-time histories were then used to apply the necessary loading conditions at the top surface of the water column for the FEM sandwich panel calculations described in Section 4.2.

4.4. Numerical investigation on the fundamental dynamics of the unit cell response. Due to the periodicity of the square honeycomb core configuration, a simplified finite element model using only one unit cell of the structure can be analyzed, and captures many aspects of dynamic responses of the core [Rabczuk et al. 2004; Xue et al. 2005; Vaziri et al. 2006]. Full three-dimensional models of the square honeycomb unit cell subjected to high intensity loading transmitted through water were developed by detailed meshing of the core. The geometry of the unit cell model was consistent with the samples used in the experimental investigations, and is shown in Figure 9. In this set of calculations, the high intensity loading was simulated as an exponential decay pressure history applied to the top face of the water column, which was modeled using acoustic elements. The material constants required for representing the water characteristics and the sample alloy properties were same as those in Section 4.2. The unit cell model was attached to a fixed rigid plate at its bottom face. In the computational model, the faces and the core webs, as well as the water column, were fully meshed. The boundary conditions applied to the unit cell on the edges of the face sheets and the core webs were consistent with sample symmetry and periodicity. The developed unit cell model is essentially one periodic unit of a plate that is infinite in both directions and which is subject to deformation due a pressure history that is transmitted through water. A second series of simulations were conducted using cells of varying width to assess the effect of the core density, and therefore strength, upon the transmitted pressure. The details of the calculations were similar to previous studies [Rabczuk et al. 2004; Xue et al. 2005; Vaziri et al. 2006].

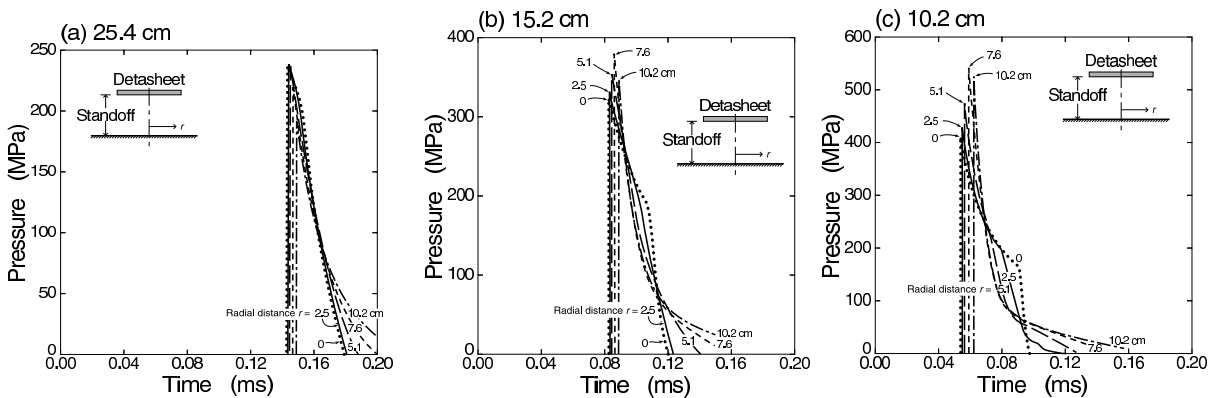


Figure 8. Pressure time loading on a rigid surface calculated from a DYSMAS hydrocode analysis for standoff distances of (a) 25.4 cm, (b) 15.2 cm, and (c) 10.2 cm.

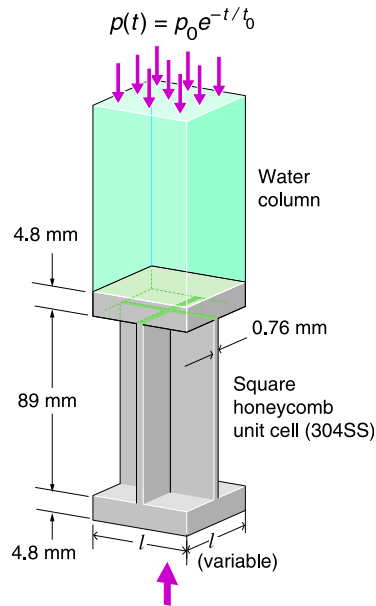


Figure 9. Square honeycomb unit cell finite element model.

5. Results

5.1. Sandwich panel responses. Figures 10 and 11 show the (dry side) pressure and impulse waveforms for sandwich panel structures following detonations at standoff distances of 25.4, 15.2, and 10.2 cm. Both experimental measurements and simulation results (using the approach described in Sections 4.2 and 4.3) from the full 3-dimensional geometry model are shown. The peak pressure measured on the back side of the specimens initially increased and then remained roughly constant as the standoff distance was decreased. At the furthestmost standoff of 25.4 cm, the transmitted pressure waveform, Figure 10a, was very similar to that measured on the calibration solid cylinder [Dharmasena et al. 2007a; Wadley et al. 2007a], and consisted of a single dominant peak with weak ringing. The peak pressure was ~ 25 MPa and the maximum transmitted impulse was 5.6 kPa·s. The experimental and full geometry finite element simulation results were generally in good agreement. This sandwich sample exhibited no evidence of permanent buckling or axial compression (verified with measurements of the sample after testing) and was therefore retested at a standoff of 10.2 cm (see Table 2).

Standoff distance (cm)	Peak pressure (MPa)	Transmitted impulse (kPa·s)	Compression (%)
25.4	25	5.6	—
15.2	35	8.2	6.2
10.2	26	9	29

Table 2. Effect of standoff on the experimentally measured transmitted pressure and impulse for a stainless steel, square honeycomb structure with a core relative density of 5%.

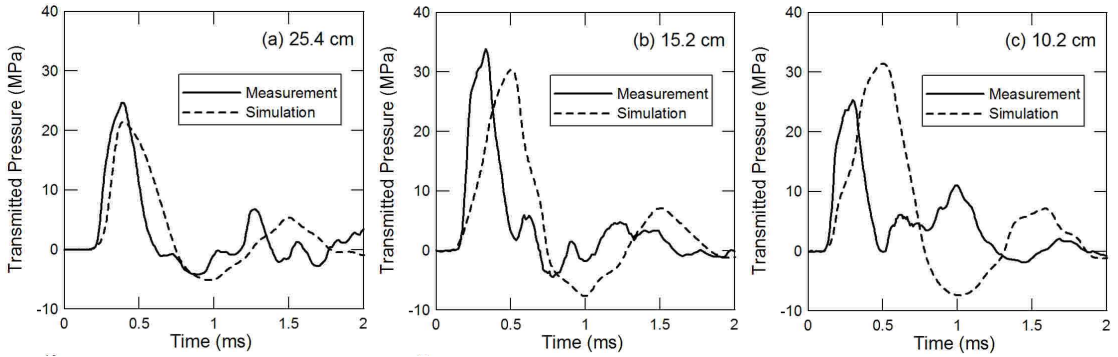


Figure 10. Measured and calculated transmitted pressure-time responses of 304SS square honeycomb core sandwich panels at standoff distances of (a) 25.4 cm, (b) 15.2 cm, and (c) 10.2 cm.

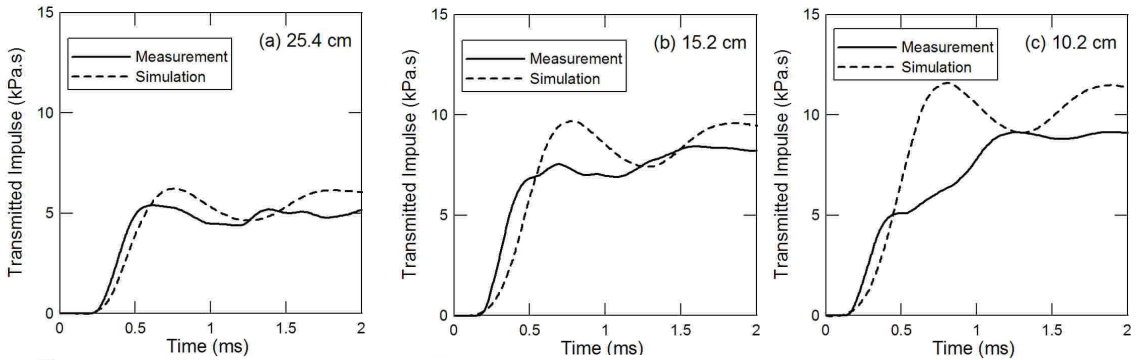


Figure 11. Measured and calculated transmitted impulse time responses of 304SS square honeycomb core sandwich panels at standoff distances of (a) 25.4 cm, (b) 15.2 cm, and (c) 10.2 cm.

Figures 10b and 11b show the dry side pressure and impulse waveforms at a standoff of 15.2 cm. The pressure response consisted of a main pressure peak with a small secondary peak followed by ring down. In this case, the measured peak pressure increased to 35 MPa and the transmitted impulse rose to ~ 8.2 kPa.s (after ~ 2 ms). The secondary peak amplitude was ~ 5 MPa and was delayed by about 0.3 ms from the main pressure peak. The simulated peak pressure and impulse were in good agreement with the experiments. The simulated peak pressure and impulse were ~ 31 MPa and ~ 8.5 kPa.s, respectively. The initial rate of impulse transfer in the simulated response was slightly less than experimentally observed.

A cross sectional view of the sample is shown in Figure 12. The sample suffered an experimentally measured, nonrecoverable axial compressive strain of 6.2%. Cooperative buckling across the full width of the sample occurred close to the bottom (stationary) face. The beginning of a second set of buckles was also evident near the top (wet side) of the specimen.

The pressure and impulse waveforms for a standoff distance of 10.2 cm are shown in Figures 10c and 11c. In this case, three pressure peaks are evident, each separated by about 0.3 ms. The main (first

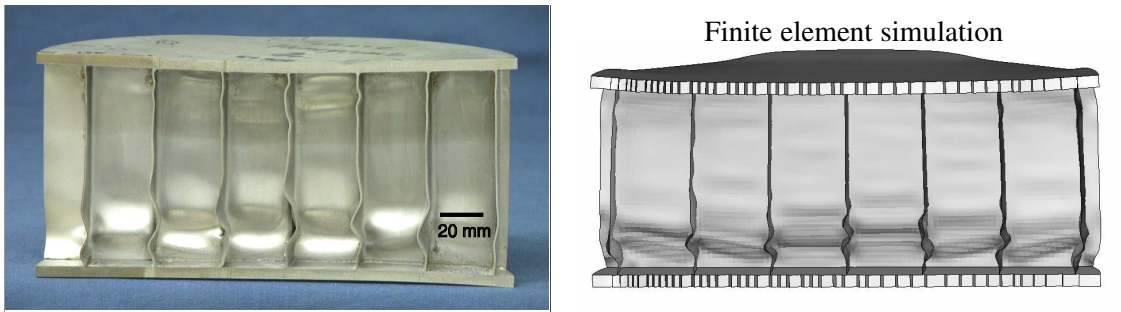


Figure 12. Experimental (left) and predicted (right) cross sections of the final deformed shapes at standoff distance of 15.2 cm.

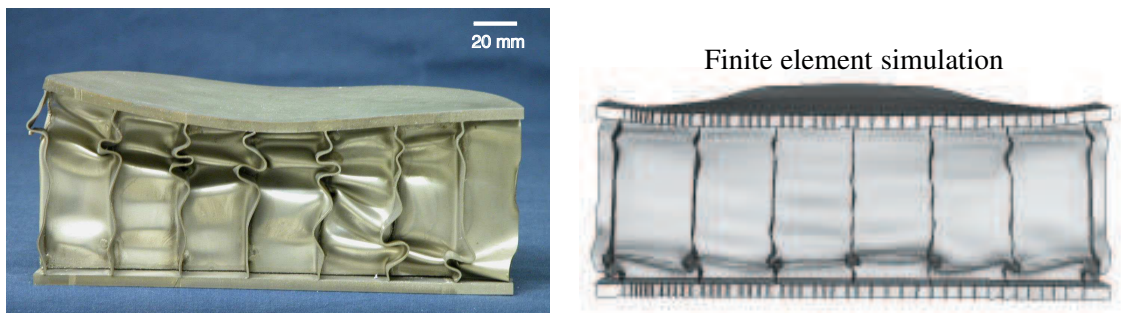


Figure 13. Experimental (left) and predicted (right) cross sections of the final deformed shapes at standoff distance of 10.2 cm.

arriving) peak had a peak pressure of ~ 26 MPa. This was slightly lower than that observed for the 15.2 cm standoff. This first peak was associated with the transfer of about a half the total impulse acquired by the sample. When the two delayed pressure pulses were included, the transmitted impulse after 3 ms reached ~ 9 kPa·s, (see [Figure 11c](#)). The predicted pressure response had a first peak of ~ 32 MPa, but failed to capture the two smaller pressure peaks in pressure-time history observed in the experiment (see [Figure 10c](#)). The total impulse was, however, similar to that measured experimentally (see [Figure 11c](#)). The experiments indicate that core crushing and impulse transfer occurred in two distinct phases, whereas only a single deformation phase was apparent in the simulations.

Cross sectional images of the experimental samples and simulation results help resolve the mechanisms of core response, and the source of the discrepancies between simulations and experiments in the most heavily loaded scenario. [Figure 13](#) shows the cross section of the specimen after testing at the shortest standoff distance. The specimen underwent an axial plastic compressive strain of 29% (measured at the center line). Extensive web buckling is evident with between 2 and 4 folds per web. The intense loading of this sample tripped buckling near both the dry and wet side face sheets. It also resulted in the wet side face sheet debonding from the core consistent with a tensile phase of loading (see [Figure 10c](#) between 1.2 and 1.7 ms). Examination of the core interior with the dry side face sheet removed indicated that the peak to peak deflection (amplitude) of the buckles was about 40% of the honeycomb wall spacing.

A cross sectional view of the simulated final deformed configurations of the sandwich panels is also shown in Figures 12 and 13 for standoff distances of 15.2 cm and 10.2 cm. The numerical simulations capture the buckling of the core webs, as well as the face sheet deformation, reasonably well for the 15.2 cm standoff distance. For this case, both the finite element simulation and the experimental results show that the core webs buckle near the bottom face sheet as plastic wave reflection occurs at the bottom face sheet interface. For the 10.2 cm standoff case, the simulation again predicts extensive honeycomb buckling near the bottom face sheet. A much smaller region of buckling near the top face sheet is also evident. However, for the closest standoff (10.2 cm) case, the experiment exhibited buckling at the bottom and top face sheets of roughly similar lateral core web displacement amplitude. At this close standoff, the test sample also exhibited a “dishing” of the front face sheet resulting in more predominant buckles forming at the center of the front face. This observation suggests that with the use of the centrally detonated 20.3 cm × 20.3 cm explosive sheet (placed above the 20.3 cm diameter test samples), there is a noticeable standoff distance effect on the planarity of the blast wave impacting the test samples. At this highest intensity loading level, it is possible that the second set of buckles near the top face sheet of the tested sample (see Figure 13) contributed to a second distinct phase of impulse transfer in the experimental response, not observed in the simulation result (see Figure 11c). These differences in buckling patterns may be a consequence of imperfections present in the experimental samples but improperly captured in the simulation geometry. The finite element simulations do show a region of significant tensile loading similar to that observed in the experiments. This was presumed to be responsible for top face sheet debonding. Figure 14 shows a time sequence of deformed sandwich panel cross sections for the 10.2 cm standoff, and illustrates the tripping of buckles with progressive folding during the first 0.4 ms of crushing.

The predicted axial crushing strain of the core, defined as the relative displacement between the center of the top and bottom face sheets divided by the original height of core, is plotted in Figure 15a as a function of time. The simulations indicate that it takes around 0.4 ms for the honeycomb core to attain its maximum strain. This corresponds to the period of impulse transfer seen in the experiments (see Figure 11). The values of final crushing strains increased as the standoff distance was decreased, and were reasonably similar to those measured (see Table 3). Figure 15b shows the core crush strain rate as a function of time and the front face velocity (obtained by multiplying the strain rate by the core’s original height). It can be seen that the predicted peak front face velocity increased with impulse from ~ 35 m/s to 104 m/s. There is some uncertainty in this estimate for the most intensely loaded experimental test, since the impulse was transferred in two stages while the velocity was deduced from a simulation that assumed more rapid impulse transfer.

Standoff distance (cm)	Experimental core strain (%)	Predicted Core strain (%)
25.4	—	7
15.2	6.2	18
10.2	29	30

Table 3. Comparison of the measured and predicted core strain.

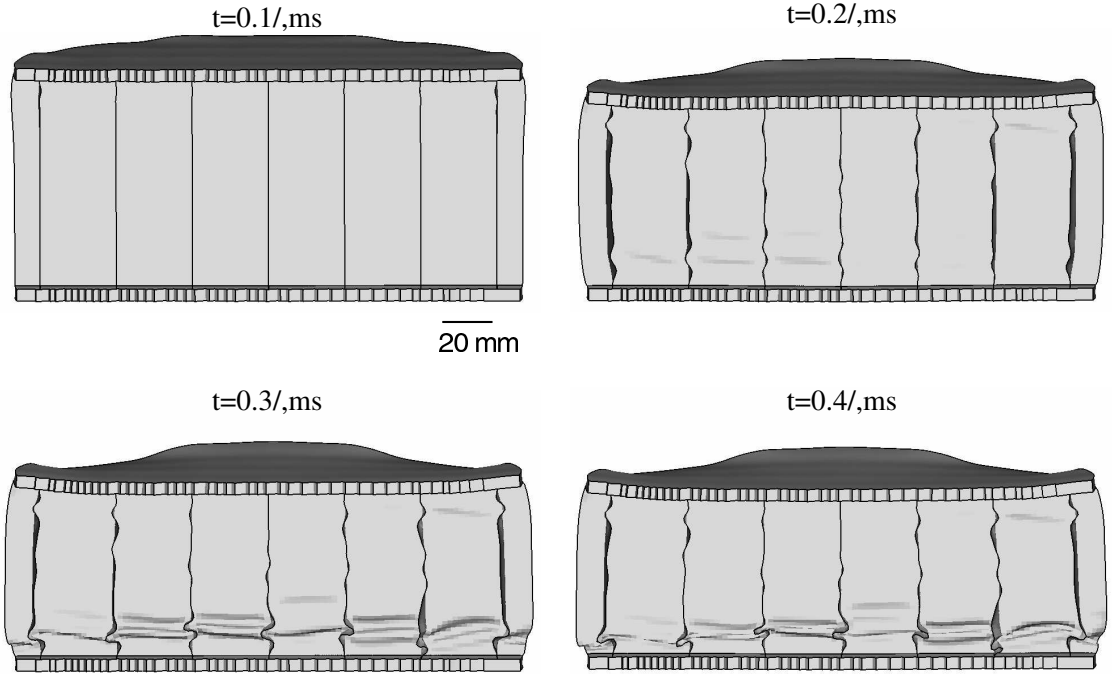


Figure 14. Time sequence of deformed shapes for a sandwich panel tested at the 10.2 cm standoff.

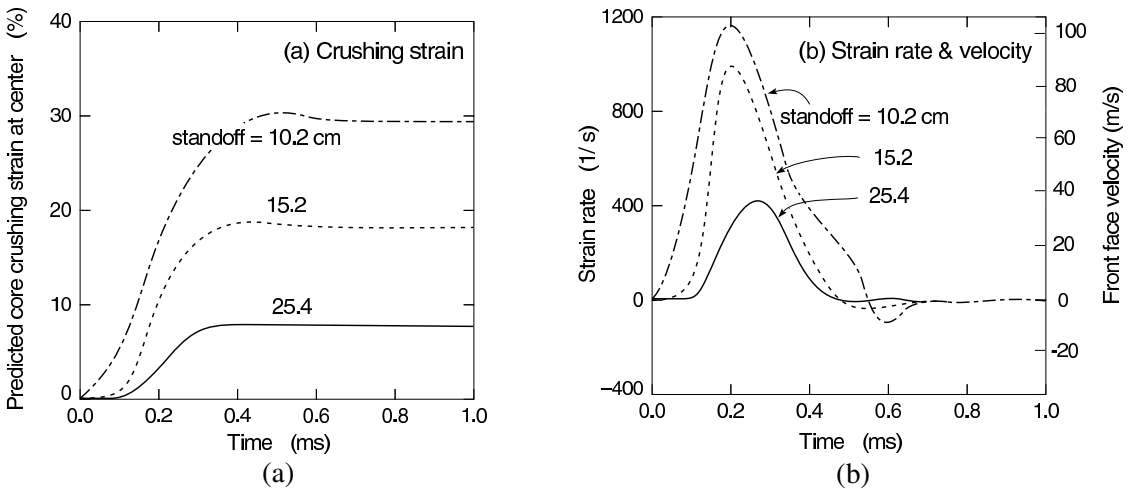


Figure 15. (a) Time dependence of the calculated effective core crushing strain of the square honeycomb panels at standoff distances of 25.4, 15.2, and 10.2 cm. (b) Calculated strain rates and front face velocities for the three standoff distances.

5.2. Unit cell simulation results. The unit cell computational models were used to investigate the effect of core relative density upon the pressure transmitted by a rigidly supported structure. The face sheet thickness (at 4.8 mm) was held constant to enable the role of the core’s crush resistance to be

independently assessed. The core relative density was adjusted by varying the unit cell size (varying the honeycomb cell wall spacing). For each core configuration, the peak load (p_0) was increased from 5 to 200 MPa. In all cases, a characteristic time decay (t_0) of 0.035 ms was chosen to be consistent with that predicted by the hydrocode simulations.

Figure 16 shows the simulation responses for peak overpressures $p_0 = 50, 100, 150,$ and 200 MPa, for relative densities between 2 and 7%. For the 7% relative density core (the strongest core analyzed), the peak transmitted pressure increased monotonically from ~ 30 MPa to ~ 52 MPa as the impulse loading was increased from 50 MPa to 200 MPa. For the 5% core, the peak pressure varied from ~ 21 MPa to ~ 38 MPa over the same overpressure range. Similar monotonic trends were observed from the simulations of the lower core density unit cell samples. These results indicate that very significant reductions in pressure can be achieved when low relative density core structures are used. For example, a 2% relative density core transmits only 16 MPa when impacted by a 200 MPa peak pressure pulse. It can be also seen that the width of the transmitted pressure pulse was inversely related to core density, indicating that the reduction in impulse was not as great as the mitigation of pressure.

Figure 17 summarizes the peak transmitted pressure variation with p_0 for each of the core relative densities. The 7% density strongest core shows a linear relationship with p_0 in the 25–200 MPa range. The 5% core shows an increasing trend with p_0 but at a lower rate of increase than the 7% core. As the core density was further decreased, a weaker dependence of the peak transmitted pressure on p_0 was observed.

6. Discussion

When back supported sandwich panel structures with square honeycomb cores are impulsively loaded in water to a level that is insufficient to cause inelastic core crushing, the transferred impulse and peak pressure are identical to those transmitted through a (back supported) solid plate. It is close to the Taylor predicted limit of $2I_0$ [Taylor 1963]. This has been corroborated by hydrocode simulations of a planar explosive sheet detonated in water at variables distances from a rigid wall [Kiddy 2006]. The experiments reported here indicated that when the incident impulse is able to cause buckling of the honeycomb webs, the transmitted impulse drops significantly from this upper limit even though the back face of the sandwich panel is fully supported and unable to move away from the water borne shock wave.

The effect of the incident overpressure, p_0 , and resulting incident impulse strength, I_0 , (varied here by changing the standoff) upon the transmitted pressure and impulse are summarized in Figure 18 for the experiments and simulations corresponding to the 3 standoff distances. As the incident impulse was increased to 5 kPa·s (see Figure 18b), core crushing and web buckling were initiated and the transmitted impulse was reduced by 20% compared to that of a solid sample at the same incident impulse. This reduction increased to 25% when the square honeycomb panel was more heavily loaded. In this case, a nearly 30% axial strain occurred in the sample and was accommodated by multiple cell wall buckling events (see Figure 13). This reduction in impulse transfer to the honeycomb sandwich panels arises from the motion of the wet side face sheet away from the incident impulse.

The impulse reductions achieved with honeycomb cores were only a little less than those obtained using pyramidal lattice cores, even though the honeycomb was approximately three times more resistant to quasistatic compression. This higher core strength resulted in a peak pressure transferred by the

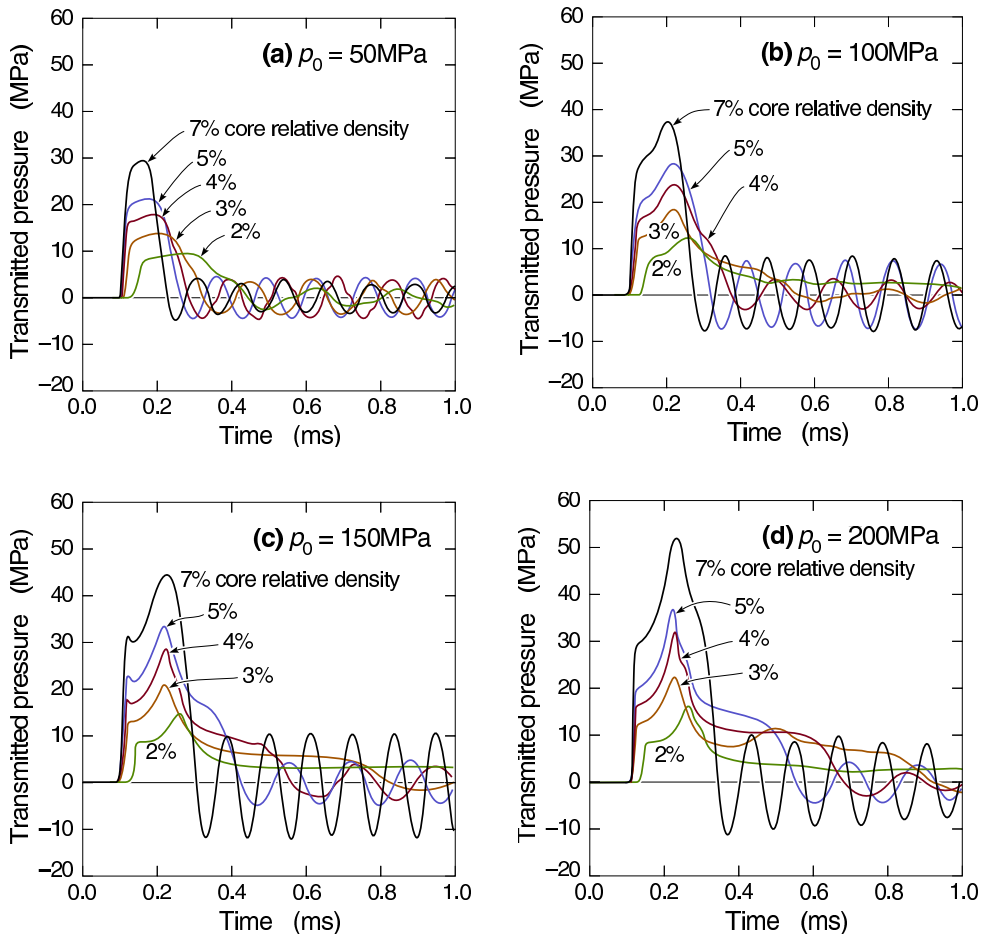


Figure 16. Calculated transmitted pressure response from the unit cell analysis, for different core densities and peak overpressures of (a) 50 MPa, (b) 100 MPa, (c) 150 MPa, and (d) 200 MPa.

honeycomb core (at the 10.2 cm standoff) of ~ 26 MPa, whereas an identically loaded pyramidal lattice structure transmitted only 12 MPa. In the softer core system, the impulse rise time was larger, enabling the total transferred impulse to reach a similar level to that of the honeycomb. Finite element analyses of the honeycomb and pyramidal cores indicate that the maximum transmitted pressure was controlled by the core dynamic strength, which depends upon the core topology and front face velocity during core compression [Deshpande 2006; Radford et al. 2007]. Here, three different impulse loadings (corresponding to three standoff distances) were used and the front face acquired an initial velocity that depended upon the impulse. Figure 15b shows the time derivative of the calculated strain versus time response (see Figure 15a) and the calculated front face velocity of the back supported honeycomb sample of initial core thickness 0.089 m. These velocities were then used with Equation (2) to estimate the dynamic strength elevation of the square honeycomb core. In Table 4 this is compared with the peak pressure deduced strengths (scaled by that measured quasistatically) for the three standoff distances. Reasonable

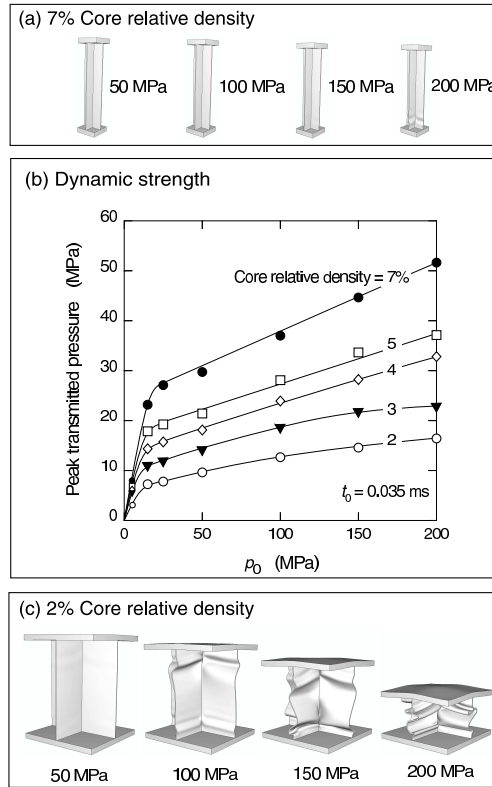


Figure 17. Deformed configurations for the 7% (a) and 2% (c) density square honeycomb unit cells. The peak transmitted back face pressure variation with overpressures (p_0), for a core density range of 2–7% (b).

agreement is observed for the two larger standoff cases, whereas the shorter standoff experiment is again consistent with a slower impulse transfer process.

Significant pressure reductions can be achieved by lowering the core relative density as illustrated in Figure 17. However, for a given impulse load, increasing crush displacements are reached as the core relative density (strength) is reduced. If core densification occurs, the impulse carried by the front face is transferred to the supports, which then experience much higher pressure levels. This can be avoided by designing sandwich panels to have a core thickness above an impulse dependent minimum value. In

Standoff distance (cm)	Calculated front face velocity (m/s)	Dynamic/quasistatic strength ratio	
		Predicted	Measured
25.4	35.6	1.73	2.08
15.2	88.9	2.98	2.92
10.2	103.7	3.32	2.12

Table 4. Effect of standoff on the front face velocity and the dynamic to static strength ratio of the square honeycomb core.

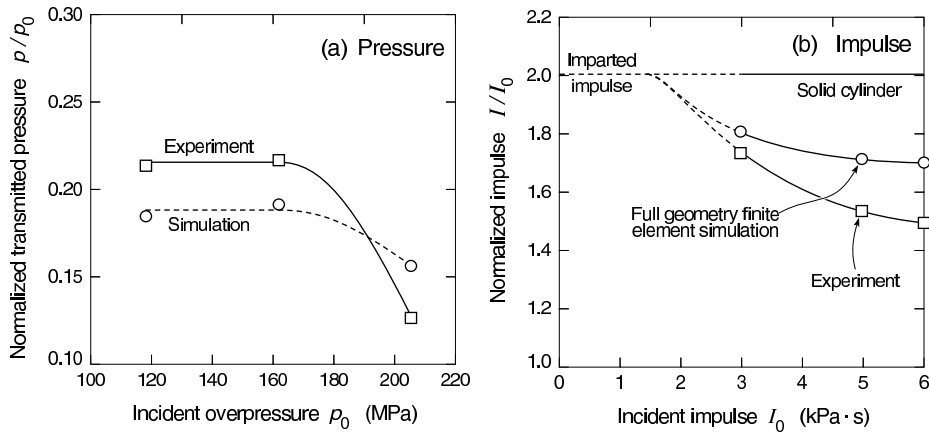


Figure 18. (a) The dependence of the transmitted pressure upon incident pressure. (b) The variation of the transmitted impulse with incident impulse.

this case, the transmitted pressure is controlled by the dynamic crush strength of the core, σ_{cD} . The required minimum thickness for the cellular core, h_{min} , can be estimated from [Ashby et al. 2000] and [Wadley et al. 2007b] as

$$h_{min} = \frac{I^2}{2m_f\sigma_{cD}(1 - \bar{\rho})},$$

where I is the impulse (momentum) per unit area imparted to the sandwich panel, m_f the mass per unit area of the front face sheet, $\bar{\rho}$ the core relative density, and σ_{cD} the dynamic crush strength of the core before densification is reached.

7. Summary

A combined experimental and computational simulation approach has been used to investigate impulse transfer during underwater shock loading of back supported sandwich structures with square honeycomb core topologies. The study indicates that significant impulse reductions occur, provided core crushing is activated. The majority of the core crushing in square honeycomb core panels occurs by web buckling. This appears to initiate at the dry side face sheet-web interface upon plastic wave reflection. The impulse transferred to these sandwich panels lies below the Taylor predicted limit ($2p_0t_0$) for a rigidly supported plate and above that of a free plate with mass per unit area corresponding to the wet side face sheet. The impulse transferred to the square honeycomb panels was slightly higher than that transferred to pyramidal core structures whose crush strength is lower than the honeycomb. The experimental study indicates that the transmitted impulse rise time was increased in the sandwich panel systems. This appears to result from the sequential tripping of regions of buckling within the most intensely loaded test structures. For a fixed impulse, increasing the rise time of the transmitted impulse reduces the transmitted pressure and provides beneficial dynamic pulse mitigation effects. “Weaker” core designs (for example a multilayer lattice structure) enhance this beneficial feature, and reduce both the transmitted peak pressure and the impulse under similar loading conditions. The fluid structure interaction for a sandwich panel is influenced by the properties of the fluid medium, the thickness and the density of the face sheet, and

the topology and strength of the sandwich core. Using a unit cell analysis, the face sheet has been kept constant, and the core strength adjusted systematically by varying the core relative density. This has enabled the investigation of the effects of the core strength on the transmitted pressure to a back supported structure. It shows that the core relative density (for a selected sandwich core topology) can be effectively used as a parameter to control the transmitted pressure, provided an adequate core thickness can be used.

Acknowledgements

This research was supported by the Office of Naval Research grant number N00014-03-1-0281 monitored by Drs. Edward Johnson and Daniel Tam, and the Blast Resistant Materials program monitored by Drs. Steve Fishman and David Shifler (grant number N00014-01-1-1051). Zhenyu Xue and Ashkan Vaziri were also supported in part by the Office of Naval Research under grants N00014-02-1-0700 and GG10376-114934 and in part by the School of Engineering and Applied Sciences, Harvard University. We are grateful to Profs. John W. Hutchinson and Vikram Deshpande for many insightful discussions.

References

- [Abaqus 2005] Hibbit, Karlsson and Sorensen Inc., *ABAQUS/Explicit User's Manual*, Hibbit, Karlsson and Sorensen Inc., 2005. Version 6.0.
- [Ashby et al. 2000] M. F. Ashby, A. G. Evans, N. A. Fleck, L. J. Gibson, J. W. Hutchinson, and H. N. G. Wadley, *Metal foams: a design guide*, Butterworth-Heinemann, 2000.
- [Baker et al. 1998] W. E. Baker, T. C. Togami, and J. C. Weyder, "Static and dynamic properties of high-density metal honeycombs", *Int. J. Impact Eng.* **21**:3 (1998), 149–163.
- [Cole 1948] R. H. Cole, *Underwater explosions*, Princeton University Press, 1948.
- [Deshpande 2006] V. S. Deshpande, Private communication, 2006.
- [Deshpande and Fleck 2005] V. S. Deshpande and N. A. Fleck, "One-dimensional shock response of sandwich plates", *J. Mech. Phys. Solids* **53** (2005), 2347–2383.
- [Deshpande et al. 2006] V. S. Deshpande, A. Heaver, and N. A. Fleck, "An underwater shock simulator", *Proc. Royal Soc. A* **462** (2006), 1021–1041.
- [Dharmasena et al. 2007a] K. P. Dharmasena, D. T. Queheillalt, H. N. G. Wadley, Y. Chen, P. Dudt, D. Knight, Z. Wei, and A. G. Evans, "Dynamic response of a multilayer prismatic structure to impulsive loads incident from water", *Int. J. Impact Eng.* (2007). accepted.
- [Dharmasena et al. 2007b] K. P. Dharmasena, H. N. G. Wadley, Z. Xue, and J. W. Hutchinson, "[Mechanical response of metallic honeycomb sandwich panel structures to high-intensity dynamic loading](#)", *Int. J. Impact Eng.* (2007).
- [Fleck and Deshpande 2004] N. A. Fleck and V. S. Deshpande, "The resistance of clamped sandwich beams to shock loading", *J. Appl. Mech.* **71** (2004), 386–401.
- [Hutchinson and Xue 2005] J. W. Hutchinson and Z. Xue, "Metal sandwich plates optimized for pressure impulses", *Int. J. Mech. Sci.* **47** (2005), 545–569.
- [Kambouchev et al. 2006] N. Kambouchev, L. Noels, and R. Radovitzky, "Compressibility effects on fluid-structure interactions and their implications on the blast loading of structures", *J. Appl. Phys.* **100**:6 (2006), 063519.
- [Kiddy 2006] K. Kiddy, Private communication, 2006.
- [Lee et al. 2006a] S. Lee, F. Barthelat, J. W. Hutchinson, and H. D. Espinosa, "Dynamic failure of pyramidal truss core materials—experiments and modeling", *Int. J. Plast.* **22** (2006), 2118–2145.
- [Lee et al. 2006b] S. Lee, F. Barthelat, N. Moldovan, H. D. Espinosa, and H. N. G. Wadley, "Deformation rate effects on failure modes of open-cell Al foams and textile cellular materials", *Int. J. Solids Struct.* **43** (2006), 53–73.

- [Liang et al. 2007] Y. Liang, A. V. Spuskanyuk, S. E. Flores, D. R. Hayhurst, J. W. Hutchinson, R. M. McMeeking, and A. G. Evans, "The response of metallic sandwich panels to water blast", *J. Appl. Mech. (Trans. ASME)* **74**:1 (2007), 81–99.
- [McShane et al. 2007] G. McShane, V. S. Deshpande, and N. A. Fleck, "The underwater blast resistance of metallic sandwich beams with prismatic lattice cores", *J. Appl. Mech. (Trans. ASME)* **74** (2007), 352–364.
- [Mori et al. 2007] L. Mori, S. Lee, Z. Xue, A. Vaziri, D. T. Queheillalt, K. P. Dharmasena, H. N. G. Wadley, J. W. Hutchinson, and H. D. Espinosa, "Deformation and fracture modes of sandwich structures subjected to underwater impulsive loads", *J. Mech. Mater. Struct.* (2007). In press.
- [Qiu et al. 2003] X. Qiu, V. S. Deshpande, and N. A. Fleck, "Finite element analysis of the dynamic response of clamped sandwich beams", *Eur. J. Mech. A/Solids* **22**:6 (2003), 801–814.
- [Rabczuk et al. 2004] T. Rabczuk, J. Y. Kim, E. Samaniego, and T. Belytschko, "Homogenization of sandwich structures", *Int. J. Numer. Methods Eng.* **61** (2004), 1009–1027.
- [Radford et al. 2005] D. D. Radford, V. S. Deshpande, and N. A. Fleck, "The use of metal foam projectiles to simulate shock loading on a structure", *Int. J. Impact Eng.* **31**:9 (2005), 1152–1171.
- [Radford et al. 2007] D. D. Radford, G. J. McShane, V. S. Deshpande, and N. A. Fleck, "Dynamic compressive response of stainless-steel square honeycombs", *J. Appl. Mech.* **74** (2007), 658–667.
- [Rathbun et al. 2006] H. J. Rathbun, D. D. Radford, Z. Xue, M. Y. He, J. Yang, V. S. Deshpande, N. A. Fleck, J. W. Hutchinson, F. W. Zok, and A. G. Evans, "Performance of metallic honeycomb-core sandwich beams under shock loading", *Int. J. Solids Struct.* **43** (2006), 1746–1763.
- [Stout and Follansbee 1986] M. G. Stout and P. S. Follansbee, "Strain rate sensitivity, strain hardening, and yield behavior of 304L stainless steel", *J. Eng. Mater. Technol. (Trans. ASME)* **108** (1986), 344–353.
- [Taylor 1963] G. I. Taylor, "The scientific papers of G. I. Taylor", pp. 287–303 in *The pressure and impulse of submarine explosion waves on plates*, vol. volume III, Cambridge University Press, Cambridge, 1963.
- [Tilbrook et al. 2006] M. T. Tilbrook, V. S. Deshpande, and N. A. Fleck, "The impulsive response of sandwich beams: Analytical and numerical investigation of regimes of behaviour", *J. Mech. Phys. Solids* **54** (2006), 2242–2280.
- [Vaughn and Hutchinson 2006] D. G. Vaughn and J. W. Hutchinson, "Bucklewaves", *Eur. J. Mech. A: Solids* **25** (2006), 1–12.
- [Vaziri and Hutchinson 2007] A. Vaziri and J. W. Hutchinson, "Metallic sandwich plates subject to intense air shocks", *Int. J. Solids Struct.* **44** (2007), 2021–2035.
- [Vaziri and Xue 2007] A. Vaziri and Z. Xue, "Mechanical behavior and constitutive modeling of metal cores", *J. Mech. Mater. Struct.* (2007). in press.
- [Vaziri et al. 2006] A. Vaziri, Z. Xue, and J. W. Hutchinson, "Metal sandwich plates with polymer foam-filled cores", *J. Mech. Mater. Struct.* **1** (2006), 95–125.
- [Wadley 2006] H. N. G. Wadley, "Multifunctional periodic cellular materials", *Phil. Trans. R. Soc. A* **364** (2006), 31–68.
- [Wadley et al. 2003] H. N. G. Wadley, A. G. Evans, and N. A. Fleck, "Fabrication and structural performance of periodic cellular metal sandwich structures", *Compos. Sci. Tech.* **63**:16 (2003), 2331–2343.
- [Wadley et al. 2007a] H. N. G. Wadley, K. P. Dharmasena, Y. Chen, P. Dudd, D. Knight, R. Charette, and K. Kiddy, "[Compressive response of multilayered pyramidal lattices during underwater shock loading](#)", *Int. J. Impact Eng.* (2007).
- [Wadley et al. 2007b] H. N. G. Wadley, K. P. Dharmasena, M. He, R. McMeeking, A. G. Evans, N. Kambouchev, and R. Radovitzky, *Cellular materials concepts for air blast mitigation*, 2007. In preparation.
- [Wardlaw and Luton 2000] A. J. Wardlaw and J. A. Luton, "Fluid-structure interaction mechanisms for close-in explosions", *Shock Vib. J.* **7** (2000), 265–275.
- [Wardlaw et al. 2003] A. J. Wardlaw, J. Luton, J. J. Renzi, and K. Kiddy, "Fluid-structure coupling methodology for undersea weapons", pp. 251–263 in *Fluid Structure Interaction II*, WIT Press, 2003.
- [Wei et al. 2007a] Z. Wei, A. G. Evans, K. P. Dharmasena, and H. N. G. Wadley, "Analysis and interpretation of a test for characterizing the response of sandwich panels to water blast", *Int. J. Impact Eng.* **34** (2007), 1602–1618.
- [Wei et al. 2007b] Z. Wei, M. Y. He, and A. G. Evans, "Application of a dynamic constitutive law to multilayer metallic sandwich panels subject to impulsive loads", *J. Appl. Mech.* **74** (2007), 636–644.

[Xue and Hutchinson 2004] Z. Xue and J. W. Hutchinson, "A comparative study of impulse-resistant metal sandwich plates", *Int. J. Impact Eng.* **30** (2004), 1283–1305.

[Xue and Hutchinson 2006] Z. Xue and J. W. Hutchinson, "Crush dynamics of square honeycomb sandwich cores", *Int. J. Numer. Methods Eng.* **65** (2006), 2221–2245.

[Xue et al. 2005] Z. Xue, A. Vaziri, and J. W. Hutchinson, "Non-uniform constitutive model for compressible orthotropic materials with application to sandwich plate cores", *Cmes-Comp. Model. Eng.* **10** (2005), 79–95.

Received 6 Sep 2007. Revised 6 Sep 2007.

HAYDN N. G. WADLEY: haydn@virginia.edu

Department of Materials Science and Engineering, University of Virginia, 395 McCormick Road, Charlottesville VA 22904, United States

KUMAR P. DHARMASENA: kumar@virginia.edu

Department of Materials Science and Engineering, University of Virginia, 395 McCormick Road, Charlottesville VA 22904, United States

DOUG T. QUEHEILLALT: dtq2j@virginia.edu

Department of Materials Science and Engineering, University of Virginia, 395 McCormick Road, Charlottesville VA 22904, United States

YUNGCHIA CHEN: yungchia.chen@navy.mil

Naval Surface Warfare Center, Carderock Division, West Bethesda MD 20817, United States

PHILIP DUDT: philip.dudt@navy.mil

Naval Surface Warfare Center, Carderock Division, West Bethesda MD 20817, United States

DAVID KNIGHT: david.e.knight@navy.mil

Naval Surface Warfare Center, Carderock Division, West Bethesda MD 20817, United States

KEN KIDDY: kenneth.kiddy@navy.mil

Naval Surface Warfare Center, Indian Head Division, Indian Head MD 20640, United States

ZHENYU XUE: xue@deas.harvard.edu

School of Engineering and Applied Sciences, Harvard University, Cambridge MA 02138, United States

ASHKAN VAZIRI: avaziri@deas.harvard.edu

School of Engineering and Applied Sciences, Harvard University, Cambridge MA 02138, United States

DYNAMIC SHEAR RUPTURE OF STEEL PLATES

KEN NAHSHON, MICHAEL G. PONTIN, ANTHONY G. EVANS,
JOHN W. HUTCHINSON AND FRANK W. ZOK

Metallic sandwich panels with prismatic cores offer the potential for superior blast resistance relative to monolithic plates of equivalent areal density. However, under sufficiently high impulse, severe plastic strains can occur at the junctions of the face sheets and the core members shortly after arrival of the pressure wave but prior to significant deformation elsewhere. The potential consequence is localized shear rupture with minimal plastic dissipation. To characterize this failure mode, a combined experimental-numerical protocol has been used to ascertain the plastic strain for dynamic shear rupture of ductile metals. The experimental component involves firing cylindrical projectiles through plates of the targeted materials and monitoring changes in projectile velocity during penetration. With appropriate combinations of plate thickness and projectile velocity, penetration occurs through propagation of an annular shear crack. In parallel, a numerical model of dynamic deformation and rupture has been employed to infer the critical strain through comparisons with projectile velocity change measurements. Experiments and analyses have been performed on both 304 stainless steel and superaustenitic AL6XN. Effects of mesh size on the resolution of the predicted strain distribution and the plastic dissipation associated with penetration are addressed.

1. Introduction

Metallic sandwich panels with prismatic cores can be designed to provide resistance to underwater blasts superior to monolithic plates at equivalent areal density. The benefits derive from a reduction in the rate at which the momentum is transmitted from the water, as well as a diminution of the pressure transferred through the core to the supports [Liang et al. 2007]. These benefits require that the plastic strains in the faces as well as at the junctions of the faces with the core members remain below that needed to cause rupture (Figure 1).

Recent assessments of steel sandwich panels subject to an underwater blast exemplify the face deformations and the tendency for rupture (Figure 2) [Liang et al. 2007]. Shortly after arrival of the pressure wave, the wet face acquires uniform velocity over most of its area (see left series of images in Figure 2). However, at the attachment points to the core members, the face remains initially stationary. A consequence of the velocity difference is the development of localized plastic strains adjacent to the junctions. Rupture would occur when the plastic strain reaches a critical value (say 0.5), causing the wet face to shear-off from the core members. This would happen about 30 ms after arrival of the pressure wave. Thereafter, this face would continue moving and slap into the bottom face.

Keywords: sandwich panels, dynamic rupture, projectile penetration, finite elements.

This work was supported by the ONR MURI program on Blast Resistant Structures through a subcontract from Harvard University to the University of California, Santa Barbara (Contract No. 123163-03). Additional support was provided by a National Defense Science and Engineering Graduate Fellowship.

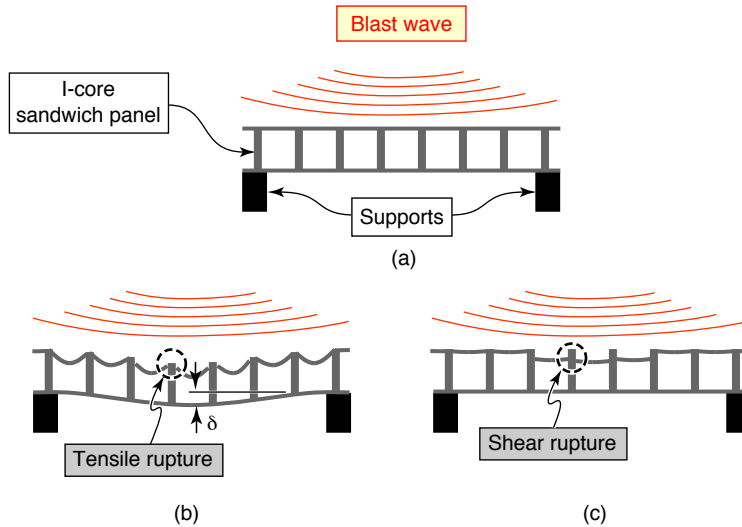


Figure 1. (a) Impingement of a blast wave onto an I-core sandwich panel with an I-core that resists crushing. (b) For moderately high impulse intensity, the face sheets undergo significant plastic bending and stretching, followed by tensile rupture. (c) At high impulse intensity, face failure occurs by *shear rupture* at the junctions with the core members shortly after impingement of the pressure wave and prior to significant deformation elsewhere, with minimal global deformation.

Experiments on impulsively loaded clamped plates reveal similar characteristics (Figure 3) [Menkes and Opat 1973; Nurick and Shave 1996]. (i) At low impulse I the plates plastically bend and stretch without rupture and the plate deflection increases monotonically with I . (ii) At intermediate I , plate stretching is followed by tensile rupture at the supports. In this domain, the degree of plastic stretching preceding rupture *diminishes* with increasing I . (iii) At high I , failure occurs by shear rupture at the supports *prior to macroscopic deformation*. For response (iii), once rupture is complete, the plate retains most of its kinetic energy and thus represents a significant remnant threat.

To probe response (iii), a high-speed impact test that duplicates the deformation of the plates at the supports has been devised and analyzed. It involves projecting hard cylinders into plates of the targeted materials and monitoring changes in projectile velocity as penetration occurs (similar to that of [Borvik et al. 2002a; 2002b]). It is demonstrated that, given an appropriate combination of sheet thickness and projectile velocity, penetration occurs through intense shear deformation and rupture along an annular ring concentric with the projectile. This mechanism is deemed the same as that experienced by the faces of impulsively-loaded panels locally, where they attach to the supports and core members. Namely, the failure criterion determined from the projectile tests is considered suitable for analysis of impulse-induced face shear-off. To devise a viable failure criterion, a numerical analysis is used to model the penetration and seek a consistent correlation with the experiments.

The article is organized as follows. The experimental protocols and test results are summarized in Sections 2 and 3. Details of the finite element model including the mesh design, the material constitutive

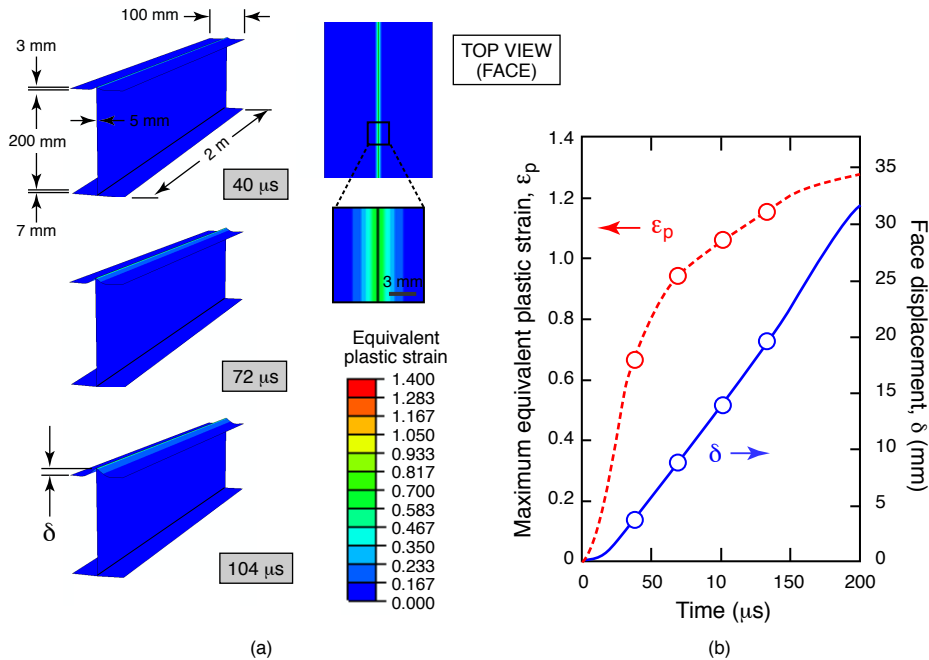


Figure 2. Evolution of peak plastic strain and displacement of the wet face in an I-core panel subject to a water blast (free-field peak pressure = 200 MPa, decay time = 100 μs , impulse intensity = 20 kPa·s). Periodic boundary conditions are applied to the sides of the unit cell shown in the series on the left. The edges of the bottom face are rigidly clamped. Times are those after initial impingement of the pressure wave on the wet face. Material properties are those of 304 stainless steel. (Courtesy A. Spuskanyuk, UCSB).

laws, and the rupture criterion, are presented in Section 4. Section 5 contains the numerical results as well as comparisons with experimental measurements.

2. Testing procedures

Projectile impact tests were performed using a single-stage gas gun (Figure 4). The gun consists of a pressurized chamber, a 5 m long, 0.30 caliber (7.62 mm diameter) barrel, and an intervening diaphragm that ruptures at a specified chamber pressure. Flat-ended cylindrical projectiles (25.4 mm in length and 7.54 mm in diameter) were fabricated from A2 tool steel and heat-treated to a hardness of 58 Rockwell C. Either nitrogen or helium was used for pressurization. Projectile velocities were controlled through selection of the diaphragm material (copper or stainless steel) as well as its thickness. Exit velocities were measured by three pairs of infrared sensors attached to the muzzle break at the end of the barrel. The velocities employed in the present study span the range 200–400 m/s. This velocity range corresponds to an initial plate momentum of approximately 2.5–5 kPa·s for the 1.5 mm plate and 5–10 kPa·s for the 3 mm plate; these are comparable to impulse intensities of present interest.

Two steels were tested: 304 stainless steel (SS) and superaustenitic AL6XN. The specimen dimensions were 70 mm \times 70 mm, with thickness of either 1.52 mm or 3.05 mm. Specimens were rigidly clamped

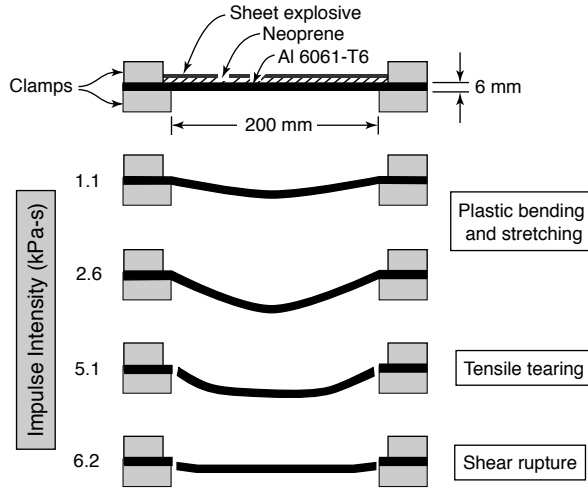


Figure 3. Transitions in deformation and failure modes in an Al alloy plate subject to increasing impulse intensity. Specimens are 25 mm wide. Impulsive loads are applied by detonation of a sheet explosive adhesively bonded to the top surface. (Adapted from [Menkes and Opat 1973].)

around their periphery leaving a central area, 50 mm × 50 mm, exposed. The fixture was attached to a steel catch chamber filled with sand to arrest the projectile and the resulting plug with little additional damage. The sides of the fixture were fabricated from clear polycarbonate to facilitate viewing by a high-speed digital camera (Imacon 200, DRS Technologies). The images were used to determine both

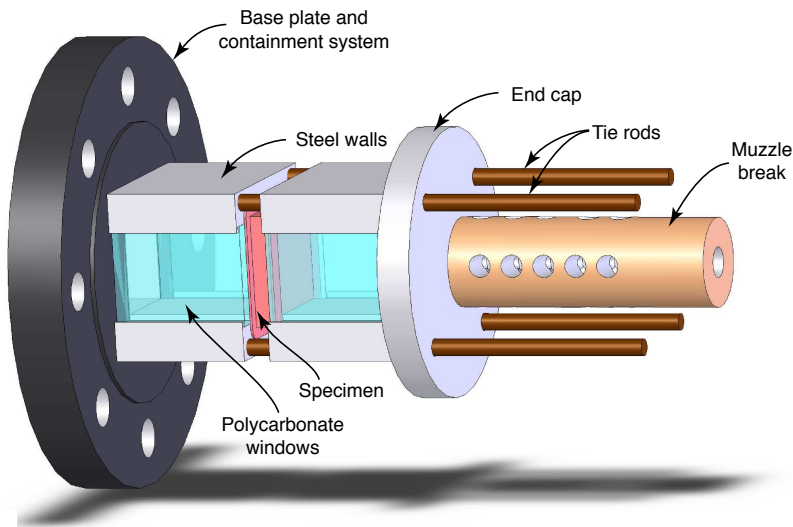


Figure 4. Schematic of test fixture.

incident and exit velocities of the projectile via calibrated image analysis software (DRS Technologies). The resolution of these measurements was ~ 2 m/s.

Following testing, normal deflections of the impacted surface were measured using a depth gauge at various radial distances from the hole edge. In some cases, the specimens were subsequently sectioned along a diametral plane through the hole in order to document the deflection profiles. Changes in projectile diameter at the impacting surface were also measured using a micrometer.

To establish a baseline of mechanical properties, quasistatic uniaxial tensile tests were performed on dog-bone specimens of both materials at a nominal strain rate of 10^{-3} s $^{-1}$. The true (logarithmic) tensile failure strain was obtained from areal measurements on optical micrographs of the fracture surfaces in combination with the measured initial cross-sectional area.

3. Experimental results

Typical photographic sequences showing projectile impact and penetration are presented in Figure 5. In all cases, fracture occurred along a well-defined annular ring concentric with the cylindrical surface of the projectile, thereby producing a cylindrical plug (Figure 6) and a corresponding hole in the plate

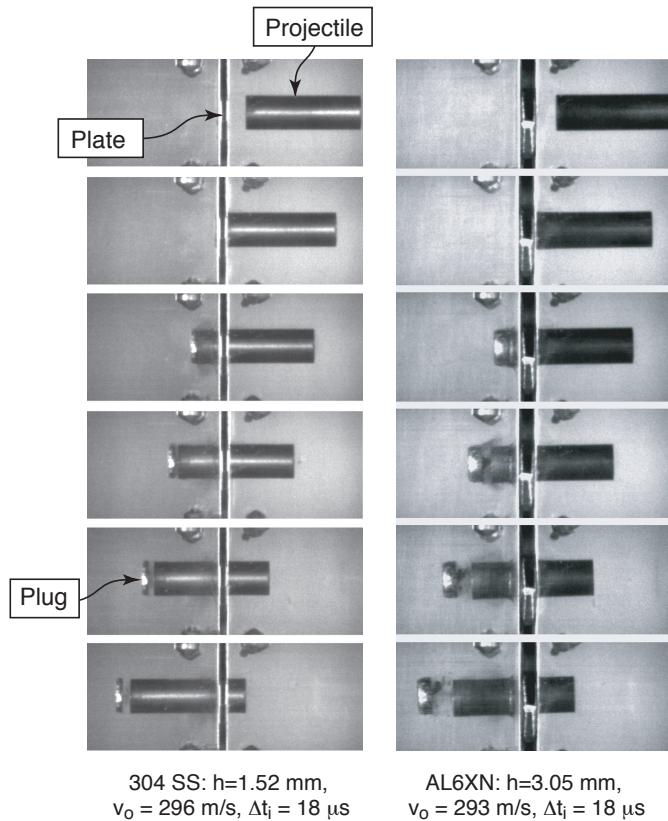


Figure 5. High speed photographs showing plug formation and projectile penetration from two representative tests (Δt_i is time between frames).

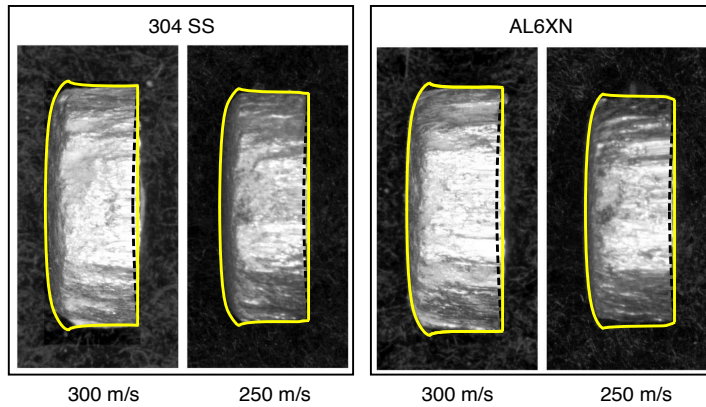


Figure 6. Photographs of typical plugs formed by projectile penetration tests. Solid overlaid lines are predicted projected shapes from the numerical simulations. The dashed lines represent the plug shape through the diametral plane (not visible in the actual plugs).

(Figure 7). The projectiles typically exhibited some “mushrooming” on the impacting face (Figure 8). The diametral strains ranged from 1 to 8%, increasing with both projectile velocity and plate thickness.

Changes in projectile velocity, Δv , with incident velocity, v_o , are plotted on Figure 9. Also shown are two boundaries that define the accessible domain. An upper bound is set by the ballistic limit, whereupon $\Delta v \leq v_o$. A lower bound is obtained by equating the momentum of the incident projectile with that of both the exiting projectile and the resulting plug for a material with zero failure strain [Teng and Wierzbicki

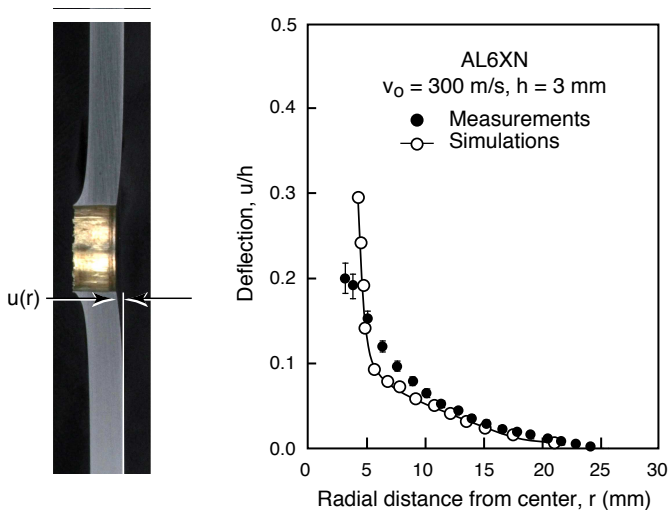


Figure 7. (a) Cross-sections through plates after testing. (b) Experimental measurements and numerical predictions of plate deflection. The latter correspond to a time $t v_o / h = 14$ after projectile impact.

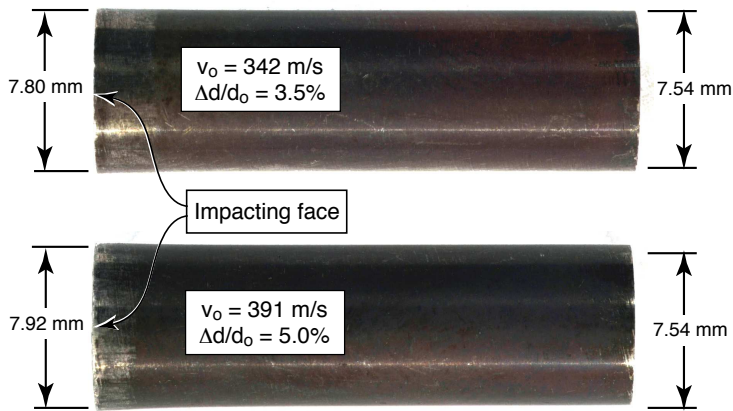


Figure 8. Projectiles after penetration through 3 mm thick plates.

2005]. Upon assuming that the plug diameter and density are the same as those for the projectile, the resulting requirement on velocity is: $\Delta v \geq v_o(1 + L_{pr}/h)^{-1}$ where L_{pr} is the projectile length. All experimental data fall in the allowable domain.

At low v_o , Δv initially decreases with v_o , attains a minimum, and thereafter rises approximately linearly with v_o . The latter appears to be essentially parallel to the boundary defined by momentum

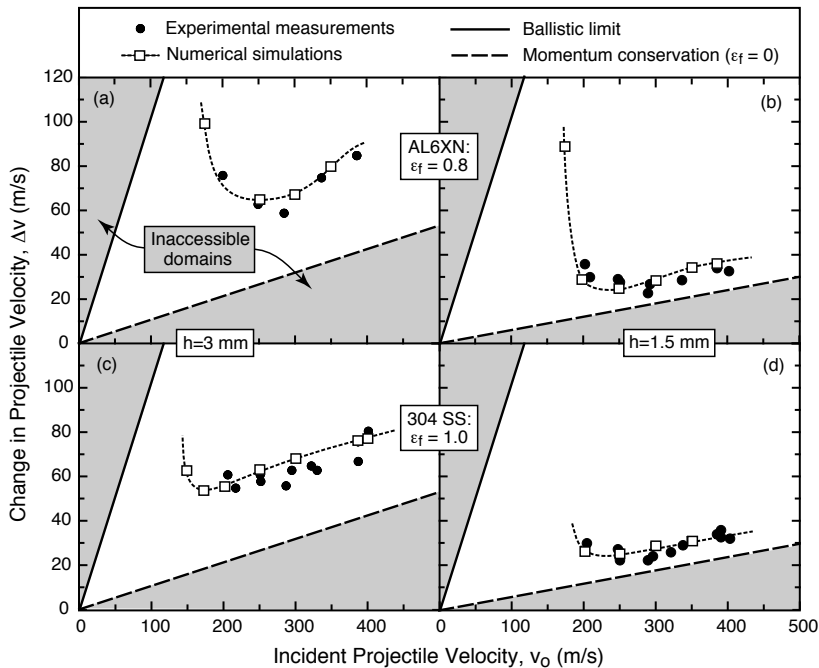


Figure 9. Changes in projectile velocity with incident velocity for (a, b) AL6XN and (c, d) 304 SS, for two plate thicknesses (1.5 and 3 mm).

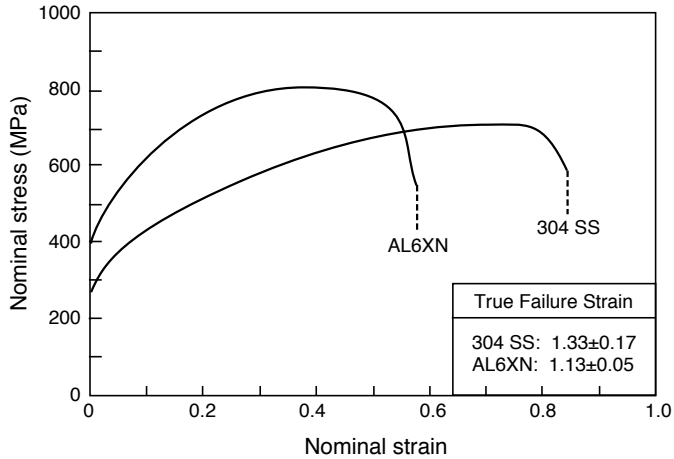


Figure 10. Quasistatic tensile stress-strain curves of both materials. Failure strains were calculated from area measurements at the fracture plane.

conservation. The inference is that the velocity change due to plug formation (above that needed to accelerate the plug) is insensitive to v_o .

The quasistatic tensile properties are summarized in Figure 10. The stress-strain curves are used subsequently in calibrating the constitutive law for the finite element model, incorporating strain-rate and temperature sensitivity data from other studies [Liu and Guo 2000; Nemat-Nasser et al. 2001]. The tensile failure strains for both materials are high, falling in the range 1.1–1.3.

4. Finite element model

Dynamic finite element calculations of the shear-out tests were performed using the finite element code ABAQUS Explicit 6.5-1. The strain required for shear rupture was inferred from comparisons of measured and simulated projectile velocities.

4.1. Mesh design. Given the cylindrical geometry of the projectile and the highly localized deformation pattern in the vicinity of the shear-out zone, an axisymmetric model was employed. The mesh near the shear-out zone was highly refined. In most cases, the mesh elements were $14\ \mu\text{m}$ and $71\ \mu\text{m}$ in the radial and through-thickness directions, respectively. These dimensions were selected to be comparable to typical shear band widths in the steels of interest: notably $10\text{--}100\ \mu\text{m}$ [Borvik et al. 1999]. Elsewhere, the meshes were significantly coarsened. The total element count was 20,000 and 6,000 for the 3 mm and 1.5 mm plates, respectively. Both the plate and the projectile were meshed using four-node bilinear elements with reduced integration and hourglass section control (CAX4R in [ABAQUS 2005]). A typical mesh in the plate near the shear zone beyond the end of the projectile is illustrated in Figure 11. Boundary conditions were applied such that the outside edge of the plate was restricted from translation and rotation. Initial conditions consisted of a uniform initial velocity applied to the projectile.

When a *fixed mesh* was employed, the finite element calculations failed to converge after about half of the projectile had passed through the plate, a consequence of severe material deformation in the ruptured elements. It will become apparent, though, that these calculations adequately capture the penetration

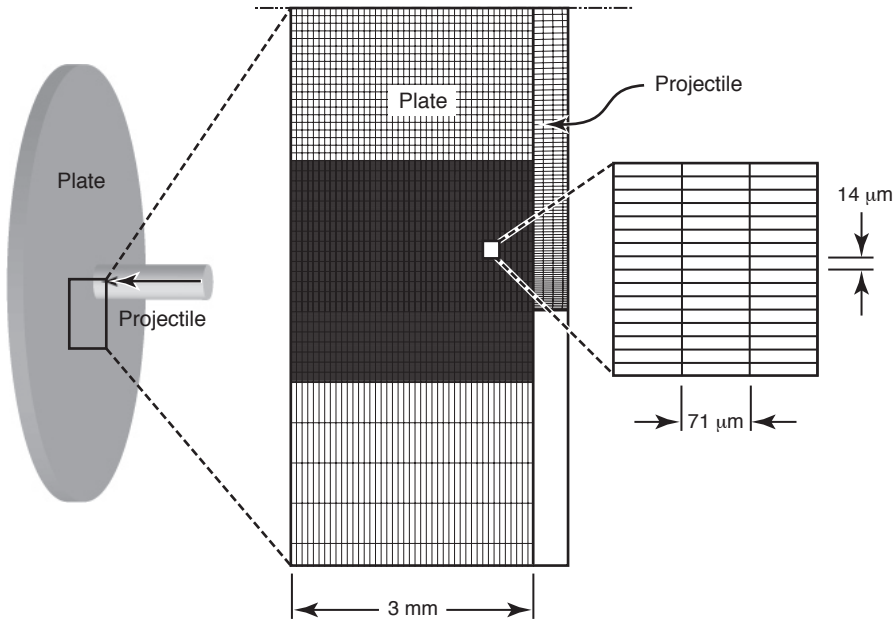


Figure 11. Finite element model used to simulate shear-out tests.

process and the associated changes in projectile velocity. They are, however, unable to predict the final plate shape because of the retained elastic deformation at the instant of penetration and the subsequent spring back. In an attempt to probe the pertinent features over longer times, additional calculations were performed using an *adaptive meshing* scheme. By moving the mesh independently of the material while keeping the mesh topology and number of elements fixed, the adaptive scheme yields a high-quality mesh even when severe deformation occurs [ABAQUS 2005]. Comparisons with the fixed mesh simulations confirmed that the two schemes yield essentially identical results at short times (wherein the fixed mesh calculations converge).

4.2. Constitutive laws. The dynamic plastic response of the plates was modeled using the Johnson–Cook constitutive law [Johnson and Cook 1985]. The flow stress is given by:

$$\sigma_y = [A + B(\varepsilon_e^{pl})^n] \left[1 + C \ln \left(\frac{\dot{\varepsilon}_e^{pl}}{\dot{\varepsilon}_0} \right) \right] (1 - \theta^m), \quad (1)$$

where $\dot{\varepsilon}_0$ is a reference strain rate, ε_e^{pl} is the equivalent plastic strain, $\dot{\varepsilon}_e^{pl}$ is the equivalent plastic strain rate, A , B , C , n , and m are experimentally derived material constants, and θ is a normalized temperature defined by

$$\theta = \frac{T - T_{tr}}{T_M - T_{tr}}, \quad (2)$$

with T being absolute temperature, T_M the melting temperature, and T_{tr} a transition temperature (taken as ambient). Material heating due to plastic deformation is assumed to occur adiabatically with 90% of

	E (GPa)	ν	ρ (kg/m ³)	A (MPa)	B (MPa)	C	n	m	$\dot{\epsilon}_0$ (s ⁻¹)	T_{tr} (K)	T_M (K)	C_p (J/kg-K)
304 SS	193	0.3	7800	310	1000	0.034	0.65	1.05	0.001	293	1800	450
AL6XN	161	0.35	7850	400	1500	0.045	0.4	1.2	0.001	293	1800	452

Table 1. Summary of parameter values for Johnson–Cook constitutive law.

the plastic work converted into heat, such that the temperature increase ΔT at any material point is

$$\Delta T = \frac{0.9}{\rho c_p} \int \sigma_{ij} d\epsilon_{ij}^p. \quad (3)$$

The pertinent material parameters were obtained from the quasistatic tensile tests (for strain hardening parameters A , B and n) coupled with complementary data for rate and temperature sensitivity (to obtain C and m) [Liu and Guo 2000; Nemat-Nasser et al. 2001]. All parameter values are listed in Table 1. Because of the small strains experienced by the projectiles, their material behavior was treated as elastic-perfectly plastic with a yield strength (2.0 GPa) selected to be consistent with the measured hardness (58 Rockwell C) and independent of strain rate.

4.3. A rupture criterion. The rupture criterion is based on a critical value of the equivalent plastic strain, ϵ_f , assumed to be independent of strain rate and stress triaxiality as will be justified in a subsequent discussion. Formally, the criterion can be expressed in terms of a damage parameter, ω , defined as

$$\omega = \int \frac{d\epsilon_e^{pl}}{\epsilon_f}.$$

Failure is predicted when ω reaches unity. Once this criterion is satisfied, the properties of the failed element are modified such that only compressive stresses can be supported. This effectively creates a mode II (shear) crack that cannot transmit either shear or normal tensile stresses. (In preliminary studies, element deletion was eliminated as a potential alternative because it removes excessive amounts of material leading to unrealistic relaxation of the constraints in the shear-out zone.) The utility of using ϵ_f as a consistent failure criterion for each material is assessed below by comparing the predicted changes in projectile velocity with the experimental measurements.

Because of the absence of a material length scale in the failure criterion, the predictions of the numerical simulations are inherently mesh-size dependent [Needleman and Tvergaard 1994; Gullerud et al. 2000]. The mesh size, coupled with the failure strain, dictate the amount of localized deformation that occurs along the fracture plane (closely analogous to the critical displacement in cohesive zone formulations). The intrinsic crack tip toughness is thus expected to be proportional to $w\epsilon_f$ (w being the element width). In addition to its role in determining toughness, the mesh size governs the resolution of the predicted strain distribution adjacent to the crack plane and, in turn, the accuracy of the global response metrics. Consequently, with the current approach, the selected mesh must be sufficiently fine to ensure adequate strain resolution yet be representative of the intrinsic width of the fracture process zone.

Most of the present simulations were based on a mesh with $14 \times 71 \mu\text{m}$ elements, which (as demonstrated below) are sufficiently refined to accurately resolve the plasticity and are broadly consistent with the scale of the fracture process zone ($10\text{--}100 \mu\text{m}$). Using this mesh, ε_f was inferred from changes in projectile velocity, Δv , with incident velocity, v_o , for both plate thicknesses and alloy types. To assess mesh-size effects, additional calculations were performed using finer ($10 \times 50 \mu\text{m}$) and coarser ($35 \times 145 \mu\text{m}$) elements. The assessment was made on the basis of the predicted Δv and the strain distribution.

5. Numerical results

5.1. Projectile penetration and velocity change. The stages of plate failure predicted by the finite element simulations are illustrated in Figure 12. An annular shear crack concentric with the projectile axis initiates shortly after impact. For the case shown, the nondimensional initiation time is $tv_o/h \approx 0.15$ (h/v_o representing the time needed for the projectile to travel a distance equal to the plate thickness at its initial velocity). Thereafter, the crack propagates at a speed 1–4 times that of the projectile. Full crack penetration is obtained before the projectile has traveled one plate thickness ($tv_o/h < 1$). During this process, plastic deformation is localized within a narrow annular band adjacent to the crack surface. Some plastic deformation also occurs within the projectile shortly after impact. The larger projectile diameter

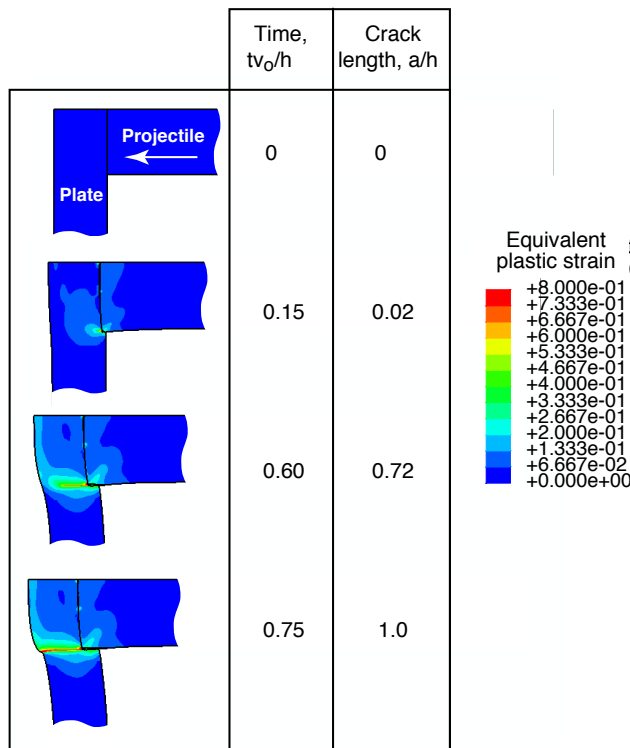


Figure 12. Evolution of plastic strain and crack growth for a 3 mm thick AL6XN plate impacted by a projectile with initial velocity $v_o = 300 \text{ m/s}$.

effectively increases the failure zone diameter and serves to increase the area over which intense plastic deformation occurs. Plate bending and stretching are negligible until the crack approaches the back surface. As $a/h \rightarrow 1$, the remaining ligament ruptures in a tensile mode.

The kinetic energy lost by the projectile is dissipated mainly by plastic deformation, both in the projectile and the shear zone of the plate. The evolution of kinetic energy, U_k , and plastic dissipation, U_p , is shown in Figure 13. Over the time period $0 \leq tv_o/h \leq 1$, U_k diminishes rapidly as U_p increases. For this specific case, about 60% of the dissipation occurs within the plate and the plug, the balance occurring within the projectile. During this period, plastic deformation in the shear zone causes a maximum temperature increase of about 300 K. The end of this stage is marked by complete crack penetration. Thereafter, the projectile kinetic energy approaches a steady-state value with small oscillations caused by reflecting stress waves. The expected period of oscillation, $t_{osc}v_o/h = v_o L_{pr} \sqrt{\rho} / h \sqrt{E} = 0.5$ (ρ being mass density and E the Young's modulus), is in excellent agreement with the numerical results. The plug kinetic energy also reaches a steady state shortly after crack penetration.

Although the kinetic energy of the plate (without the plug) represents a small fraction of the total, it exhibits oscillations with a long period (typically $t_{osc}v_o/h = 5$), a consequence of remnant plate vibration.

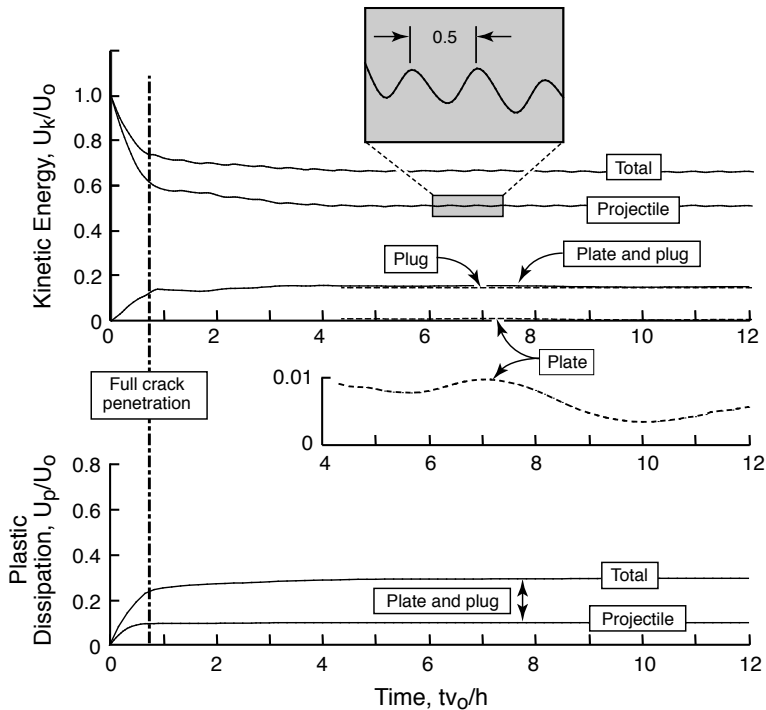


Figure 13. Evolution of kinetic energy and plastic dissipation during a shear out test (AL6XN, $h = 3$ mm, $v_o = 300$ m/s, $\varepsilon_f = 0.8$). Insets in the top graph illustrate the oscillatory nature of projectile and plate kinetic energies as well as the pertinent time scales. U_o is the initial projectile kinetic energy.

The vibration persists for times well beyond those of the present simulations. The consequences are evident in the remnant plate shape, described below (Section 5.3).

The predicted changes in Δv with v_o are plotted on Figure 9. For 304 SS, it is apparent that all results are well reproduced for a fixed failure strain, $\varepsilon_f \approx 1.0$. Similar consistency is apparent for AL6XN, albeit for a slightly lower critical strain, $\varepsilon_f \approx 0.8$. Attaining such consistency over a wide range of parameter space provides justification for application of the critical strain approach to shear rupture in these materials. The inferred values represent about 70% of the respective tensile failure strains under quasistatic loading (Figure 10).

An assessment of the selected element size ($14 \times 71 \mu\text{m}$) was made by examining the plastic strain distributions in the vicinity of the crack. Results for a 3 mm thick AL6XN plate impacted by a projectile with initial velocity $v_o = 300 \text{ m/s}$, at a crack length $a/h \approx 0.6$, are plotted on Figure 14(a). The distributions correspond to three trajectories perpendicular to the crack plane: one passing through the crack tip (A) and the other two (B and C) at distances of 0.07 mm (one element) and 0.14 mm (two elements) ahead of the tip (see inset). With this mesh, the plastic zone is spread over many elements ($\gg 10$) on either side of the crack plane. The conclusion is that the mesh is sufficiently refined to accurately resolve the plasticity.

The evolution of the stress triaxiality around the crack tip for this mesh is plotted on Figure 14(b). Although the crack propagates nominally in mode II, finite triaxiality is obtained at its tip. Moreover, the triaxiality increases slightly with crack growth, from about $-1/3$ for short cracks to about $1/3$ for long cracks. The latter is consistent with a purely tensile rupture in the final stages of penetration arising from plate bending and stretching. Nevertheless, these levels of triaxiality are deemed to be small (in relation to those obtained in mode I for example) and justify neglect of the triaxiality dependence of the failure strain in the present model.

5.2. Mesh sensitivity. Mesh sensitivity effects were probed by comparing the preceding results with those obtained using coarser and finer meshes. The resolution of the resulting strain distributions (Figure 15) for the two finer meshes ($10 \times 50 \mu\text{m}$ and $14 \times 71 \mu\text{m}$) is deemed to be adequate. In contrast, the coarsest mesh yields unacceptable results.

The coupled effects of mesh size and failure strain on the projectile velocity change are illustrated in Figure 16(a). Significant mesh sensitivity is evident (although the results for the coarsest mesh are likely inaccurate because of the poor strain resolution). Since the global dissipation (characterized by the change in kinetic energy of the projectile and the plug) is expected to scale with the intrinsic crack tip toughness [Tvergaard and Hutchinson 1992; Suo et al. 1993], and the tip toughness is proportional to $w\varepsilon_f$, it follows that the global dissipation should also be proportional to $w\varepsilon_f$. When the numerical results are plotted accordingly (Figure 16(b)), it becomes evident that the dissipation does indeed scale with $w\varepsilon_f$ for the two finer meshes, with the proportionality constant being only weakly dependent on ε_f . In the limit where $w \rightarrow 0$, the tip toughness vanishes and no global dissipation is obtained. Consequently, efforts to further refine the mesh to increase the strain resolution would have the adverse effect of yielding anomalously low dissipation. This scaling seemingly fails for the coarsest mesh, again likely a manifestation of the poor strain resolution.

5.3. Remnant deformation. A secondary assessment of the numerical model was made by comparing the predicted shapes of the plugs with those observed experimentally. Predicted shapes are overlaid on

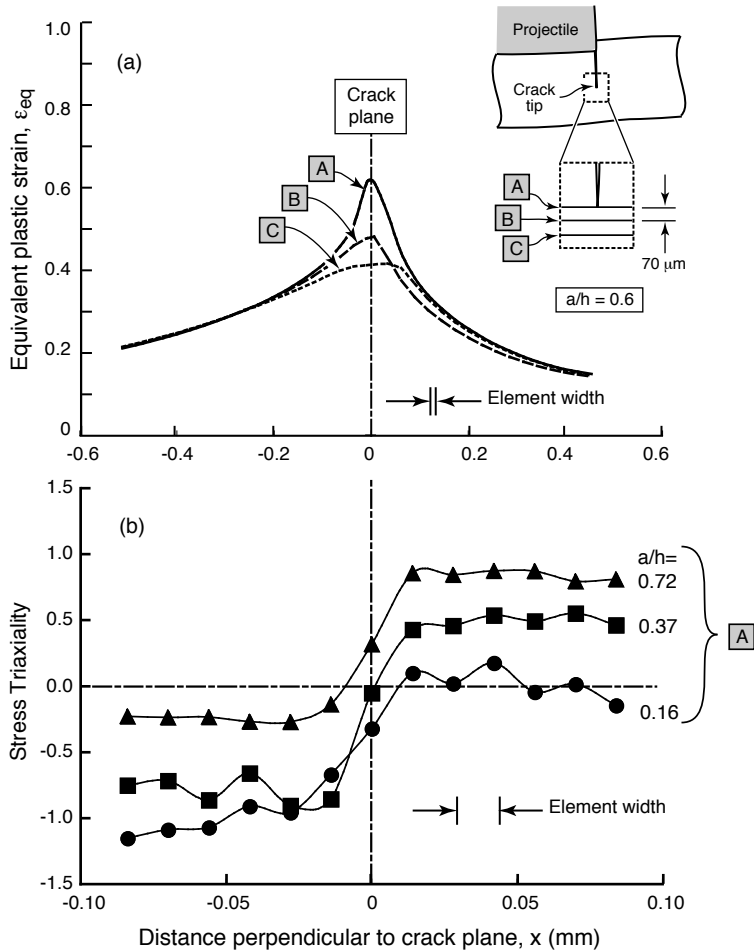


Figure 14. (a) Distribution of equivalent plastic strain ahead of a crack tip during shear-out. For the mesh size employed here ($14 \mu\text{m} \times 71 \mu\text{m}$), the zone of intense plasticity is spread over many elements, thereby precluding the anomalous localization that occurs with a coarser mesh (compare with Figure 15i). (b) Corresponding stress triaxiality at various crack lengths, a/h . The triaxiality along the failure plane ($x = 0$) varies from about $-1/3$ to $1/3$.

the corresponding photographs in Figure 6. The only detectable discrepancy is in the flaring of the plug near the face opposite that being impacted; this feature is predicted but not evident experimentally. It is attributable to slight rotation of the elements during the final stages of fracture (due to plate bending and stretching), coupled with restrictions on crack path imposed by element shape.

Additionally, an attempt was made to predict the shape of the plate after penetration. One set of results is plotted on Figure 7. Although the agreement with the experimental measurements appears

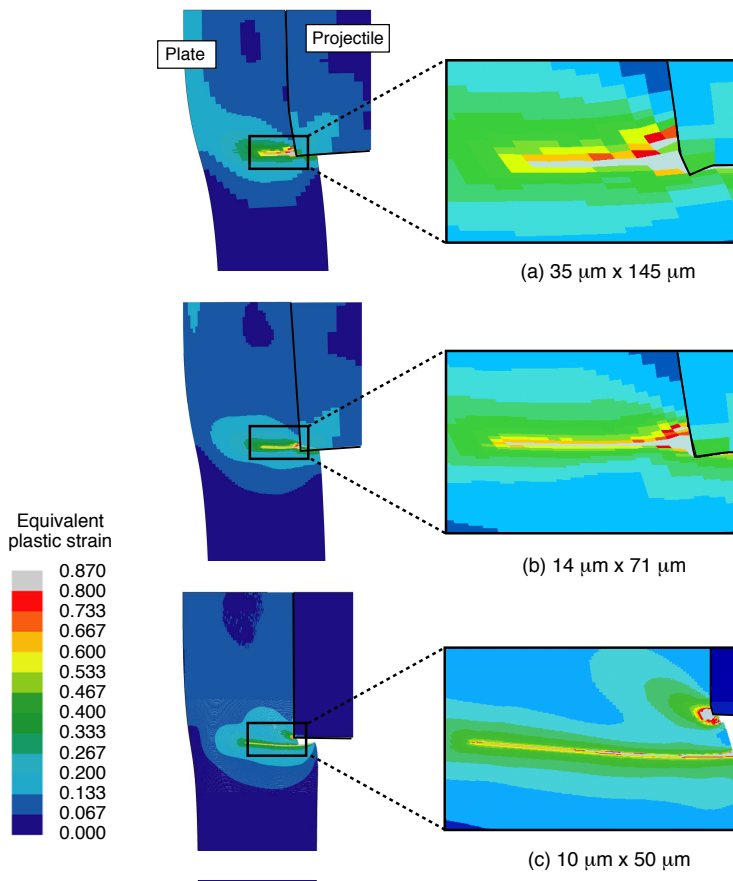


Figure 15. Effects of mesh size on plastic strain distributions around the crack tip ($\varepsilon_f = 0.8$).

reasonable, the accuracy of the predictions is compromised by plate vibrations that persist well after complete penetration. The vibration is evident in the oscillations in both the kinetic energy (Figure 13) and the plate deflection (Figure 17) with time. Accurate predictions would require significant extensions in the simulation times. Because each “long” simulation (with adaptive meshing) required several days to complete, the additional computational effort needed to properly simulate the plate deflection is deemed impractical. The conclusion is that plate deflection is a poor metric for assessment of the model.

6. Concluding remarks

A methodology for ascertaining the dynamic shear rupture strain of metal plates has been devised and demonstrated. Using a critical plastic strain criterion for rupture, the predictions of the numerical model agree well with the experimental measurements on two stainless steel alloys over a range of projectile velocities and plate thicknesses. The failure strains inferred in this manner represent about 70% of the corresponding quasistatic tensile failure strain. However, the inferred strains are strictly valid only when used with the specified mesh.

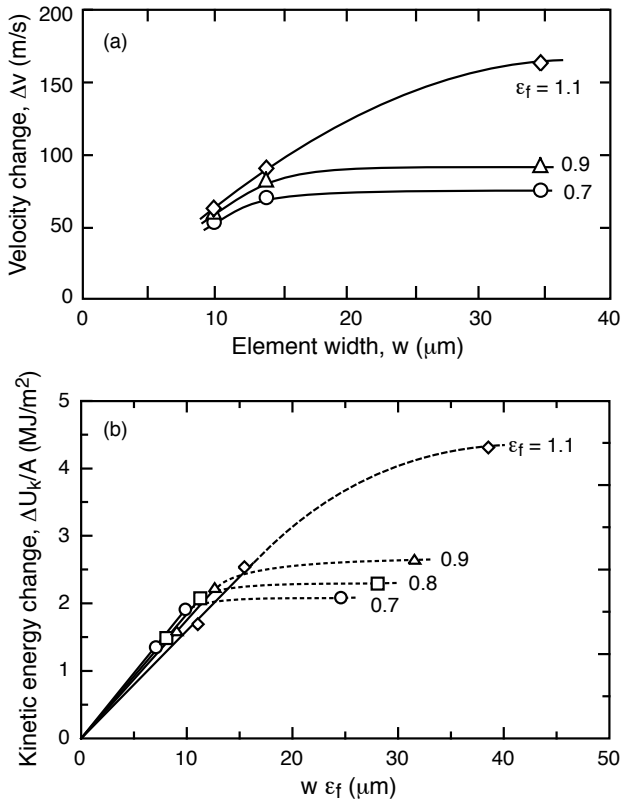


Figure 16. Effects of mesh size and failure strain on (a) predicted projectile velocity and (b) change in kinetic energy of the plate and the plug, normalized by the nominal crack area, A . (Same case as that in Figure 13).

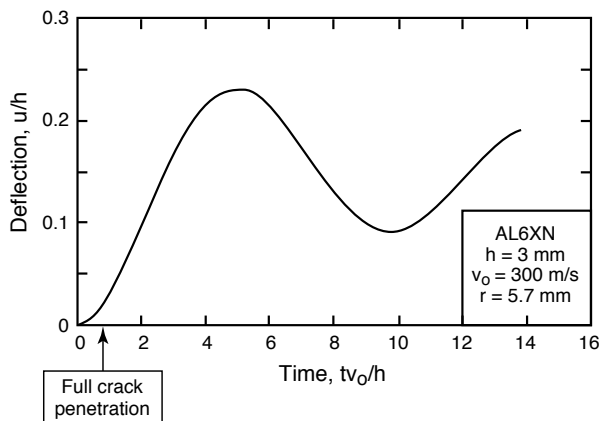


Figure 17. Temporal variation in plate deflection at a point on the impacted surface 5.7 mm from the hole center (same case as that in Figure 13). The plate remains in motion at the end of the simulation.

Generally, selection of the mesh size for this class of problems is dictated by three factors. (i) For realism, the mesh size should be broadly consistent with the known dimensions of the fracture process zone (typically 10–100 μm in ductile steels). (ii) The mesh in the vicinity of the crack plane should be sufficiently refined to ensure acceptable resolution in the predicted plastic strains. Otherwise, the accuracy of the plastic dissipation and other metrics associated with the global response will be inaccurate. (iii) Excessive refinement should be avoided, since it leads to unrealistically low dissipation while also greatly increasing computational time. Moreover, it may require the use of unrealistically high failure strains in order to match predictions with experimental measurements. The expectation is that a reasonably broad range of mesh sizes should satisfy these criteria and yield acceptable predictive capability, provided the failure strain is selected consistently with the mesh size.

References

- [ABAQUS 2005] Providence, R.I: Abaqus Inc., *ABAQUS/Explicit User's Manual, Version 6.5-1*, Providence, R.I: Abaqus Inc., 2005.
- [Borvik et al. 1999] T. Borvik, M. Langseth, O. S. Hopperstad, and K. A. Malo, "Ballistic penetration of steel plates", *Int. J. Impact Eng.* **22** (1999), 855–86.
- [Borvik et al. 2002a] T. Borvik, O. S. Hopperstad, T. Berstad, and M. Langseth, "Perforation of 12 mm thick steel plates by 20 mm diameter projectiles with flat, hemispherical and conical noses: part II: numerical simulations", *Int. J. Impact Eng.* **27**:1 (2002), 37–64.
- [Borvik et al. 2002b] T. Borvik, M. Langseth, O. S. Hopperstad, and K. A. Malo, "Perforation of 12 mm thick steel plates by 20 mm diameter projectiles with flat, hemispherical and conical noses: part I: experimental study", *Int. J. Impact Eng.* **27**:1 (2002), 19–35.
- [Gullerud et al. 2000] A. S. Gullerud, X. Gao, B. Dodds Jr., and R. Haj-Ali, "Simulation of ductile crack growth using computational cells: numerical aspects", *Eng. Fract. Mech.* **66** (2000), 65–92.
- [Johnson and Cook 1985] G. R. Johnson and W. H. Cook, "Fracture characteristics of three metals subjected to various strains, strain rates, temperatures and pressures", *Eng. Fract. Mech.* **21** (1985), 31–48.
- [Liang et al. 2007] Y. Liang, A. V. Spuskanyuk, S. E. Flores, D. R. Hayhurst, J. W. Hutchinson, R. M. McMeeking, and A. G. Evans, "Response of metallic sandwich panels to water blasts", *J. Appl. Mech.* **74**:1 (2007), 81–99.
- [Liu and Guo 2000] C. R. Liu and Y. B. Guo, "Finite element analysis of sequential cuts and tool-chip friction on residual stresses in a machined layer", *Int. J. Mech. Sci.* **42** (2000), 1069–1086.
- [Menkes and Opat 1973] S. B. Menkes and H. J. Opat, "Tearing and shear failure in explosively loaded clamped beams", *Exp. Mech.* **13** (1973), 480–486.
- [Needleman and Tvergaard 1994] A. Needleman and V. Tvergaard, "Mesh effects in the analysis of dynamic ductile crack growth", *Eng. Fract. Mech.* **47**:1 (1994), 75–91.
- [Nemat-Nasser et al. 2001] S. Nemat-Nasser, W. G. Guo, and D. P. Kihl, "Thermomechanical response of AL6-XN stainless steel over a wide range of strain rates", *J. Mech. Phys. Solids* **49** (2001), 1823–1846.
- [Nurick and Shave 1996] G. N. Nurick and G. C. Shave, "The deformation and tearing of thin square plates subjected to impulsive loads- an experimental study", *Int. J. Mech. Sci.* **18**:1 (1996), 99–116.
- [Suo et al. 1993] Z. Suo, C. F. Shih, and A. G. Varias, "A theory for cleavage cracking in the presence of plastic flow", *Acta Metall. Mater.* **41**:5 (1993), 1551–1557.
- [Teng and Wierzbicki 2005] X. Teng and T. Wierzbicki, "Dynamic shear plugging of beams and plates with an advancing crack", *Int. J. Impact Eng.* **31** (2005), 667–698.
- [Tvergaard and Hutchinson 1992] V. Tvergaard and J. W. Hutchinson, "The relation between crack growth resistance and fracture process parameters in elastic-plastic solids", *J. Mech. Phys. Solids* **40**:6 (1992), 1377–1397.

Received 29 Oct 2007. Accepted 29 Oct 2007.

KEN NAHSHON: ken.nahshon@navy.mil

Division of Engineering and Applied Sciences, Harvard University, Cambridge, MA 02138, United States

MICHAEL G. PONTIN: mpontin@engineering.ucsb.edu

Materials Department, University of California, Santa Barbara, CA 93106-5050, United States

ANTHONY G. EVANS: agevans@engineering.ucsb.edu

Materials Department, University of California, Santa Barbara, CA 93106-5050, United States

JOHN W. HUTCHINSON: jutchins@fas.harvard.edu

Division of Engineering and Applied Sciences, Harvard University, Cambridge, MA 02138, United States

FRANK W. ZOK: zok@engineering.ucsb.edu

Materials Department, University of California, Santa Barbara, CA 93106, United States

SUBMISSION GUIDELINES

ORIGINALITY

Authors may submit manuscripts in PDF format on-line. Submission of a manuscript acknowledges that the manuscript is *original and has neither previously, nor simultaneously, in whole or in part, been submitted elsewhere*. Information regarding the preparation of manuscripts is provided below. Correspondence by email is requested for convenience and speed. For further information, write to:

[Marie-Louise Steele](#)
Division of Mechanics and Computation
Durand Building, Room 262
Stanford University
Stanford CA 94305

LANGUAGE

Manuscripts must be in English. A brief abstract of about 150 words or less must be included. The abstract should be self-contained and not make any reference to the bibliography. Also required are keywords and subject classification for the article, and, for each author, postal address, affiliation (if appropriate), and email address if available. A home-page URL is optional.

FORMAT

Authors are encouraged to use L^AT_EX and the standard article class, but submissions in other varieties of T_EX, and, exceptionally in other formats, are acceptable. Electronic submissions are strongly encouraged in PDF format only; after the refereeing process we will ask you to submit all source material.

REFERENCES

Bibliographical references should be listed alphabetically at the end of the paper and include the title of the article. All references in the bibliography should be cited in the text. The use of B^IB_T_EX is preferred but not required. Tags will be converted to the house format (see a current issue for examples), however, in the manuscript, the citation should be by first author's last name and year of publication, e.g. "as shown by Kramer, et al. (1994)". Links will be provided to all literature with known web locations and authors are encouraged to provide their own links on top of the ones provided by the editorial process.

FIGURES

Figures prepared electronically should be submitted in Encapsulated PostScript (EPS) or in a form that can be converted to EPS, such as GnuPlot, Maple, or Mathematica. Many drawing tools such as Adobe Illustrator and Aldus FreeHand can produce EPS output. Figures containing bitmaps should be generated at the highest possible resolution. If there is doubt whether a particular figure is in an acceptable format, the authors should check with production by sending an email to:

production@mathscipub.org

Each figure should be captioned and numbered so that it can float. Small figures occupying no more than three lines of vertical space can be kept in the text ("the curve looks like this:"). It is acceptable to submit a manuscript with all figures at the end, if their placement is specified in the text by means of comments such as "Place Figure 1 here". The same considerations apply to tables.

WHITE SPACE

Forced line breaks or page breaks should not be inserted in the document. There is no point in your trying to optimize line and page breaks in the original manuscript. The manuscript will be reformatted to use the journal's preferred fonts and layout.

PROOFS

Page proofs will be made available to authors (or to the designated corresponding author) at a web site in PDF format. Failure to acknowledge the receipt of proofs or to return corrections within the requested deadline may cause publication to be postponed.

Journal of Mechanics of Materials and Structures

Volume 2, Nº 10 December 2007

Special issue on Recent Advances in Impact Engineering

- Mechanics of polycarbonate during high-rate tension** S. S. SARVA AND M. C. BOYCE 1853
- Two-dimensional shock induced collapse of gas bubble near a semiinfinite deformable solid**
W. XIE AND Y. L. YOUNG 1881
- Experimental and computational evaluation of compressive response of single and hex-arrayed aluminum tubes**
S. NEMAT-NASSER, M. R. AMINI, J. Y. CHOI AND J. ISAACS 1901
- An approach to modeling extreme loading of structures using peridynamics**
P. N. DEMMIE AND S. A. SILLING 1921
- Performance and failure of metal sandwich plates subjected to shock loading**
A. VAZIRI, Z. XUE AND J. W. HUTCHINSON 1947
- Computational modeling of tungsten carbide sphere impact and penetration into high-strength-low-alloy (HSLA)-100 steel targets**
C. G. FOUNTZOULAS, G. A. GAZONAS AND B. A. CHEESEMAN 1965
- Deformation and fracture modes of sandwich structures subjected to underwater impulsive loads**
L. F. MORI, S. LEE, Z. Y. XUE, A. VAZIRI, D. T. QUEHEILLALT, K. P. DHARMASENA, H. N. G. WADLEY, J. W. HUTCHINSON AND H. D. ESPINOSA 1981
- Dynamic failure of clamped circular plates subjected to an underwater shock**
S. KAZEMAHVAZI, D. RADFORD, V. S. DESHPANDE AND N. A. FLECK 2007
- Dynamic compression of square honeycomb structures during underwater impulsive loading**
H. N. G. WADLEY, K. P. DHARMASENA, D. T. QUEHEILLALT, Y. CHEN, P. DUDT, D. KNIGHT, K. KIDDY, Z. XUE AND A. VAZIRI 2025
- Dynamic shear rupture of steel plates**
K. NAHSHON, M. G. PONTIN, A. G. EVANS, J. W. HUTCHINSON AND F. W. ZOK 2049